

DISCRETIZED BOND-BASED PERIDYNAMICS FOR SOLID MECHANICS

By

Wenyang Liu

A DISSERTATION

Submitted to  
Michigan State University  
in partial fulfillment of the requirements  
for the degree of

DOCTOR OF PHILOSOPHY

Civil Engineering

2012

## ABSTRACT

### DISCRETIZED BOND-BASED PERIDYNAMICS FOR SOLID MECHANICS

By

Wenyang Liu

The numerical analysis of spontaneously formed discontinuities such as cracks is a long-standing challenge in the engineering field. Approaches based on the mathematical framework of classical continuum mechanics fail to be directly applicable to describe discontinuities since the theory is formulated in partial differential equations, and a unique spatial derivative, however, does not exist on the singularities. Peridynamics is a reformulated theory of continuum mechanics. The partial differential equations that appear in the classical continuum mechanics are replaced with integral equations. A spatial range, which is called the horizon  $\delta$ , is associated with material points, and the interaction between two material points within a horizon is formed in terms of the bond force. Since material points separated by a finite distance in the reference configuration can interact with each other, the peridynamic theory is categorized as a nonlocal method.

The primary focus in this research is the development of the discretized bond-based peridynamics for solid mechanics. A connection between the classical elasticity and the discretized peridynamics is established in terms of peridynamic stress. Numerical micromoduli for one- and three-dimensional models are derived. The elastic responses of one- and three-dimensional peridynamic models are examined, and the boundary effect associated with the size of the horizon is discussed. A pairwise compensation scheme is introduced in this research for simulations of an elastic body of Poisson ratio not equal to  $1/4$ . In order to enhance the computational efficiency, the research-purpose peridynamics code is implemented in an

NVIDIA graphics processing unit for the highly parallel computation. Numerical studies are conducted to investigate the responses of brittle and ductile material models. Stress-strain behaviors with different grid sizes and horizons are studied for a brittle material model. A comparison of stresses and strains between finite element analyses and peridynamic solutions is performed for a ductile material. To bridge material models at different scales, a multiscale procedure is proposed.

An approach to couple the discretized peridynamics and the finite element method is developed to take advantage of the generality of peridynamics and the computational efficiency of the finite element method. The coupling of peridynamic and finite element subregions is achieved by means of interface elements. Two types of coupling schemes, the VL-coupling scheme and the CT-coupling scheme respectively, are introduced. Numerical examples are presented to validate the proposed coupling approach including one- and three-dimensional elastic problems and the mixed mode fracture in a double-edge-notched concrete specimen.

A numerical scheme for the contact-impact procedure ensuring compatibility between a peridynamic domain and a non-peridynamic domain is developed. A penalty method is used to enforce displacement constraints for transient analyses by the explicit time integration. In the numerical examples, the impact between two rigid bodies is investigated to validate the contact algorithm. The ballistic perforation through a steel plate is investigated, and the residual velocities of the projectile are compared with the results by an analytical model.

Peridynamics is applied to study porous brittle materials. An algorithm is developed to generate randomly distributed cubic voids and spherical voids for a given porosity. The material behaviors at the macroscopic level including the resultant Young's modulus and the strength are studied with varying amounts of porosities. The degradations of Young's modulus and strength are compared with empirical and analytical solutions.

To my mother, without whom I could not have completed this work

## ACKNOWLEDGMENT

I would like to express my deepest appreciation to all the people who have inspired and helped me during the course of my studies. First of all, I would like to express my gratitude to my advisor, Professor Jung-Wuk Hong. I appreciate the opportunity he gave me to study computational mechanics at Michigan State University. I thank him for his guidance, support, and countless hours of insightful discussion. I would like to thank Professors Venkatesh Kodur, Nizar Lajnef, and Xinran Xiao for joining my Ph.D. guidance committee, for their valuable time, and for their advice throughout my education at Michigan State University.

A special appreciation is given to the Department of Civil and Environmental Engineering at Michigan State University. I thank the department for all their assistance, for supporting me to attend a conference, and for my fellowship. I am thankful to all instructors with whom I took courses at MSU, Professors Seungik Baek, Xinran Xiao, Thomas Pence, Giles Brereton, Venkatesh Kodur, Jung-Wuk Hong, and Parviz Soroushian. The knowledge I learned from them has provided me a solid background to conduct research. I thank the staff at High Performance Computing Center at MSU for helping me using their computational resources. I thank Zeynep Altinsel for teaching me speaking skills and all the encouragement she gave me. I thank all of my friends for their support.

The research in this dissertation has been supported by the U.S. Air Force Office of Scientific Research (Grant FA 9550-10-1-0222) and the MSU startup fund of Professor Jung-Wuk Hong.

# TABLE OF CONTENTS

<b>List of Tables</b> . . . . .	<b>ix</b>
<b>List of Figures</b> . . . . .	<b>xvi</b>
<b>List of Symbols</b> . . . . .	<b>xvii</b>
<b>Chapter 1</b>	
<b>Introduction</b> . . . . .	<b>1</b>
1.1 Overview of peridynamics . . . . .	1
1.2 Research Objectives . . . . .	4
1.3 Scope . . . . .	5
<b>Chapter 2</b>	
<b>Literature review</b> . . . . .	<b>7</b>
2.1 Numerical predictions of crack growth . . . . .	7
2.2 Peridynamics . . . . .	10
<b>Chapter 3</b>	
<b>Discretized Peridynamics for Linear Elastic Solids</b> . . . . .	<b>14</b>
3.1 Introduction . . . . .	14
3.2 Theory . . . . .	15
3.2.1 Peridynamic formulation . . . . .	15
3.2.2 Micromodulus of elastic materials . . . . .	20
3.2.2.1 One-dimensional model . . . . .	21
3.2.2.2 Three-dimensional model . . . . .	23
3.2.3 Pairwise compensation scheme . . . . .	27
3.3 Case studies . . . . .	30
3.3.1 Numerical implementation . . . . .	30
3.3.2 Comparison of peridynamics and analytical solution( $\nu = \frac{1}{4}$ ) . . . . .	31
3.3.2.1 One-dimensional bar . . . . .	31
3.3.2.2 Three-dimensional bar . . . . .	32
3.3.3 Comparison of modified peridynamics and analytical solution ( $\nu \neq \frac{1}{4}$ ) . . . . .	39
3.4 Summary . . . . .	42

<b>Chapter 4</b>	
<b>Discretized Peridynamics for Brittle and Ductile Solids . . . . .</b>	<b>43</b>
4.1 Introduction . . . . .	43
4.2 Theory . . . . .	44
4.3 Computation . . . . .	45
4.3.1 Numerical implementation . . . . .	45
4.3.2 Implementing Peridynamics in GPU . . . . .	45
4.4 Case studies . . . . .	53
4.4.1 Brittle material . . . . .	53
4.4.2 Ductile material . . . . .	61
4.5 Summary . . . . .	69
<b>Chapter 5</b>	
<b>Coupling of Discretized Peridynamics with Finite Element Method . . .</b>	<b>71</b>
5.1 Introduction . . . . .	71
5.2 Theory . . . . .	73
5.2.1 Finite element formulations . . . . .	73
5.3 Coupling between the peridynamic and finite element subregions . . . . .	76
5.3.1 Coupling schemes . . . . .	76
5.3.2 Inverse isoparametric mapping . . . . .	81
5.4 Numerical applications . . . . .	85
5.4.1 One-dimensional bar . . . . .	85
5.4.2 Three-dimensional bar . . . . .	88
5.4.3 Mixed mode fracture in a tension-shear specimen . . . . .	97
5.5 Summary . . . . .	103
<b>Chapter 6</b>	
<b>Discretized Peridynamics for Contact-Impact Problems . . . . .</b>	<b>105</b>
6.1 Introduction . . . . .	105
6.2 Theory . . . . .	110
6.2.1 Peridynamic short-range forces . . . . .	110
6.2.2 Inverse isoparametric mapping . . . . .	111
6.2.3 Contact algorithm . . . . .	112
6.2.4 Penalty method . . . . .	114
6.3 Ballistic limit . . . . .	116
6.4 Numerical studies . . . . .	118
6.4.1 Material behavior and modeling . . . . .	118
6.4.2 Rigid-body impact . . . . .	123
6.4.3 Ballistic perforation . . . . .	126
6.5 Summary . . . . .	134
<b>Chapter 7</b>	
<b>Modeling of Porous Brittle Solids using Peridynamics . . . . .</b>	<b>136</b>
7.1 Introduction . . . . .	136
7.2 Theory . . . . .	139

7.3	Numerical implementation . . . . .	142
7.4	Case studies . . . . .	143
7.4.1	Cubic voids . . . . .	143
7.4.2	Spherical voids . . . . .	148
7.5	Summary . . . . .	156
<b>Chapter 8</b>		
	<b>Conclusions and Recommendations . . . . .</b>	<b>157</b>
8.1	Conclusions . . . . .	157
8.2	Contributions . . . . .	161
8.3	Recommendations for future research . . . . .	162
<b>Appendix A</b>		
	<b>Derivation of Three-dimensional Micromodulus . . . . .</b>	<b>166</b>
<b>Appendix B</b>		
	<b>Derivation of Modified Peridynamic Young's Modulus . . . . .</b>	<b>169</b>
<b>Appendix C</b>		
	<b>Nonlinear Least Squares Method . . . . .</b>	<b>172</b>
<b>Appendix D</b>		
	<b>Newton-Raphson Method for Multi-dimensional Nonlinear Systems . .</b>	<b>175</b>
<b>Bibliography . . . . .</b>		<b>178</b>



## LIST OF TABLES

Table 3.1	Micromodulus $c_1$ in one-dimensional domain. . . . .	23
Table 3.2	Micromodulus $c_3$ in three-dimensional domain. . . . .	26
Table 4.1	Dependent loops (Algorithm 1). . . . .	49
Table 4.2	Independent loops (Algorithm 2). . . . .	50
Table 4.3	The wall-clock time to calculate bond forces for one time-step using a node in the CPU. The three-dimensional peridynamic model has 4,725 nodes, the horizon $\delta = 2\Delta x$ and $\Delta x = 0.5$ mm. . . . .	51
Table 4.4	The wall-clock time to run peridynamic models for 500,000 time-steps on GPU and CPU, respectively. Peridynamic models have the horizon $\delta = 2\Delta x$ and $\Delta x = 0.5$ mm. . . . .	51
Table 6.1	Explicit contact algorithm. . . . .	116
Table 6.2	Numerical results of residual velocities. . . . .	127
Table 7.1	Algorithm to generate randomly distributed spherical voids. . . . .	143
Table 7.2	Young's modulus and tensile strength of specimens containing cubic voids. . . . .	144
Table 7.3	Young's modulus and tensile strength of specimens containing spherical voids within the boundary. . . . .	149
Table 7.4	Young's modulus and tensile strength of specimens containing spherical voids intersecting with boundaries. . . . .	150

## LIST OF FIGURES

Figure 1.1	Schematic of peridynamics. (For interpretation of the references to color in this and all other figures, the reader is referred to the electronic version of this dissertation.) . . . . .	2
Figure 3.1	(a) Relationships among relative position vector and the relative displacement vector within a peridynamic horizon. (b) Pairwise force vector. . . . .	16
Figure 3.2	Discretized domain for computation. . . . .	19
Figure 3.3	Volume calculation scheme for discretized peridynamics. The volume is reduced on the boundary of a horizon. . . . .	19
Figure 3.4	Volumetric ratio in a horizon. The ratio decreases to 1/2 at the border of a horizon [135]. . . . .	20
Figure 3.5	Pairwise forces acting through a cross section of a node for $\delta = 2\Delta x$ in a one-dimensional domain. Each node, represented by a sphere, has a volume of $(\Delta x)^3$ . . . . .	22
Figure 3.6	Pairwise forces acting through a cross section of a node for $\delta = 2\Delta x$ in a three-dimensional domain. Each node, represented by a sphere, has a volume of $(\Delta x)^3$ . . . . .	24
Figure 3.7	Number of bonds acting through a cross section of a node in a three-dimensional domain. . . . .	25
Figure 3.8	Micromodulus for different horizons ( $E = 70$ GPa, and $\nu = 1/4$ ). . .	26
Figure 3.9	Pairwise compensation scheme. . . . .	27
Figure 3.10	Three-dimensional bar subjected to a tension. . . . .	29

Figure 3.11	Three-dimensional bar subjected to a tension. Lateral forces are added to take account of $\nu \neq \frac{1}{4}$ . . . . .	29
Figure 3.12	Strain distribution of the one-dimensional bar in x-direction. . . . .	32
Figure 3.13	Three-dimensional bar discretized by $21 \times 15 \times 15$ nodes. . . . .	33
Figure 3.14	Strain distribution along the x-axis in the three-dimensional bar. (a) Numerical micromodulus $c_3$ given in Table 3.2 is used for each horizon and (b) analytical micromodulus $\tilde{c}_3$ given in Equation (3.14) is used. The classical (local) elasticity solution of strain $\varepsilon_x = 0.005$ . . . . .	34
Figure 3.15	(a) Strain- and (b) stress-distributions on the cross section at $x = 5.0$ mm. The classical (local) elasticity solution of strain $\varepsilon_x = 0.005$ and stress $\sigma_x = 350$ MPa. The horizon $\delta = 2\Delta x$ , and the numerical micromodulus $c_3$ is utilized in the simulation. . . . .	35
Figure 3.16	Poisson ratio along the three-dimensional peridynamic bar as shown in Figure 3.13. The given Poisson ratio of the material is $\nu = \frac{1}{4}$ . The horizon $\delta = 2\Delta x$ , and the numerical micromodulus $c_3$ is utilized in the simulation. . . . .	36
Figure 3.17	Strain distribution at the end surface of the bar for different horizons using the numerical micromodulus: (a) $\delta = 2\Delta x$ , (b) $\delta = 3\Delta x$ , (c) $\delta = 4\Delta x$ , and (d) $\delta = 5\Delta x$ . The classical (local) elasticity solution of strain $\varepsilon_x = 0.005$ . . . . .	37
Figure 3.18	(a) Strain $\varepsilon_x$ and (b) Poisson ratio $\nu$ along the bar by the modified peridynamic formulation. The classical (local) elasticity solution of strain $\varepsilon_x = 0.005$ , and the Poisson ratio $\nu$ of the material is 0.3. The horizon $\delta = 2\Delta x$ , and the modified numerical micromodulus $\hat{c}_3$ for pairwise compensation scheme is utilized in the simulation. . . . .	41
Figure 4.1	(a) Bond force as a function of bond stretch in a brittle material model. (b) Bond force as a function of bond stretch in a ductile material model. . . . .	44
Figure 4.2	NVIDIA Tesla Block Diagram [186]. . . . .	47
Figure 4.3	A benchmark problem of matrix multiplication. . . . .	48

Figure 4.4	Comparison between the GPU enabled version of peridynamics code and the serial version. (a) Wall-clock time and (b) the speedup of the GPU version over the serial version. . . . .	52
Figure 4.5	(a) The geometry of a three-dimensional bar and the boundary conditions; (b) Displacement of the boundary region versus time. . . . .	54
Figure 4.6	Stress on the cross section at $x = 5.0$ mm for (a) different horizon $\delta$ with the grid size $\Delta x = 0.5$ mm and (b) different grid size $\Delta x$ with the horizon $\delta = 2\Delta x$ . $\varepsilon_x$ is the engineering strain imposed by the displacement at both ends of the bar. . . . .	56
Figure 4.7	Strain $\varepsilon_x$ at time $t = 1.0 \times 10^{-3}$ s as denoted by I in Figure 4.6(b). The horizon $\delta = 2\Delta x$ . (a) $\Delta x = 0.50$ mm; (b) $\Delta x = 0.25$ mm; (c) the cross section at $z = 3.5$ mm, $\Delta x = 0.50$ mm; (d) the cross section at $z = 3.5$ mm, $\Delta x = 0.25$ mm. . . . .	57
Figure 4.8	Strain $\varepsilon_x$ at time $t = 1.6 \times 10^{-3}$ s as denoted by II in Figure 4.6(b). The horizon $\delta = 2\Delta x$ . (a) $\Delta x = 0.50$ mm; (b) $\Delta x = 0.25$ mm; (c) the cross section at $z = 3.5$ mm, $\Delta x = 0.50$ mm; (d) the cross section at $z = 3.5$ mm, $\Delta x = 0.25$ mm. . . . .	58
Figure 4.9	Strain $\varepsilon_x$ at time $t = 1.8 \times 10^{-3}$ s as denoted by III in Figure 4.6(b). The horizon $\delta = 2\Delta x$ , the grid spacing $\Delta x = 0.50$ mm. (a) bird's-eye view of bar; (b) the cross section at $z = 3.5$ mm; (c) the cross section at $x = 5.0$ mm. . . . .	59
Figure 4.10	Strain $\varepsilon_x$ at time $t = 1.8 \times 10^{-3}$ s as denoted by III in Figure 4.6(b). The horizon $\delta = 2\Delta x$ , the grid spacing $\Delta x = 0.25$ mm. (a) bird's-eye view of bar; (b) the cross section at $z = 3.5$ mm; (c) the cross section at $x = 5.0$ mm. . . . .	60
Figure 4.11	A comparison between peridynamic and FEA solutions. (a) The material model used in FEA which is identical to the constitutive for bonds in peridynamics; (b) Stress $\sigma_x$ on the cross section at $x = 5.0$ mm; (c) Stress $\sigma_x$ on an element which has a node at the center of the bar ( $x = 5.0$ mm, $y = 3.5$ mm and $z = 3.5$ mm) and the stress $\sigma_x$ on the peridynamic node at the center of the bar; (d) Strain $\varepsilon_x$ at the center of the bar ( $x = 5.0$ mm, $y = 3.5$ mm and $z = 3.5$ mm). $u_x$ is the displacement of the boundary region as shown in Figure 4.5. . . . .	64

Figure 4.12	A comparison between peridynamic and FEA solutions. (a) The modified material model used in FEA to incorporate retrieved macroscopic material properties from the peridynamic model; (b) Stress $\sigma_x$ on the cross section at $x = 5.0$ mm; (c) Stress $\sigma_x$ on an element which has a node at the center of the bar ( $x = 5.0$ mm, $y = 3.5$ mm and $z = 3.5$ mm) and the stress $\sigma_x$ on the peridynamic node at the center of the bar; (d) Strain $\varepsilon_x$ at the center of the bar ( $x = 5.0$ mm, $y = 3.5$ mm and $z = 3.5$ mm). $u_x$ is the displacement of the boundary region as shown in Figure 4.5. . . . .	66
Figure 4.13	Strain $\varepsilon_x$ when the boundary displacement $u_x = 0.025$ mm. (a) LS-DYNA and (b) peridynamics. . . . .	68
Figure 5.1	Partition of the domain. The FE subregion and the peridynamic (PD) subregion are bridged by interface elements. . . . .	77
Figure 5.2	Interface element for the coupling of FE subregion and peridynamic subregion. . . . .	78
Figure 5.3	VL-coupling scheme that divides a coupling force $\mathbf{f}^{cp}$ among FE nodes comprising the interface element. . . . .	80
Figure 5.4	CT-coupling scheme that divides a coupling force $\mathbf{f}^{cp}$ among FE nodes comprising the interface segment. . . . .	80
Figure 5.5	Projection of an embedded peridynamic node on an interface segment. . . . .	83
Figure 5.6	Discretization of a one-dimensional bar. . . . .	86
Figure 5.7	Axial displacement along the bar using (a) VL-coupling scheme and (b) CT-coupling scheme. . . . .	87
Figure 5.8	Three-dimensional bar subjected to tension. . . . .	89
Figure 5.9	Displacements (a) $u_x$ and (b) $u_y$ at different locations using the VL-coupling scheme. Coordinates of the measuring position are given in parenthesis. . . . .	92
Figure 5.10	Displacements (a) $u_x$ and (b) $u_y$ at different locations using the CT-coupling scheme. Coordinates of the measuring position are given in parenthesis. . . . .	93

Figure 5.11	Axial displacement along the edge using the CT-coupling scheme. . . . .	94
Figure 5.12	Strain $\varepsilon_x$ distributions (a) on the bar and (b) on the interface when the applied traction $\sigma_x = 700$ MPa. The CT-coupling scheme is used in the simulation. . . . .	95
Figure 5.13	Summation of coupling forces in the longitudinal direction on the interface elements at the left end of the bar. The CT-coupling scheme is used in the simulation. . . . .	96
Figure 5.14	Mixed mode fracture test: (a) geometry of the specimen; (b) subregions of the coupling model. . . . .	98
Figure 5.15	Numerical prediction of crack paths using the VL-coupling scheme. Boundary displacement: (a) $u_n = 0.0220$ mm; (b) $u_n = 0.0225$ mm; (c) $u_n = 0.03$ mm; (d) $u_n = 0.09$ mm. . . . .	101
Figure 5.16	Numerical prediction of crack paths using the CT-coupling scheme. Solid curves are crack paths observed in the experiments from [130]. Boundary displacement: (a) $u_n = 0.0220$ mm; (b) $u_n = 0.0225$ mm; (c) $u_n = 0.03$ mm; (d) $u_n = 0.09$ mm. . . . .	102
Figure 6.1	Slave node and four master segments. . . . .	111
Figure 6.2	Projection of the vector $\mathbf{g}$ onto a master segment. . . . .	113
Figure 6.3	Slave node projected on the intersection of two master segments. . . . .	113
Figure 6.4	Location of a contact point. . . . .	114
Figure 6.5	Perforation of a thin plate by a blunt projectile. . . . .	116
Figure 6.6	Peridynamic bar subjected to tension. . . . .	117
Figure 6.7	(a) Constitutive model defined for peridynamic bonds; (b) macroscopic material response of the peridynamic bar (strain $\varepsilon_x$ in the range of 0.00 to 0.05); (c) macroscopic material response of the peridynamic bar; (d) comparison of peridynamic material behavior at the macroscopic level to the experimental result of Weldox 460 E steel (strain rate in the range of $0.00074 \text{ s}^{-1}$ to $1522 \text{ s}^{-1}$ ) presented in [21]. . . . .	120

Figure 6.8	Strain $\varepsilon_x$ contour: (a) boundary displacement $u_x = 0.12$ mm; (b) boundary displacement $u_x = 0.50$ mm; (c) boundary displacement $u_x = 1.00$ mm; (d) boundary displacement $u_x = 2.50$ mm. . . . .	122
Figure 6.9	Impact between two rigid bodies. . . . .	123
Figure 6.10	(a) Displacement of the projectile and (b) velocity of the projectile. . . . .	125
Figure 6.11	Modeling of a peridynamic plate impacted by a cylindrical projectile. . . . .	126
Figure 6.12	(a) Projectile displacement and (b) residual velocity. . . . .	129
Figure 6.13	Indentation formed by the projectile with an initial velocity $v_i = 250$ m/s: (a) bird's-eye view of the plate; (b) lateral view of the plate. . . . .	130
Figure 6.14	Perforation of the plate by the projectile an the initial velocity $v_i = 300$ m/s: (a) $t = 30$ $\mu$ s, bird's-eye view of the plate; (b) $t = 30$ $\mu$ s, lateral view of the plate; (c) $t = 70$ $\mu$ s, bird's-eye view of the plate; (d) $t = 70$ $\mu$ s, lateral view of the plate; (e) $t = 120$ $\mu$ s, bird's-eye view of the plate; (f) $t = 120$ $\mu$ s, lateral view of the plate. . . . .	132
Figure 6.15	Perforation of the plate by the projectile an the initial velocity $v_i = 400$ m/s: (a) $t = 30$ $\mu$ s, bird's-eye view of the plate; (b) $t = 30$ $\mu$ s, lateral view of the plate; (c) $t = 70$ $\mu$ s, bird's-eye view of the plate; (d) $t = 70$ $\mu$ s, lateral view of the plate; (e) $t = 120$ $\mu$ s, bird's-eye view of the plate; (f) $t = 120$ $\mu$ s, lateral view of the plate. . . . .	133
Figure 7.1	Finite and heterogeneous solid [169]. . . . .	136
Figure 7.2	(a) Relative density versus angle of coalescence and (b) theoretical solution of Young's modulus of porous materials. . . . .	141
Figure 7.3	Spherical pores with annular flaws [99]. . . . .	142
Figure 7.4	Cubic voids in a specimen of dimensions of 25 mm $\times$ 25 mm $\times$ 25 mm. Porosity $P = 5\%$ . . . . .	145
Figure 7.5	Cross-sectional stress versus strain of specimens containing cubic voids. . . . .	146
Figure 7.6	(a) Normalized Young's modulus and (b) normalized tensile strength of specimens containing cubic pores. . . . .	147

Figure 7.7	Spherical pore distributions in the specimen and distributions at the cross section along the longitudinal direction. Porosities (a) $P = 5\%$ , (b) $P = 10\%$ , (c) $P = 15\%$ , and (d) $P = 20\%$ . Pores are generated within the specimen boundaries. . . . .	151
Figure 7.8	Cross-sectional stress versus strain of specimens containing spherical pores within the boundary. . . . .	152
Figure 7.9	(a) Normalized Young's modulus and (b) tensile strength of specimens containing spherical pores within the boundary. . . . .	153
Figure 7.10	Spherical pore distributions in the specimen. Porosities (a) $P = 5\%$ , (b) $P = 10\%$ , (c) $P = 15\%$ , and (d) $P = 20\%$ . Pores intersect with specimen boundaries. . . . .	154
Figure 7.11	Cross-sectional stress versus strain of specimens containing spherical pores intersecting with boundaries. . . . .	154
Figure 7.12	(a) Normalized Young's modulus and (b) tensile strength of specimens containing spherical pores intersecting with boundaries. . . . .	155
Figure 8.1	State-based peridynamics [156]. . . . .	163



## LIST OF SYMBOLS

$\mathbf{x}$	Material point in the reference configuration
$\mathbf{x}'$	Neighboring material point in the reference configuration
$\rho$	Density
$\mathbf{u}$	Displacement field
$\nabla$	Divergence
$\boldsymbol{\sigma}$	Stress matrix
$\mathbf{b}$	Body force density vector
$\mathcal{H}_x$	Neighborhood of the material point at $\mathbf{x}$
$V_{\mathbf{x}'}$	Volume of neighboring material point
$\boldsymbol{\xi}$	Relative position vector
$\boldsymbol{\eta}$	Relative displacement vector
$\mathbf{f}$	Bond force
$\delta$	Horizon
$\Delta x$	Grid spacing
$c$	Micromodulus
$s$	Bond stretch
$r_j$	Volume reduction distance
$w$	Micropotential

$\tilde{c}_1$	One-dimensional analytical micromodulus
$\tilde{c}_3$	Three-dimensional analytical micromodulus
$c_1$	One-dimensional numerical micromodulus
$c_3$	Three-dimensional numerical micromodulus
$E$	Young's modulus
$\nu$	Poisson ratio
$A$	Nodal cross-sectional area
$N_{\mathcal{L}}$	Set of bonds
$f_V^{\mathcal{L}}$	Summation of bond forces
$E_{pd}$	Peridynamic Young's modulus
$\hat{\mathbf{f}}$	Compensation force
$\hat{E}_{pd}$	Modified peridynamic Young's modulus
$\hat{\boldsymbol{\sigma}}$	Lateral stress
$\hat{c}_3$	Modified three-dimensional numerical micromodulus
$N_{\mathcal{H}_I}$	Number of neighboring nodes
$\mu$	Scalar function to determine bond failure
$s_y$	Yield stretch
$s_0$	Critical stretch
$G_f$	Energy release rate
$k$	Bulk modulus
$\mathbf{C}$	Elastic constitutive matrix
$\boldsymbol{\varepsilon}$	Strain
$\mathbf{H}$	Displacement interpolation matrix

$\mathbf{B}$	Strain-displacement matrix
$\mathbf{M}$	Mass matrix
$\mathbf{K}$	Stiffness matrix
$\mathbf{F}$	Force vector
$\mathbf{F}^{int}$	Internal force
$\mathbf{F}^{ext}$	External force
$\mathbf{F}^{cp}$	Coupling force
$\phi$	Shape function
$\mathbf{U}_{eb}$	Displacement of an embedded node
$\xi, \eta, \psi$	Natural coordinates of an embedded node
$\xi_c, \eta_c$	Natural coordinates of a projection point
$\mathbf{I}$	Converged solution of natural coordinates of an embedded node
$\mathbf{t}$	Position vector of an embedded node
$\mathbf{r}$	Position vector of a projection point
$\mathbf{f}_s$	Peridynamic short-range force
$d_s$	Maximum distance for none-zero short-range force
$m_s$	Master node
$n_s$	Slave node
$\mathbf{g}$	Vector from master node to slave node
$\mathbf{c}$	Vectors along segment edge
$\mathbf{m}$	Unit normal vector of a segment
$\mathbf{s}$	Projection of vector $\mathbf{g}$
$l$	Penetration length

$k_{cs}$	Contact stiffness
$m_1$	Nodal mass of a slave node
$m_2$	Segment mass
$\Xi_p$	Penalty scale factor
$\Xi_s$	Scale factor of slave stiffness
$\Xi_m$	Scale factor of master stiffness
$\mathbf{F}_p$	Penalty force
$v_i$	Initial velocity
$v_{bl}$	Ballistic limit velocity
$v_r$	Residual velocity
$m_p$	Projectile mass
$m_t$	Plug mass
$P$	Porosity
$X$	Relative density
$\theta$	Coalescence angle
$D$	Pore diameter

# Chapter 1

## Introduction

### 1.1 Overview of peridynamics

The analysis of problems involving discontinuities such as cracks is a long-standing challenge in the engineering field. Fundamentals of linear elastic fracture mechanics were established around 1960 [5]. The development of fracture mechanics provides a more reliable methodology than the traditional strength-based approach for engineering designs. However, the primary concern of the classical fracture mechanics is related to problems with pre-existing defects within a body, rather than spontaneous formations of discontinuities in the material. With the advent of computers, the finite element method has been developed for solving a wide range of engineering problems, for example, structural mechanics, heat transfer, and fluid flows [11]. Despite the effectiveness and applicability of the finite element method in many engineering analyses, it is difficult to use the finite element method for numerical predictions of crack growth and damage since the finite element formulations are based on the partial differential equations in classical continuum mechanics.

Peridynamics [153] is a reformulated theory of continuum mechanics. In the peridynamic theory, the partial differential equations that appear in the classical continuum mechanics are replaced with integral equations. Specifically, the stress divergence term in the equation of motion for a continuum is replaced with an integral function. Consider a body occupying

the region  $\mathcal{R}$  as shown in Figure 1.1. A spatial range, which is called the horizon  $\delta$ , is associated with a material point  $\mathbf{x}$  in the reference configuration. The material point  $\mathbf{x}$  can interact with all material points within the horizon  $\delta$ . The interaction between the material point  $\mathbf{x}$  and the material points  $\mathbf{x}'$  is formed in terms of the bond force  $\mathbf{f}$ . In the mathematical framework, the total interacting force on the material point  $\mathbf{x}$  is determined by integrating all bond forces over the spatial domain  $\mathcal{H}_x$ , which represents the neighborhood of the material point  $\mathbf{x}$  within the horizon  $\delta$ . In dynamic analyses, the acceleration of the material point  $\mathbf{x}$  is determined by the total interacting force and applied external forces.

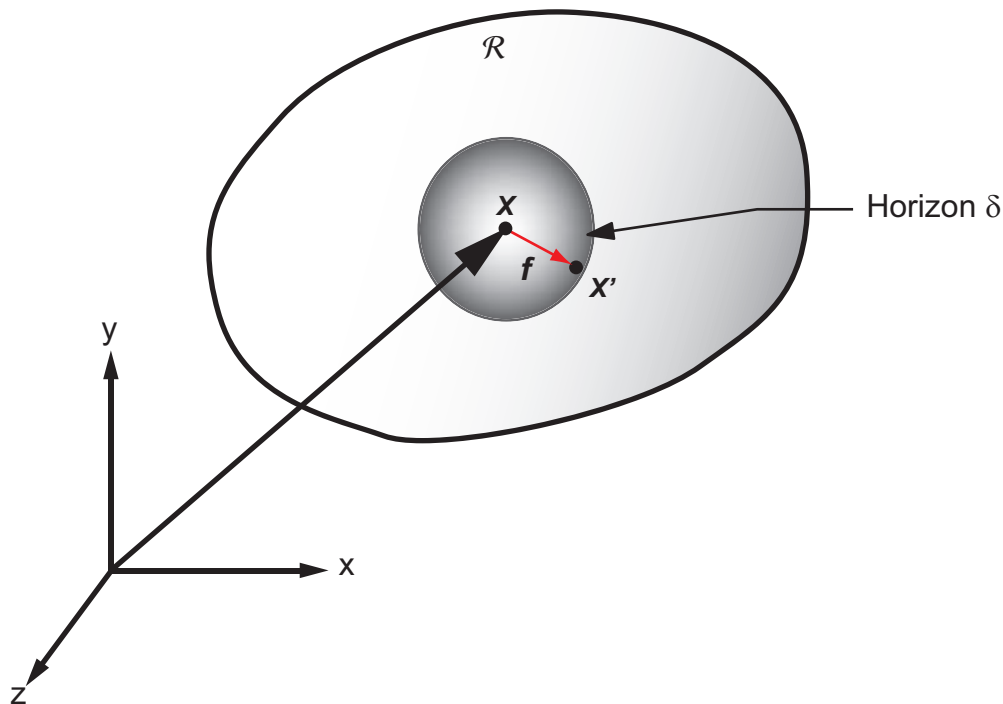


Figure 1.1: Schematic of peridynamics. (For interpretation of the references to color in this and all other figures, the reader is referred to the electronic version of this dissertation.)

The main advantage of peridynamics is that it is directly applicable to represent discontinuities. This is in contrast to approaches based on the mathematical framework of classical continuum mechanics. Special techniques are needed to treat discontinuities in the classical

approaches since the spatial derivatives in the equation of motion are undefined along discontinuities. For example, cohesive crack models [10, 44] were introduced to take account of nonlinearity near crack tips. In order to incorporate cohesive zone models into finite element analyses, interface elements are inserted *a priori* into the finite element mesh [39]. In the extended finite element method [13], enrichment functions, which work as an additional set of functions for the approximate displacement field, are added to the global displacement field for simulations of crack propagation.

In local continuum models, material points can only interact with adjacent material points by means of contact forces [113]. In contrast, materials points separated by a finite distance in the reference configuration can interact with each other in the peridynamic theory. Therefore, the peridynamic theory is categorized as a nonlocal method [153]. Although a substantial amount of research on nonlocal methods has been done before the development of peridynamics, most nonlocal modelings involve spatial derivatives [153]. Prior to the development of peridynamics, research progress has been made on mesh free particle methods [106] such as smoothed particle hydrodynamics and meshfree Galerkin methods. The differences between peridynamics and meshfree particle methods deserve to be noticed. In the smoothed particle hydrodynamics, for example, the acceleration of a particle is governed by partial differential equations [124]. On the contrary, the motion of a node in peridynamics is governed by an integral equation. In numerical implementations of peridynamics, a material region is discretized into nodes. Since peridynamics is a continuum model in essence, it might be considered as a continuum version of molecular dynamics [115].

## 1.2 Research Objectives

Compared with the classical theory, peridynamics is a relatively new methodology. The thrust of research on peridynamics is providing an alternative theory to the classical continuum mechanics that is directly applicable for numerical simulations of spontaneously formed discontinuities. In this dissertation, the primary focus is the development of the discretized bond-based peridynamics for solid mechanics. The following research objectives are identified:

- Establish a connection between the classical elasticity and the discretized peridynamics for one- and three-dimensional models.
- Investigate material behaviors of peridynamic models and the influence of the horizon.
- Develop a numerical scheme for peridynamic simulations of materials with Poisson's ratio not equal to  $1/4$ .
- Develop an algorithm enabling optimal parallelization and implement the peridynamics code in graphics processing units for high performance computing.
- Compare the macroscopic material behaviors of peridynamic models and finite element analyses and propose a multiscale approach to bridge material models defined at the different scales.
- Develop a coupling approach of discretized peridynamics and finite element method to take advantage of the generality of peridynamics in the presence of discontinuities and the computational efficiency of finite element method. For the validation of the proposed coupling approach, elastic and fracture problems will be examined.



- Propose numerical scheme for the modeling of contact between a peridynamic domain and a non-peridynamic domain such as conventional finite elements and rigid bodies. Rigid-body impact and perforation of thin plate will be investigated to validate the numerical scheme for contact-impact problems.
- Develop an algorithm to generate voids for a given porosity in peridynamic models to study the degradations of Young's modulus and strength of porous brittle materials.

### 1.3 Scope

The dissertation is organized as follows: In Chapter 1, the overview of peridynamics and the differences compared with the classical theory are summarized. In Chapter 2, the literature review regarding numerical predictions of crack growth and the development of peridynamics is provided. In Chapter 3, a connection between the classical elasticity and the discretized peridynamics is addressed in terms of peridynamic stress. Micromoduli are determined numerically for one- and three-dimensional simulations. A pairwise compensation scheme is proposed for the simulations of materials with Poisson ratio other than  $1/4$ . In Chapter 4, peridynamics is employed to study brittle and ductile materials. In order to enhance the computational efficiency, a peridynamics code is parallelized using an NVIDIA graphics processing unit in the form of a high-level implicit programming model. A multiscale procedure is proposed to bridge the peridynamic material model at the bond scale and the material model at the macroscopic scale for finite element analyses. In Chapter 5, an approach to couple discretized peridynamics with finite elements is proposed. An interface element is introduced to couple peridynamic and finite element subregions, and two types of coupling schemes are examined. The coupling approach is employed to study elastic deformations

of one- and three-dimensional models and the mixed-mode fracture in a concrete specimen. In Chapter 6, a contact-impact procedure is developed for the modeling of contact between a peridynamic domain and a non-peridynamic domain such as conventional finite elements and rigid bodies. The proposed procedure is applied to study the impact between two rigid bodies and the ballistic perforation of a thin plate. In Chapter 7, porous brittle material is studied using peridynamics. The effects of porosity on the degradation of Young's modulus and strength are investigated. The last chapter is the conclusion and descriptions of future works.

# Chapter2

## Literature review

Fracture is one of major concerns in engineering field for a long time, and researchers have made substantial efforts in order to understand material failures and alleviate potential dangers. Inglis, Griffith, and other researchers made contributions to the early development of fracture analyses [5]. Irwin extended the Griffith approaches by developing the energy release rate [5]. The fracture mechanics provides a more reliable methodology for engineering design than the traditional strength based approach. However, the classical fracture mechanics has its limitations. For example, a pre-existing crack needs to be defined, and the fracture process zone is required to be small compared to geometrical dimensions [86, 87].

### 2.1 Numerical predictions of crack growth

Numerical predictions of crack initiation and growth have been considered as a class of challenging problems. Approaches based on the mathematical framework of classical continuum mechanics fail to be directly applicable to describe discontinuities since the theory is formulated in partial differential equations, and a unique spatial derivative, however, does not exist on the singularities. In order to model crack growth and material damage, a considerable amount of research has been done.

Barenblatt [10] and Dugdale [44] first introduced the cohesive crack models, which address

relationships between the cohesive tractions resisting the separation of cracks and the crack opening displacement [151]. The cohesive zone models are incorporated into finite element models using, for example, interface elements and contact surfaces. Numerous researchers have adopted cohesive zone models in numerical simulations. For example, Foulk *et al.* [60] implemented a cohesive zone model in nonlinear finite element formulations. Ruiz *et al.* [151] studied dynamic mixed-mode fracture using three-dimensional cohesive models. Overviews of cohesive crack models have been presented by Elices *et al.* [48] and Planas *et al.* [141].

The partition of unity finite element method (PUFEM) was presented by Melenk and Babuska [120]. Belytschko and collaborators [13, 123, 167] investigated the partition of unity principle for numerical simulations of fracture problems and introduced the extended finite element method (XFEM) to alleviate shortcomings of the conventional finite element method. XFEM allows the discontinuity not constrained to element boundaries, and it can model the discontinuity without remeshing [35]. Moës and Belytschko [122] used the extended finite element method to model the growth of arbitrary cohesive cracks. Sukumar *et al.* [168, 83] implemented XFEM with Dynaflow and conducted crack growth simulations of channel-cracking in thin films. Mariani and Perego [117] presented a method for the simulation of quasi-static cohesive crack propagation using XFEM for quasi-brittle materials. Cox [35] proposed enrichment functions to represent the discontinuity using an analytical investigation of the cohesive crack problem. Considering a global level of minimizing the total energy of the system, Meschke and Dumstorff [121] proposed a variational form of XFEM for the propagation of cohesive and cohesionless cracks in quasi-brittle solids.

A large number of different techniques have been carried out by researchers. For example, Ibrahimbegovic and Delaplace [85] used microscale and mesoscale discrete models to study dynamic fracture. Kozicki *et al.* [98] showed a lattice based discrete approach to model

fracture in brittle materials. Moslemi and Khoei [125] employed an adaptive finite element analysis to model curved crack growth. Ooi and Yang [132] presented the scaled boundary finite element method to study crack propagation problems. Citarella and Buchholz [33] investigated crack growth by the dual boundary element method.

Different from FEA in which elements are connected by a topological mesh, meshfree particle methods employ a finite number of discrete particles to describe the state of a system [106]. The meshfree particle methods can be classified into microscopic, mesoscopic and macroscopic meshfree particle methods according to the length scales [109]. The difficulties for simulating many engineering problems such as penetration and fragmentation include remeshing and mapping the state variables from the old mesh to the new mesh [106]. Unlike finite element methods, meshfree particle methods eliminate mesh constraints, and demonstrate advantages in many applications. Chen *et al.* [30] presented large deformation analysis of nonlinear elastic and inelastic structures based on Reproducing Kernel Particle Method (RKPM). The application of RKPM includes, for example, elastic-plastic deformation and hyperelasticity [111]. Meshfree particle methods [106] demonstrate capability for numerical simulations of material failures. Molecular dynamics, for example, is capable of investigating nonlinearities in the vicinity of cracks, the bond breaking between atoms, and the formation of extended defects [150, 63, 25]. Holian *et al.* [78] simulated the opening-mode fracture under the tensile loading using molecular dynamics. Research on coupling finite element methods and meshless methods [108] has also been conducted. De *et al.* [37] presented development of the method of finite spheres. Hong *et al.* [79, 80] used analytical transformations before the numerical integration to improve the method of finite spheres and proposed a technique to couple finite element and finite sphere discretizations.

## 2.2 Peridynamics

Compared with the classical continuum mechanics, peridynamics is a relatively new development. Researchers have studied the peridynamic theory, its convergence to the classical theory, and numerical applications. In the following, the development of peridynamics and some crucial articles are going to be reviewed.

The first paper on the topic of peridynamics was published by Silling [153]. The development of peridynamic theory was motivated to propose an alternative theory of continuum mechanics that is useful for solving problems involving spontaneous formations of discontinuities without any special treatment on discontinuities. The main difference between peridynamics and the classical theory and other nonlocal methods is that spatial derivatives are eliminated in the peridynamic theory. The theory in [153] is specified as the bond-based peridynamics since a pairwise force function is used to describe the interaction between two material points.

The peridynamic formulation was used to study the deformation of an infinite elastic bar by Silling *et al.* [161]. In this work, it is found that the peridynamic solution converges to the classical solution as the horizon goes to zero. In addition, the solution shows some special features of peridynamics that are not presented in the classical theory. For example, the oscillation of the displacement field decays from the loading region and spreads out to infinity. The same smoothness between the displacement field and the body force field is found in the peridynamic theory. On the other hand, the displacement field is two-order smoother in derivatives than the body force field in the classical theory. On the one-dimensional bar problem, Bobaru *et al.* [20] discussed three types of numerical convergence in peridynamics, the adaptive refinement, and scaling. Other theoretical works include

the dynamic responses of a peridynamic bar [183] and the well-posedness and structural properties in the peridynamic equation [50].

A generalized formulation of bond-based peridynamics was described by Silling *et al.* [156], which is referred to as the state-based peridynamics. A force state similar to the stress tensor in the classical continuum mechanics is introduced. Different from the bond-based peridynamics, the interaction between two material points might not be along the direction of the deformed bond in the state-based peridynamics. The convergence of peridynamic state to the classical elasticity was studied by Silling and Lehoucq [157]. It is shown that the peridynamic stress tensor converges to a Piola-Kirchhoff stress tensor as the length scale goes to zero. Using the state-based peridynamic method, elastic deformation and fracture of a bar were studied by Warren *et al.* [181], and viscoplasticity was studied by Foster *et al.* [58, 59]. Silling and Lehoucq [158] presented the development of peridynamic theory of solid mechanics.

With the general applicability of peridynamics, many applications of the theory have been studied. The first publication on the numerical simulation using the peridynamic model was authored by Silling and Askari [155]. In their work, the bond-based peridynamics is employed to study the numerical convergence in an opening-mode fracture problem and the impact of a sphere on a brittle target. Dayal and Bhattacharya [36] studied the kinetics of phase transformations using peridynamics without any additional kinetic relation or the nucleation criterion. By adding pairwise peridynamic moments, Gerstle *et al.* [65] proposed a micropolar peridynamic model. Demmie and Silling [40] reviewed the development in peridynamics and conducted simulations of extreme loading on concrete structures using peridynamics. Kilic and Madenci [93] studied structural stability and failure analysis, and employed peridynamics to predict crack paths in a quenched glass plate [92]. Using

the bond-based peridynamics, Ha and Bobaru [70, 69] reproduced dynamic fracture phenomenon observed in experiments and found the source of asymmetry in the crack path in a perfectly symmetric computational model. Silling *et al.* [160] proposed a material stability condition for crack nucleation in an elastic peridynamic body. By comparing with experimental studies, Agwai *et al.* [3] conducted a comparative study of the extended finite element method, cohesive zone model, and peridynamics. Peridynamics can be implemented within the framework of molecular dynamics [134].

Peridynamics has also been applied to study composites. By introducing fiber bonds, matrix bonds, and interply bonds, Xu *et al.* [8, 188] applied peridynamics to model damage and failure in composites. Bonds break irreversibly when the bond stretch exceeds a critical value. Kilic *et al.* [91] used a random number generator to determine fiber locations in a lamina, and studied the damage in center-cracked laminates with different fiber orientations using peridynamics. Hu *et al.* [81, 82] derived the critical stretches for fiber bonds and matrix bonds considering intralamina fracture energy for longitudinal and transverse loadings, and proposed a homogenized peridynamic description of fiber-reinforced composites.

Compared with the finite element method, peridynamics is computationally expensive. Macek and Silling [115] compared computer wall-clock run times between the EMU and FEA implementations of peridynamics. The FEA implementation is much faster than the direct meshless method. Askari *et al.* [8] applied peridynamics to model material and structural failures using the Columbia Supercomputer at NASA Advanced Supercomputing Division. In order to take advantage of the general applicability of peridynamics and the efficiency of the finite element method, Macek and Silling [115] used embedded nodes and elements to couple the peridynamic domain and conventional meshes. Similar technique was employed to study shock and vibration reliability of leadfree electronics [103]. Kilic and Madenci [94]



proposed a coupling approach using overlapping regions in which both peridynamic and finite element equations are utilized. From the perspective of energy equivalence, Lubineau *et al.* [113] developed a morphing strategy for the coupling of non-local and local continuum mechanics.

# Chapter 3

## Discretized Peridynamics for Linear Elastic Solids

### 3.1 Introduction

Peridynamics is a new development of continuum mechanics that can simulate fractures and other discontinuities [153]. It reformulates the mathematical description of continuum mechanics in the forms of integral equations rather than partial differential equations [159]. The essence of peridynamics is that it computes forces on a material point using integral equations, and it might be considered as a continuum version of molecular dynamics [155]. The interacting forces between material points over certain distance render the methodology in the category of the nonlocal theory [46, 49, 183]. Unlike classical continuum mechanics, the definitions of the stress and strain have not been established in the peridynamic theory due to the nonlocal interactions. Although some efforts have been made to introduce the peridynamic stress [104], the complexity of the definition itself inhibits implementation in numerical simulations.

The bond-based peridynamics has limitations in representing continuum material properties. It can only simulate materials with Poisson ratio of  $1/4$  due to the property of Cauchy crystal that only involves two-particle interactions [155]. In order to extend the capability of peridynamics to model various materials that have different material properties, a gen-

eralized peridynamics was proposed, which directly incorporates a constitutive model from conventional solid mechanics [156, 154, 181, 58]. Gerstle *et al.* [65] proposed the micropolar peridynamics by adding rotational degrees of freedom in the links. However, straightforward numerical schemes to model peridynamic materials of Poisson ratio other than  $1/4$  have been under development.

In this chapter, micromoduli for one- and three-dimensional discretized peridynamic models are derived by equilibrating the peridynamic Young's modulus and the conventional Young's modulus under constant strain condition. The peridynamic stress corresponds to the stress in the classical (local) continuum theory, and the conventional constitutive law is utilized to obtain the peridynamic Young's modulus. Numerical studies are performed using the numerically derived micromoduli for one- and three-dimensional simulations, respectively. Comparisons of strain distributions between the peridynamic solutions and classical (local) elasticity solutions are conducted, and we discuss the boundary effect observed in the simulations. In addition, a new pairwise compensation scheme for discretized peridynamics is proposed to model materials of Poisson ratios other than  $1/4$ , and the methodology is verified with a numerical example.

## 3.2 Theory

### 3.2.1 Peridynamic formulation

The equation of motion in the classical continuum mechanics is derived from the principle of linear momentum that the rate of change of linear momentum equals the force applied on

the body as [118]

$$\rho \ddot{\mathbf{u}} = \nabla \cdot \boldsymbol{\sigma} + \mathbf{b}, \quad (3.1)$$

where  $\rho$  is the density,  $\ddot{\mathbf{u}}$  is the acceleration vector,  $\boldsymbol{\sigma}$  is the stress matrix, and  $\mathbf{b}$  is the body force vector. The formulation requires a unique spatial derivative which, however, does not exist along discontinuities. In contrast, peridynamics uses integration to compute the force on a material point, and the equation of motion of the material point at  $\mathbf{x}$  in the reference configuration at time  $t$ , as shown in Figure 1.1, is written as [135]

$$\rho \ddot{\mathbf{u}}(\mathbf{x}, t) = \int_{\mathcal{H}_{\mathbf{x}}} \mathbf{f}(\boldsymbol{\eta}, \boldsymbol{\xi}) dV_{\mathbf{x}'} + \mathbf{b}(\mathbf{x}, t), \quad (3.2)$$

where  $\mathbf{f}$  is a pairwise force vector that the material point at  $\mathbf{x}'$  exerts on the material point at  $\mathbf{x}$ , and  $\mathcal{H}_{\mathbf{x}}$  is a neighborhood of the material point at  $\mathbf{x}$ .

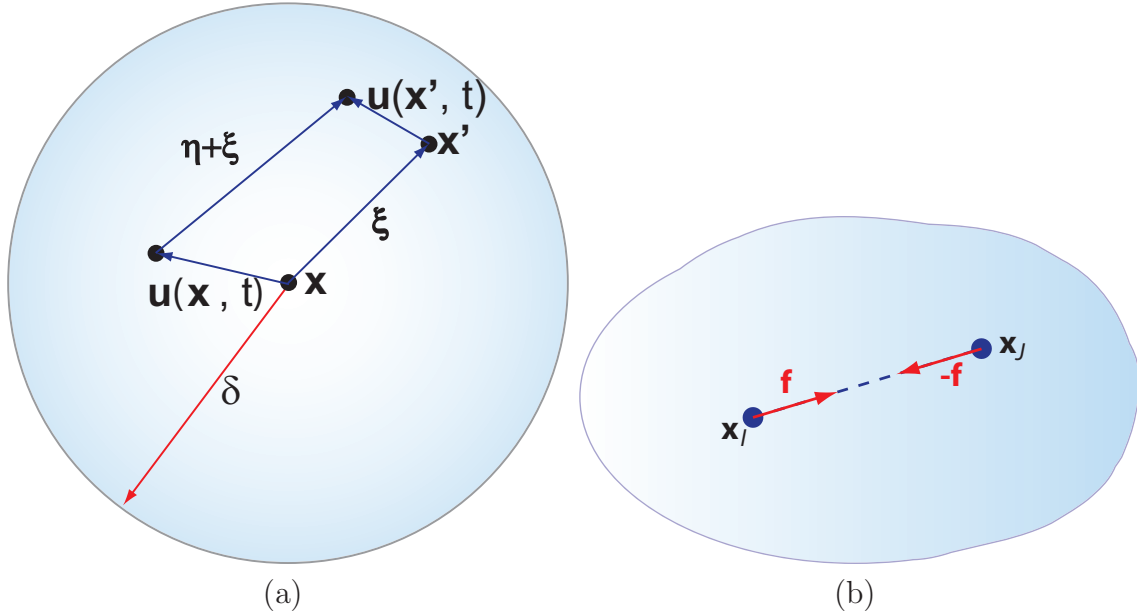


Figure 3.1: (a) Relationships among relative position vector and the relative displacement vector within a peridynamic horizon. (b) Pairwise force vector.

The relative position vector in the reference configuration shown in Figure 3.1 is expressed

as [155]

$$\boldsymbol{\xi} = \mathbf{x}' - \mathbf{x}, \quad (3.3)$$

and the relative displacement vector at time  $t$  is written as

$$\boldsymbol{\eta} = \mathbf{u}(\mathbf{x}', t) - \mathbf{u}(\mathbf{x}, t). \quad (3.4)$$

For each material point, a scalar  $\delta$ , called the horizon, is assumed to exist to determine the interacting spatial range between the material point at  $\mathbf{x}$  and the material point at  $\mathbf{x}'$  such that

$$\mathbf{f}(\boldsymbol{\eta}, \boldsymbol{\xi}) = \mathbf{0} \quad \forall \boldsymbol{\eta}, \quad \text{if } \|\boldsymbol{\xi}\| > \delta. \quad (3.5)$$

The pairwise force vector  $\mathbf{f}$  has the direction of  $\boldsymbol{\eta} + \boldsymbol{\xi}$ , which connects the material point at  $\mathbf{x}$  and the material point at  $\mathbf{x}'$  in the deformed body, as

$$\mathbf{f}(\boldsymbol{\eta}, \boldsymbol{\xi}) = f(\boldsymbol{\eta}, \boldsymbol{\xi}) \frac{\boldsymbol{\eta} + \boldsymbol{\xi}}{\|\boldsymbol{\eta} + \boldsymbol{\xi}\|}, \quad (3.6)$$

where  $f$  is a scalar-valued pairwise force function, and  $\|\cdot\|$  is the Euclidean norm. The force vector  $\mathbf{f}$  has following properties [153]: The first property is

$$\mathbf{f}(-\boldsymbol{\eta}, -\boldsymbol{\xi}) = -\mathbf{f}(\boldsymbol{\eta}, \boldsymbol{\xi}) \quad \forall \boldsymbol{\eta}, \boldsymbol{\xi}, \quad (3.7)$$

that describes the balance of linear momentum. The other property

$$(\boldsymbol{\eta} + \boldsymbol{\xi}) \times \mathbf{f}(\boldsymbol{\eta}, \boldsymbol{\xi}) = \mathbf{0} \quad (3.8)$$

arises from the balance of angular momentum. It should be noted that the balance of angular momentum is satisfied by the sum of force couples which produces zero moment [156]. For the material point at  $\mathbf{x}'$  within the horizon of the material point at  $\mathbf{x}$ , the scalar-valued pairwise force function is expressed as

$$f(\boldsymbol{\eta}, \boldsymbol{\xi}) = c \times s(t, \boldsymbol{\eta}, \boldsymbol{\xi}), \quad (3.9)$$

where  $c$  is the micromodulus, and  $s$  is the bond stretch which possesses a similar concept of the strain in elasticity. The bond stretch  $s$  is defined as

$$s(t, \boldsymbol{\eta}, \boldsymbol{\xi}) = \frac{\|\boldsymbol{\eta} + \boldsymbol{\xi}\| - \|\boldsymbol{\xi}\|}{\|\boldsymbol{\xi}\|}, \quad (3.10)$$

where  $\|\boldsymbol{\xi}\|$  is the original bond length in the reference coordinate, and  $\|\boldsymbol{\eta} + \boldsymbol{\xi}\|$  is the current bond length. If the stretch  $s = 0$ , then there is no pairwise force  $f$  between material points.

To evaluate the interactive forces among material points and to solve peridynamic equation of motion, the material domain is discretized with a number of nodes as shown in Figure 3.2. The distance between two adjacent nodes is  $\Delta x$  in  $x$ -,  $y$ -, and  $z$ -directions. All nodes have the same volume  $(\Delta x)^3$ .

In order to consider the volume reduction of a node which has an intersection with the horizon boundary as illustrated in Figure 3.3, a volume reduction scheme is introduced as [135]

$$V_J(\|\boldsymbol{\xi}\|) = \begin{cases} \left( \frac{\delta - \|\boldsymbol{\xi}\|}{2r_j} + \frac{1}{2} \right) V_J & \text{if } (\delta - r_j) \leq \|\boldsymbol{\xi}\| \leq \delta \\ V_J & \text{if } \|\boldsymbol{\xi}\| \leq (\delta - r_j) \\ 0 & \text{otherwise} \end{cases}, \quad (3.11)$$

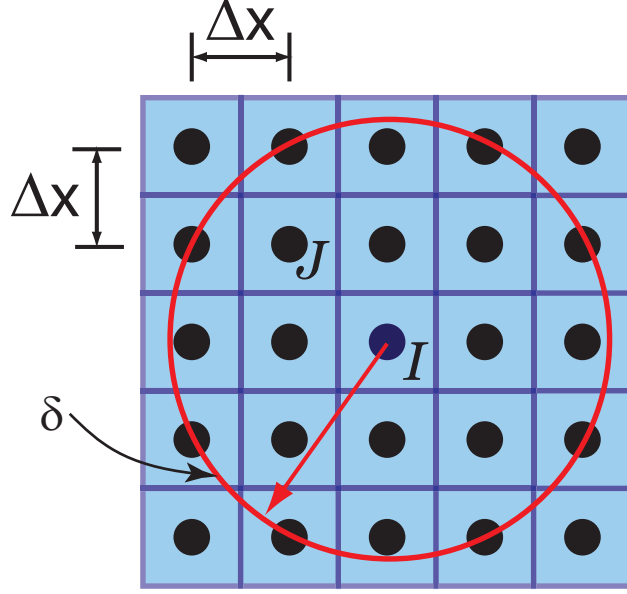


Figure 3.2: Discretized domain for computation.

where  $(\delta - r_j)$  is the distance from which the volume is reduced, and  $r_j$  is chosen to be half of the grid spacing  $\Delta x$  in numerical implementations. Figure 3.4 illustrates the volume change of the node  $J$  as the distance between the node  $I$  and the node  $J$  increases.

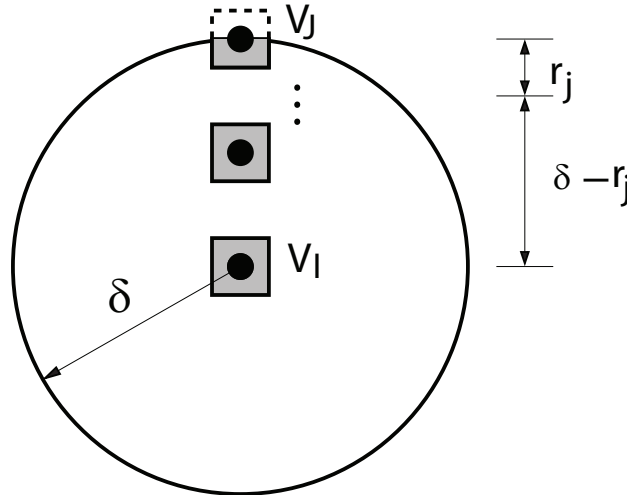


Figure 3.3: Volume calculation scheme for discretized peridynamics. The volume is reduced on the boundary of a horizon.

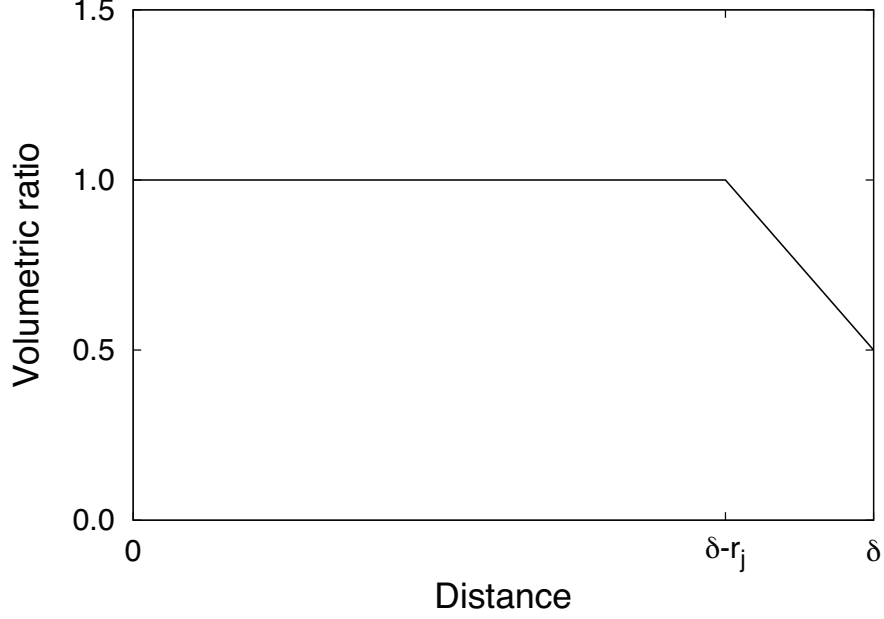


Figure 3.4: Volumetric ratio in a horizon. The ratio decreases to 1/2 at the border of a horizon [135].

### 3.2.2 Micromodulus of elastic materials

A peridynamic material is considered to be microelastic if the bond force is defined as [153, 189]

$$\mathbf{f}(\boldsymbol{\eta}, \boldsymbol{\xi}) = \frac{\partial w}{\partial \boldsymbol{\eta}}(\boldsymbol{\eta}, \boldsymbol{\xi}) \quad \forall \boldsymbol{\eta}, \boldsymbol{\xi}, \quad (3.12)$$

where  $w$  is the micropotential. Setting the strain energies of peridynamics and classical linear elasticity identical, the constant micromodulus  $\tilde{c}_1$  for one-dimensional peridynamics is obtained as [20]

$$\tilde{c}_1 = \frac{2E}{A\delta^2}, \quad (3.13)$$

where  $A$  is the cross-sectional area, and  $\tilde{c}_3$  for three-dimensional models is [49, 50]

$$\tilde{c}_3 = \frac{18k}{\pi\delta^4}, \quad (3.14)$$



where  $k$  is the material bulk modulus. In the derivation, the Poisson ratio  $\nu$  is a fixed value of  $1/4$ .

### 3.2.2.1 One-dimensional model

Consider a bar subjected to a uniaxial tension in the longitudinal direction as illustrated in Figure 3.5. The distance between nearest nodes is  $\Delta x$ , and each node has a constant volume  $(\Delta x)^3$ . The bonds can be considered as springs for elastic materials. Let  $\mathcal{L}$  be the set of bonds passing through or ending at the cross section  $A_I$  of a node from the positive side. The total force per unit volume acting through the cross section of the node  $I$  that has the horizon  $\delta = 2\Delta x$  is written as

$$\begin{aligned} f_V^{\mathcal{L}}(\mathbf{x}_I) &= \sum_{J=1}^{N_{\mathcal{L}}} f(\boldsymbol{\eta}, \boldsymbol{\xi}) V_J \\ &= fV_J + \frac{1}{2}fV_J + \frac{1}{2}fV_J = 2c_1 s V_J, \end{aligned} \tag{3.15}$$

where  $N_{\mathcal{L}}$  is the number of bonds in the set  $\mathcal{L}$ . The force contribution is reduced to 50% if the distance between two interacting nodes is equal to the horizon by applying the volume reduction scheme in Equation (3.11).

The resultant force through the cross section of the node  $I$  is given by

$$F = 2c_1 s V_J V_I, \tag{3.16}$$

and the peridynamic stress  $\sigma_x$  at the node  $I$  is calculated as

$$\sigma_x = 2c_1 s V_J V_I / A_I = 2c_1 s \Delta x^4. \tag{3.17}$$

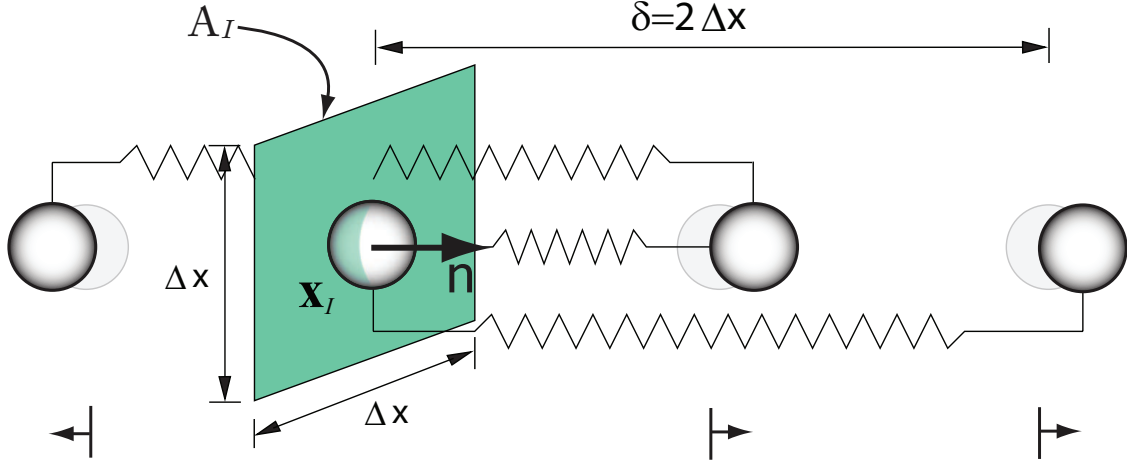


Figure 3.5: Pairwise forces acting through a cross section of a node for  $\delta = 2\Delta x$  in a one-dimensional domain. Each node, represented by a sphere, has a volume of  $(\Delta x)^3$ .

By applying Hooke's law, the corresponding peridynamic Young's modulus  $E_{pd}$  in one-dimensional peridynamic models can be obtained in terms of the peridynamic stress and the bond stretch as

$$E_{pd} = \frac{\sigma_x}{s} = 2c_1 \Delta x^4. \quad (3.18)$$

Setting the peridynamic Young's modulus  $E_{pd}$  equal to the Young's modulus  $E$  of the isotropic material, the micromodulus  $c_1$  for one-dimensional peridynamic models is obtained as

$$c_1 = \frac{E}{2\Delta x^4}. \quad (3.19)$$

The micromodulus  $c_1$  for different horizons in one-dimensional models are listed in Table 3.1. We designate  $c$  as *numerical micromodulus* since the number of bonds passing through the cross-sectional area of a node needs to be calculated numerically for different horizons. Compared with the one-dimensional micromodulus given in Equation (3.13) which is obtained from the elastic energy density in the classical theory, it can be shown that the one-dimensional analytical micromodulus yields the numerical micromoduli summarized in

Table 3.1 if  $j\Delta x$  ( $j = 2, 3, 4$  and  $5$ ) is substituted to  $\delta$ , and  $(\Delta x)^2$  is substituted to  $A$  in Equation (3.13).

Horizon $\delta$	Micromodulus $c_1$ (N/m <sup>6</sup> )
$2\Delta x$	$\frac{E}{2\Delta x^4}$
$3\Delta x$	$\frac{2E}{9\Delta x^4}$
$4\Delta x$	$\frac{E}{8\Delta x^4}$
$5\Delta x$	$\frac{2E}{25\Delta x^4}$

Table 3.1: Micromodulus  $c_1$  in one-dimensional domain.

### 3.2.2.2 Three-dimensional model

In the three-dimensional domain, an elastic body is subjected to the external force such that the bond stretch is a constant value  $s$  in the domain. Let  $\mathcal{L}$  be the set of bonds passing through or ending at the cross section  $A_I$  of a node from the positive side as shown in Figure 3.6. The horizons of  $2\Delta x$ ,  $3\Delta x$ ,  $4\Delta x$ , and  $5\Delta x$  are selected since the horizon smaller than  $1\Delta x$  would lead to no peridynamic bonds within the horizon, and horizons larger than  $5\Delta x$  will make the computation expensive. On the other hand, if  $\delta = 1\Delta x$ , the peridynamic model reduces to a truss-type system, in which each node is only connected to its nearest neighbors. Figure 3.7 represents the number of bonds in the set  $\mathcal{L}$  for different horizons. The number of bonds is 11 for the horizon  $\delta = 2\Delta x$ , and it increases to 631 for the horizon  $\delta = 5\Delta x$ .

The projection of the pairwise force  $\mathbf{f}$  in  $x$ -direction is expressed as

$$f_x = f \frac{|x_J - x_I|}{\|\boldsymbol{\xi}\|}, \quad (3.20)$$

where  $f = c_3 s$  is the magnitude of the pairwise force between node  $I$  and node  $J$ ,  $c_3$  is the

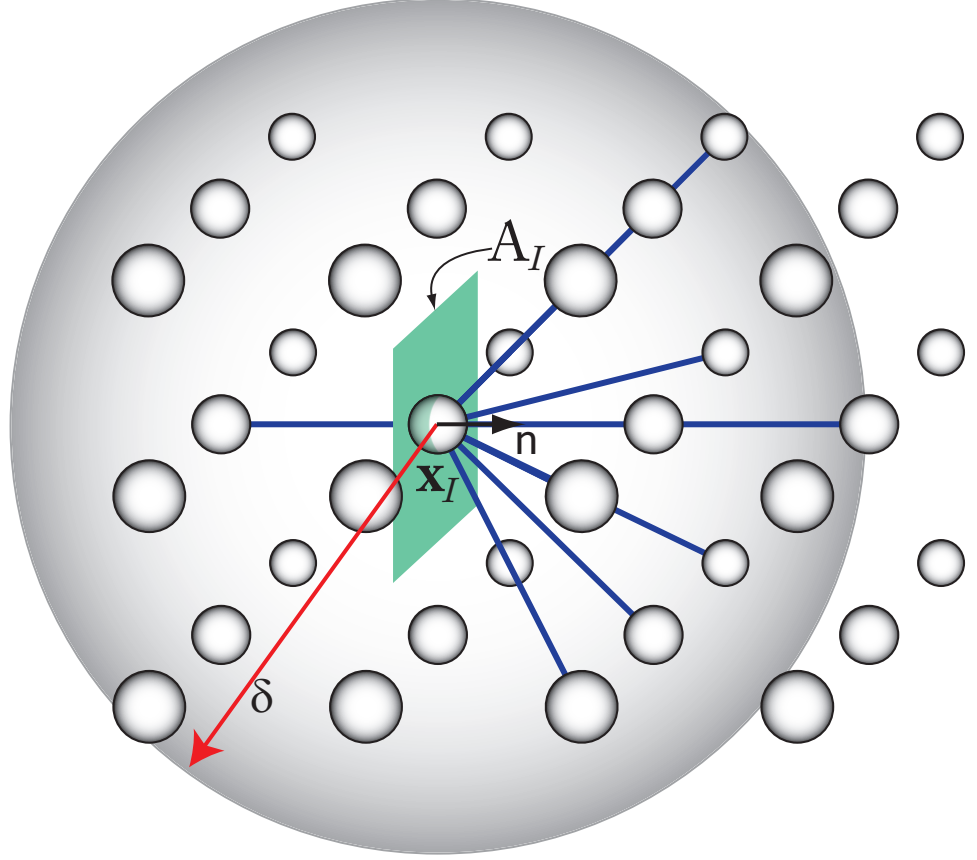


Figure 3.6: Pairwise forces acting through a cross section of a node for  $\delta = 2\Delta x$  in a three-dimensional domain. Each node, represented by a sphere, has a volume of  $(\Delta x)^3$ .

micromodulus for the three-dimensional model, and  $|x_J - x_I|$  is the distance between two nodes in the  $x$ -coordinate. It should be noted that the bond force is reduced to  $1/2$  if it passes through the edge of the cross section, and is reduced to  $1/4$  if it passes through the corner of the cross section since the portion of the forces within the domain reduce by 50% and 75%, respectively. Considering all nodes have the same volume  $(\Delta x)^3$ , the peridynamic stress  $\sigma_x$  on the cross section of the nodes  $I$  is given by

$$\sigma_x = \frac{1}{A_I} \sum_{J=1}^{N_{\mathcal{L}}} (f_x V_J) V_I, \quad (3.21)$$

where  $N_{\mathcal{L}}$  is the number of bonds in the set  $\mathcal{L}$ , and the cross-sectional area  $A_I = \Delta x^2$  in the

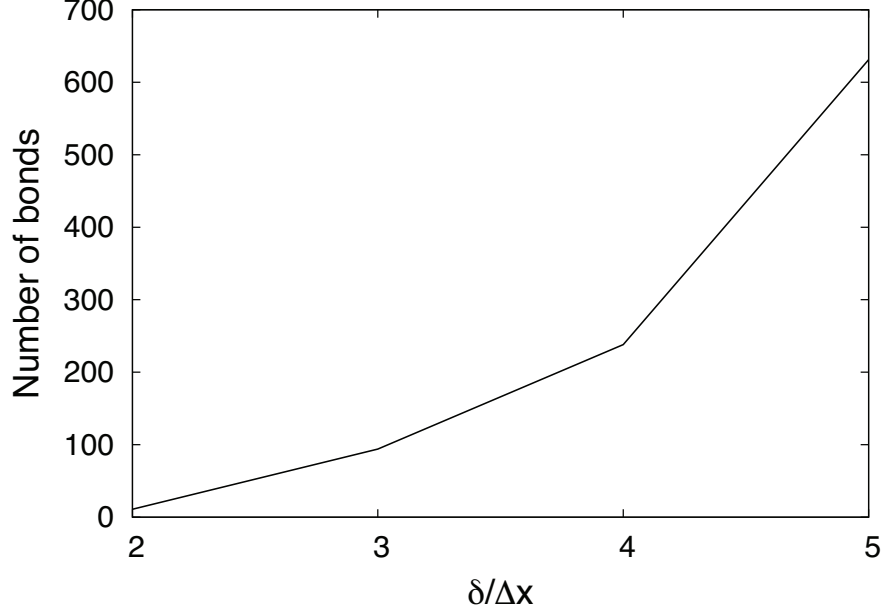


Figure 3.7: Number of bonds acting through a cross section of a node in a three-dimensional domain.

uniformly discretized grid. Since the elastic body is subjected to the isotropic expansion, the stresses in  $y$ - and  $z$ -directions are identical to the  $x$ -directional stress  $\sigma_x$ , expressed as  $\sigma_y = \sigma_z = \sigma_x$ . By applying Hooke's law of linear elasticity, the peridynamic Young's modulus  $E_{pd}$  can be obtained as

$$E_{pd} = \frac{\sigma_x}{s} - \frac{\nu(\sigma_y + \sigma_z)}{s}, \quad (3.22)$$

where Poisson ratio  $\nu = 1/4$ . By substituting Equations (3.20) and (3.21) to Equation (3.22) and setting the peridynamic Young's modulus  $E_{pd}$  in Equation (3.22) equal to the Young's modulus of the material  $E$ , the micromodulus  $c_3$  can be calculated. For example, the micromodulus for the horizon  $\delta = 2\Delta x$  is

$$c_3 = 0.302942 \frac{E}{(\Delta x)^4}, \quad (3.23)$$

which has dimensions of force per unit volume squared. The micromoduli  $c_3$  for horizons ranging from  $2\Delta x$  to  $5\Delta x$  are summarized in Table 3.2. Figure 3.8 compares the micromoduli  $c_3$  and  $\tilde{c}_3$  for an elastic material which has Young's modulus  $E = 70$  GPa and Poisson ratio  $\nu = 1/4$ . The numerically determined micromoduli  $c_3$  for discretized peridynamics are larger than the analytical micromoduli  $\tilde{c}_3$ . For the horizon  $\delta = 2\Delta x$ , numerically determined micromodulus  $c_3$  is 1.27 times larger than the micromodulus  $\tilde{c}_3$ . As the horizon to grid spacing ratio increases, the numerical micromodulus  $c_3$  converges to the analytical micromodulus  $\tilde{c}_3$ .

Horizon $\delta$	Micromodulus $c_3$ (N/m <sup>6</sup> )
$2\Delta x$	$0.302942 \frac{E}{\Delta x^4}$
$3\Delta x$	$0.052385 \frac{E}{\Delta x^4}$
$4\Delta x$	$0.017290 \frac{E}{\Delta x^4}$
$5\Delta x$	$0.006819 \frac{E}{\Delta x^4}$

Table 3.2: Micromodulus  $c_3$  in three-dimensional domain.

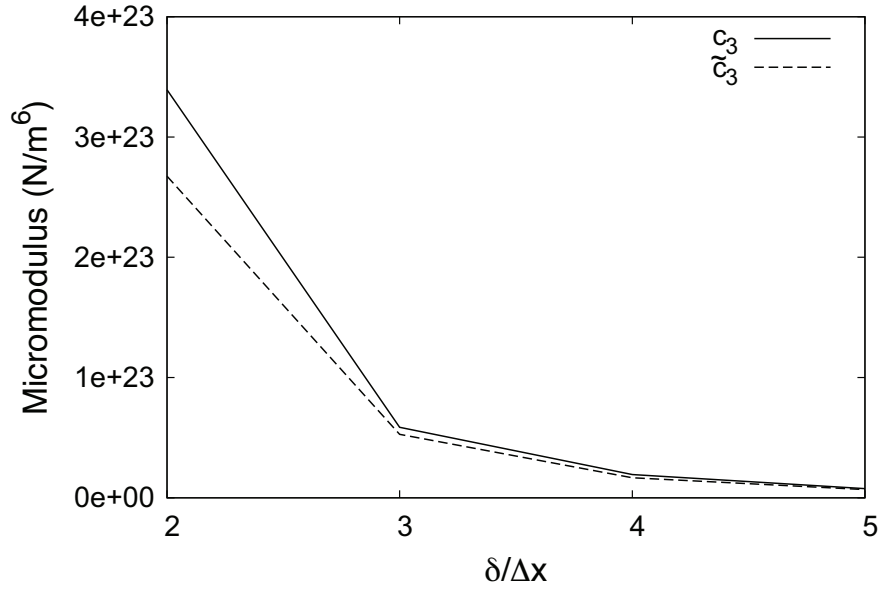


Figure 3.8: Micromodulus for different horizons ( $E = 70$  GPa, and  $\nu = 1/4$ ).

### 3.2.3 Pairwise compensation scheme

For an elastic body which has Poisson ratio not equal to  $1/4$ , we introduce a compensation force  $\hat{\mathbf{f}}$  for each node subjected to the pairwise force  $\mathbf{f}$  due to the stretch of peridynamic bonds. A set of compensation forces  $\hat{\mathbf{f}}$  is superposed in the transverse directions perpendicular to the direction of the force  $\mathbf{f}$ , resulting in additional transverse deformations which simulate the effect of Poisson ratios other than  $1/4$ . It should be noted that two pairs of compensation forces in  $y$ – and  $z$ –directions are added to nodes in three-dimensional domains.

If a node is enclosed completely in an elastic body, the added compensation forces  $\hat{\mathbf{f}}$  are balanced, and the resultant nodal force becomes zero. On the other hand, there exists a force added to the nodes located at the boundary. Therefore, the direction of the resultant force is towards inside of the body if Poisson ratio is larger than  $1/4$ , as shown in Figure 3.9.

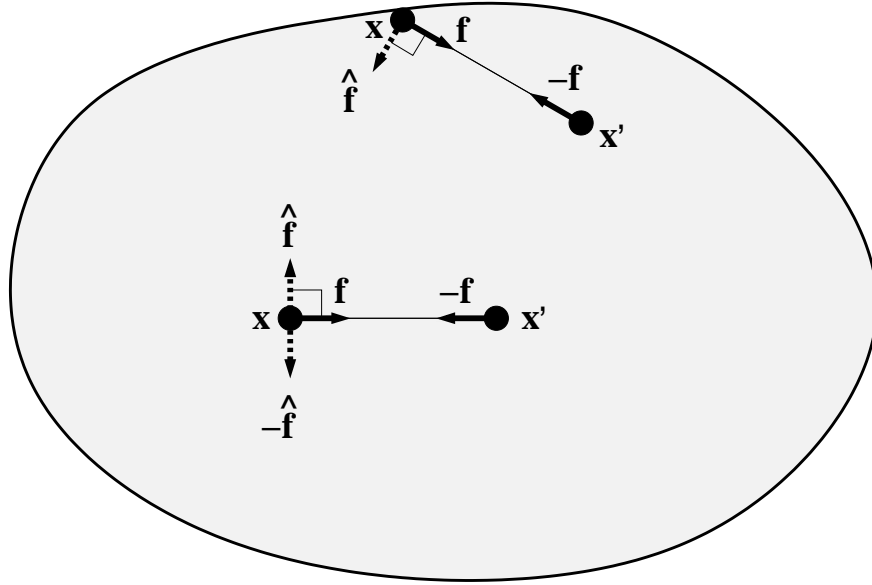


Figure 3.9: Pairwise compensation scheme.

Consider a three-dimensional rectangular bar, which has Young's modulus  $E$  and Poisson ratio  $\nu$ . The bar is subjected to a uniaxial tension as shown in Figure 3.10. The compensation

forces acting on the lateral surfaces are superposed on the nodes at boundaries as shown in Figure 3.11. The peridynamic Young's modulus  $\hat{E}_{pd}$  needs to be determined such that the strains in Figure 3.11 are identical to the strains in the configuration of Figure 3.10. For Poisson ratio larger than  $1/4$ , the modified peridynamic Young's modulus  $\hat{E}_{pd}$  should be larger than  $E_{pd}$  to keep the strain identical. The longitudinal strain in  $x$ -direction in Figure 3.11 equals the strain in Figure 3.10, which is written as

$$\frac{\sigma_x}{E_{pd}} = \frac{\sigma_x}{\hat{E}_{pd}} - \frac{1}{4} \left( \frac{\hat{\sigma}_y}{\hat{E}_{pd}} + \frac{\hat{\sigma}_z}{\hat{E}_{pd}} \right), \quad (3.24)$$

where  $\hat{\sigma}_y$  and  $\hat{\sigma}_z$  are superposed stresses from the compensation forces for  $\nu \neq 1/4$ . The strains in  $y$ - and  $z$ -directions also need to be identical to the strains in the original peridynamic model shown in Figure 3.10. Therefore, the equilibrium of the strain  $\varepsilon_y$  is expressed as

$$-\nu \frac{\sigma_x}{E_{pd}} = \frac{\hat{\sigma}_y}{\hat{E}_{pd}} - \frac{1}{4} \left( \frac{\sigma_x}{\hat{E}_{pd}} + \frac{\hat{\sigma}_z}{\hat{E}_{pd}} \right). \quad (3.25)$$

Since the compensation forces are identical in all lateral directions perpendicular to the pairwise force  $\mathbf{f}$ , the lateral stresses are equal as

$$\hat{\sigma}_y = \hat{\sigma}_z. \quad (3.26)$$

Solving Equations (3.24) to (3.26), the transverse lateral stresses in  $y$ - and  $z$ -directions are obtained as

$$\hat{\sigma}_y = \frac{1 - 4\nu}{3 - 2\nu} \sigma_x, \quad \hat{\sigma}_z = \frac{1 - 4\nu}{3 - 2\nu} \sigma_x. \quad (3.27)$$

Substituting Equation (3.27) to Equation (3.24), the modified peridynamic Young's modulus



can be derived as

$$\hat{E}_{pd} = \frac{5}{6 - 4\nu} E_{pd}. \quad (3.28)$$

Hence, the micromodulus  $\hat{c}_3$  corresponding to  $\hat{E}_{pd}$  should be modified as

$$\hat{c}_3 = \frac{5}{6 - 4\nu} c_3, \quad (3.29)$$

where  $c_3$  is the numerically determined micromodulus summarized in Table 3.2.

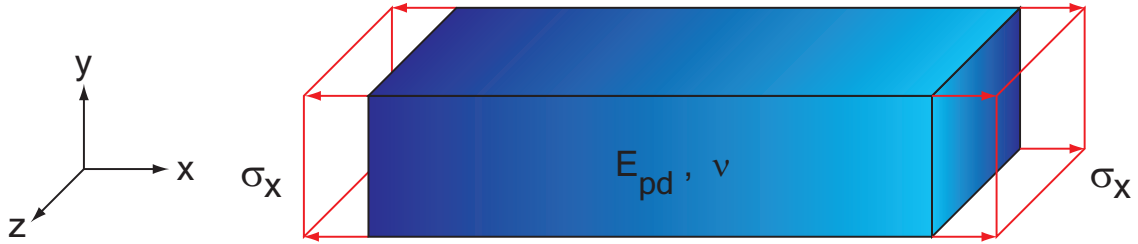


Figure 3.10: Three-dimensional bar subjected to a tension.

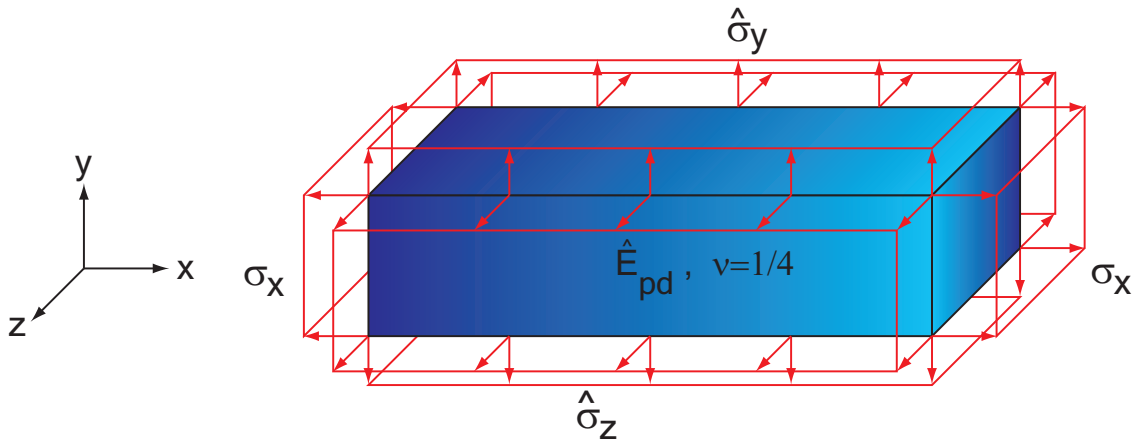


Figure 3.11: Three-dimensional bar subjected to a tension. Lateral forces are added to take account of  $\nu \neq \frac{1}{4}$ .

### 3.3 Case studies

#### 3.3.1 Numerical implementation

The material region is discretized isotropically in all the directions in space such that the distance between two adjacent nodes is  $\Delta x$  in  $x$ -,  $y$ -, and  $z$ -directions as shown in Figure 3.2. All nodes have the same volume  $(\Delta x)^3$ . The equation of motion in Equation (3.2) is rewritten as

$$\rho \ddot{\mathbf{u}}_I^t = \sum_{J=1}^{N_{\mathcal{H}_I}} \mathbf{f}(\boldsymbol{\eta}^t, \boldsymbol{\xi}) V_J + \mathbf{b}_I^t, \quad (3.30)$$

where  $\ddot{\mathbf{u}}_I^t$  is the acceleration of the node  $I$  at time  $t$ ,  $\mathbf{f}(\boldsymbol{\eta}^t, \boldsymbol{\xi})$  is the pairwise force,  $N_{\mathcal{H}_I}$  is the total number of nodes within the horizon of the node  $I$ , and  $\mathbf{b}_I^t$  is the body force at time  $t$ . The velocity-Verlet scheme [51] is used for the time integration to update positions, velocities and accelerations as

$$\mathbf{x}(t + \Delta t) = \mathbf{x}(t) + \mathbf{v}(t)\Delta t + \frac{1}{2}\mathbf{a}(t)\Delta t^2, \quad (3.31)$$

$$\mathbf{v}(t + \Delta t/2) = \mathbf{v}(t) + \frac{1}{2}\mathbf{a}(t)\Delta t, \quad (3.32)$$

$$\mathbf{a}(t) = \frac{1}{\rho}\mathbf{f}_V(t), \quad (3.33)$$

$$\mathbf{v}(t + \Delta t) = \mathbf{v}(t + \Delta t/2) + \frac{1}{2}\mathbf{a}(t + \Delta t)\Delta t, \quad (3.34)$$

where  $\mathbf{x}$  is the position vector,  $\mathbf{v}$  is the velocity vector,  $\mathbf{a}$  is the acceleration vector, and  $\mathbf{f}_V$  is the scaled force vector which is defined as

$$\mathbf{f}_V = \sum_{J=1}^{N_{\mathcal{H}_I}} \mathbf{f}(t) V_J. \quad (3.35)$$

The acceleration is calculated by dividing the scaled pairwise force  $\mathbf{f}_V$ , which has the unit of force per volume, by the density  $\rho$ .

For the numerical simulation, peridynamics is implemented in the framework of LAMMPS [135]. The research code is compiled and run in the parallel mode in a workstation which has dual quad-core 64 bit CPU's at 2 GHz, 16 GB memory and a 2 TB hard disk drive.

### 3.3.2 Comparison of peridynamics and analytical solution( $\nu = \frac{1}{4}$ )

#### 3.3.2.1 One-dimensional bar

Consider a one-dimensional bar subjected to a uniaxial tension. The length of the bar is 10 mm, and the size of the horizon is set to 1.0 mm. The grid spacing  $\Delta x$  is 0.5 mm, which corresponds to  $\delta/\Delta x = 2$ . Young's modulus  $E$  is 70 GPa, and the density  $\rho = 2700 \text{ kg/m}^3$ . The magnitude of nodal force applied to the nodes at both ends is 87.5 N, and the force is gradually increased for 1000 time steps, setting the time step  $dt = 5 \times 10^{-8}$  sec. The classical (local) stress  $\sigma = 87.5 \text{ N}/(0.0005 \text{ m})^2 = 350 \text{ MPa}$ , and the classical (local) strain  $\varepsilon = 0.005$ . Substituting Young's modulus and the grid spacing to Equation (3.19), the micromodulus is calculated as  $c_1 = 5.6 \times 10^{23} \text{ N/m}^6$ .

Figure 3.12 shows the strain distribution from the middle ( $x=5.0 \text{ mm}$ ) to the right end of the bar ( $x=10.0 \text{ mm}$ ). The strain in the middle of the bar ( $x=5.0 \text{ mm}$ ) is 0.00498, and the strain increases to 0.00516 at the end of the bar. The strain distribution is very close to the classical (local) elasticity solution. However, the boundary effect exists near the end of the one-dimensional bar. The total force per unit volume acting through the cross section of the bar  $f_V^{\mathcal{L}} = 6.98 \times 10^{11} \text{ N/m}^3$ . The resultant force obtained by multiplying the volume  $V_I$  is 87.2 N. The peridynamic stress on the cross section is calculated as  $\sigma = 348.8 \text{ MPa}$ . Dividing

the stress by the measured strain, the resultant Young's modulus through back-calculation is 70.043 GPa. The peridynamic results show good agreement in the strain and the resultant Young's modulus.

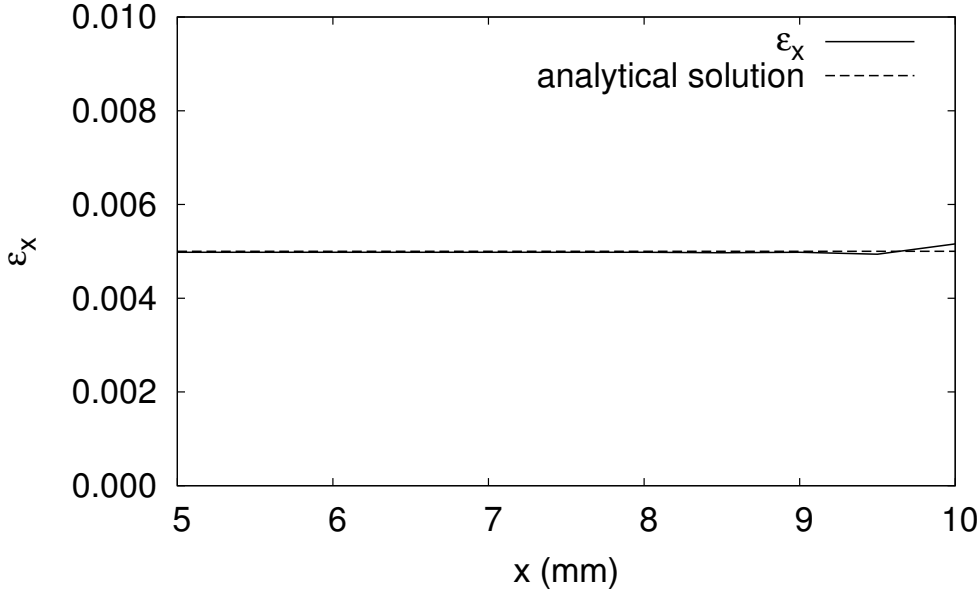


Figure 3.12: Strain distribution of the one-dimensional bar in x-direction.

### 3.3.2.2 Three-dimensional bar

We examine material responses of a three-dimensional rectangular bar of dimensions 10 mm  $\times$  7 mm  $\times$  7 mm with horizons of 1.0 mm, 1.5 mm, 2.0 mm and 2.5 mm. The bar is discretized with nodes distributed uniformly in a fixed  $21 \times 15 \times 15$  grid as shown in Figure 3.13. The grid spacing  $\Delta x$  is 0.5 mm, which leads the horizon to grid spacing ratios  $\delta/\Delta x$  to be 2, 3, 4, and 5. Young's modulus  $E$  of the elastic material is 70 GPa, Poisson ratio  $\nu = 0.25$ , and the density  $\rho = 2700 \text{ kg/m}^3$ . Nodes at both ends of the bar are subjected to a tensile loading gradually increasing up to 87.5 N. The corresponding classical (local) stress  $\sigma = 350 \text{ MPa}$ , and the analytical (local) strain  $\varepsilon_x = 0.005$ .

Figures 3.14(a) and (b) show the comparison of longitudinal strain  $\varepsilon_x$  along the center

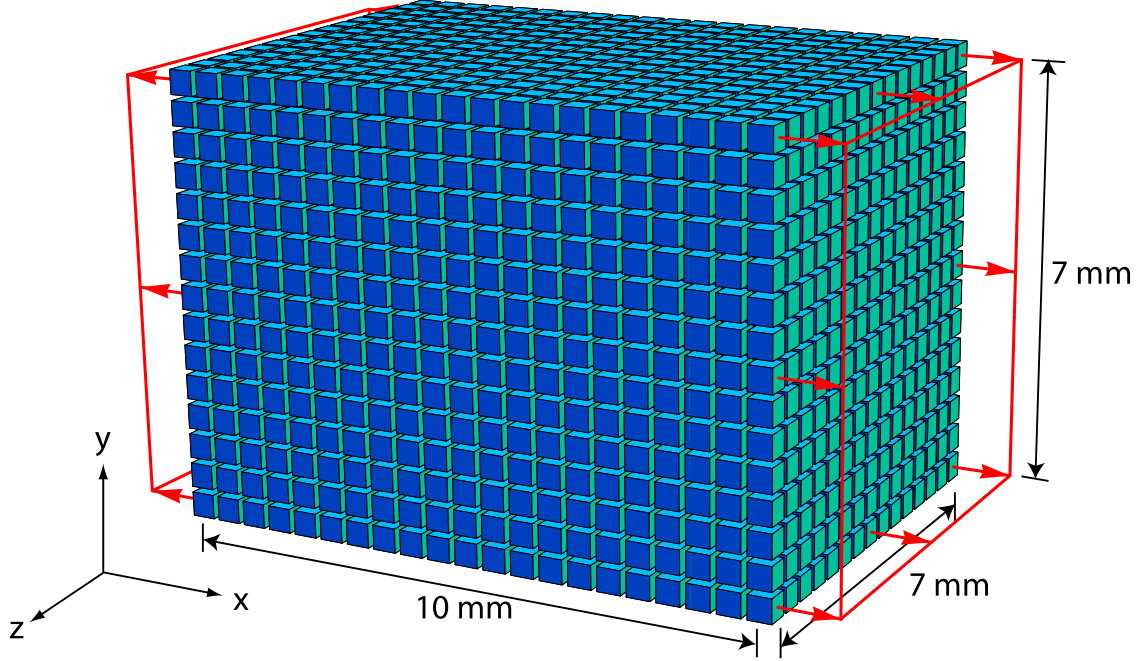


Figure 3.13: Three-dimensional bar discretized by  $21 \times 15 \times 15$  nodes.

line of the bar using  $c_3$  and  $\tilde{c}_3$  in the numerical studies, respectively. With  $c_3$ , as shown in Figure 3.14(a), the longitudinal strain for  $\delta = 2\Delta x$  is close to the classical (local) solution  $\varepsilon_x = 0.005$ . The strain  $\varepsilon_x = 0.00486$  in the middle of the bar ( $x = 5.0$  mm), and the strain  $\varepsilon_x = 0.00492$  at the right end ( $x = 10.0$  mm). As shown in Figure 3.14(b), the strain obtained using the analytical micromodulus  $\tilde{c}_3$  in the simulation is larger than the classical elasticity solution, and the increase of the horizon lowers the strain in all the domain except the boundary. Therefore, the corresponding resultant Young's modulus through back-calculation is smaller than the Young's modulus  $E$  of the material. The strain increases in the three layers of the nodes close to the ends.

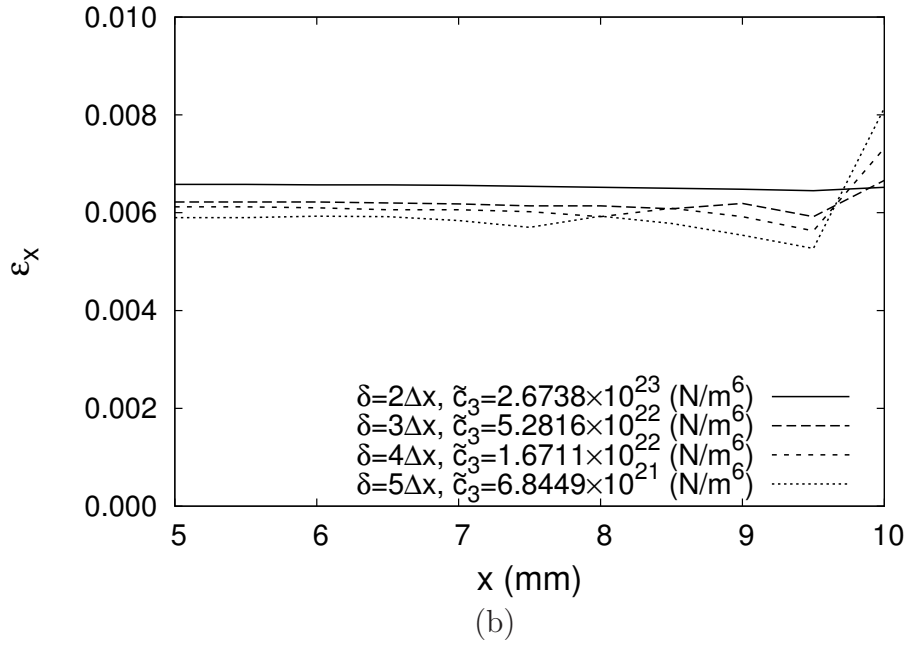
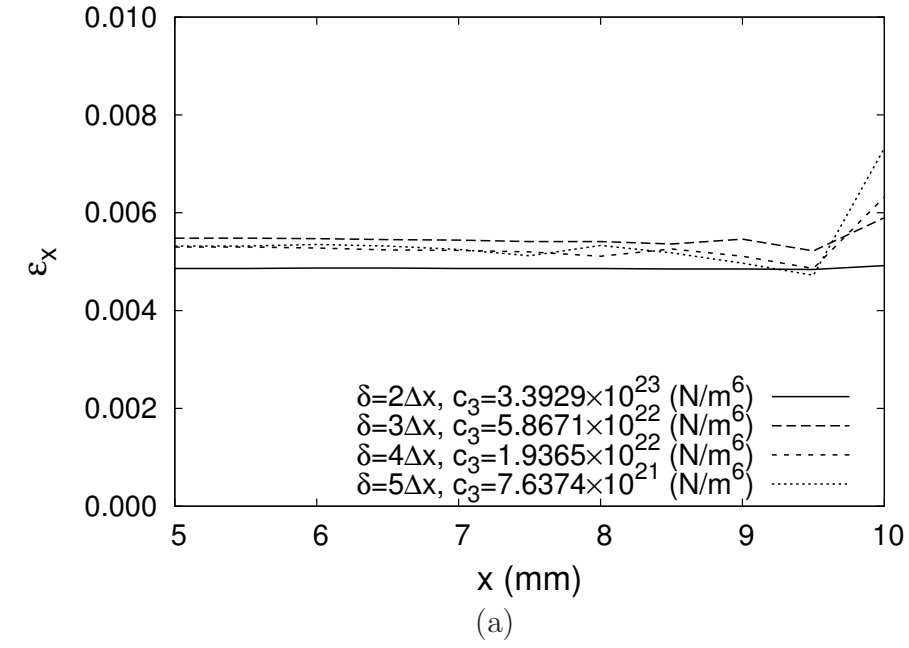


Figure 3.14: Strain distribution along the x-axis in the three-dimensional bar. (a) Numerical micromodulus  $c_3$  given in Table 3.2 is used for each horizon and (b) analytical micromodulus  $\tilde{c}_3$  given in Equation (3.14) is used. The classical (local) elasticity solution of strain  $\varepsilon_x = 0.005$ .

The strain and stress distributions on the cross section at  $x = 5.0$  mm are shown in Figures 3.15(a) and (b), respectively for the horizon  $\delta = 2\Delta x$ . The numerical micromodulus is utilized in the simulation. The strain is 0.00486 at the center of the cross section at  $x = 5.0$  mm, and the strain is 0.00494 at the corner. The average of the strain over the cross section at  $x = 5.0$  mm is 0.00491. The total force per volume acting through the cross section of the bar  $f_V^{\mathcal{L}} = 1.53 \times 10^{14}$  N/m<sup>3</sup>, and the peridynamic stress  $\sigma_x = 339.9$  MPa. The resultant Young's modulus calculated by dividing the peridynamic stress by the strain is 69.27 GPa in the middle of the bar ( $x = 5.0$  mm). For the horizon  $\delta = 2\Delta x$ , the average strain at the end of the bar ( $x = 10.0$  mm) is 0.00503, and the resultant Young's modulus through back-calculation is 69.58 GPa. In  $y$ -direction, the strain  $\varepsilon_y$  in the middle of the bar is -0.00121, and the resultant Poisson ratio is  $\nu = 0.249$ . Figure 3.16 shows Poisson ratio obtained from the longitudinal and transverse strains from the middle to the right end of the bar.

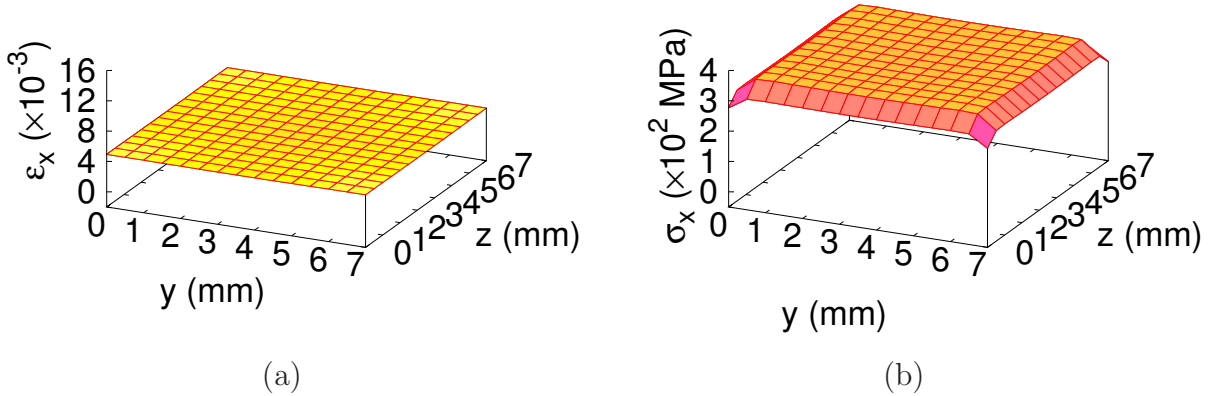


Figure 3.15: (a) Strain- and (b) stress-distributions on the cross section at  $x = 5.0$  mm. The classical (local) elasticity solution of strain  $\varepsilon_x = 0.005$  and stress  $\sigma_x = 350$  MPa. The horizon  $\delta = 2\Delta x$ , and the numerical micromodulus  $c_3$  is utilized in the simulation.

Figure 3.17 shows the strain distributions at the end of the bar ( $x = 10.0$  mm) for

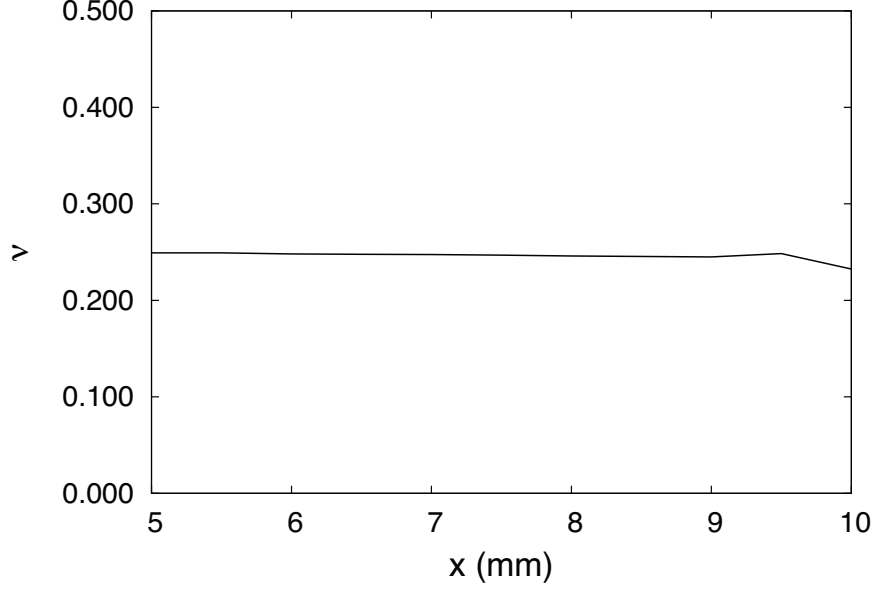


Figure 3.16: Poisson ratio along the three-dimensional peridynamic bar as shown in Figure 3.13. The given Poisson ratio of the material is  $\nu = \frac{1}{4}$ . The horizon  $\delta = 2\Delta x$ , and the numerical micromodulus  $c_3$  is utilized in the simulation.

different horizons using the numerical micromodulus summarized in Table 3.2. As the horizon increases, the strain also increases at the end of the bar. For the horizon  $\delta = 2\Delta x$ , the strain at the center of the cross section at the end is 0.00492, the strain is 0.00540 at the corner, and the average strain over the cross section is 0.00503 as shown in Figure 3.17(a). For the horizon  $\delta = 5\Delta x$ , the strain at the center of the cross section at  $x = 10.0$  mm is 0.00732, and the strain increases significantly to 0.01580 at corners as shown in Figure 3.17(d). The average strain over the cross section at the end of the bar for the horizon  $\delta = 5\Delta x$  is 0.00893, which is much larger than the classical (local) solution  $\varepsilon_x = 0.005$ .

Compared with the classical (local) elasticity solution  $\varepsilon_x = 0.005$ , the boundary effect increases as the horizon increases since the larger horizon causes larger loss of bond contribution near the ends of the bar where tractions are applied and near the lateral surfaces. Consequently, the bond stretch  $s$  between those nodes close to the boundaries gets larger due to the smaller fraction of the contributing bonds among the total number of bonds.



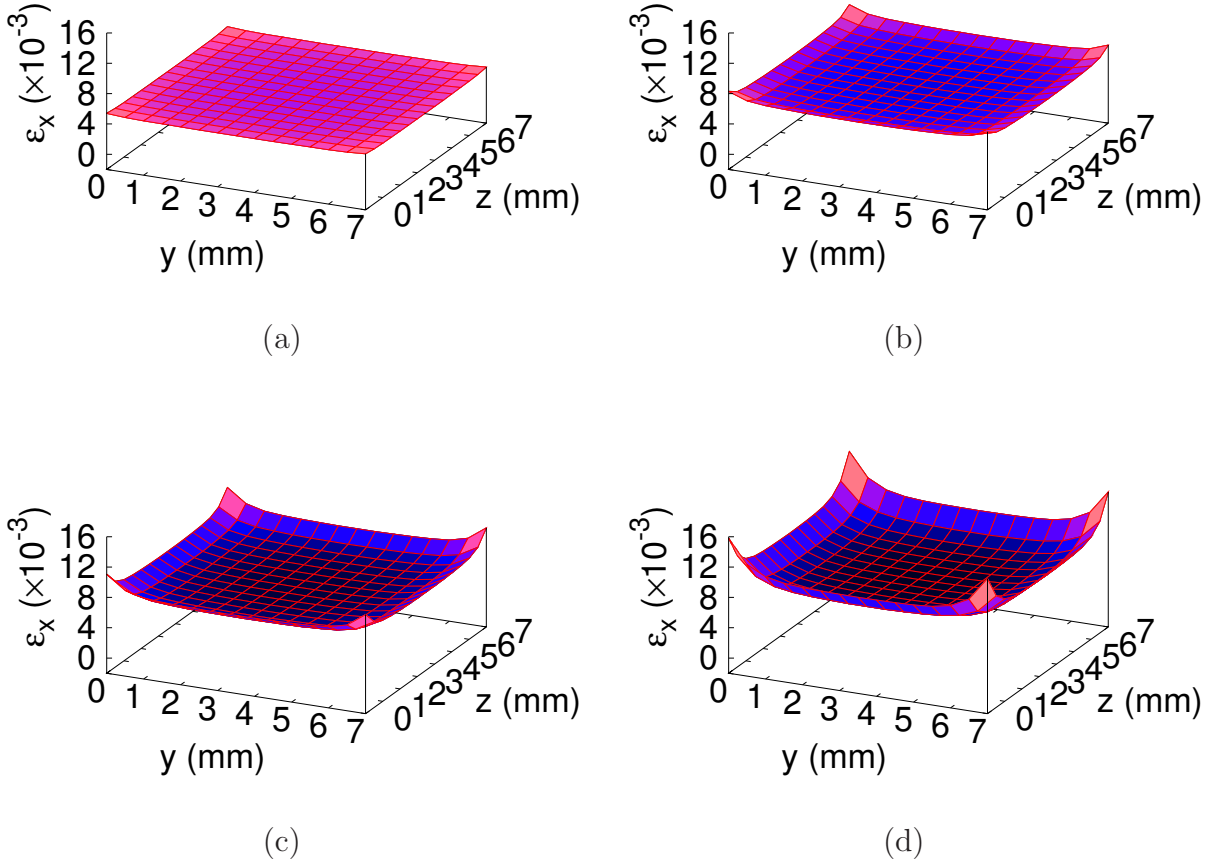


Figure 3.17: Strain distribution at the end surface of the bar for different horizons using the numerical micromodulus: (a)  $\delta = 2\Delta x$ , (b)  $\delta = 3\Delta x$ , (c)  $\delta = 4\Delta x$ , and (d)  $\delta = 5\Delta x$ . The classical (local) elasticity solution of strain  $\varepsilon_x = 0.005$ .

It has been observed that the peridynamic solution converges to the classical (local) elasticity solution as the horizon decreases in one-dimensional models [161, 20]. Similarly, for the selected range of the horizons ( $2\Delta$  to  $5\Delta$ ) of three-dimensional models, material responses, using the horizon  $\delta = 2\Delta x$  and the corresponding numerical micromodulus  $c_3$ , are very close to classical (local) solutions. However, the use of the micromodulus  $\tilde{c}_3 = \frac{18k}{\pi\delta^4}$  yields larger responses in strains since the analytical micromodulus  $\tilde{c}_3$  is smaller than  $c_3$ , summarized in Table 3.2.

It should be noted that a different horizon may be chosen for different types of problems such as large-strain plastic response and fracture phenomena. For example, in crack branching problems, the horizon  $\delta = 4\Delta x$  is proven to be effective [70, 69] since adequate number of nodes inside the horizon are required for the development of crack path. On the other hand, larger error from the use of larger horizons at the vicinity of the boundaries might be alleviated by normalizing forces or adding correction factors as proposed by researchers [115, 90].

### 3.3.3 Comparison of modified peridynamics and analytical solution ( $\nu \neq \frac{1}{4}$ )

We introduce the concept of compensation force  $\hat{\mathbf{f}}$  for each pairwise force  $\mathbf{f}$  to extend the discretized bond-based peridynamics to simulate materials that have Poisson ratios  $\nu \neq \frac{1}{4}$ . Consider a rectangular bar of dimensions 10 mm×7 mm×7 mm and choose the horizon  $\delta = 1.0$  mm. The bar is discretized with the grid spacing  $\Delta x = 0.5$  mm so that the peridynamic solutions might be close to the classical (local) elasticity solutions. Each node on the ends of the bar is subjected to a tension of 87.5 N in the longitudinal direction. The density  $\rho = 2700$  kg/m<sup>3</sup>, Young's modulus  $E = 70$  GPa, and Poisson ratio  $\nu = 0.3$ . The applied traction on the ends is  $\sigma = 350$  MPa, and the corresponding classical, local, elastic strain  $\varepsilon_x$  is 0.005.

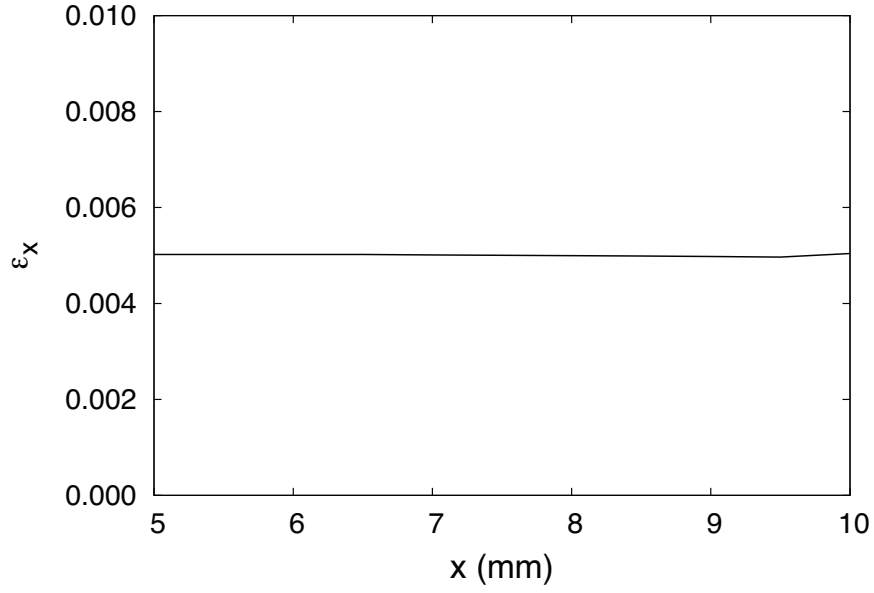
For each pairwise bond force on a node, two pairs of compensation forces are applied in the perpendicular directions of the force vector  $\mathbf{f}$  as shown in Figure 3.9. The compensation forces are self-balanced for the nodes inside the body. Therefore, the resultant compensation forces vanish. However, for the nodes on the boundary, the forces are superposed to the surface normal direction.

Additional tractions are applied on all the lateral surfaces to simulate Poisson effect as shown in Figure 3.11. The applied additional traction on lateral surfaces is given by Equation (3.27). Substituting the target Poisson ratio  $\nu = 0.3$  and traction  $\sigma_x = 350$  MPa to Equation (3.27), we obtain  $\hat{\sigma}_y = -29.2$  MPa. After multiplying the cross-sectional area  $(\Delta x)^2$ , the forces applied on each node on the lateral boundary surfaces are  $-7.289$  N in  $y$ - and  $z$ -directions.

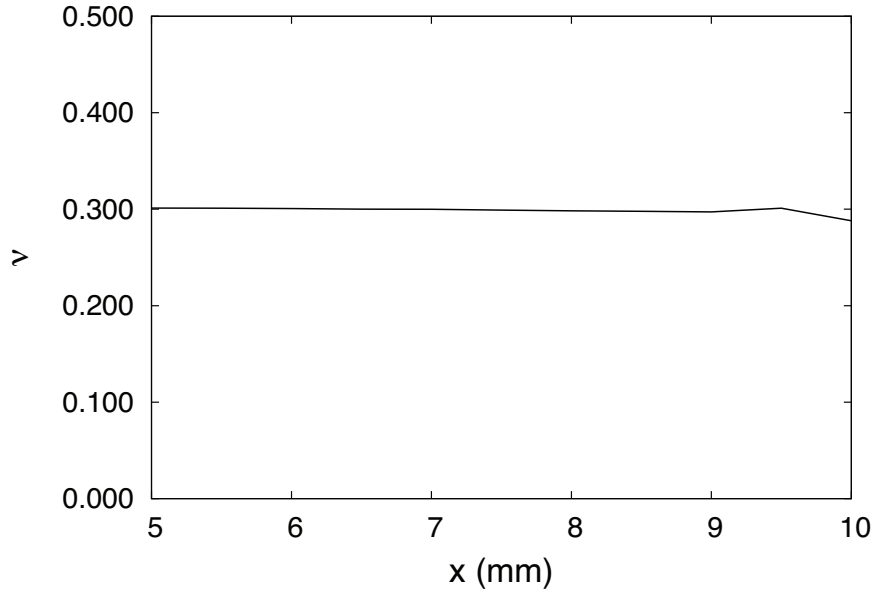
Setting  $\delta = 2\Delta x$  and substituting  $c_3 = 0.302942 E/\Delta x^4$  given in Table 3.2 to Equa-

tion (3.29), the micromodulus is modified to  $\hat{c}_3 = 3.5343 \times 10^{23} \text{ N/m}^6$ . Figure 3.18 shows the strain and the resultant Poisson ratio calculated from the measured longitudinal and transverse strains along the center line of the bar. The strain  $\varepsilon_x$  at the center of the cross section at  $x = 5.0 \text{ mm}$  is 0.00502, and the average strain over the cross section is 0.00509. The sum of forces acting through the cross section of the bar is 19842 N, and the corresponding peridynamic stress  $\sigma_x$  on the cross section of the bar is calculated by dividing the sum of forces by the cross-sectional area of the bar. The corresponding peridynamic stress is 352.7 MPa, and the resultant Young's modulus is 70.26 GPa through back-calculation.

Figure 3.18(b) shows the back-calculated Poisson ratio along the bar. Compared with the Poisson ratio of the material  $\nu = 0.3$ , the numerical results show good agreement. The boundary effect is also observed in the distribution of Poisson ratio. Poisson ratio  $\nu$  decreases close to the end of the bar since the longitudinal strain increases at locations close to the end of the bar.



(a)



(b)

Figure 3.18: (a) Strain  $\varepsilon_x$  and (b) Poisson ratio  $\nu$  along the bar by the modified peridynamic formulation. The classical (local) elasticity solution of strain  $\varepsilon_x = 0.005$ , and the Poisson ratio  $\nu$  of the material is 0.3. The horizon  $\delta = 2\Delta x$ , and the modified numerical micromodulus  $\hat{c}_3$  for pairwise compensation scheme is utilized in the simulation.

### 3.4 Summary

The one-dimensional micromodulus  $c_1$  and the three-dimensional micromodulus  $c_3$  are derived for discretized peridynamic models. The micromoduli are calculated by introducing the peridynamic stress corresponding to the classical (local) stress, calculating the corresponding peridynamic Young's modulus, and equilibrating the peridynamic Young's modulus with the conventional Young's modulus. For three-dimensional models, the numerically determined micromodulus  $c_3$  is larger than the analytically obtained micromodulus  $\tilde{c}_3$ . The micromoduli  $c_3$  and  $\tilde{c}_3$  converge as the horizon to grid spacing ratio  $\delta/\Delta x$  increases.

Material responses of peridynamic bars with numerical micromoduli and conventional analytical micromoduli are investigated. Compared with classical (local) elasticity solutions, the peridynamic results of strain and the resultant Young's modulus by back-calculation show good agreement for the horizon  $\delta = 2\Delta x$  using the numerical micromodulus. The corresponding peridynamic solutions of strain using the analytical micromodulus are larger than the classical (local) elasticity solutions. The errors due to the boundary effect are almost negligible for the horizon  $\delta = 2\Delta x$ , but increase in the results of strain as the horizon  $\delta$  increases. Therefore, the horizon  $\delta = 2\Delta x$  can be recommended in the linear elastic regime although larger horizons might be chosen for fracture problems [70, 69]. In the numerical implementation, a horizon might be determined first, and then the grid spacing can be selected considering the range of material behaviors.

To model materials that have Poisson ratios other than  $1/4$ , a force compensation scheme adding additional forces on each pairwise force between nodes is proposed for discretized peridynamics. The numerical results match classical (local) solutions in the material responses including the stress, the strain, back-calculated Young's modulus, and Poisson ratio.

# Chapter 4

## Discretized Peridynamics for Brittle and Ductile Solids

### 4.1 Introduction

Compared with macroscopic modeling such as FEA, three-dimensional peridynamic analyses of large simulations are computationally intensive due to the nonlocal property of peridynamics. Macek *et al.* [115] compared computer wall-clock run times between the EMU and FEA implementations of peridynamics. The FEA implementation is much faster than the direct meshless method. Askari *et al.* [8] applied peridynamics to model material and structural failures using the Columbia Supercomputer at NASA Advanced Supercomputing Division.

In this chapter, a peridynamics code for three-dimensional simulations is implemented using an NVIDIA Tesla C1060 GPU for parallel computing. A significant speedup over the serial calculation in a CPU is achieved, varying with the number of discretization nodes in peridynamic models. The effects of different horizons and grid sizes are investigated for a brittle material. The stresses and strains of FEA and peridynamic solutions, respectively, are compared for a ductile material. A multiscale procedure is proposed to bridge plastic simulations at different scales. The results after applying the proposed procedure show good agreements between FEA and peridynamics.

## 4.2 Theory

The peridynamic formulations are introduced in Section 3.2, where elastic peridynamic models are examined. In this chapter, brittle and ductile materials are going to be investigated. Figure 4.1(a) shows a brittle material model defined for peridynamics. In the elastic regime, the bond force is a scalar-function of the bond stretch  $s$ . In order to simulate damage in peridynamic models, a critical stretch for bond failure is introduced as  $s_0$ . Once a bond fails, it can not sustain force any more, which makes the peridynamic model hysteretic. Figure 4.1(b) defines a ductile material model for peridynamics. A bond yields at the yield limit  $s_y$ , and shows perfect plasticity upto  $s_0$ .

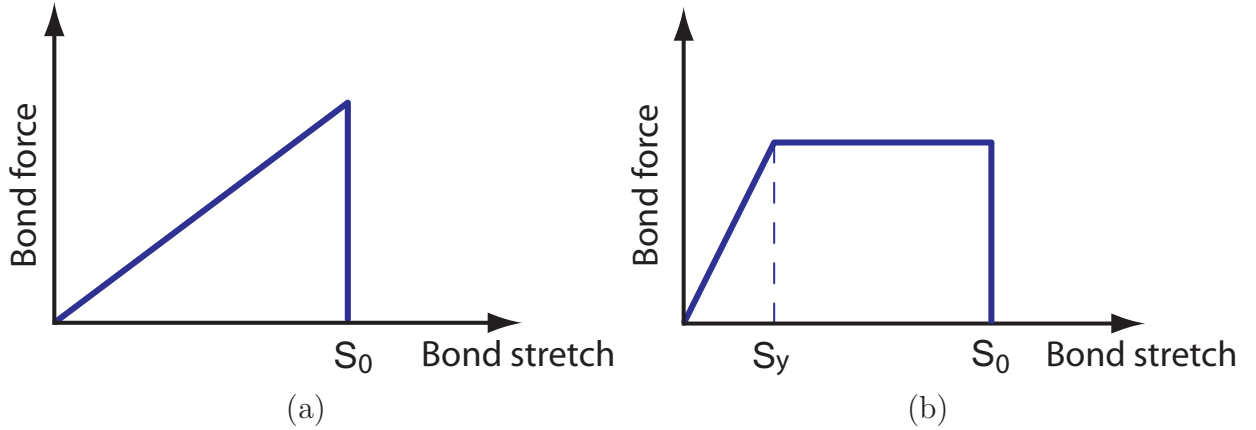


Figure 4.1: (a) Bond force as a function of bond stretch in a brittle material model. (b) Bond force as a function of bond stretch in a ductile material model.

For microbrittle materials, the bond force, which is a scalar function of the bond stretch  $s$ , is expressed as

$$f(\boldsymbol{\eta}, \boldsymbol{\xi}) = c \times s(t, \boldsymbol{\eta}, \boldsymbol{\xi}) \times \mu(t, \boldsymbol{\eta}, \boldsymbol{\xi}), \quad (4.1)$$

where  $c$  is the micromodulus summarized in Tables 3.1 and 3.2 for one- and three-dimensional models respectively, and  $\mu$  is the scalar function to determine the bond failure. The scalar



function  $\mu$  is related with the critical bond stretch as

$$\mu(t, \boldsymbol{\eta}, \boldsymbol{\xi}) = \begin{cases} 1 & \text{if } s(t', \boldsymbol{\eta}, \boldsymbol{\xi}) < s_0 \quad \text{for all } 0 \leq t' \leq t, \\ 0 & \text{otherwise.} \end{cases} \quad (4.2)$$

The critical bond stretch  $s_0$  for microbrittle material is obtained by setting the work required to break all the bonds per unit fracture area identical to the energy release rate  $G_f$  [155]:

$$s_0 = \sqrt{\frac{5G_f}{9k\delta}}. \quad (4.3)$$

By considering broken bonds, damage dependencies can be introduced into the critical bond stretch [155, 69].

## 4.3 Computation

### 4.3.1 Numerical implementation

To calculate the bond forces on peridynamic nodes after discretization, a neighbor list is created for each node in the reference configuration. In the subsequent calculations, the neighbor list is referred to determine the total bond forces acting on a node. The velocity-Verlet scheme [51] is used for the time integration to update displacements and velocities. The procedures of the velocity-Verlet algorithm are explained in Section 3.3.1.

### 4.3.2 Implementing Peridynamics in GPU

GPUs, originally developed for the acceleration for graphics rendering, have a large number of transistors devoted to data processing rather than data caching and flow control [131]. This

advantage has been taken for numerical computations. GPUs have evolved for many data-parallel and computing-intensive programs, and a variety of compilers have been developed. Researchers have used GPUs for highly parallel computation. Harris [73] described a method to simulate stable fluid using a GPU. Kruger *et al.* [101] introduced a framework for solving sets of algebraic equations in GPUs. Manavski *et al.* [116] used GPUs as an accelerator for Smith-Waterman sequence alignment. Phillips *et al.* [138] implemented a multi-block turbulent flow solver in GPU processors.

We use a GPU, NVIDIA Tesla C1060, that has 4 GB memory and 30 multiprocessors, and each multiprocessor has 8 cores. Therefore, 240 cores are available in total. Each core can execute a sequential thread, and the clock rate is 1,296 MHz. Figure 4.2 shows the block diagram of a GPU accelerator [186]. The GPU has its own memory which is called the device memory, and the accelerator communicates with CPU using IO commands and DMA memory transfer [186]. The data bandwidth is 512-bits wide. To port the peridynamics code to a GPU platform, PGI Fortran Accelerator Programming Model [143, 142], a high-level implicit programming model for the general purpose computation on GPUs, is utilized. A set of compiler directives designed for GPUs is available to specify regions of the code to be offloaded from the CPU to the GPU. The code implemented with accelerator directives is portable even without a GPU unit since the directives are considered as comments by other Fortran compilers.

A benchmark problem for multiplication of a matrix  $\mathbf{A}_{n \times n}$  and a vector  $\mathbf{b}_{n \times 1}$  is written with directives as:

```
!$acc region
do k=1,1000,1
do i =1,n
```

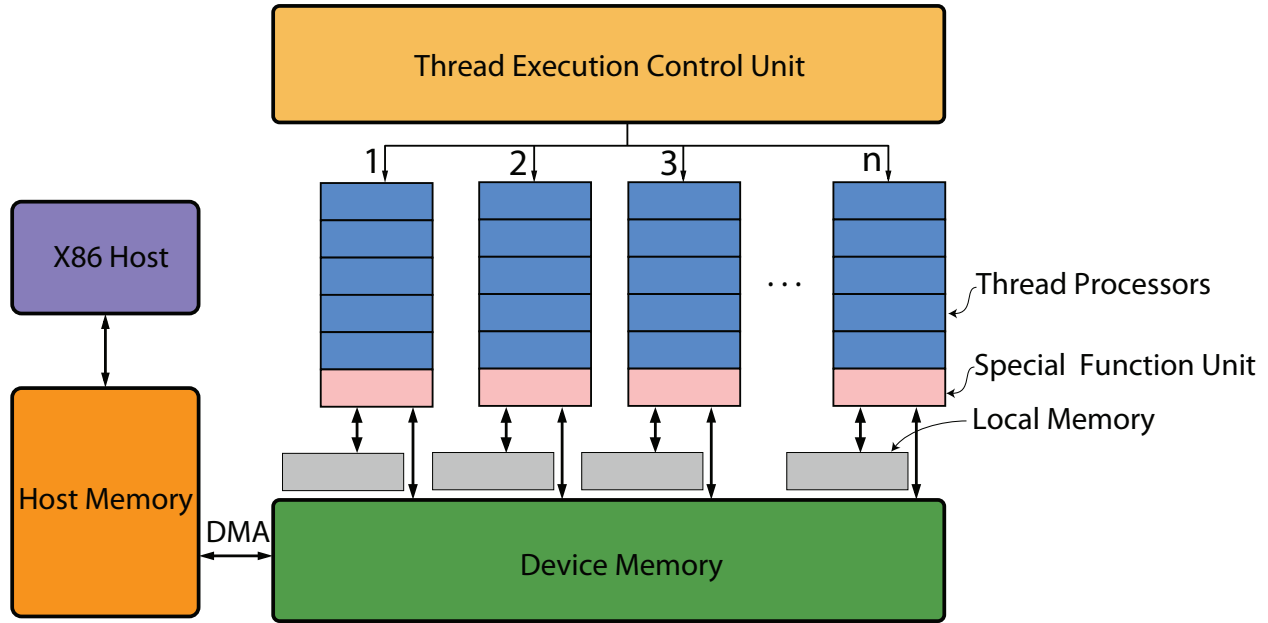


Figure 4.2: NVIDIA Tesla Block Diagram [186].

```

r(i)=0
do j = 1,n
    r(i)=r(i)+A(i,j)*b(j)
enddo
enddo
enddo
!$acc end region

```

In the fixed format, PGI Accelerator directives are specified with the sentinel `!$acc`. The directive `!$acc region` defines the region to be compiled for execution in the GPU [142]. For benchmarking, the multiplication is repeated one thousand times, and the summation is stored in a vector `r`. Figure 4.3 compares the wall-clock times by serial calculation in the CPU and by the parallelized calculation in the GPU. For the matrix of size  $n$  smaller than 5,000, the GPU calculation is merely a few times faster than the serial calculation.

However, as the size of the matrix increases, the speedup of the GPU calculation over the serial calculation increases significantly.

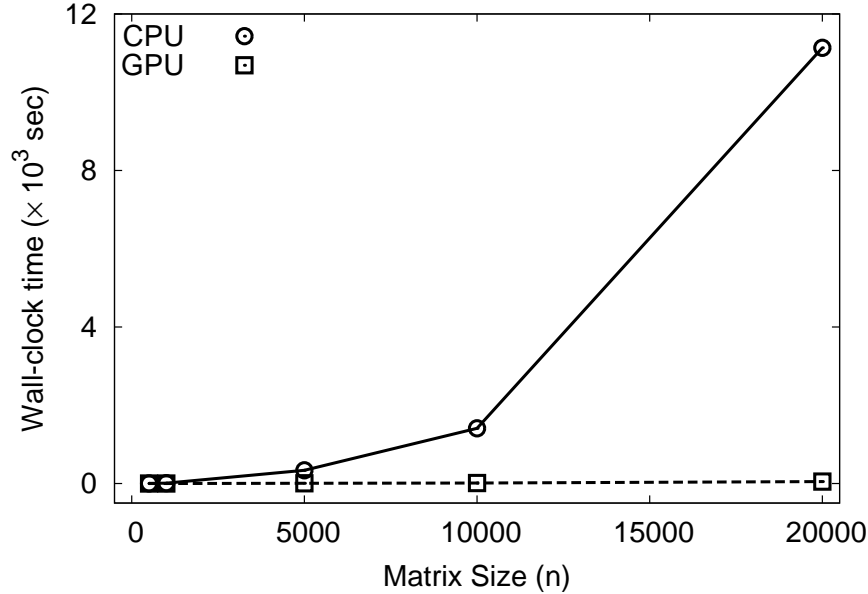


Figure 4.3: A benchmark problem of matrix multiplication.

For the effective parallelization in GPUs, all the necessary information in the main memory is required to be transferred to the GPU memory for the calculation. We use the data clauses to control the transfer of selected data between the CPU and the GPU, which reduces the system overhead in copying data. The peridynamic model is initialized in the CPU, and then variables and arrays are copied to the GPU for the calculation within the data region using directives as

```
!$acc data region copyin(list), local(list)
!$acc updateout(list)
!$acc end data region
```

The clause `copyin(list)` is used to copy the listed variables and arrays from the CPU to the GPU memory, and the clause `local(list)` declares local variables and arrays to be allocated

only in the GPU memory [142]. Calculation results in the GPU are copied to the main memory once per multiple calculation steps using the directive `!$acc updateout(list)`. It should be noted that copying the whole array is faster than copying the noncontiguous subarrays [186].

In the subroutine to calculate bond forces on each node in a discretized peridynamic model, the conventional algorithm includes two dependent loops as shown in Table 4.1, which is referred to as Algorithm 1. However, the loop dependency disables optimal parallelization on GPUs. Thus the nested loops are separated into two independent loops as shown in Table 4.2, which is referred to as Algorithm 2. Peridynamics codes using Algorithm 1 and Algorithm 2, respectively, are compiled with PGFORTRAN v10.3 for the serial calculation in the CPU. We compared the wall-clock time to calculate bond forces in a three-dimensional peridynamic model, which has 4,725 nodes with the horizon  $\delta = 2\Delta x$ . As summarized in Table 4.3, it takes 13,113 milliseconds to complete 1 time-step using Algorithm 1 for bond force calculations, and Algorithm 2 spends 21,080 milliseconds. By explicitly setting the memory considering the maximum number of neighbors in the peridynamic model, Algorithm 2 consumes more memory and time than Algorithm 1 if no GPU is utilized. Overall, Algorithm 1 is 1.61 times faster than Algorithm 2 in the CPU.

---

```

do i = 1, all nodes
  M = number of neighbors of the node i
  {Calculate bond forces on the node i}
  do j = 1, M
    f(i) = f(i) + c*s
  end do
end do

```

---

Table 4.1: Dependent loops (Algorithm 1).

For the comparison of the performance by the GPU enabled calculation using Algorithm

---

```

N = all nodes
M = maximum number of neighbors of all nodes
{Calculate each bond force}
do i = 1, N*M
    f_bond(i)=c*s
end do

{Sort bond forces to each node}
do j = 1, all nodes
    f(j) = summation of f_bond sorted on the node j
end do

```

---

Table 4.2: Independent loops (Algorithm 2).

2 and the serial calculation executed in the CPU using Algorithm 1, three-dimensional peridynamic simulations are conducted, and the wall-clock times are summarized in Table 4.4. With the grid size  $\Delta x = 0.5$  mm, the first peridynamic model consists of  $11 \times 8 \times 8$  nodes, the second model consists of  $21 \times 15 \times 15$  nodes, and the third model consists of  $41 \times 29 \times 29$  nodes. Young's modulus  $E$  is 70 GPa, Poisson ratio is 0.25, and the critical bond stretch is  $s_0 = 0.004$ . The time-step is set to  $dt = 1 \times 10^{-8}$  s. Each simulation is carried out for 500,000 time-steps. Figure 4.4(a) shows the wall-clock time to run the peridynamic models. For the first peridynamic model which has 704 nodes, the GPU calculation takes 3.5 minutes while the serial calculation spends 19.5 minutes in the CPU. The GPU calculation is 5.6 times faster than the serial calculation of the peridynamics code. For the second peridynamic model which has 4,725 nodes, the GPU calculation spends 10.5 minutes while the serial calculation spends 144.0 minutes. For the third peridynamic model which has 34,481 nodes, the GPU calculation spends 65.7 minutes while the serial calculation uses 1294.1 minutes. The GPU calculation is 19.7 times faster than the serial calculation. In general, as the number of nodes in a peridynamic model increases, the speedup of the GPU enabled version of the peridynamics code over the serial version in the CPU increases as shown in Figure 4.4(b).

	Algorithm 4.1	Algorithm 4.2
Wall-clock time (millisecond)	13,113	21,080

Table 4.3: The wall-clock time to calculate bond forces for one time-step using a node in the CPU. The three-dimensional peridynamic model has 4,725 nodes, the horizon  $\delta = 2\Delta x$  and  $\Delta x = 0.5$  mm.

Number of nodes	Time (minute) by the GPU	Time (minute) by the CPU
$11 \times 8 \times 8$	3.5	19.5
$21 \times 15 \times 15$	10.5	144.0
$41 \times 29 \times 29$	65.7	1294.1

Table 4.4: The wall-clock time to run peridynamic models for 500,000 time-steps on GPU and CPU, respectively. Peridynamic models have the horizon  $\delta = 2\Delta x$  and  $\Delta x = 0.5$  mm.

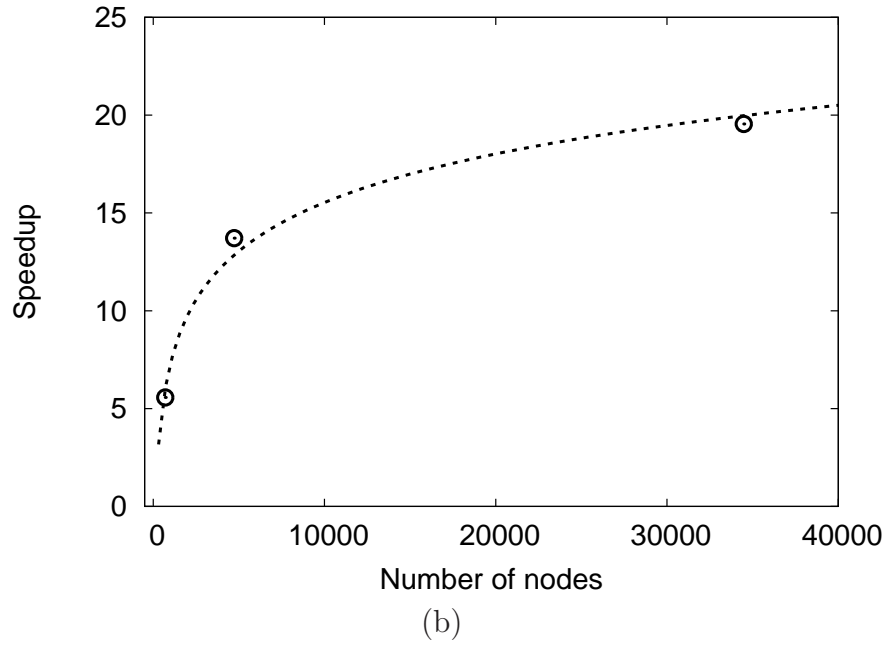
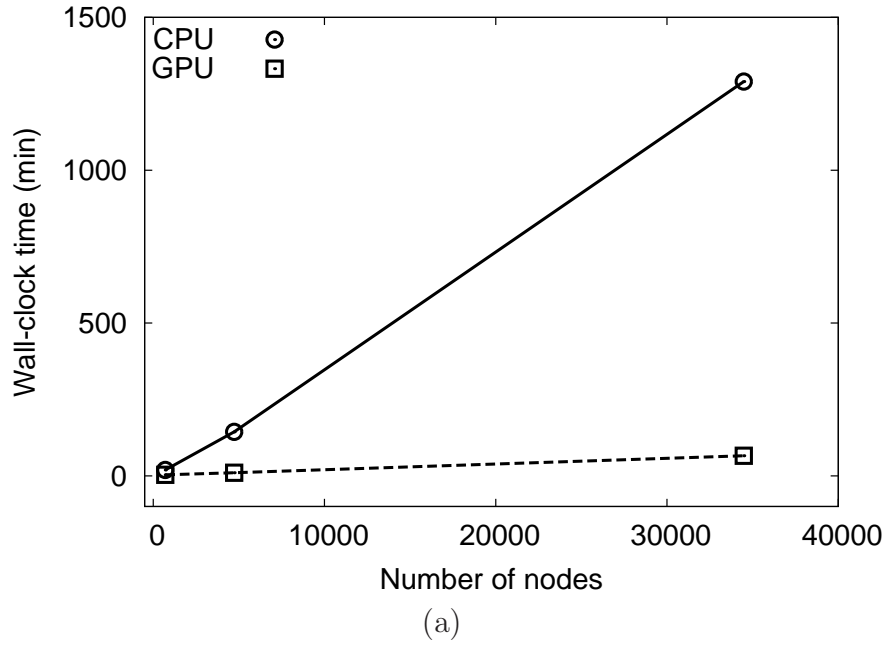


Figure 4.4: Comparison between the GPU enabled version of peridynamics code and the serial version. (a) Wall-clock time and (b) the speedup of the GPU version over the serial version.

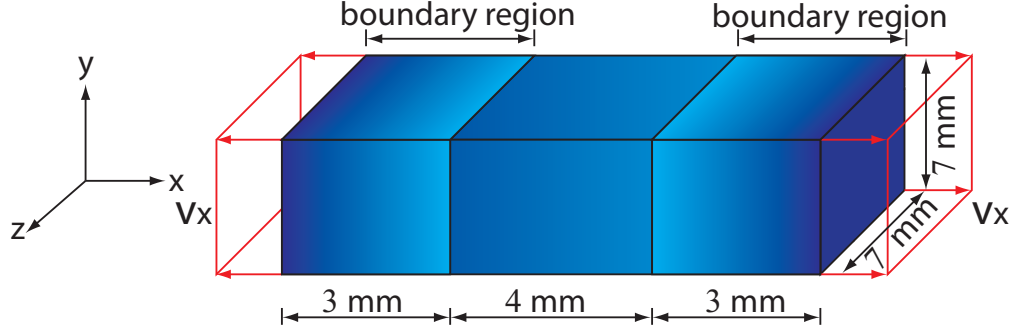


## 4.4 Case studies

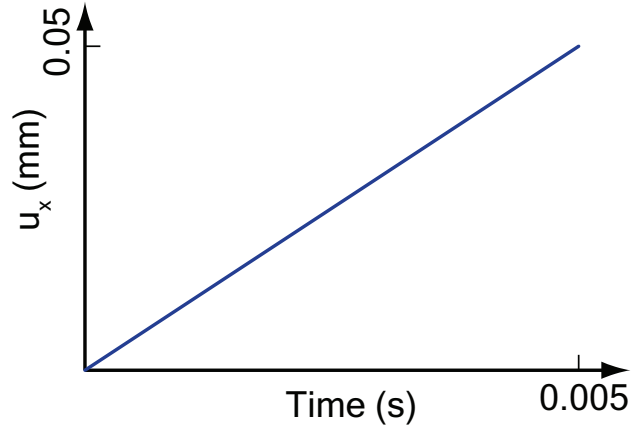
### 4.4.1 Brittle material

In the peridynamic framework, a three-dimensional rectangular bar is modeled as shown in Figure 4.5(a). The dimensions of the peridynamic bar are  $10 \text{ mm} \times 7 \text{ mm} \times 7 \text{ mm}$ . Boundary conditions are set by imposing a constant velocity to a region of nodes on both ends of the bar such that  $v_x = -10 \text{ mm/s}$  at the left-end boundary region and  $v_x = 10 \text{ mm/s}$  at the right-end boundary region. For the material, Young's modulus  $E$  is 70 GPa, and Poisson ratio  $\nu$  is 0.25. Time-step  $dt$  is set to  $dt = 5 \times 10^{-8} \text{ s}$ . To simulate brittle failure of materials, the critical stretch  $s_0$  for bond failure is set as 0.01.

To study the response of the peridynamic bar for different horizons, the rectangular bar is uniformly discretized with nodes distributed in a  $21 \times 15 \times 15$  grid. The grid size  $\Delta x$  is 0.5 mm, and the horizons  $\delta$  of  $2\Delta x$ ,  $3\Delta x$  and  $4\Delta x$  are used in the model. In order to calculate the cross-sectional stress, the summation of all interaction forces between peridynamic nodes passing through the cross section of the bar is projected on the x-axis. Then the cross-sectional stress is obtained by dividing the resultant force by the sectional area. The macroscopic engineering strain is measured by dividing the variation of the length by the original length. Figure 4.6(a) shows the stress  $\sigma_x$  versus the strain  $\varepsilon_x$  on the cross section at  $x = 5.0 \text{ mm}$  for different horizons. By calculating the tangent of the stress-strain curves for the horizon  $\delta = 2\Delta x$  in Figure 4.6(a), the back-calculated Young's modulus  $E$  is 70.46 GPa. Compared with the exact value  $E = 70.00 \text{ GPa}$  of the material, the error by the back-calculated Young's modulus is 0.66%. For the horizon  $\delta = 3\Delta x$  and  $\delta = 4\Delta x$ , the back-calculated Young's moduli are smaller than the exact value as shown in Figure 4.6(a).



(a)

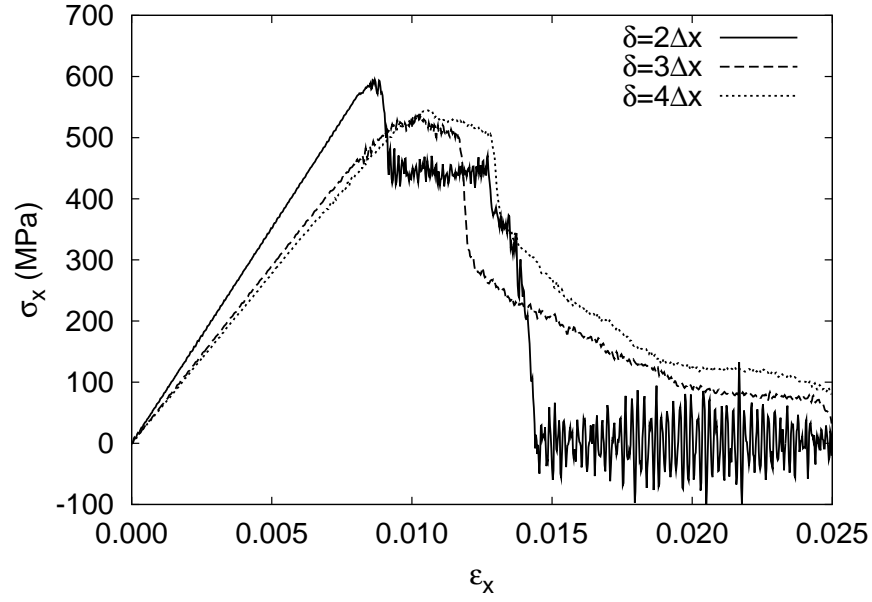


(b)

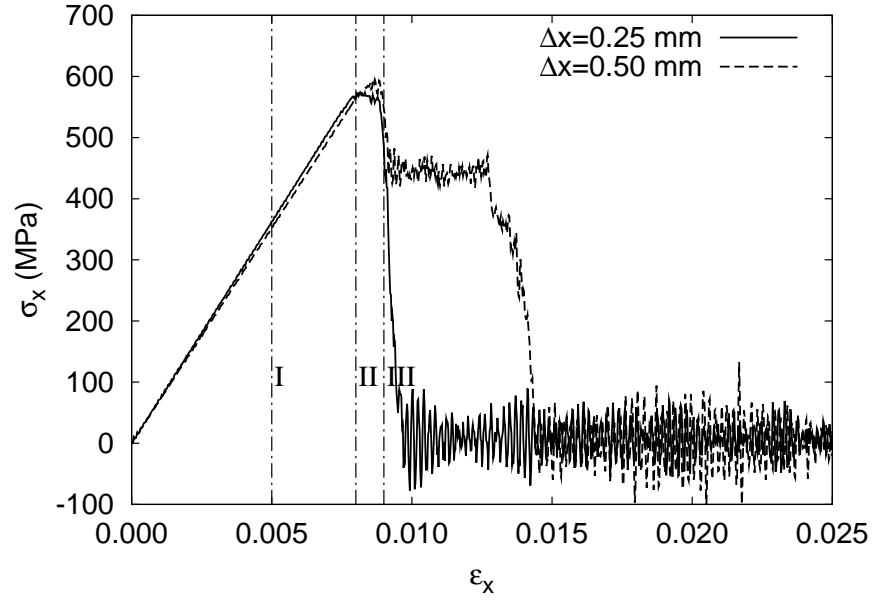
Figure 4.5: (a) The geometry of a three-dimensional bar and the boundary conditions; (b) Displacement of the boundary region versus time.

To investigate the effect of grid size, the peridynamic bar is discretized in a  $21 \times 15 \times 15$  grid with a grid size  $\Delta x = 0.50$  mm and in a  $41 \times 29 \times 29$  grid with a grid size  $\Delta x = 0.25$  mm, respectively. Figure 4.6(b) compares the cross-sectional stress  $\sigma_x$  at  $x = 5.0$  mm for the grid size  $\Delta x = 0.25$  mm and  $\Delta x = 0.50$  mm, where the horizon  $\delta$  is set as  $2\Delta x$ . As evident in Figure 4.6(b), the back-calculated Young's modulus  $E$  for the grid size  $\Delta x = 0.25$  mm is very close to the back-calculated Young's modulus  $E$  for the grid size  $\Delta x = 0.50$  mm. Since stresses and strains are not intrinsic variables in the peridynamic theory, the average bond stretch within the grid width  $\Delta x$  is calculated for each node as nodal strain. Strain distributions at times  $t = 1.0 \times 10^{-3}$  s,  $t = 1.6 \times 10^{-3}$  s and  $t = 1.8 \times 10^{-3}$  s denoted by

I (no bond failure), II (a few bond failure) and III (massive bond failure) in Figure 4.6(b), respectively, are plotted. As the strain contours demonstrate, strain  $\varepsilon_x$  is about 0.005 at time  $t = 1.0 \times 10^{-3}$  s as shown in Figure 4.7. At time  $t = 1.6 \times 10^{-3}$  s, the cross-sectional stress  $\sigma_x$  reaches its maximum value, and the strain  $\varepsilon_x$  near the boundary regions is larger than 0.01 as shown in Figure 4.8(b). On the cross section at  $z = 3.5$  mm, those nodes having the nodal strain  $\varepsilon_x$  in the range of 0.007 to 0.010 form diagonal patterns as shown in Figure 4.8(d). At time  $t = 1.8 \times 10^{-3}$  s when the cross-sectional stress  $\sigma_x$  significantly decreases due to massive bond failure, nodes having the nodal strain  $\varepsilon_x$  over 0.010 form an elliptical distribution on the cross section at  $z = 3.5$  mm as shown in Figure 4.9(b) and Figure 4.10(b). On the cross section at  $x = 5.0$  mm, interior nodes have the nodal strain  $\varepsilon_x$  over 0.01, and a failure core is formed on the cross section as shown in Figure 4.9(c) and Figure 4.10(c).



(a)



(b)

Figure 4.6: Stress on the cross section at  $x = 5.0$  mm for (a) different horizon  $\delta$  with the grid size  $\Delta x = 0.5$  mm and (b) different grid size  $\Delta x$  with the horizon  $\delta = 2\Delta x$ .  $\epsilon_x$  is the engineering strain imposed by the displacement at both ends of the bar.

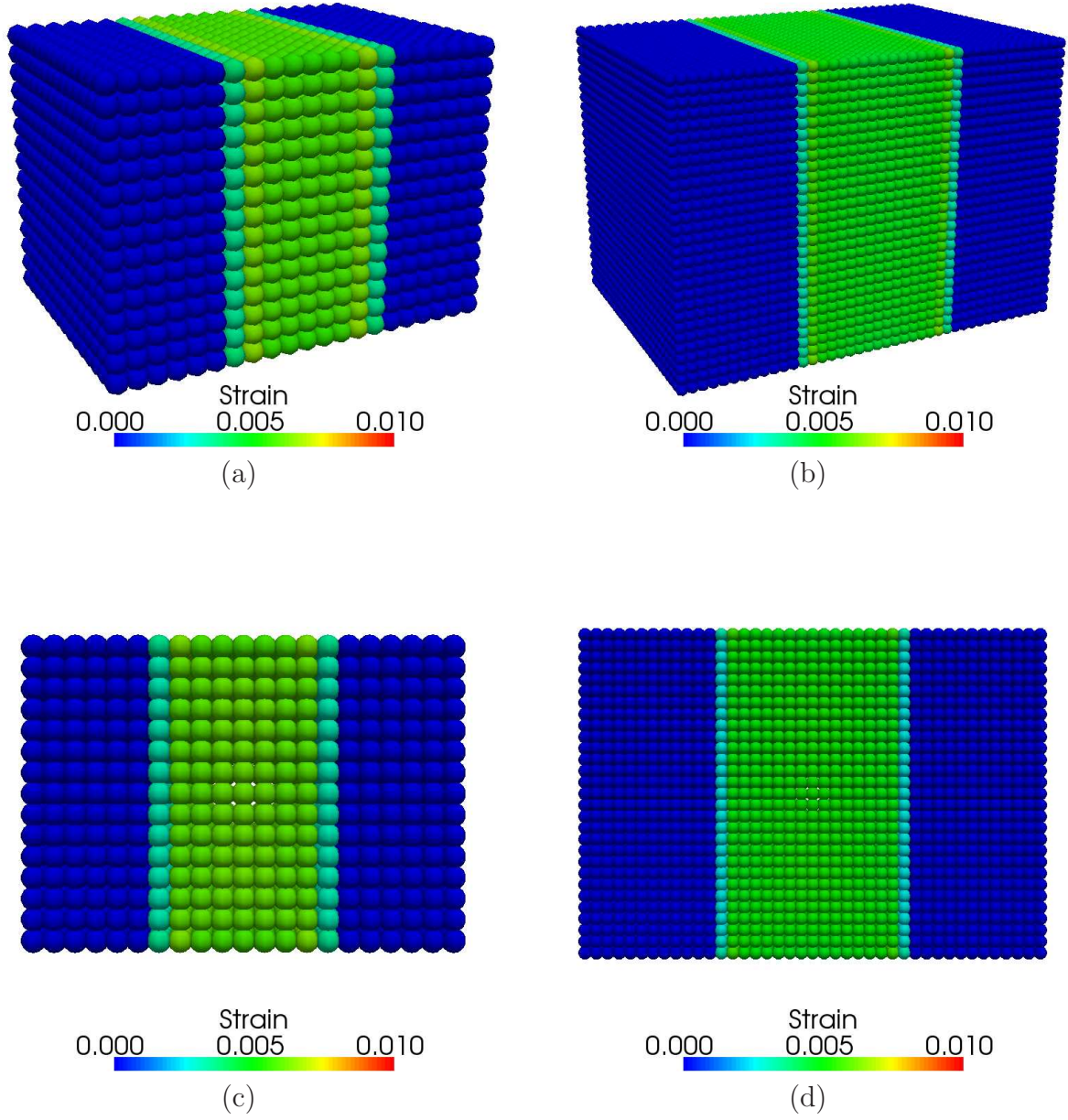


Figure 4.7: Strain  $\varepsilon_x$  at time  $t = 1.0 \times 10^{-3}$  s as denoted by I in Figure 4.6(b). The horizon  $\delta = 2\Delta x$ . (a)  $\Delta x = 0.50$  mm; (b)  $\Delta x = 0.25$  mm; (c) the cross section at  $z = 3.5$  mm,  $\Delta x = 0.50$  mm; (d) the cross section at  $z = 3.5$  mm,  $\Delta x = 0.25$  mm.

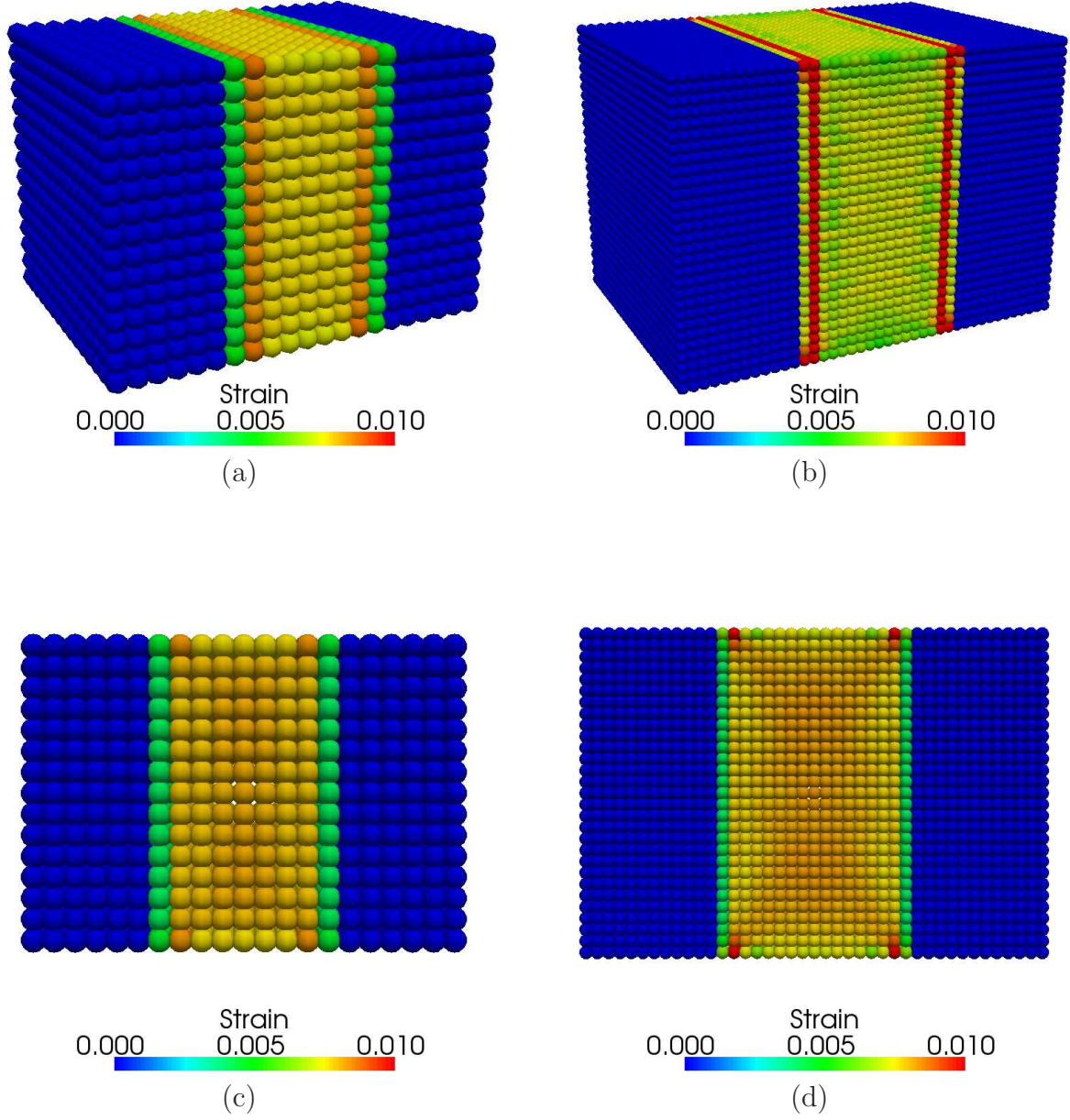


Figure 4.8: Strain  $\varepsilon_x$  at time  $t = 1.6 \times 10^{-3}$  s as denoted by II in Figure 4.6(b). The horizon  $\delta = 2\Delta x$ . (a)  $\Delta x = 0.50$  mm; (b)  $\Delta x = 0.25$  mm; (c) the cross section at  $z = 3.5$  mm,  $\Delta x = 0.50$  mm; (d) the cross section at  $z = 3.5$  mm,  $\Delta x = 0.25$  mm.



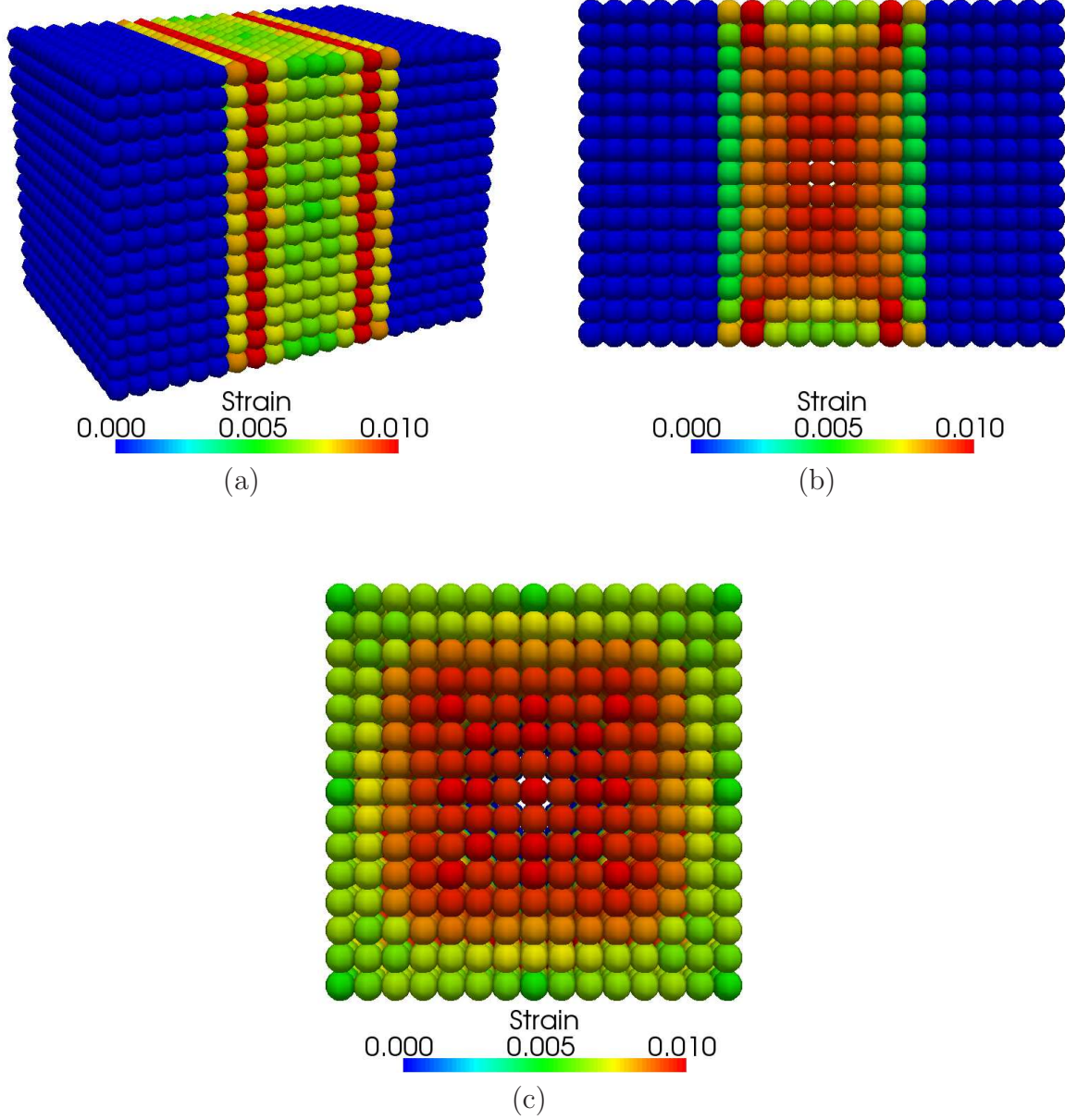


Figure 4.9: Strain  $\varepsilon_x$  at time  $t = 1.8 \times 10^{-3}$  s as denoted by III in Figure 4.6(b). The horizon  $\delta = 2\Delta x$ , the grid spacing  $\Delta x = 0.50$  mm. (a) bird's-eye view of bar; (b) the cross section at  $z = 3.5$  mm; (c) the cross section at  $x = 5.0$  mm.

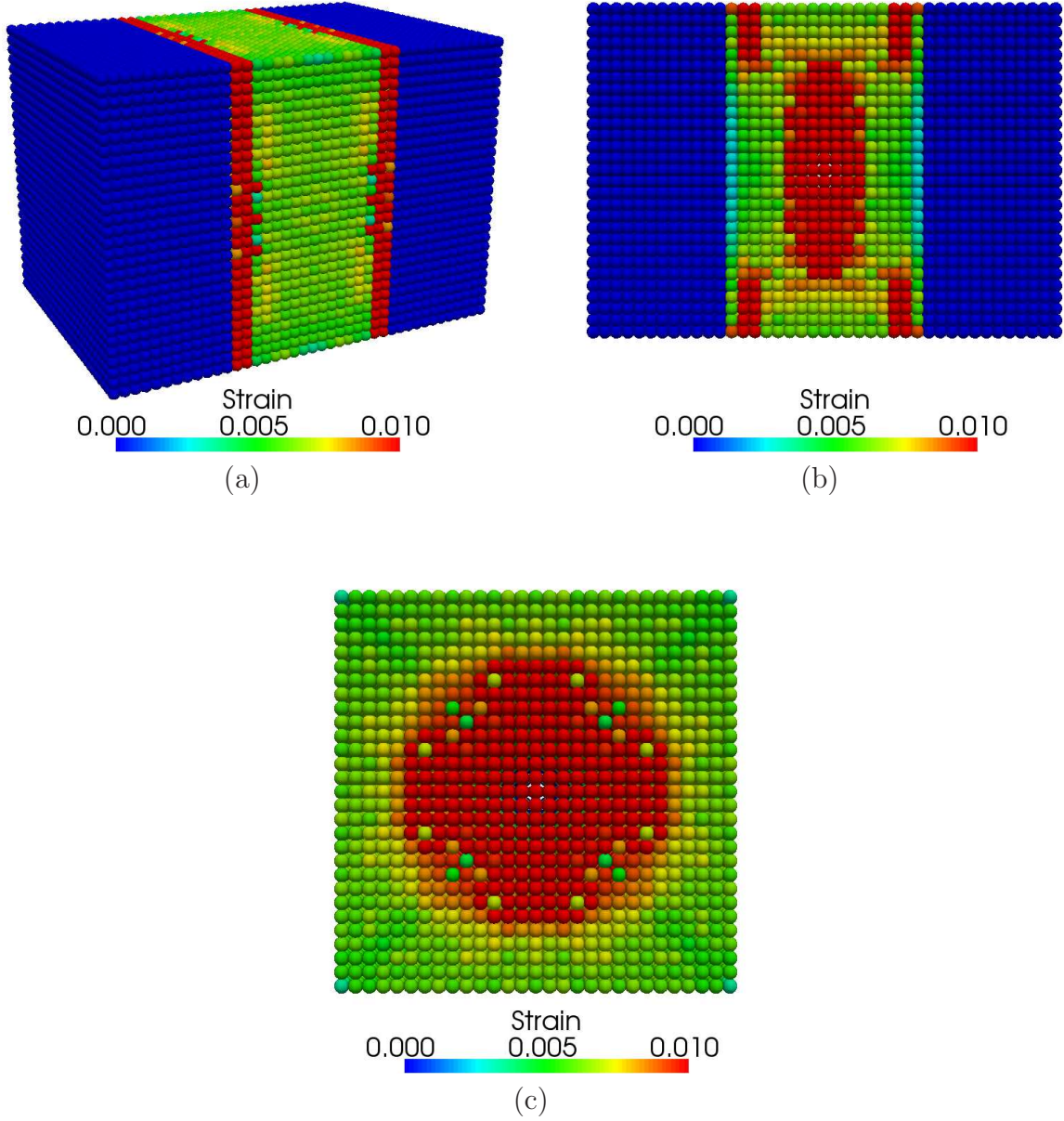


Figure 4.10: Strain  $\varepsilon_x$  at time  $t = 1.8 \times 10^{-3}$  s as denoted by III in Figure 4.6(b). The horizon  $\delta = 2\Delta x$ , the grid spacing  $\Delta x = 0.25$  mm. (a) bird's-eye view of bar; (b) the cross section at  $z = 3.5$  mm; (c) the cross section at  $x = 5.0$  mm.



#### 4.4.2 Ductile material

We consider a rectangular bar subjected to a stretch by imposing a constant velocity on nodes located at the boundary regions such that  $v_x = -10$  mm/s at the left-end boundary region and  $v_x = 10$  mm/s at the right-end boundary region as shown in Figure 4.5(a). The dimensions of the bar are 10 mm in length, 7 mm in width, and 7 mm in thickness. The bar is uniformly discretized with nodes in a  $21 \times 15 \times 15$  grid, and the horizon  $\delta = 2\Delta x$ . Young's modulus  $E$  is 70 GPa, Poisson ratio  $\nu$  is 0.25, and the density  $\rho$  is 2700 kg/m<sup>3</sup>. Peridynamic bonds are assumed to yield at the bond stretch  $s_y = 0.004$ , and the critical stretch for bonds to break is set as  $s_0 = 0.02$ . The calculation time-step is  $dt = 5 \times 10^{-8}$  s.

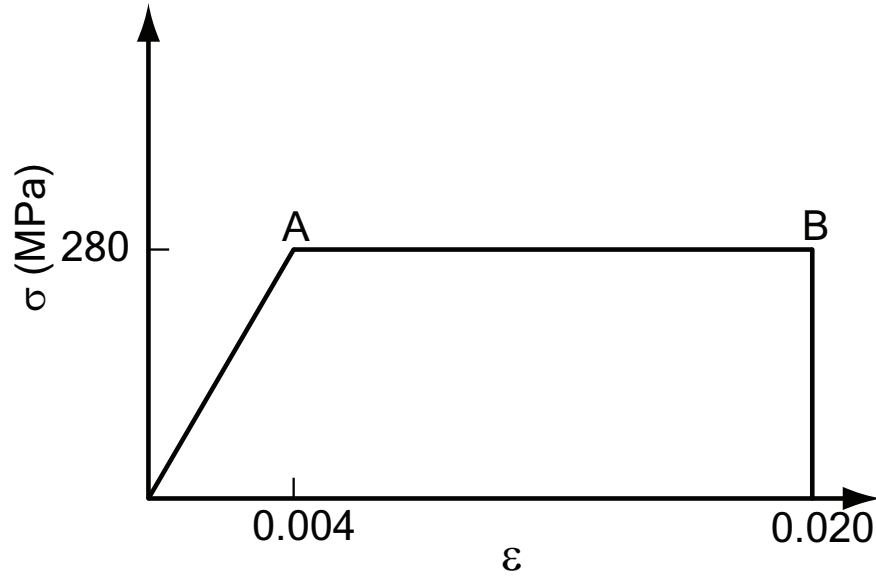
The peridynamics results are compared with the results by the finite element analysis (FEA) using a commercial FEA software, LS-DYNA [112]. In the FEA, the identical boundary conditions to the peridynamic model are imposed, and the time-step  $dt$  is automatically calculated. The material model used in the FEA is identical to the material model in peridynamics: Young's modulus  $E$  is 70 GPa, and Poisson ratio  $\nu$  is 0.25. The yield stress  $\sigma_y$  is 280 MPa obtained by multiplying the yield bond stretch  $s_y = 0.004$  and Young's modulus. The limit strain is set to be 0.020, and the corresponding plastic strain is 0.016. Figure 4.11(a) shows the material properties implemented in LS-DYNA.

Figure 4.11(b) compares the average stress on the cross section at  $x = 5.0$  mm by peridynamics and the finite element analysis. After the yielding, the cross-sectional stress continues to increase as the boundary displacement  $u_x$  increases in the peridynamic model while the FE model shows almost perfect plasticity. The cross-sectional stress demonstrates a trilinear response in the peridynamics. As shown in Figure 4.11(b), the end of the second piecewise linear line approximately corresponds to the displacement  $u_x = 0.017$  mm, and

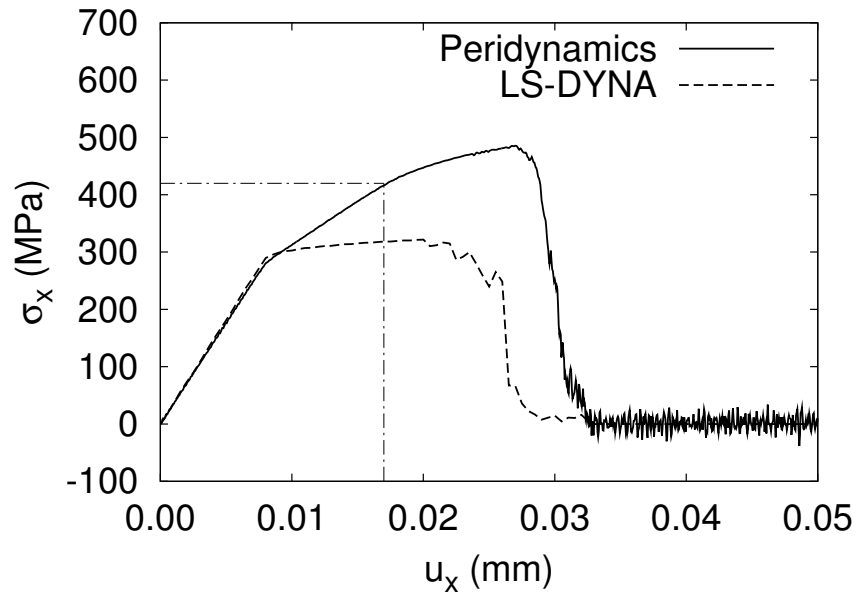
the stress is  $\sigma_x = 420$  MPa. For the stress of a node in the peridynamic model, the total bond forces acting through the cross section of a node are calculated. Figure 4.11(c) shows the comparison of the stress  $\sigma_x$  of the element which has a node at the center of the bar ( $x = 5.0$  mm,  $y = 3.5$  mm and  $z = 3.5$  mm) and the stress  $\sigma_x$  of the peridynamic node located at the center of the peridynamic bar. Similar to the average stress on the cross section, the stress of the peridynamic node at the center of the bar shows a trilinear response while the stress in the element in the FEA has a bilinear response. It is noticed that the outer bonds of a node yield earlier than the inner bonds in the peridynamic model, and the stiffness of the peridynamic model gets closer to the value of the FE model after all the bonds yield, as shown in Figure 4.11(c). The nodal strains  $\varepsilon_x$  at the center of the bar ( $x = 5.0$  mm,  $y = 3.5$  mm and  $z = 3.5$  mm) obtained by peridynamics and FEA are compared in Figure 4.11(d). The cause of the differences might be the scales at which the material model is defined. Therefore, to bridge the different scales, it is proposed to modify the scheme to define the material in the finite element analysis rather than using the identical material model to peridynamics. The material response obtained in Figure 4.11(b) is interpolated to a trilinear line as shown in Figure 4.12(a). The point  $B$  is determined from the macroscopic response of the peridynamic model.

A piecewise linear plastic model available in LS-DYNA [112] is used in the FE simulation in which the effective stress versus effective plastic strain  $\varepsilon_{eff}^p$  curve is defined, where the effective plastic strain is given as  $\varepsilon_{eff}^p = \int_0^t \sqrt{\frac{2}{3} \dot{\varepsilon}_{ij}^p \dot{\varepsilon}_{ij}^p} dt$  [72]. The plastic strain starts to increase after the strain reaches the yield strain  $\varepsilon = 0.004$ . The effective plastic strain can be approximated by integrating the strain rate after yielding, imposed by displacements at both ends. By evaluating the integration, the effective plastic strain  $\varepsilon_{eff}^p$  corresponding to  $\sigma_x = 420$  MPa is obtained as  $\varepsilon_{eff}^p = 0.0037$ . The average stress on the cross section at

$x = 5.0$  mm and the stress at the center point of the section are plotted in Figures 4.12(b) and (c). The nodal strains at the center of the bar are compared in Figure 4.12(d), and the results show good agreement. As shown in Figures 4.12(b) to (d), the differences between the solutions by peridynamics and FEA are reduced substantially. The developed scheme can bridge the simulations at different scales at which the material model is defined. First, a mesoscale modeling is performed using peridynamics, and material properties are retrieved from the macroscopic material response. Then the properties are described as a modified material model at the macroscale for the FEA. Strains  $\varepsilon_x$  by peridynamics and FEA when the displacement at the boundary  $u_x = 0.025$  mm ( $t = 2.5 \times 10^{-3}$  s) are compared in Figure 4.13, and the distribution of strains shows almost identical results.



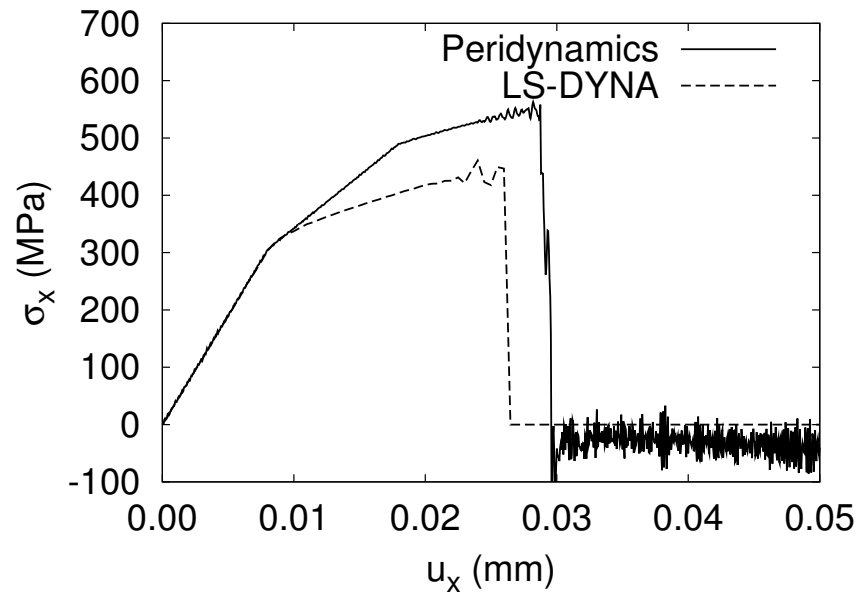
(a)



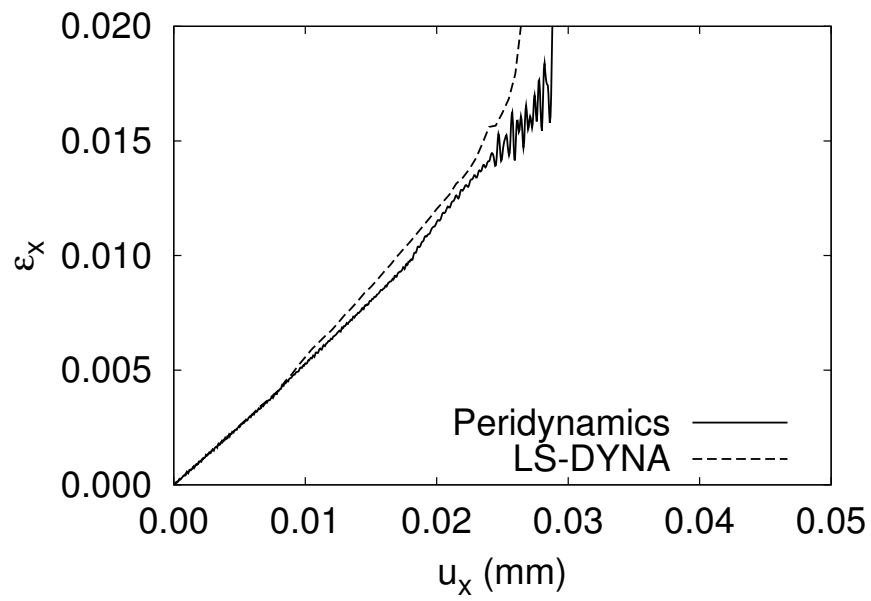
(b)

Figure 4.11: A comparison between peridynamic and FEA solutions. (a) The material model used in FEA which is identical to the constitutive for bonds in peridynamics; (b) Stress  $\sigma_x$  on the cross section at  $x = 5.0$  mm; (c) Stress  $\sigma_x$  on an element which has a node at the center of the bar ( $x = 5.0$  mm,  $y = 3.5$  mm and  $z = 3.5$  mm) and the stress  $\sigma_x$  on the peridynamic node at the center of the bar; (d) Strain  $\varepsilon_x$  at the center of the bar ( $x = 5.0$  mm,  $y = 3.5$  mm and  $z = 3.5$  mm).  $u_x$  is the displacement of the boundary region as shown in Figure 4.5.

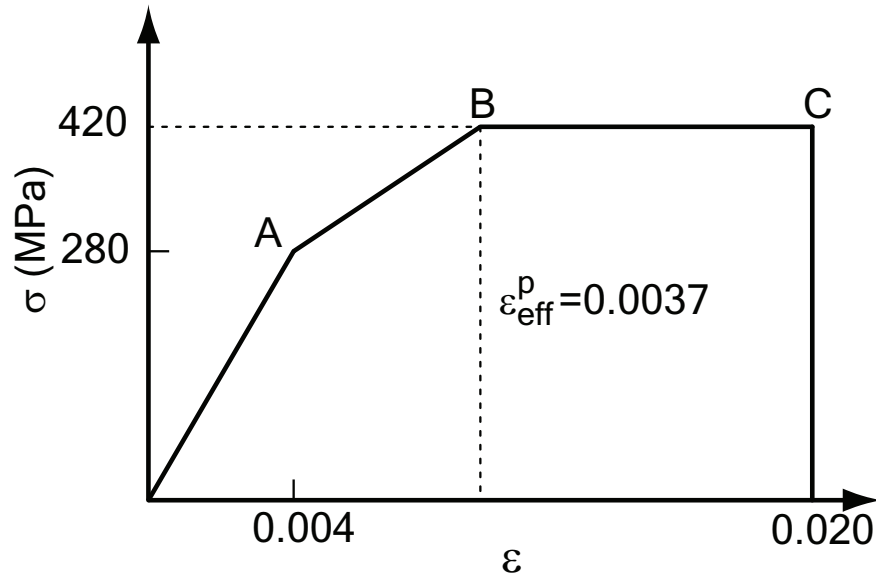
Figure 4.11 (cont'd)



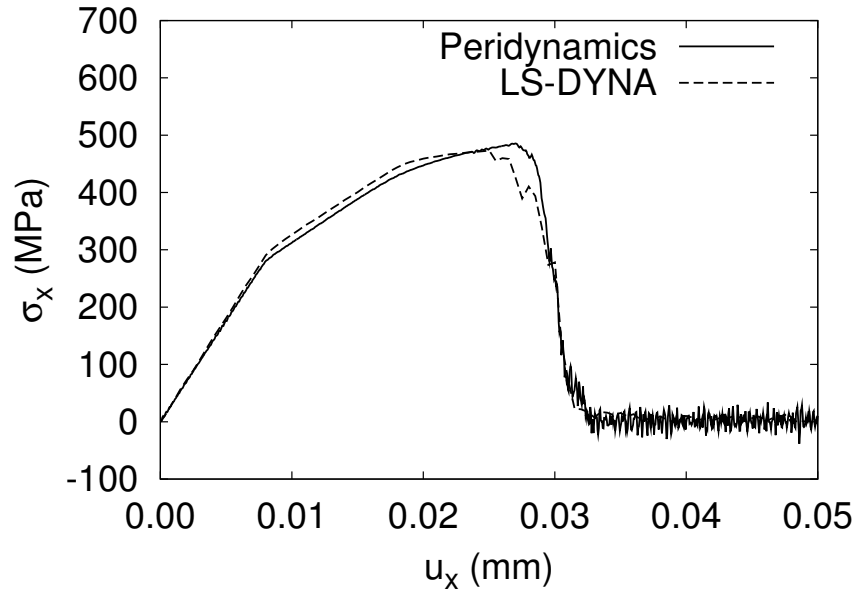
(c)



(d)



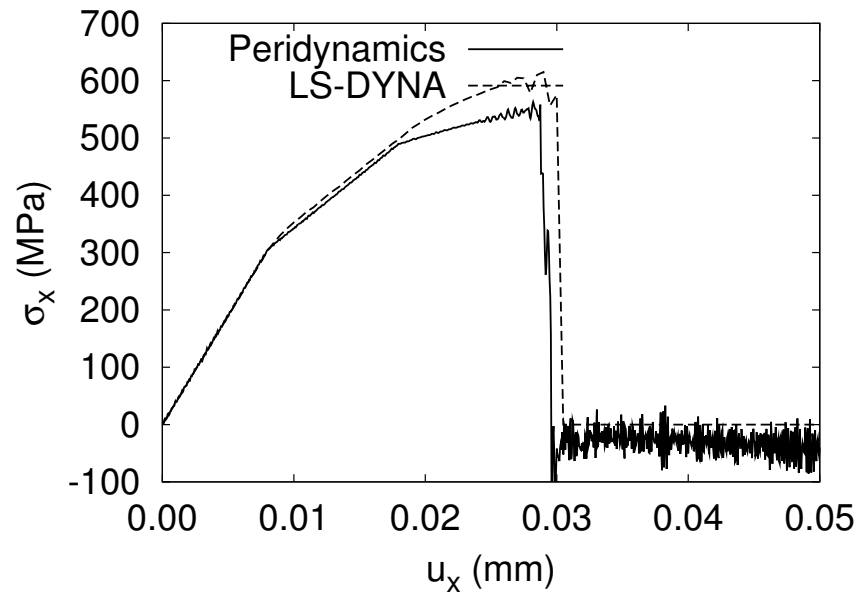
(a)



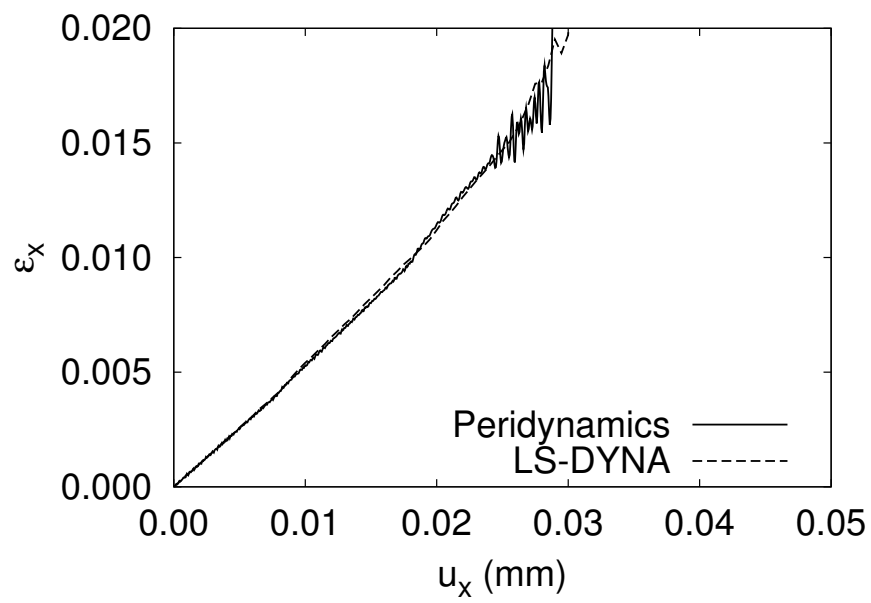
(b)

Figure 4.12: A comparison between peridynamic and FEA solutions. (a) The modified material model used in FEA to incorporate retrieved macroscopic material properties from the peridynamic model; (b) Stress  $\sigma_x$  on the cross section at  $x = 5.0$  mm; (c) Stress  $\sigma_x$  on an element which has a node at the center of the bar ( $x = 5.0$  mm,  $y = 3.5$  mm and  $z = 3.5$  mm) and the stress  $\sigma_x$  on the peridynamic node at the center of the bar; (d) Strain  $\varepsilon_x$  at the center of the bar ( $x = 5.0$  mm,  $y = 3.5$  mm and  $z = 3.5$  mm).  $u_x$  is the displacement of the boundary region as shown in Figure 4.5.

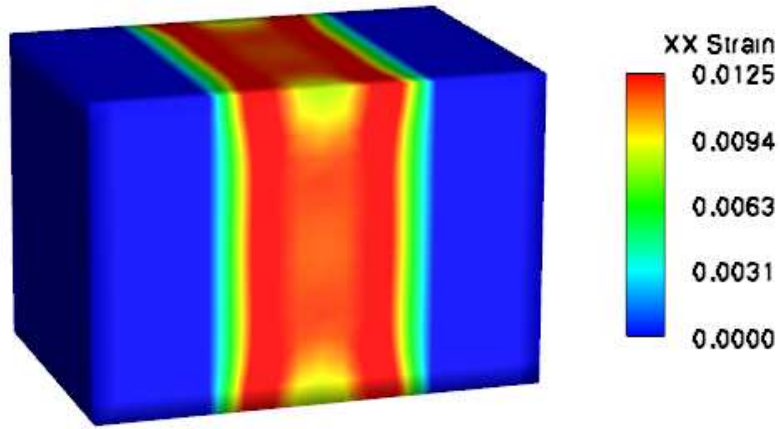
Figure 4.12 (cont'd)



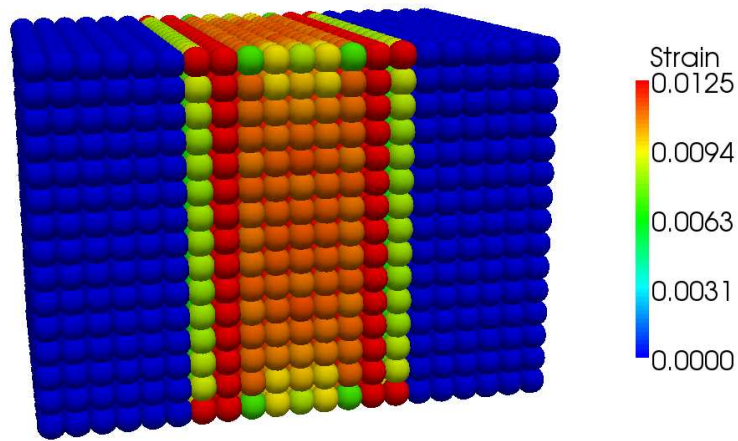
(c)



(d)



(a)



(b)

Figure 4.13: Strain  $\varepsilon_x$  when the boundary displacement  $u_x = 0.025$  mm. (a) LS-DYNA and (b) peridynamics.



## 4.5 Summary

A peridynamics code is developed for three-dimensional simulations using numerical micro-moduli for discretized peridynamic models. To enhance the efficiency in the calculation, we use the PGI Accelerator Programming model on an NVIDIA Tesla C1060 GPU for the parallelization. A benchmark problem of matrix multiplication is conducted to compare the wall-clock time between the parallelized algebraic computation on the GPU and the serial computation on the CPU. In order to eliminate the loop dependency in the peridynamics code for efficient parallelization, an algorithm that separates nested loops into independent loops is adopted in the GPU implementation. We compared the wall-clock times of the parallelized calculation in GPU and the serial calculation in CPU for different peridynamic models. As the number of nodes in the peridynamic model increases, a significant speedup over the serial calculation is achieved in the GPU.

The responses of the peridynamic model for the horizon  $\delta$  of  $2\Delta x$ ,  $3\Delta x$  and  $4\Delta x$  are investigated for a brittle material. For the horizon  $\delta = 2\Delta x$ , the back-calculated Young's modulus matches the exact value of the material. On the other hand, for the horizon larger than  $2\Delta x$ , the back-calculated Young's moduli are smaller than the exact value. With the horizon  $\delta = 2\Delta x$ , the responses of the peridynamic bar discretized with different grid sizes ( $\Delta x = 0.50$  mm and  $\Delta x = 0.25$  mm) are compared, and numerical results of the back-calculated Young's modulus show good agreements. The strain distributions at different times in the simulations are demonstrated. After a large number of bonds reach the critical stretch, a failure core is formed inside the peridynamic model.

For a ductile material, the peridynamic stresses and strains are compared with the results by FEA using LS-DYNA. When the material model used in FEA is identical to that of the

peridynamic model, the stresses of FEA show bilinear responses while the peridynamic model demonstrates trilinear responses with the horizon  $\delta = 2\Delta x$ . The nodal strains by FEA and peridynamics at the center of the bar are not identical. Therefore, to bridge material models at different scales, the material properties are retrieved from the macroscopic response of the peridynamic model. These retrieved properties are used to modify the material model in FEA. By applying the proposed procedure, the differences between FEA and peridynamic solutions reduce substantially. This proposed scheme will be useful for coupling peridynamics and FEM. Instead of directly applying the material model defined for peridynamic bonds to FEA in a coupled model, which may not lead to an accurate result, the plastic material model in FEA might be obtained from the macroscopic responses of peridynamic models.

# Chapter 5

## Coupling of Discretized Peridynamics with Finite Element Method

### 5.1 Introduction

As a reformulated theory of continuum mechanics, peridynamics eliminates the spatial derivatives, and it is valid regardless of discontinuities [153, 159]. Therefore, peridynamics is useful to solve problems involving spontaneously emerged discontinuities. Compared with the finite element method (FEM), peridynamics is computationally expensive. Macek and Silling [115] implemented peridynamics in a commercial finite element analysis code, ABAQUS, using truss elements. The conventional FE mesh is coupled with the peridynamic truss mesh using the embedded element feature available in the finite element analysis code. Lall *et al.* [103] used the peridynamics based finite element model to study shock and vibration reliability of electronics. Kilic and Madenci [94] presented a coupling approach using overlapping regions in which both peridynamic and FE equations are utilized. Agwai *et al.* [2] and Oterkus [133] employed the submodeling approach to couple the FEM with peridynamics. In their approach, the global analysis by means of finite element analysis is performed first, and then peridynamics is used for submodeling. A morphing strategy based on the energy equivalence was proposed by Lubineau *et al.* [113]. In this chapter, we introduce a coupling approach of discretized peridynamics with finite elements. Differ-

ent from the approach in [115, 103] implementing peridynamic model in the framework of the conventional FEM and the submodeling approach [2, 133], the peridynamic subregion is directly coupled to the finite element subregion in the present approach. An interface element is introduced to calculate coupling forces instead of using overlapping regions [94] or the morphing strategy [113] to couple peridynamic and FE subregions. Depending on how coupling forces are divided to FE nodes of an interface element, we further discuss two types of coupling schemes.

A great deal of research effort has been made to study many fracture problems. One common benchmark problem characterized by the mixed mode fracture is the test of a double-edge-notched concrete specimen conducted by Nooru-Mohamed *et al.* [130]. The test of Nooru-Mohamed was adopted by De Borst [38] in the discussion of computational modeling of concrete fracture. For the analyses, the finite element smeared-crack approach with the gradient Rankine plasticity model, Cruch-Crack model, and Ottosen's model has been used for numerical studies of Nooru-Mohamed's experiment by Di Prisco *et al.* [41]. A comparative study of three-dimensional constitutive models for the double-edge-notched test was performed by Pivonka *et al.* [140]. Gasser and Holzapfel [64] employed the cohesive crack model with the PUFEM for the numerical modeling of the test. The XFEM was utilized by Cox [35], Meschke and Dumstorff [121], and Unger *et al.* [174] for the simulations. An adaptive mesh refinement technique applied to a nonlocal version of anisotropic damage model was employed by Patzák and Jirásek [136]. Réthoré *et al.* [146] used a hybrid analytical and XFEM to study the propagation of curved cracks in the double-edge-notched concrete specimen.

The remainder of this chapter is organized as follows. In Section 5.2, the finite element formulations are summarized. In Section 5.3, we present two types of coupling schemes de-

pending on the distributing schemes of coupling forces to FE nodes of interface elements, and the inverse isoparametric mapping that is essential in the coupling approach is summarized. In Section 5.4, numerical examples under quasi-static conditions are provided to validate the proposed coupling approach including one- and three-dimensional elastic problems and the mixed mode fracture in a double-edge-notched concrete specimen. The results by applying two types of coupling schemes for numerical simulations are discussed. In the last section, concluding remarks are summarized.

## 5.2 Theory

### 5.2.1 Finite element formulations

The equation of motion in the conventional continuum mechanics is derived from the principle of linear momentum. The temporal change rate of linear momentum is equal to the force applied on the body as [118]

$$\rho \ddot{u}_i = \sigma_{ij,j} + f_i^B \quad \text{in } \Omega, \quad (5.1)$$

where  $\rho$  is the density,  $\ddot{u}_i$  is the acceleration field,  $\sigma_{ij}$  is the Cauchy stress tensor, and  $f_i^B$  is the body force density field. The essential boundary condition  $\Gamma_u$  and natural boundary condition  $\Gamma_f$  are defined, respectively, as [11]

$$u_i = U_i \quad \text{on } \Gamma_u, \quad (5.2)$$

$$\sigma_{ij}n_j = F_i^s \quad \text{on } \Gamma_f, \quad (5.3)$$

where the surface of the body  $\Gamma = \Gamma_u \cup \Gamma_f$ ,  $\Gamma_u \cap \Gamma_f = \emptyset$ , and  $n_j$  means the components of the unit outer normal vector on  $\Gamma$ . The constitutive equation for continuum is stated as

$$\sigma_{ij} = C_{ijkl}\varepsilon_{kl}, \quad (5.4)$$

where  $C_{ijkl}$  is the elastic constitutive coefficient, and the components of strains are defined as

$$\varepsilon_{ij} = \frac{1}{2} (u_{i,j} + u_{j,i}). \quad (5.5)$$

Applying the principle of virtual work to Equation (5.1), we have

$$\int_{\Omega} (\sigma_{ij,j} + f_i^B - \rho \ddot{u}_i) \delta u_i d\Omega = 0, \quad (5.6)$$

where  $\delta u_i$  is the virtual displacement. After integrating by parts and applying the divergence theorem, the weak formulation is obtained as [110]

$$-\int_{\Omega} \sigma_{ij} \delta u_{i,j} d\Omega + \int_{\Gamma} \sigma_{ij} n_j \delta u_i dS + \int_{\Omega} f_i^B \delta u_i d\Omega - \int_{\Omega} \rho \ddot{u}_i \delta u_i d\Omega = 0. \quad (5.7)$$

Considering the symmetry of the stress tensor ( $\sigma_{ij} = \sigma_{ji}$ ) and applying the boundary conditions, we have

$$\int_{\Omega} \rho \ddot{u}_i \delta u_i d\Omega + \int_{\Omega} \sigma_{ij} \delta \varepsilon_{ij} d\Omega = \int_{\Gamma_f} F_i^s \delta u_i dS + \int_{\Omega} f_i^B \delta u_i d\Omega. \quad (5.8)$$

Substituting the constitutive law in Equation (5.4) into Equation (5.8), we obtain the finite element formulation

$$\int_{\Omega} \rho \ddot{u}_i \delta u_i d\Omega + \int_{\Omega} C_{ijkl} \varepsilon_{kl} \delta \varepsilon_{ij} d\Omega = \int_{\Gamma_f} F_i^s \delta u_i dS + \int_{\Omega} f_i^B \delta u_i d\Omega. \quad (5.9)$$

In the finite element analysis, the displacements within each element are interpolated by means of shape functions as [11]

$$\mathbf{u}^{(e)} = \mathbf{H}^{(e)} \mathbf{U}^{(e)}, \quad (5.10)$$

where  $\mathbf{H}^{(e)}$  is the displacement interpolation matrix, the superscript  $e$  represents the element  $e$ , and the nodal displacement vector  $\mathbf{U}^{(e)}$  is expressed as  $\mathbf{U}^{(e)T} = \{u_1 \ v_1 \ w_1 \ \cdots \ u_n \ v_n \ w_n\}$  for an element of  $n$  nodes. The strain vector is evaluated by

$$\boldsymbol{\varepsilon}^{(e)} = \mathbf{B}^{(e)} \mathbf{U}^{(e)}, \quad (5.11)$$

where  $\mathbf{B}^{(e)}$  is the strain-displacement matrix which is written as

$$\mathbf{B}^{(e)} = \begin{bmatrix} \frac{\partial h_1}{\partial x} & & & & \frac{\partial h_n}{\partial x} \\ & \frac{\partial h_1}{\partial y} & & & \frac{\partial h_n}{\partial y} \\ & & \frac{\partial h_1}{\partial z} & & \frac{\partial h_n}{\partial z} \\ \frac{\partial h_1}{\partial y} & \frac{\partial h_1}{\partial x} & & \cdots & \frac{\partial h_n}{\partial y} & \frac{\partial h_n}{\partial x} \\ & \frac{\partial h_1}{\partial z} & \frac{\partial h_1}{\partial y} & & \frac{\partial h_n}{\partial z} & \frac{\partial h_n}{\partial y} \\ \frac{\partial h_1}{\partial z} & \frac{\partial h_1}{\partial x} & & & \frac{\partial h_n}{\partial z} & \frac{\partial h_n}{\partial x} \end{bmatrix}. \quad (5.12)$$

Substituting Equations (5.10) and (5.11) into Equation (5.9), we have the weak formulation in matrix form as

$$\mathbf{M}\ddot{\mathbf{U}} + \mathbf{K}\mathbf{U} = \mathbf{F}, \quad (5.13)$$

where  $\mathbf{M}$  is the mass matrix,  $\mathbf{K}$  is the stiffness matrix, and  $\mathbf{F}$  is the force vector. The assembled matrices following the convention of direct stiffness method [11] are summarized as

$$\mathbf{M} = \sum_e \mathbf{M}^{(e)}, \quad \mathbf{M}^{(e)} = \int_{\Omega^{(e)}} \rho^{(e)} \mathbf{H}^{(e)T} \mathbf{H}^{(e)} d\Omega^{(e)}, \quad (5.14)$$

$$\mathbf{K} = \sum_e \mathbf{K}^{(e)}, \quad \mathbf{K}^{(e)} = \int_{\Omega^{(e)}} \mathbf{B}^{(e)T} \mathbf{C}^{(e)} \mathbf{B}^{(e)} d\Omega^{(e)}, \quad (5.15)$$

$$\begin{aligned} \mathbf{F} &= \sum_e \mathbf{F}_s^{(e)} + \sum_e \mathbf{F}_B^{(e)}, \\ \mathbf{F}_s^{(e)} &= \int_{\Gamma_f^{(e)}} \mathbf{H}^{(e)T} \mathbf{F}^{S(e)} dS^{(e)}, \quad \mathbf{F}_B^{(e)} = \int_{\Omega^{(e)}} \mathbf{H}^{(e)T} \mathbf{f}^{B(e)} d\Omega^{(e)}. \end{aligned} \quad (5.16)$$

## 5.3 Coupling between the peridynamic and finite element subregions

### 5.3.1 Coupling schemes

To gain the efficiency from finite element analyses and exploit the generality of peridynamics in the presence of discontinuities, a domain is partitioned into a conventional FE subregion and a peridynamic subregion as shown in Figure 5.1. With the coupling approach, the subregion where failure is expected can be modeled using peridynamics. The overall computational cost is reduced by using FEM for the remainder of the domain.



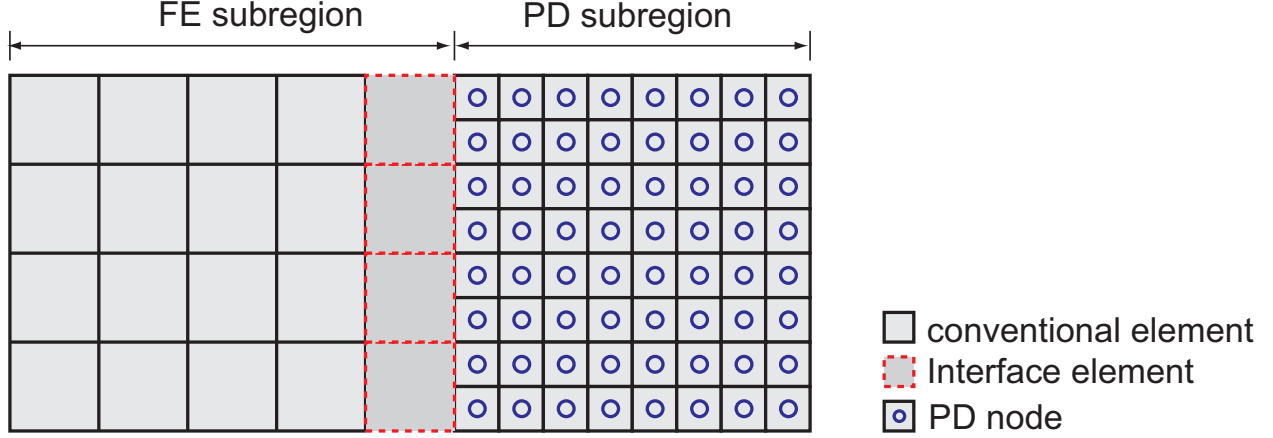


Figure 5.1: Partition of the domain. The FE subregion and the peridynamic (PD) subregion are bridged by interface elements.

In the conventional FE subregion, the lumped mass matrix is formed by distributing the total element mass to nodes of the element [11]. The internal forces on FE nodes can be calculated as

$$\mathbf{F}^{int} = \sum_e \mathbf{F}^{int(e)} = \sum_e \mathbf{K}^{(e)} \mathbf{U}^{(e)}, \quad (5.17)$$

where  $\mathbf{K}^{(e)}$  is the element stiffness matrix. The equation of motion of an FE node is obtained as

$$M_I \ddot{\mathbf{U}}_I = \mathbf{F}_I^{ext} - \mathbf{F}_I^{int}, \quad (5.18)$$

where  $M_I$  is the lumped mass of node  $I$ ,  $\ddot{\mathbf{U}}_I$  is the acceleration vector field,  $\mathbf{F}_I^{ext}$  is the external force applied on the node  $I$  by evaluating the corresponding components of  $\mathbf{F}$  in Equation (5.16), and  $\mathbf{F}_I^{int}$  is the internal force vector of the node  $I$ . Because the mass matrix is diagonal, Equation (5.18) can be solved without factorizing a global stiffness matrix.

To bridge the FE subregion and the peridynamic subregion, we introduce an interface element. A three-dimensional interface element consisting of eight FE nodes is illustrated in Figure 5.2. In an interface element, a number of peridynamic nodes are embedded for the calculation of coupling forces. The interacting forces between embedded peridynamic

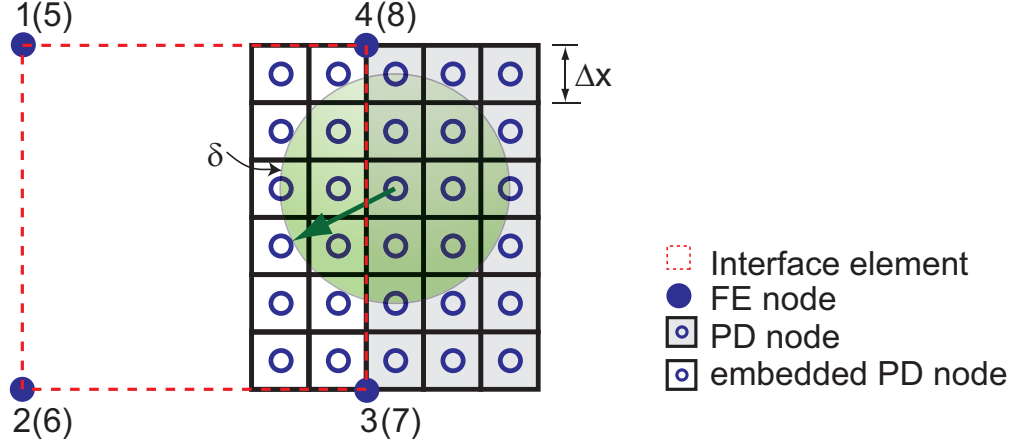


Figure 5.2: Interface element for the coupling of FE subregion and peridynamic subregion.

nodes and peridynamic nodes out of interface elements are called coupling forces. It is worth noting that interactions between embedded peridynamic nodes are not considered as coupling forces. The number of embedded peridynamic nodes is determined by the size of the horizon, and there should be sufficient embedded nodes within the horizon of nodes near the interface of the peridynamic subregion and the FE subregion as shown in Figure 5.2. To evaluate coupling forces, each embedded peridynamic node represents a material volume of  $(\Delta x)^3$  inside an interface element. However, embedded peridynamic nodes are not involved in the global equation. In other words, the displacements of embedded peridynamic nodes are not calculated by solving the equation of motion. Therefore, the mass of an interface element is equally distributed to FE nodes of the interface element. Consider an embedded peridynamic node subjected to the coupling force  $\mathbf{f}^{cp}$  as shown in Figure 5.3, the coupling force is then divided to FE nodes of the interface element by means of shape functions as

$$\mathbf{f}_i^{cp} = \phi_i(\xi, \eta, \psi) \mathbf{f}^{cp}, \quad i = 1, \dots, 8, \quad (5.19)$$

where  $\phi_i$  is the shape function of the node  $i$  belonging to the interface element,  $(\xi, \eta, \psi)$  are the natural coordinates of the embedded node in the interface element, which should be determined by the inverse isoparametric mapping. We designate this coupling scheme as the *VL-coupling scheme* since the whole volume of the interface element is subjected to coupling forces. On the other hand, different from the VL-coupling scheme, we might divide coupling forces only to the FE nodes on the interface segment as shown in Figure 5.4. Therefore, FE nodes not on the interface segment are subjected to internal forces arising from the element stiffness only. Since the interface between the peridynamic and FE subregions is similar to a contact surface, the scheme demonstrated in Figure 5.4 is designated as the *CT-coupling scheme*. To implement the CT-coupling scheme, interfaces between the peridynamic subregion and the FE subregion have to be defined prior to analyses. Coupling forces on embedded nodes are divided to those FE nodes on the interface segment as shown in Figure 5.4 by

$$\mathbf{f}_i^{cp} = \phi_i(\xi_c, \eta_c) \mathbf{f}^{cp}, \quad i = 3, 4, 7, 8, \quad (5.20)$$

where  $\phi_i$  is the shape function on the interface segment, and  $(\xi_c, \eta_c)$  are the natural coordinates of the projection of an embedded node onto the interface segment.

In general, the equation of motion for FE nodes of an interface element is written as

$$M_I \ddot{\mathbf{U}}_I = \mathbf{F}_I^{ext} - \hat{\mathbf{F}}_I^{int}, \quad (5.21)$$

where  $\mathbf{F}_I^{ext}$  is the external force by evaluating Equation (5.16), and the internal force is given as

$$\hat{\mathbf{F}}_I^{int} = \mathbf{F}_I^{int} + \mathbf{f}_I^{cp} = \left[ \sum_e \mathbf{K}^{(e)} \mathbf{U}^{(e)} \right]_I + \mathbf{f}_I^{cp}, \quad (5.22)$$

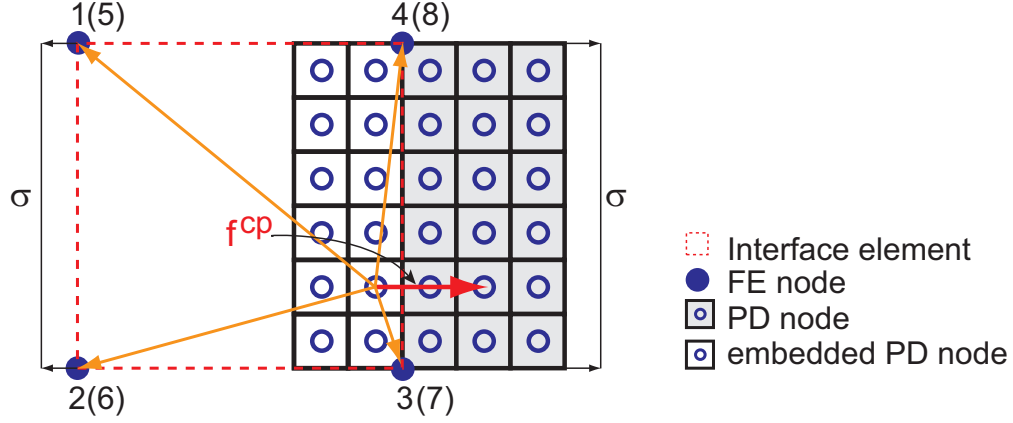


Figure 5.3: VL-coupling scheme that divides a coupling force  $\mathbf{f}^{cp}$  among FE nodes comprising the interface element.

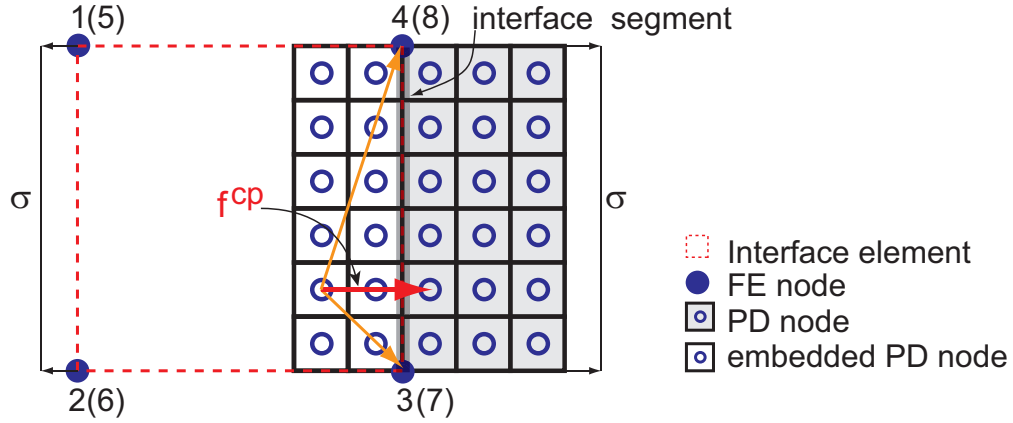


Figure 5.4: CT-coupling scheme that divides a coupling force  $\mathbf{f}^{cp}$  among FE nodes comprising the interface segment.

in which  $[\cdot]_I$  denotes the corresponding components of a vector associated with the node  $I$  of the interface element, and  $\mathbf{f}_I^{cp}$  is the summation of coupling forces on the node  $I$ . The explicit algorithm is employed for the transient dynamic analyses. Nodal accelerations are calculated first, and nodal velocities and displacements are updated subsequently. After the displacements of FE nodes of the interface elements are calculated, the displacements of

embedded peridynamic nodes are then determined by

$$\mathbf{U}_{eb} = \phi_i(\xi, \eta, \psi) \mathbf{U}_i, \quad i = 1, \dots, 8, \quad (5.23)$$

in which  $(\xi, \eta, \psi)$  are the natural coordinates of an embedded peridynamic node in the interface element, and  $\mathbf{U}_i$  is the nodal displacement of an interface element. For peridynamic nodes out of the interface elements, Equation (3.30) is used to update nodal accelerations.

### 5.3.2 Inverse isoparametric mapping

To couple peridynamic subregions with finite element subregions, a certain number of peridynamic nodes are embedded in the interface elements. If the Cartesian coordinates of an embedded peridynamic node are known, the natural coordinates of the embedded peridynamic node in an interface element should be determined by the inverse isoparametric mapping, which is essential especially for random discretizations. However, the inverse isoparametric mapping from the Cartesian coordinates to the natural coordinates is nontrivial since equations to be solved are nonlinear. Murti and Valliappan [127] presented a numerical technique by bisecting a line passing a point and a node of known natural coordinates, and this method was extended to the three-dimensional space by Murti *et al.* [128]. However, the bisection method has its limitations [31]. A more generalized approach for the inverse isoparametric mapping is presented by Chinnaswamy *et al.* [31]. For the inverse mapping of an embedded peridynamic node with known Cartesian coordinates  $(\hat{x}, \hat{y}, \hat{z})$ , the equation to be solved is

written as

$$\mathbf{f} = \begin{Bmatrix} f_1(\xi, \eta, \psi) \\ f_2(\xi, \eta, \psi) \\ f_3(\xi, \eta, \psi) \end{Bmatrix} = \begin{Bmatrix} \sum_{i=1}^n \phi_i(\xi, \eta, \psi) x_i - \hat{x} \\ \sum_{i=1}^n \phi_i(\xi, \eta, \psi) y_i - \hat{y} \\ \sum_{i=1}^n \phi_i(\xi, \eta, \psi) z_i - \hat{z} \end{Bmatrix} = \begin{Bmatrix} 0 \\ 0 \\ 0 \end{Bmatrix}, \quad (5.24)$$

where  $(\xi, \eta, \psi)$  are the natural coordinates of an embedded peridynamic node in an interface element to be determined. By expanding the vector  $\mathbf{f}$  in Taylor's series and omitting the second and higher order terms, it can be shown that [31]

$$\mathbf{I} = \mathbf{I}_0 - \begin{bmatrix} \frac{\partial f_1}{\partial \xi} & \frac{\partial f_1}{\partial \eta} & \frac{\partial f_1}{\partial \psi} \\ \frac{\partial f_2}{\partial \xi} & \frac{\partial f_2}{\partial \eta} & \frac{\partial f_2}{\partial \psi} \\ \frac{\partial f_3}{\partial \xi} & \frac{\partial f_3}{\partial \eta} & \frac{\partial f_3}{\partial \psi} \end{bmatrix}_0^{-1} \mathbf{f}_0, \quad (5.25)$$

where  $\mathbf{I}_0 = [\xi_0, \eta_0, \psi_0]^T$  is an approximate solution, and  $\mathbf{f}_0$  is the vector  $\mathbf{f}$  evaluated at the approximate solution  $\mathbf{I}_0$ . Equation (5.25) can be rewritten as

$$\mathbf{I} = \mathbf{I}_0 - \begin{bmatrix} \sum \frac{\partial \phi_i}{\partial \xi} x_i & \sum \frac{\partial \phi_i}{\partial \eta} x_i & \sum \frac{\partial \phi_i}{\partial \psi} x_i \\ \sum \frac{\partial \phi_i}{\partial \xi} y_i & \sum \frac{\partial \phi_i}{\partial \eta} y_i & \sum \frac{\partial \phi_i}{\partial \psi} y_i \\ \sum \frac{\partial \phi_i}{\partial \xi} z_i & \sum \frac{\partial \phi_i}{\partial \eta} z_i & \sum \frac{\partial \phi_i}{\partial \psi} z_i \end{bmatrix}_0^{-1} \begin{Bmatrix} \sum \phi_i x_i - \hat{x} \\ \sum \phi_i y_i - \hat{y} \\ \sum \phi_i z_i - \hat{z} \end{Bmatrix}_0, \quad (5.26)$$

and it can be simplified as

$$\mathbf{I} = \mathbf{I}_0 + \Delta \mathbf{I}, \quad (5.27)$$

where

$$\Delta \mathbf{I} = \begin{Bmatrix} \Delta \xi \\ \Delta \eta \\ \Delta \psi \end{Bmatrix} = -\mathbf{J}_0^{-1} \mathbf{f}_0. \quad (5.28)$$

The updated solution of  $\mathbf{I}$  is used as the value of  $\mathbf{I}_0$  in Equation (5.27) for the next iteration.

A few iterations are performed till the solution of  $\mathbf{I}$  converges.

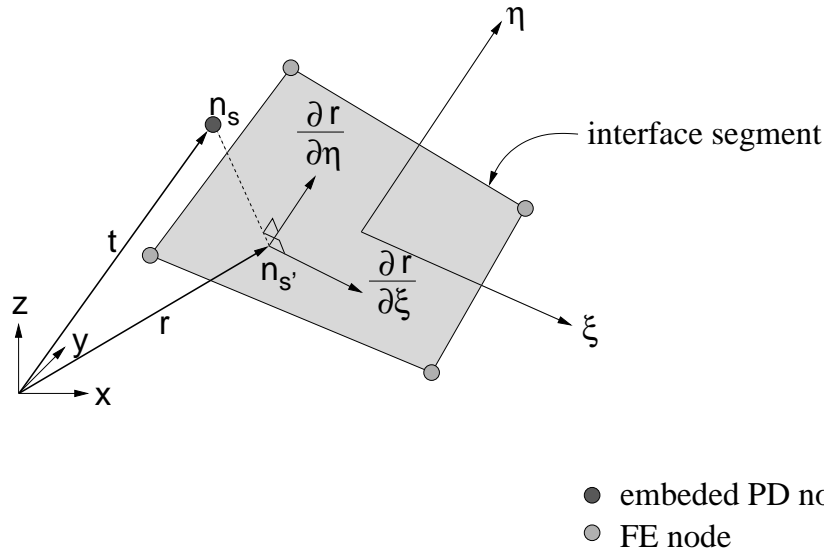


Figure 5.5: Projection of an embedded peridynamic node on an interface segment.

If the CT-coupling scheme is employed, coupling forces on embedded peridynamic nodes are only distributed to FE nodes on the interface segment as shown in Figure 5.4. Hence, the natural coordinates of the projection of an embedded peridynamic node onto the interface segment have to be determined. Let  $\mathbf{t}$  be the position vector of an embedded node  $n_s$ , and the projection of  $n_s$  onto the interface segment is denoted by  $n_{s'}$  as shown in Figure 5.5. The position vector  $\mathbf{r}$  of the point  $n_{s'}$  on the interface segment can be expressed as

$$\mathbf{r} = f_1(\xi_c, \eta_c) \mathbf{e}_1 + f_2(\xi_c, \eta_c) \mathbf{e}_2 + f_3(\xi_c, \eta_c) \mathbf{e}_3, \quad (5.29)$$

where  $(\xi_c, \eta_c)$  are the natural coordinates of the point  $n_{s'}$  on the interface segment, and

$$f_i(\xi, \eta) = \sum_{j=1}^4 \phi_j x_i^j, \quad (5.30)$$

in which  $\phi_j$  is the shape function of the node  $j$  on the interface segment. The natural coordinates  $(\xi_c, \eta_c)$  of the point  $n_{s'}$  on the interface segment must satisfy [72]

$$\frac{\partial \mathbf{r}}{\partial \xi} \cdot (\mathbf{t} - \mathbf{r}) = 0, \quad (5.31)$$

$$\frac{\partial \mathbf{r}}{\partial \eta} \cdot (\mathbf{t} - \mathbf{r}) = 0. \quad (5.32)$$

However, there is no analytical solution to Equations (5.31) and (5.32). To solve numerically, a few iterations of the least-squares projection are used to generate an initial guess as

$$\xi_0 = 0, \quad \eta_0 = 0, \quad (5.33)$$

$$\begin{bmatrix} \mathbf{r}_{,\xi} \cdot \mathbf{r}_{,\xi} & \mathbf{r}_{,\xi} \cdot \mathbf{r}_{,\eta} \\ \mathbf{r}_{,\eta} \cdot \mathbf{r}_{,\xi} & \mathbf{r}_{,\eta} \cdot \mathbf{r}_{,\eta} \end{bmatrix} \begin{Bmatrix} \Delta \xi \\ \Delta \eta \end{Bmatrix} = - \begin{Bmatrix} \mathbf{r}_{,\xi} \cdot (\mathbf{r} - \mathbf{t}) \\ \mathbf{r}_{,\eta} \cdot (\mathbf{r} - \mathbf{t}) \end{Bmatrix}, \quad (5.34)$$

$$\xi_{i+1} = \xi_i + \Delta \xi, \quad \eta_{i+1} = \eta_i + \Delta \eta. \quad (5.35)$$

With an initial guess, Newton-Raphson method is then utilized to find the solution of Equations (5.31) and (5.32) as [187]

$$\mathbf{H} \begin{Bmatrix} \Delta \xi \\ \Delta \eta \end{Bmatrix} = - \begin{Bmatrix} \mathbf{r}_{,\xi} \cdot (\mathbf{r} - \mathbf{t}) \\ \mathbf{r}_{,\eta} \cdot (\mathbf{r} - \mathbf{t}) \end{Bmatrix}, \quad (5.36)$$



$$\mathbf{H} = \begin{bmatrix} \mathbf{r}_{,\xi} \cdot \mathbf{r}_{,\xi} & \mathbf{r}_{,\xi} \cdot \mathbf{r}_{,\eta} \\ \mathbf{r}_{,\eta} \cdot \mathbf{r}_{,\xi} & \mathbf{r}_{,\eta} \cdot \mathbf{r}_{,\eta} \end{bmatrix} + \begin{bmatrix} (\mathbf{r} - \mathbf{t}) \cdot \mathbf{r}_{,\xi\xi} & (\mathbf{r} - \mathbf{t}) \cdot \mathbf{r}_{,\xi\eta} \\ (\mathbf{r} - \mathbf{t}) \cdot \mathbf{r}_{,\xi\eta} & (\mathbf{r} - \mathbf{t}) \cdot \mathbf{r}_{,\eta\eta} \end{bmatrix}, \quad (5.37)$$

$$\xi_{i+1} = \xi_i + \Delta\xi, \quad \eta_{i+1} = \eta_i + \Delta\eta. \quad (5.38)$$

The solutions of  $\xi_{i+1}$  and  $\eta_{i+1}$  are used to update the value of the position vector  $\mathbf{r}$ , and then Equation (5.36) is evaluated again for the next iteration. The converged solutions of  $\xi_{i+1}$  and  $\eta_{i+1}$  are the natural coordinates of the point  $n_{s'}$  on the interface segment.

## 5.4 Numerical applications

### 5.4.1 One-dimensional bar

For benchmarking, the present coupling approach of peridynamics with FEM is employed to study the axial deformation of a one-dimensional bar. The length of the bar is 9.5 mm, and dimensions of the cross section are 0.5 mm by 0.5 mm. Young's modulus  $E$  of the bar is 70 GPa, and the density is 2700 kg/m<sup>3</sup>. Figure 5.6 shows the multiscale discretization of the bar. The finite element mesh size is 1.5 mm, and the conventional bar elements are utilized. The stiffness of a bar is  $k = \frac{EA}{L}$ , where  $A$  is the cross-sectional area and  $L$  is the length of the bar. The peridynamic grid spacing is 0.5 mm, which is equal to the width of the bar. By setting the horizon to  $2\Delta x$ , the one-dimensional micromodulus  $c_1$  is  $5.6 \times 10^{23}$  N/m<sup>6</sup>. Two interface elements are used to couple peridynamic and finite element subregions, and each interface element has two embedded peridynamic nodes for the calculation of coupling forces as shown in Figure 5.6.

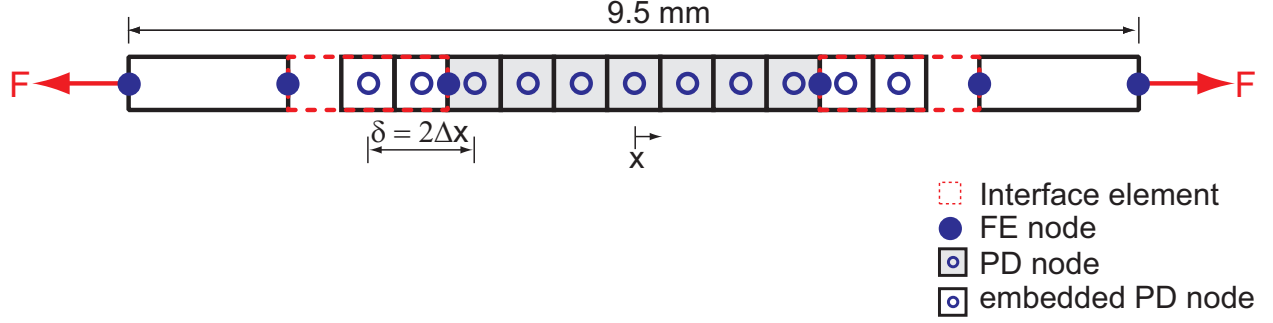
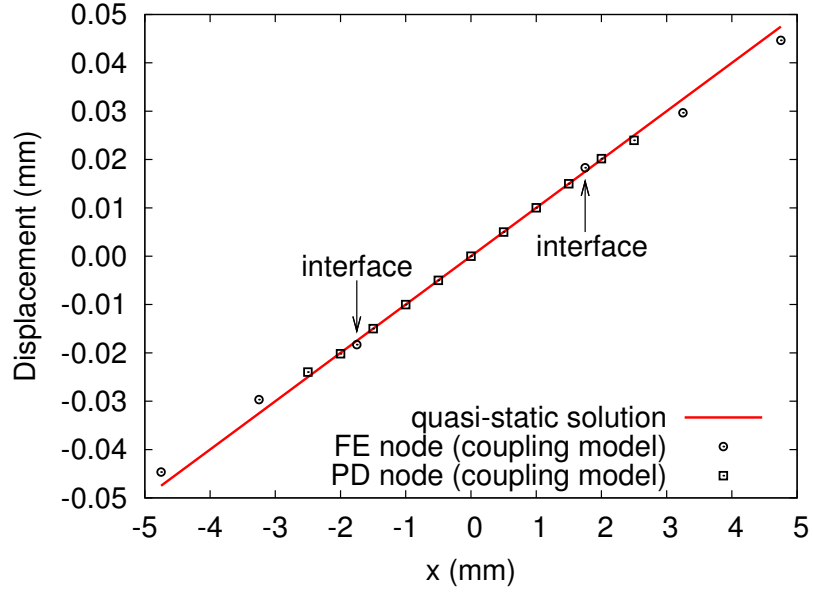
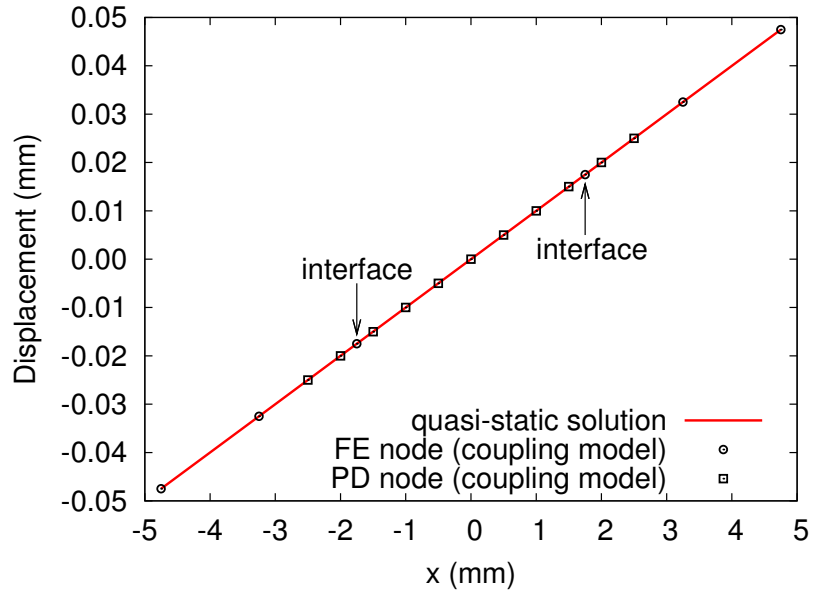


Figure 5.6: Discretization of a one-dimensional bar.

A tensile loading with the magnitude of  $F = 175$  N is applied on both ends of the bar under the quasi-static condition. The force is gradually increased during 50,000 steps with the calculation time step  $dt = 5 \times 10^{-8}$  s, which is less than the critical time step for the explicit time integration. Figure 5.7(a) shows the displacement along the bar using the VL-coupling scheme. Nodal displacements in the peridynamic subregion show good agreement with the quasi-static solution. The displacements of the FE nodes, however, show small discrepancies. The reason is that coupling forces in an interface element are divided among all FE nodes of the element using the VL-coupling scheme so that FE nodes at the interfaces of subregions ( $x = \pm 1.75$  mm) only receive partial coupling forces. FE nodes at the other end of the interface elements ( $x = \pm 3.25$  mm) receive the rest of coupling forces, and are also subjected to internal forces contributed by the element stiffness. Consequently, the displacements of FE nodes at the interfaces are slightly overestimated, and displacements of other FE nodes are underestimated as indicated in Figure 5.7(a). In contrast, the solution using the CT-coupling scheme, which distributes coupling forces only to FE nodes at interfaces, is almost identical to the quasi-static solution as shown in Figure 5.7(b). Hence, for the calculation of axial displacement, the CT-coupling scheme is more effective than the VL-coupling scheme to achieve the coupling between the peridynamic subregion and the finite element subregion.



(a)



(b)

Figure 5.7: Axial displacement along the bar using (a) VL-coupling scheme and (b) CT-coupling scheme.

### 5.4.2 Three-dimensional bar

A three-dimensional bar subjected to tension is examined to compare the solutions of the present coupling approach and the classical (local) elasticity solutions. The dimensions of the bar are taken to be 10 mm in length, 7 mm in width, and 7 mm in thickness as shown in Figure 5.8. The three-dimensional model is partitioned into two FE subregions and one peridynamic subregion. Each FE subregion consists of four eight-node solid interface elements, and the mesh size of the interface element is 3.5 mm. The peridynamic subregion is uniformly discretized with the grid spacing  $\Delta x = 0.5$  mm, and the size of the horizon is set to  $\delta = 1.0$  mm. In the interface element, two additional layers of peridynamic nodes are embedded along the longitudinal direction to ensure sufficient nodes in the horizon of peridynamic nodes near the interfaces. Traction at both end surfaces are gradually applied up to  $\sigma_x = 700$  MPa during 100,000 steps as quasi-static loading, and the calculation time step is set to  $dt = 5 \times 10^{-8}$  s. Young's modulus of the bar is 70 GPa, Poisson ratio is 0.25, and the density is 2700 kg/m<sup>3</sup>.

We first examine the numerical solutions using the VL-coupling scheme. The longitudinal displacements  $u_x$  at three measuring positions are compared to the quasi-static results as shown in Figure 5.9(a). The displacement  $u_x$  at the position  $p_1$ , which is at the end surface, is underestimated compared with the quasi-static solution. On the other hand, the displacement at  $p_2$ , which is at the interface of the peridynamic subregion and the FE subregion, and the displacement at  $p_3$ , which is inside the peridynamic subregion, show good agreement with the quasi-static solutions. To look into Poisson effect, the transverse displacements measured at different positions are plotted in Figure 5.9(b). The transverse displacement  $q_1$  at the end surface is smaller than the quasi-static value since the longitudinal

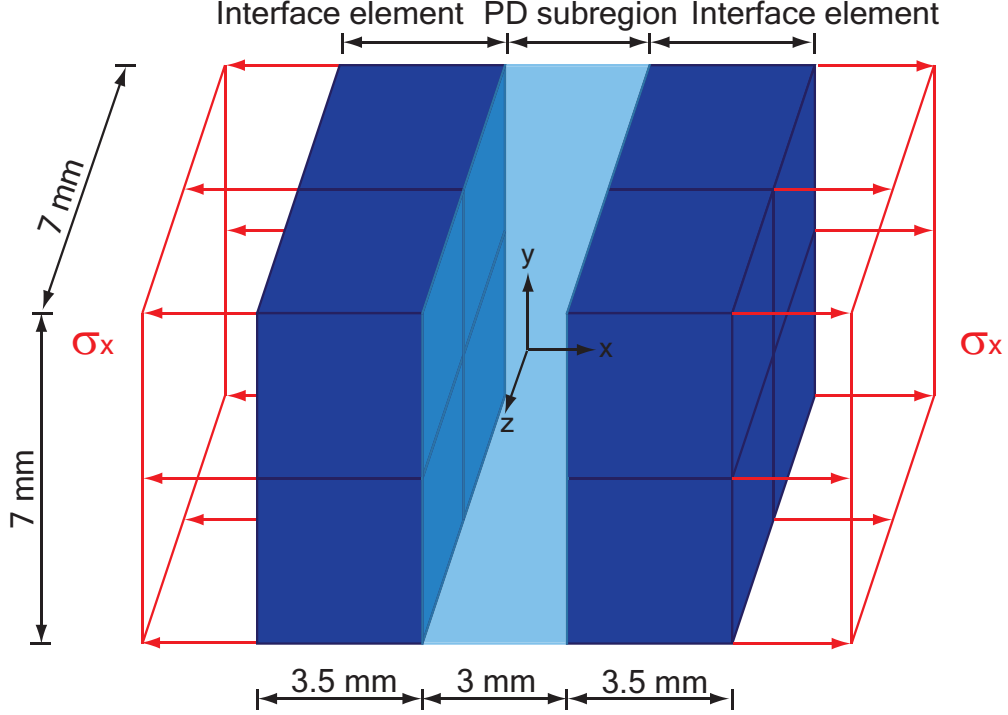


Figure 5.8: Three-dimensional bar subjected to tension.

displacement at the end surface is underestimated. Nevertheless, the transverse displacement  $q_2$  at the interface demonstrates close agreement with the quasi-static solution, which indicates that Poisson effect is preserved at the interface. The transverse displacement at  $q_3$ , which is inside the peridynamic subregion, also matches the quasi-static solution.

For the comparison of two types of coupling schemes, the CT-coupling scheme, which achieves coupling by considering the interfaces of subregions similar to contact surfaces, is then employed to study this quasi-static problem. As shown in Figure 5.10(a), the longitudinal displacement  $p_1$  at the end surface is close to the quasi-static solution with the error less than 2%. The longitudinal displacements at interface and inside the peridynamic subregion, denoted by  $p_2$  and  $p_3$  respectively in Figure 5.10(a), are almost identical to the quasi-static solutions. The transverse displacements measured at different positions are plotted in Figure 5.10(b). With the improved solution of longitudinal displacement at the end surface,

the transverse displacement  $q_1$  at the end surface turns to be very close to the quasi-static solution. On the other hand, the transverse displacement  $q_2$  at the interface is overestimated. This phenomenon occurs due to the reason that decompositions of coupling forces in the transverse direction are divided only among FE nodes at the interface. By comparing Figures 5.9 and 5.10, it is observed that the CT-coupling scheme is effective in resolving displacements normal to the interface of peridynamic and FE subregions. On the other hand, the VL-coupling scheme, which divides coupling forces among all FE nodes comprising the interface element, is capable to preserve Poisson effect at the interface.

Figure 5.11 shows the longitudinal displacement along the edge of the bar solved by the CT-coupling scheme. It is noted that a smooth curve can be obtained if the nodal displacements are connected, which is different from the results in [94] where a jump in displacement is observed at the interface. The strain  $\varepsilon_x$  distributions on the bar and at the interface are plotted in Figure 5.12. Nodal strains in the FE subregions are obtained by evaluating Equation (5.5), and nodal strains in the peridynamic subregion are calculated as the average bond stretch within the grid width  $\Delta x$ . Considering the quasi-static condition, the analytical value of strain  $\varepsilon_x$  is 0.01. The strain of the coupling model is in the range of 0.0099 to 0.0105 as shown in Figure 5.12, which agrees with the quasi-static solution.

The essence of coupling forces is interactions between nodes in the peridynamic subregion and material volumes of an adjacent continuous body (i.e. interface elements) represented by embedded peridynamic nodes. Therefore, the ratio of the grid spacing of peridynamic nodes to the mesh size of interface elements should not have affect the results. To illustrate this point, Figure 5.13 shows the summation of coupling forces in the longitudinal direction on the interface elements at the left end of the bar as the applied traction increases. As indicated by the comparison in Figure 5.13, differences in the results using the grid spacing

$\Delta x = 1.0$  mm and  $\Delta x = 0.5$  mm are insignificant.

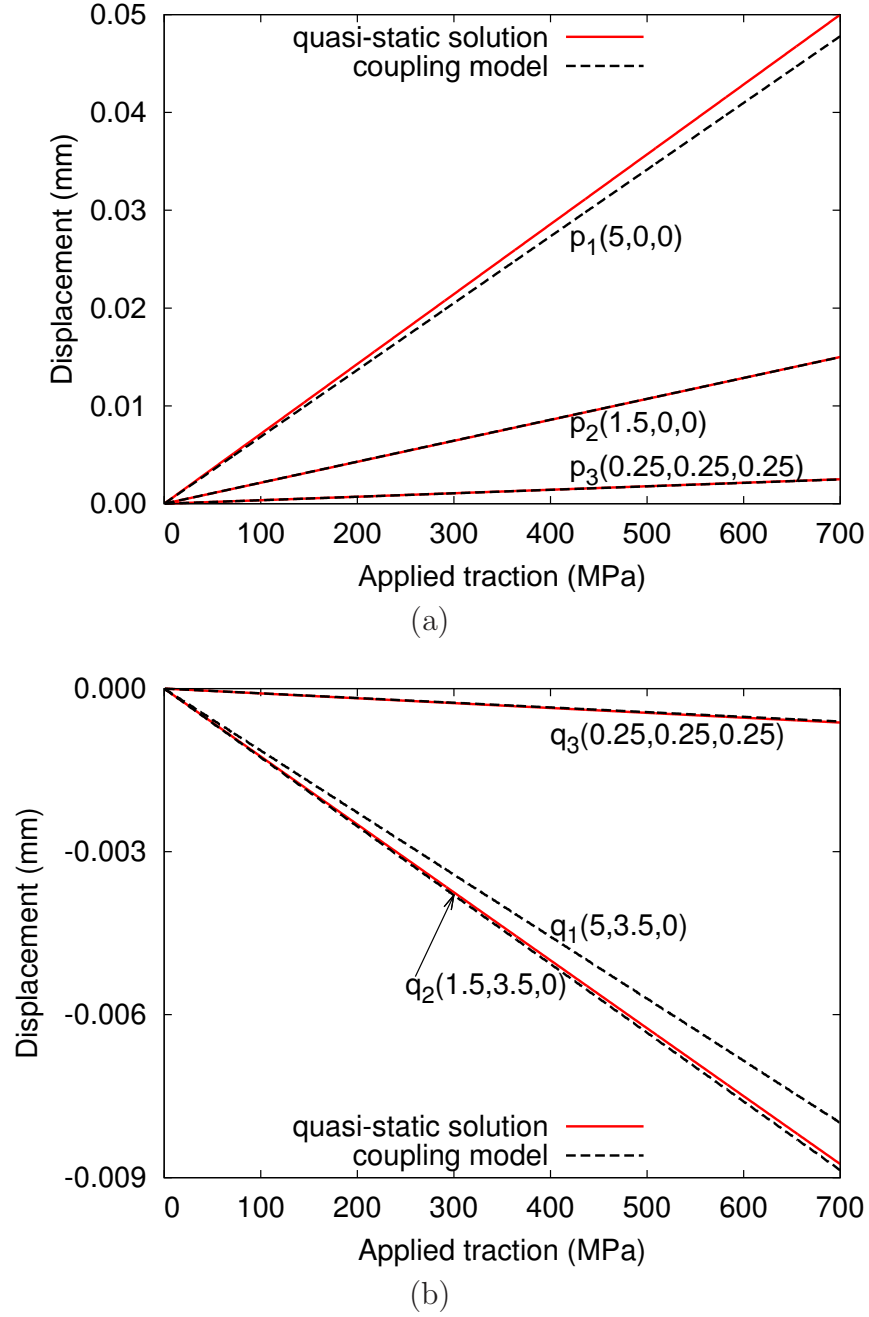


Figure 5.9: Displacements (a)  $u_x$  and (b)  $u_y$  at different locations using the VL-coupling scheme. Coordinates of the measuring position are given in parenthesis.



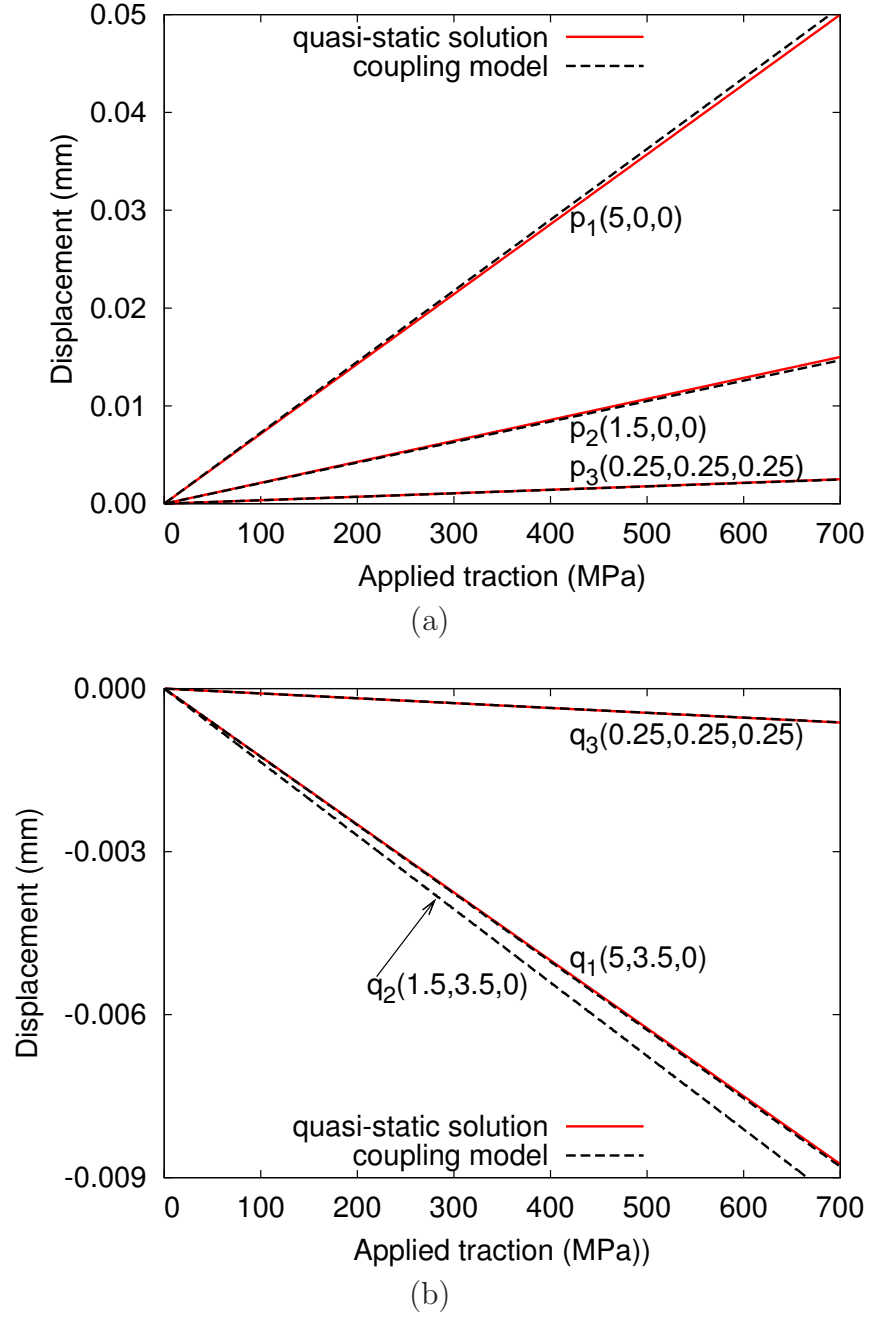


Figure 5.10: Displacements (a)  $u_x$  and (b)  $u_y$  at different locations using the CT-coupling scheme. Coordinates of the measuring position are given in parenthesis.

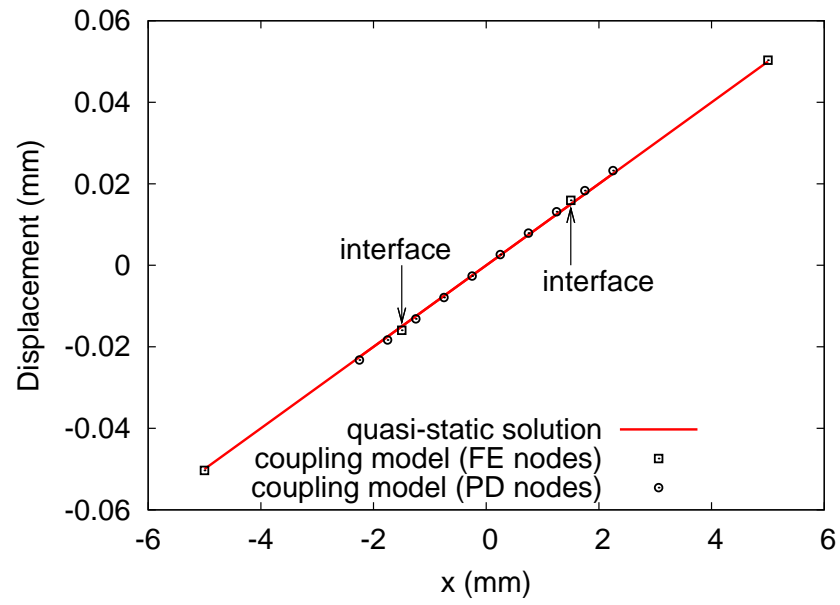
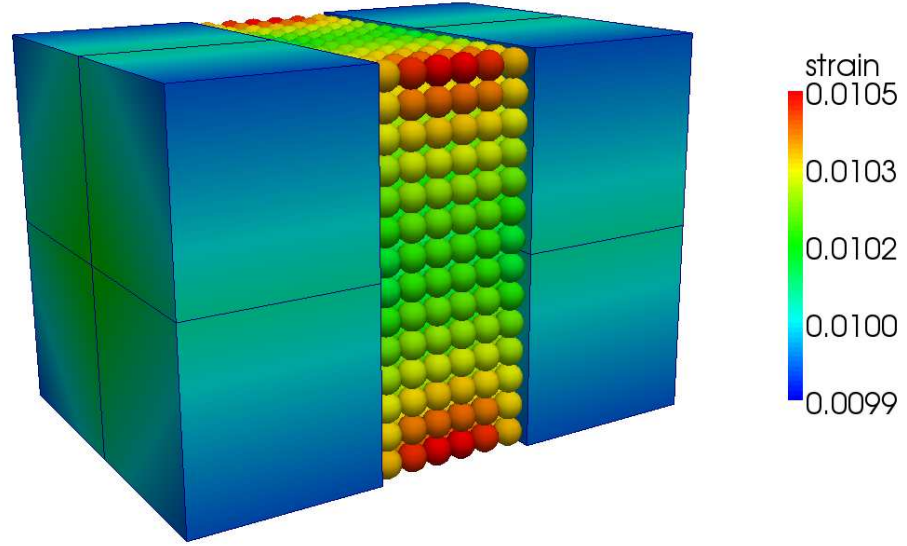
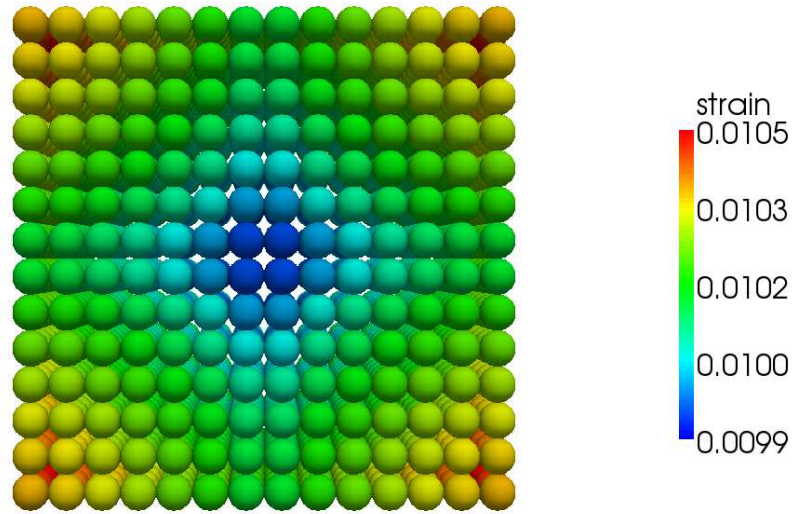


Figure 5.11: Axial displacement along the edge using the CT-coupling scheme.



(a)



(b)

Figure 5.12: Strain  $\varepsilon_x$  distributions (a) on the bar and (b) on the interface when the applied traction  $\sigma_x = 700$  MPa. The CT-coupling scheme is used in the simulation.

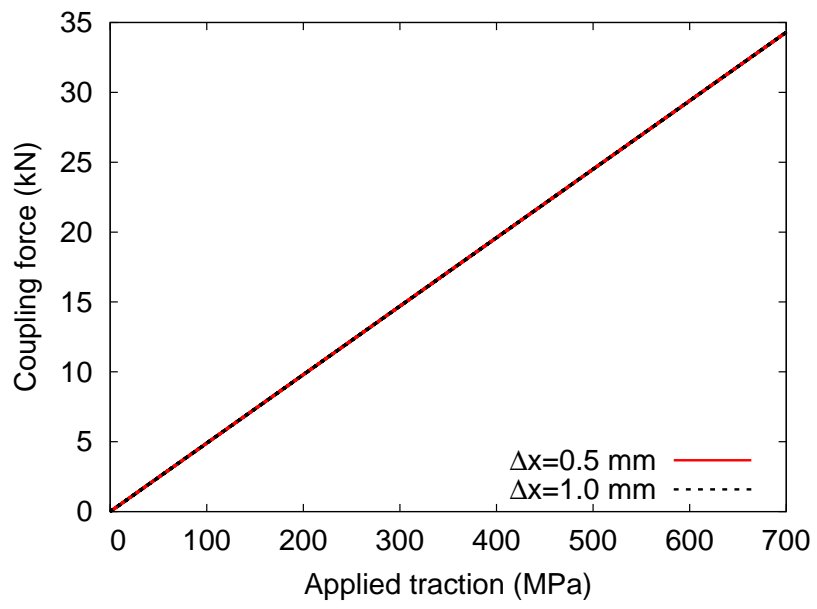


Figure 5.13: Summation of coupling forces in the longitudinal direction on the interface elements at the left end of the bar. The CT-coupling scheme is used in the simulation.

### 5.4.3 Mixed mode fracture in a tension-shear specimen

A benchmark problem of mixed mode crack propagation in a concrete specimen has been investigated experimentally by Nooru-Mohamed *et al.* [130]. The double-edge-notched specimen is illustrated in Figure 5.14(a). The dimensions of the specimen are taken to be 200 mm in both length and height, 50 mm in width, and two notches at edges are 25 mm in length, 5 mm in height, and 50 mm in width. For the numerical study, the specimen is partitioned into two finite element subregions and one peridynamic subregion as shown in Figure 5.14(b). The FE subregion is discretized with two mesh sizes,  $10\text{ mm} \times 10\text{ mm} \times 16.25\text{ mm}$  and  $10\text{ mm} \times 10\text{ mm} \times 13\text{ mm}$ , respectively. The peridynamic subregion is discretized with the grid spacing  $\Delta x = 5.0\text{ mm}$ , which is  $1/10$  of the specimen thickness, and the horizon is set to  $\delta = 1.0\text{ mm}$ . The notches in the peridynamic subregion are introduced by deleting nodes along two notches and removing all bonds across the notches. Since the ratio of the horizon to the grid spacing is equal to two, two layers of peridynamic nodes adjacent to interfaces are embedded in interface elements for the calculation of coupling forces. Young's modulus, Poisson ratio, and fracture energy were not measured in the experiments. Therefore, we adopt the material properties  $E = 30\text{ GPa}$  and  $G_f = 110\text{ J/m}^2$  as in [35]. For Poisson ratio, it is estimated as  $\nu = 0.2$  in the numerical studies in [121, 35] and  $\nu = 0.3$  is used in [125]. In the present study, Poisson ratio  $\nu = 0.25$  is assumed. The density is calculated from the concrete composition given in [130] as  $\rho = 2265\text{ Kg/m}^3$ . By applying Equation (4.3), the critical bond stretch is obtained as  $s_0 = 5.5277 \times 10^{-4}$ . The brittle material model illustrated in Figure 4.1(a) is utilized for the peridynamic subregion, and the linear elastic model is employed for the remaining FE subregions, where material parameters  $E = 30\text{ GPa}$  and  $\nu = 0.25$  are used.

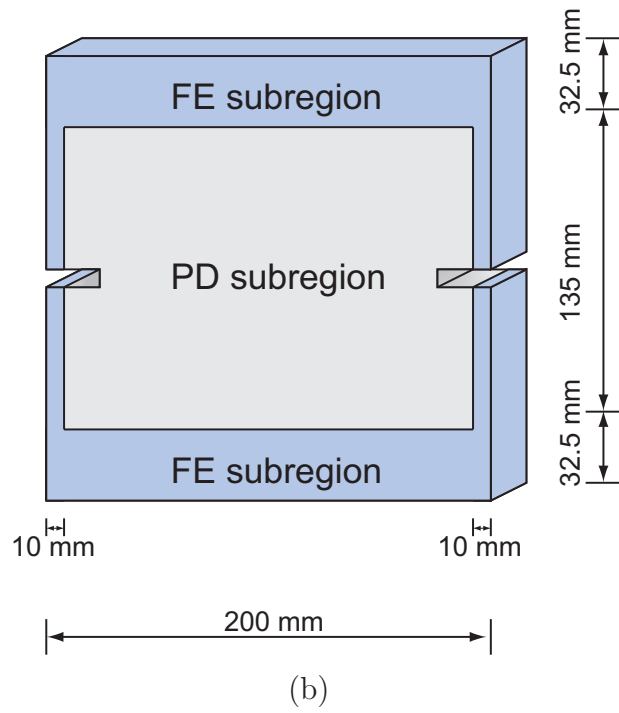
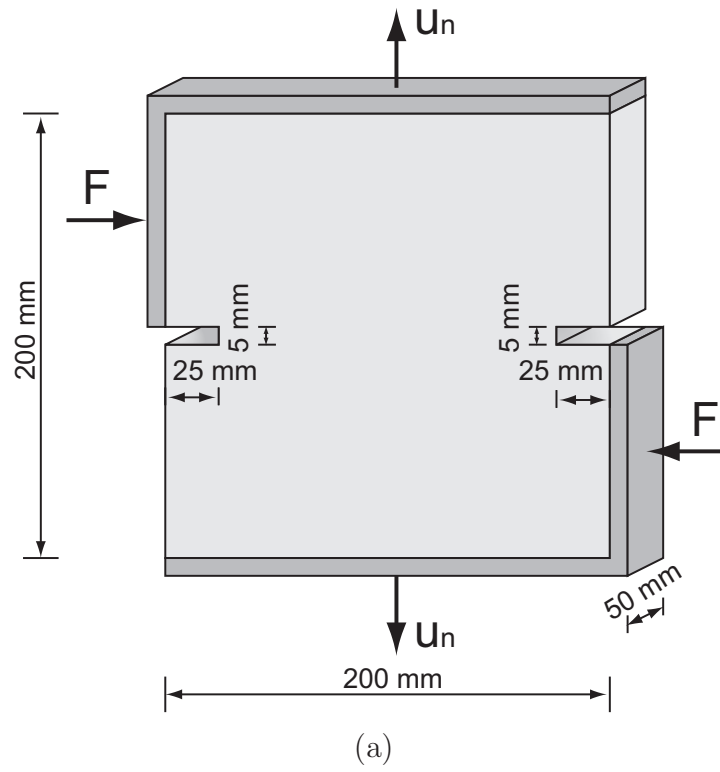


Figure 5.14: Mixed mode fracture test: (a) geometry of the specimen; (b) subregions of the coupling model.

For the comparison, the load-path 1b (specimen 46-05) in [130] is considered. A horizontal shear force of 10 kN is applied first, and then the vertical displacement  $u_n$  is applied on the top and bottom of the specimen as shown in Figure 5.14(a). For the numerical calculation, the time step is set to  $dt = 1 \times 10^{-7}$  s, which is less than the critical time step for the explicit time integration. The vertical displacement  $u_n$  is applied by imposing a constant velocity of 10 mm/s as quasi-static loading. We first examine the numerical predictions of crack paths using the VL-coupling scheme. The cracks initiate near the notches as shown in Figure 5.15(a), and propagate along the horizontal direction for about 50 mm. As the boundary displacement increases, the direction of propagation changes as shown in Figures 5.15(b) and 5.15(c). At the boundary displacement  $u_n = 0.09$  mm, two cracks are connected as shown in Figure 5.15(d). The numerical prediction of crack paths using the VL-coupling scheme shows differences with the experimental observations in [130].

We then apply the CT-coupling scheme for the numerical simulation. Interfaces are predefined in the reference configuration, and there are 280 interface segments with the given mesh sizes. Natural coordinates of the projections of embedded nodes onto interface segments are saved to a list. In the subsequent calculations, the natural coordinates of projected points are referred, and the coupling forces on embedded peridynamic nodes are divided among FE nodes at interface segments. The damage evolution is shown in Figure 5.16. Crack initiation occurs at the left and right notches as shown in Figure 5.16(a), and materials ahead of crack tips are damaged for the length of around 15 to 20 mm. Due to the angle change of the principle stress, cracks propagate with an angle as shown in Figure 5.16(b). As the boundary displacement increases, two curvilinear crack paths are clearly observed in Figure 5.16(c). An enclosed area is gradually formed between two curvilinear cracks as indicated in Figure 5.16(d). The numerical prediction of cracks shows agreement, especially for the lower crack, with

the experimental observation presented in [130], which is illustrated using the solid line in Figure 5.16(d). The small discrepancies appeared in Figure 5.16(d) might be caused by the perfectly brittle material model adopted in the numerical simulation. More investigation of material models for concrete in the framework of peridynamics is required in the future. Note that the numerically predicted crack paths are in perfect symmetry. On the contrary, the cracks in the experiments do not show perfect symmetry, and we might speculate on symmetry breaking caused by the slight differences in the loading condition and material heterogeneity.

Compared with the numerical results using the VL-coupling scheme, the results using the CT-coupling scheme demonstrate better agreement with the experimental observation. The reason for the inferiority of the VL-coupling scheme in this mixed mode fracture problem is that the horizontal displacement at edges caused by the constant shear loading is underestimated after the applied vertical displacement at boundaries reaches the critical value for the crack initiation at two notches. Consequently, the opening-mode fracture dominates, and the large area ahead of crack tips is damaged in the plane of notches. After the intact region in the middle of the specimen becomes relatively small, rotations of crack paths then take place as shown in Figure 5.15.



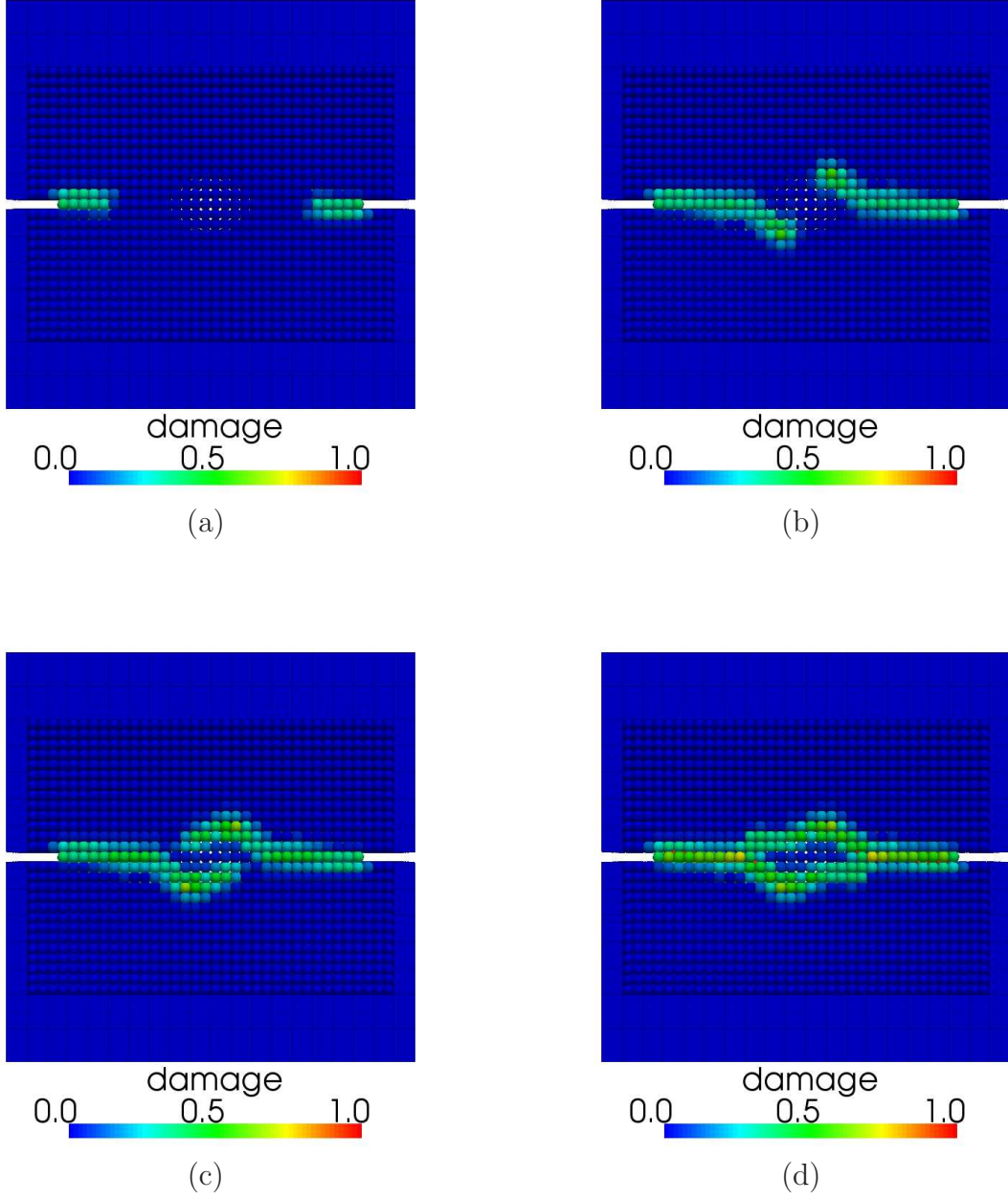


Figure 5.15: Numerical prediction of crack paths using the VL-coupling scheme. Boundary displacement: (a)  $u_n = 0.0220$  mm; (b)  $u_n = 0.0225$  mm; (c)  $u_n = 0.03$  mm; (d)  $u_n = 0.09$  mm.

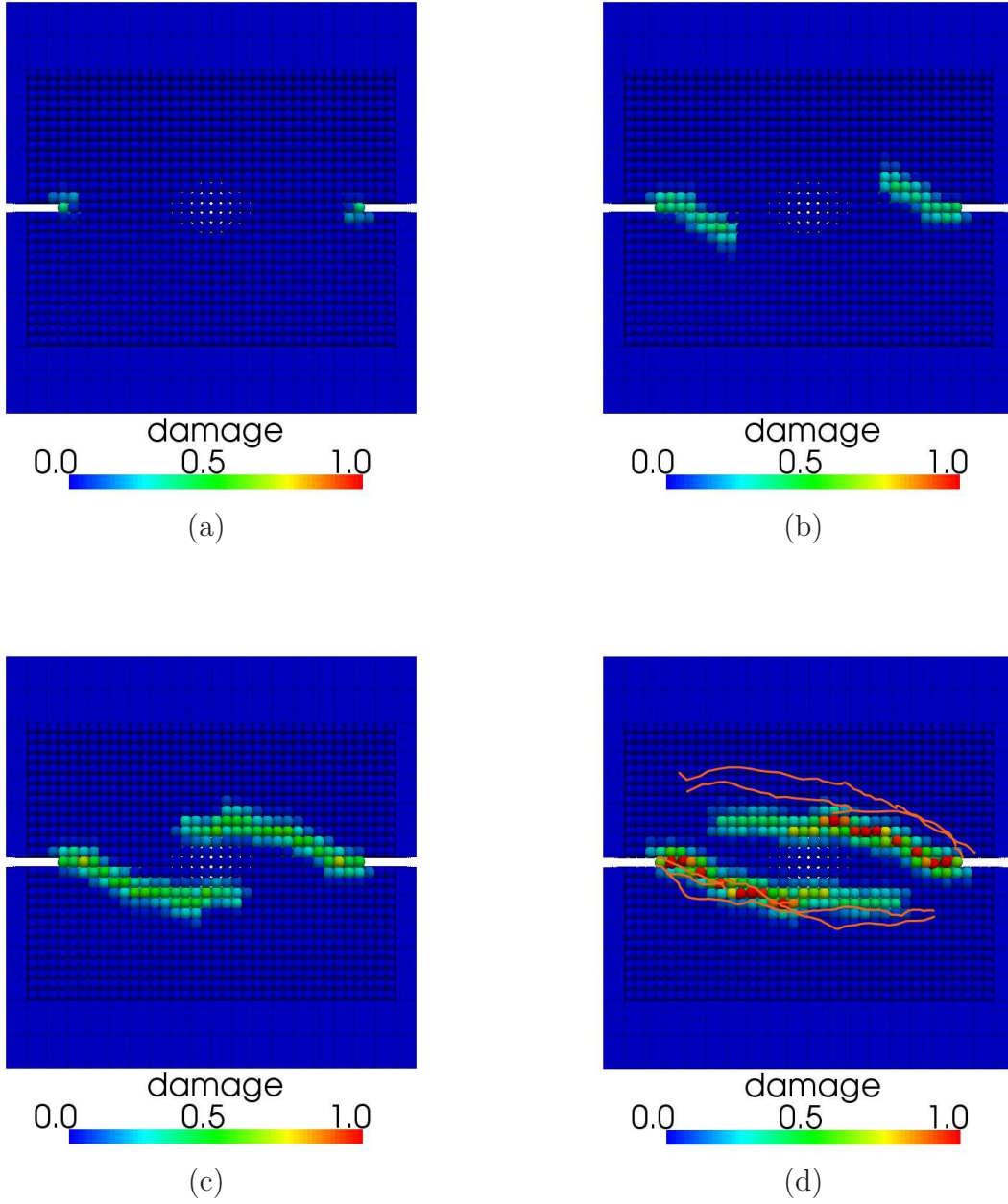


Figure 5.16: Numerical prediction of crack paths using the CT-coupling scheme. Solid curves are crack paths observed in the experiments from [130]. Boundary displacement: (a)  $u_n = 0.0220$  mm; (b)  $u_n = 0.0225$  mm; (c)  $u_n = 0.03$  mm; (d)  $u_n = 0.09$  mm.

## 5.5 Summary

A coupling approach of discretized peridynamics with FEM is presented in this chapter. To bridge conventional FE subregions and peridynamic subregions, an interface element is introduced. The proposed coupling approach is different from other methods in the sense of direct coupling via interface elements. Depending on the size of the horizon, a number of peridynamic nodes are embedded in an interface element. The embedded peridynamic nodes are not involved in the global equation, but essential in the calculation of coupling forces. The coupling forces describe interactions between embedded peridynamic nodes in interface elements and peridynamic nodes in peridynamic subregions. Two types of coupling schemes are introduced. In the VL-coupling scheme, coupling forces on embedded peridynamic nodes are divided to FE nodes of interface elements. On the other hand, coupling forces are divided only to FE nodes on interface segments in the CT-coupling scheme. The inverse isoparametric mapping techniques to determine the natural coordinates of embedded peridynamic nodes in the interface elements and the natural coordinates of projected points on the interface segments are summarized.

Numerical simulations are conducted to compare the computational results using the coupling approach to the classical elasticity solutions. The axial deformation of a one-dimensional bar under quasi-static loading is studied. It is found that the displacements at interfaces of subregions are slightly overestimated, and the displacements in the FE subregions are underestimated using the VL-coupling scheme. On the other hand, the numerical solution using the CT-coupling scheme is almost identical to the quasi-static solution in all subregions and interfaces. For three-dimensional simulations, a bar subjected to quasi-static tension is partitioned into a peridynamic subregion and two FE subregions consisting of

eight-node interface elements at both ends of the bar. By measuring displacements at different positions, the CT-coupling scheme is found to be effective in resolving displacements normal to the interface of peridynamic and FE subregions, and the VL-coupling scheme is capable to preserve Poisson effect at the interfaces. Longitudinal strain distributions in the bar and at the interface using the CT-coupling scheme demonstrate good agreement with the quasi-static solution.

The last numerical example is the mixed mode fracture in a concrete specimen subjected to quasi-static loading. The region where failure is expected is modeled using peridynamics, and the remaining region is modeled using conventional FEM to reduce the computational cost. Numerical predictions of crack paths using the VL-coupling scheme and the CT-coupling scheme are studied. Two independent curvilinear crack paths are observed in the results using the CT-coupling scheme, and the numerical predictions of crack patterns are close to the experimental observations presented in [130].

# Chapter6

## Discretized Peridynamics for Contact-Impact Problems

### 6.1 Introduction

Impact, which involves the collision of two or more objects, encompasses a wide range of phenomena such as automobile accidents, drop of electric devices, and even molecular collisions [66]. When bodies collide, the contact force is developed to prevent them from overlapping in material regions. A compatible contact surface enveloping the initial contact points is formed by the reaction force [165]. The stress waves developed by the collision travel away from the region of contact [66]. As the initial velocity increases, penetration of targets occurs. Penetration involves perforation, embedment, and ricochet [9].

Although the dynamic behavior of materials in the process of impact is complicated, only a few highly influential mechanisms play the governing roles [145]. Therefore, it is possible to use relatively simple analytical models to describe the impact process. Bishop *et al.* [17] first studied the analytical methods for penetration mechanics. Recht and Ipson [145] developed analytical equations of ballistic perforation dynamics, and confirmed the proposed analytical models by comparing with experimental data. Tate [170, 171] modified the hydrodynamic theory to incorporate strength effects for the prediction of the deceleration of a long rod penetrating into a target, and studied the deformation of a soft rod striking

a rigid target. Jones *et al.* [88] modified the one-dimensional penetration theory proposed by Tate by taking account of mass transfer and the mushroom strain into the analysis. Cinnamon *et al.* [32] presented a one-dimensional analysis to predict penetration depths and profile hole diameters for rod penetrators in semi-infinite targets. Grace [68] proposed a one-dimensional model to predict the penetration of long rods into targets. Warren and Forrestal [179] presented penetration models using the spherical cavity-expansion approximation for rigid spherical-nosed rods that penetrate aluminum targets. Analytical models that describe forces and penetration depths for rigid long rod and aluminum targets were developed by Forrestal *et al.* [55, 54, 57]. In addition, Forrestal *et al.* [52, 53] proposed a dimensionally consistent empirical equation for the depth of penetration into concrete targets based on experimental data, and studied the deceleration of penetration in concrete targets. An empirical relationship describing the penetration hole diameter in thin plate was proposed by Hill [76]. A review of simplified analytical models for ballistic penetration into different media was presented by Ben-Dor *et al.* [16].

Most research progress on penetration has been made in experimental investigations, and a large number of studies can be found. Stock and Thompson [164] studied the penetration of aluminum alloys by projectiles and showed that the formation of bands of intense shear reduces the ability of the material to withstand further penetration. Calder and Goldsmith [27] studied the plastic deformation and perforation of thin plates subjected to projectile impact using a high speed framing camera. Doyle [42] performed experimental measurements of the contact force during the transverse impact of an aluminum plate using dynamic strain gage, and comparisons were made with the finite element analysis. Bless *et al.* [19] studied hypervelocity penetration of ceramics and penetration phenomena, which are dependent on ceramic properties. The penetration of hard layers by rod projectiles was analyzed

by Bless and Anderson [18]. The penetration of long rod into aluminum was investigated under different impact velocities by Hohler *et al.* [77]. Trucano and Grady [173] presented experimental, analytical, and computational techniques to study impact shock and penetration in low density media. Subramanian *et al.* [166] conducted reverse impact experiments for aluminum penetrations to study the penetration rate, consumption velocity, and total penetration. Rosenberg *et al.* [148] carried out ballistics experiments of ceramic tiles and studied a simplified Johnson-Holmquist failure mode for brittle materials. Murr *et al.* [126] studied the low velocity to hypervelocity penetration transition in metal targets. Frew *et al.* [62, 61] conducted depth-of-penetration experiments of steel projectile into concrete, and conducted experiments in which penetration depths of limestone targets were measured and compared to an analytical penetration equation. Piekutowski *et al.* [139] performed depth-of-penetration experiments using steel projectiles and aluminum targets. Similarly, Forrestal and Piekutowski [56] conducted penetration experiments with 6061-T6511 aluminum targets and spherical-nose steel projectiles. Lundberg *et al.* [114] studied the interaction of a metallic projectiles and a ceramic target. Gomez and Shukla [67] performed an experimental study of projectile penetration into concrete. Warren and Poormon [180] presented experimental, analytical, and numerical results of penetration of aluminum targets by ogive-nosed projectiles at oblique angles. Børvik and colleagues [24, 21, 23, 22] examined the ballistic penetration of steel plates by cylindrical projectiles by experimental, analytical, and numerical investigations, and studied a constitutive model for non-linear finite element analyses. Behner *et al.* [12] experimentally studied the penetration and failure of glass by rod impact. Anderson *et al.* [7] investigated the failure and penetration response of glass impacted by short rods so that there is no steady driving stress.

Due to the complexity and the experimental cost in laboratory tests, researchers resort

to effective numerical methods for the analyses of contact-impact problems. Wilkins [185] investigated influence of material properties on perforation of targets using a finite difference program. Anderson *et al.* [6] used Eulerian wave propagation program to examine the long-rod penetration as a function of impact velocity. Taylor *et al.* [172] used the hydrocode modeling to study hypervelocity impact on brittle materials. Warren and Tabbara [182] performed simulations of penetration without the need for discretizing the target and the need for a contact algorithm. Heinstein *et al.* [75] proposed a method for the contact-impact modeling of large deformation in explicit transient dynamics. Rosenberg and Dekel [147] presented two-dimensional simulations to investigate penetration of rigid short projectiles into semi-infinite targets and perforation of thin metal plates.

As a well-established method for analyzing a wide range of engineering problems, the finite element method has been employed to study contact and impact problems. Hughes *et al.* [84] presented the theory and numerical implementation of the finite element method for contact-impact problems using a node-to-node scheme. A numerical method for the analysis of contact between three-dimensional bodies was presented by Chaudhary and Bathe[29]. Belytschko and Lin [14] presented an algorithm for three-dimensional impact simulations, and Belytschko and Neal [15] developed a pinball algorithm as a simplified contact-impact algorithm that can be readily vectorized. Carpenter *et al.* [28] developed an approach for the fulfillment of surface contact conditions in the transient non-linear finite element analysis. Anderheggen *et al.* [4] introduced a numerical contact algorithm with an explicit time integration scheme in the finite element method. Hahn and Wriggers [71] proposed an explicit multi-body contact algorithm. Elabbasi *et al.* [47] addressed reliability issues that are necessary for analyzing the accuracy and effectiveness of engineering designs involving contact conditions.



The primary focus in this chapter is the numerical scheme for the modeling of contact between a peridynamic domain and a non-peridynamic domain such as conventional finite elements and rigid bodies. Macek and Silling [115] presented a plate perforation example, in which the peridynamic model is implemented using truss elements and a kinetic contact algorithm available in the commercial FEA package is employed. Littlewood [107] implemented contact modeling between the peridynamic and finite element portions by an iterative approach. The contact algorithm utilized in [107] has to work with planar facets, and consequently each peridynamic node is represented by an icosahedron. Different from approaches in [115, 107], the contact between a discretized peridynamic domain and a non-peridynamic domain is directly modeled as a node-to-surface type in the present research, and a penalty method without iterations is used for transient analyses by the explicit time integration.

The remainder of this chapter is organized as follows. First, a short-range force model is introduced into the peridynamic theory. The inverse isoparametric mapping, which is useful to determine whether a peridynamic node penetrates into an element, is summarized. A contact algorithm for the calculation of the contact point and the penetration depth is then explained. For the transient analyses by the explicit time integration, a penalty method is employed to enforce displacement constraints on the contact surfaces. In the numerical examples, the material behavior of a peridynamic model is examined. Then the impact between two rigid bodies is presented to validate the contact algorithm. The last numerical example is a steel plate, which is modeled using peridynamics, perforated by a blunt-nosed cylindrical rigid projectile, and the residual velocities are compared with the analytical values.

## 6.2 Theory

### 6.2.1 Peridynamic short-range forces

In the peridynamic theory introduced in Section 3.2, material points interact through pre-defined bonds. However, in applications involving damage, two material points, which are beyond the horizon of each other in the reference configuration, might come into contact. In order to consider contact forces between material points, a short-range force model [115] is incorporated into the peridynamic theory as

$$\mathbf{f}_s = \frac{\boldsymbol{\eta} + \boldsymbol{\xi}}{\|\boldsymbol{\eta} + \boldsymbol{\xi}\|} \min \left\{ 0, c_s \left( \frac{\|\boldsymbol{\eta} + \boldsymbol{\xi}\|}{d_s} - 1 \right) \right\}, \quad (6.1)$$

where  $c_s$  is the spring constant for contact forces, and  $d_s$  is a constant such that the contact force is nonzero if the distance between two material points is smaller than  $d_s$ . In numerical implementations,  $c_s$  is set to be  $15c$  as in [115], and  $d_s$  is chosen to be  $d_s = 0.9\Delta x$ , where  $\Delta x$  is the grid spacing for the discretization.

The peridynamic equation of motion after discretization is written as

$$\rho \ddot{\mathbf{u}}_I^t = \sum_{J=1}^{N_{\mathcal{H}_I}} \mathbf{f} V_J + \sum_{K=1}^{N_s} \mathbf{f}_s V_K + \mathbf{b}_I^t, \quad (6.2)$$

where  $\ddot{\mathbf{u}}_I^t$  is the acceleration of the node  $I$  at time  $t$ ,  $N_{\mathcal{H}_I}$  is the total number of nodes within the horizon of the node  $I$  in the reference configuration,  $N_s$  is the number of nodes within the contact force range  $d_s$  of the node  $I$ ,  $V$  is the nodal volume, and  $\mathbf{b}_I^t$  is the body force at time  $t$ .

### 6.2.2 Inverse isoparametric mapping

The isoparametric finite element compared to the generalized coordinate finite element is more effective in evaluating element matrices [11]. The physical element is mapped into a reference element that is a square or a cube, and there exists a one-to-one mapping between the Cartesian coordinate system  $(x, y, z)$  and the natural coordinate system  $(\xi, \eta, \psi)$  [34]. If the natural coordinates of a point in an element are known, the Cartesian coordinates can easily be calculated as

$$\mathbf{x} = \sum_{i=1}^n N_i(\xi, \eta, \psi) \mathbf{x}_i, \quad (6.3)$$

where  $N_i$  are shape functions, and  $\mathbf{x}_i$  represent the Cartesian coordinates of the node  $i$ . However, the inverse isoparametric mapping from the Cartesian coordinates to the natural coordinates is nontrivial, and it is often required in the dynamic analyses due to, for example, the remeshing in the crack propagation [127]. In the contact-impact problems, the inverse isoparametric mapping is useful to determine whether a node penetrates into an element. The details of three-dimensional inverse isotropic mapping are introduced in Section 5.3.2

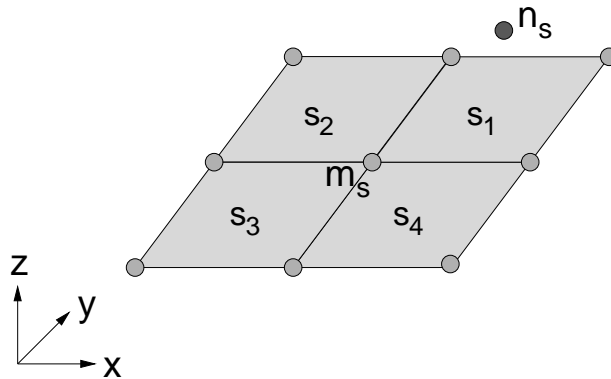


Figure 6.1: Slave node and four master segments.

### 6.2.3 Contact algorithm

Consider a slave node  $n_s$  lies above a master surface as shown in Figure 6.1, and the master surface consists of four segments  $s_1$ ,  $s_2$ ,  $s_3$ , and  $s_4$ . In order to find the contact point and the corresponding master segment, the first step is to search for the master node  $m_s$  that is nearest to the slave node  $n_s$ . The vector beginning at  $m_s$  and ending at  $n_s$  is denoted by  $\mathbf{g}$  as shown in Figure 6.2. Vectors  $\mathbf{c}_1$  and  $\mathbf{c}_2$  are along edges of a segment, and point outward from the master node  $m_s$ . The unit normal vector of the segment can be calculated by

$$\mathbf{m} = \frac{\mathbf{c}_1 \times \mathbf{c}_2}{|\mathbf{c}_1 \times \mathbf{c}_2|}, \quad (6.4)$$

and the projection of the vector  $\mathbf{g}$  onto the segment is expressed as

$$\mathbf{s} = \mathbf{g} - (\mathbf{g} \cdot \mathbf{m})\mathbf{m}. \quad (6.5)$$

A slave node  $n_s$  lies on the segment if the following criteria are satisfied [72]:

$$(\mathbf{c}_1 \times \mathbf{s}) \cdot (\mathbf{c}_1 \times \mathbf{c}_2) > 0, \quad (6.6)$$

$$(\mathbf{c}_1 \times \mathbf{s}) \cdot (\mathbf{s} \times \mathbf{c}_2) > 0. \quad (6.7)$$

However, if the slave node is above the intersection of two master segments as shown in Figure 6.3, the criteria given in Equations (6.6) and (6.7) would fail to be satisfied. Instead, the segment intersection on which the slave node lies can be determined by finding the

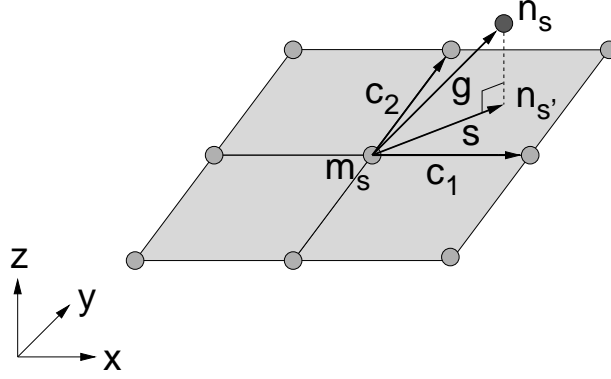


Figure 6.2: Projection of the vector  $\mathbf{g}$  onto a master segment.

maximum value of the following expression [72]:

$$\frac{\mathbf{g} \cdot \mathbf{c}_i}{|\mathbf{c}_i|}, \quad i = 1, 2, \dots, n, \quad (6.8)$$

where  $n$  is the number of segment intersections at  $m_s$ . In the case shown in Figure 6.3, the value of  $n$  is 4.

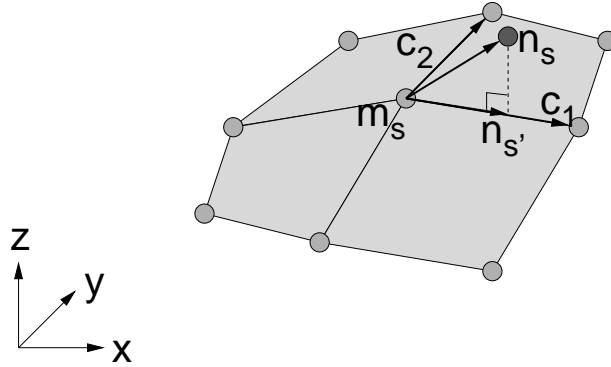


Figure 6.3: Slave node projected on the intersection of two master segments.

Assume that a master segment has been detected for the slave node  $n_s$  as shown in Figure 6.4. Then the contact point  $n_{s'}$ , which is the nearest point on the master segment to the slave node, needs to be determined. The method to find the contact point is the same as the technique introduced in Section 5.3.2

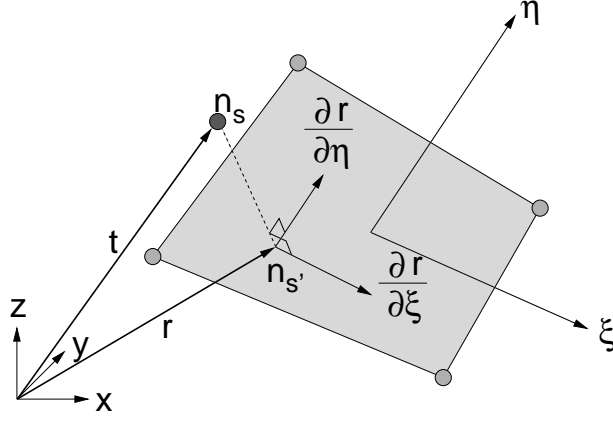


Figure 6.4: Location of a contact point.

Penetration of the slave node  $n_s$  through the master segment occurs if

$$l = \mathbf{n} \cdot (\mathbf{t} - \mathbf{r}) < 0, \quad (6.9)$$

where  $l$  is the penetration depth, and  $\mathbf{n}$  is the unit normal vector of the master segment containing the contact point.

#### 6.2.4 Penalty method

For transient analyses by the explicit integration, the penalty method is employed to enforce the displacement constraints at contact surfaces. The contact between a peridynamic domain and a non-peridynamic domain can be conveniently treated as a node-to-surface contact. The nodes in the discretized peridynamic domain are assumed to be slave nodes, and the surfaces of the non-peridynamic domain, which might come into contact with the peridynamic domain, are considered as master surfaces. The standard penalty formulation [72] is usually utilized to calculate the contact force, which is dependent on material constants. However, the standard penalty formulation is mainly suitable for similar materials coming into contact. For contact between dissimilar materials, the segment-based penalty

formulation [72] is recommended, and the contact stiffness is given as

$$k_{cs} = 0.5 \times \Xi_p \times \left\{ \begin{array}{c} \Xi_s \\ \text{or} \\ \Xi_m \end{array} \right\} \frac{m_1 m_2}{m_1 + m_2} \frac{1}{dt^2}, \quad (6.10)$$

where  $\Xi_p$  is the penalty scale factor which is 0.1 by default,  $\Xi_s$  and  $\Xi_m$ , which are 1.0 by default, are scale factors of slave and master penalty stiffnesses respectively,  $m_1$  is the nodal mass of the slave node, and  $m_2$  is the segment mass which can be taken to be half of the element mass [72].

If the slave node  $n_s$  penetrates the master segment, i.e.  $l < 0$  in Equation (6.9), a penalty force is then applied to the slave node and the master segment. The force, which is proportional to the penetration depth, is given by

$$\mathbf{F}_p = (k_{cs} \times l) \mathbf{n}, \quad (6.11)$$

and the penalty force applied to each node of the master segment can be determined using shape functions as

$$\mathbf{F}_p^i = \phi_i(\xi_c, \eta_c) \mathbf{F}_p, \quad (6.12)$$

where  $i$  indicates nodes that comprise the master segment.

Nodal accelerations are calculated by considering the internal forces, external forces, and contact forces. Subsequently, nodal velocities and displacements are updated using the Velocity-Verlet algorithm. The flowchart of the explicit algorithm for transient dynamic analyses is summarized in Table 6.1, which is similar to the scheme presented in [15].

- 
1. Initialize.
  2. Calculate the external forces.
  3. Calculate the internal forces.
    - (a) In the peridynamic domain, compute the internal forces from bond forces.
    - (b) In the non-peridynamic domain, e.g. finite elements, compute the internal forces arising from the element stress.
  4. Calculate the contact forces.
  5. Assemble external forces, internal forces, and contact forces into a force array.
  6. Compute nodal accelerations.
  7. Integrate the accelerations to calculate the nodal velocities and displacements.
  8. Go to step 2 for the next time step.
- 

Table 6.1: Explicit contact algorithm.

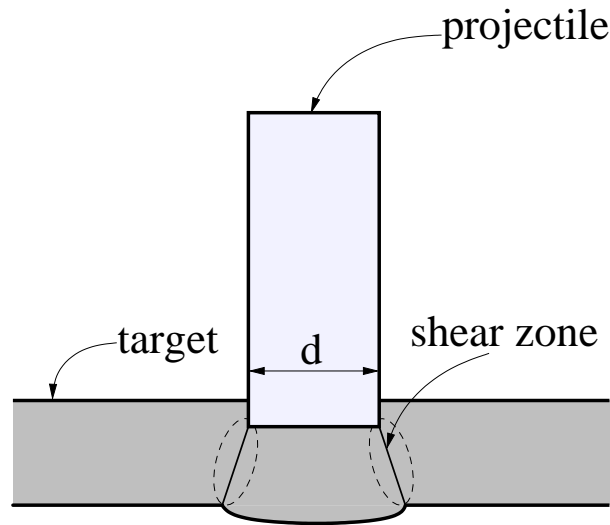


Figure 6.5: Perforation of a thin plate by a blunt projectile.

### 6.3 Ballistic limit

The perforation of a plate depends on the geometry and the strength of material [145]. Ballistic limit velocity is the minimum perforation velocity [145]. During perforation of a plate, damage develops in the shear zone surrounding the projectile as shown in Figure 6.5, and a plug in the target plate is formed by indentation. The residual velocity of a blunt



projectile after perforating a thin plate is expressed as [145]

$$v_r = a(v_i^p - v_{bl}^p)^{1/2}, \quad (6.13)$$

where  $v_i$  is the initial velocity,  $v_{bl}$  is the ballistic limit velocity, the constant  $p$  is equal to 2, and the mass ratio is

$$a = \frac{m_p}{m_p + m_t}, \quad (6.14)$$

where  $m_p$  is the mass of the projectile, and  $m_t$  is the mass of the plug formed by perforation. The value of  $m_t$  can be approximated by [24]

$$m_t \approx \frac{\pi}{4} d^2 \rho_t h_t, \quad (6.15)$$

where  $d$  is the diameter of the cylindrical projectile,  $\rho_t$  is the density of the target plate, and  $h_t$  is the thickness of the plate. On the other hand, constants  $a$  and  $p$  in Equation (6.13) can also be determined by fitting the experimental data [24].

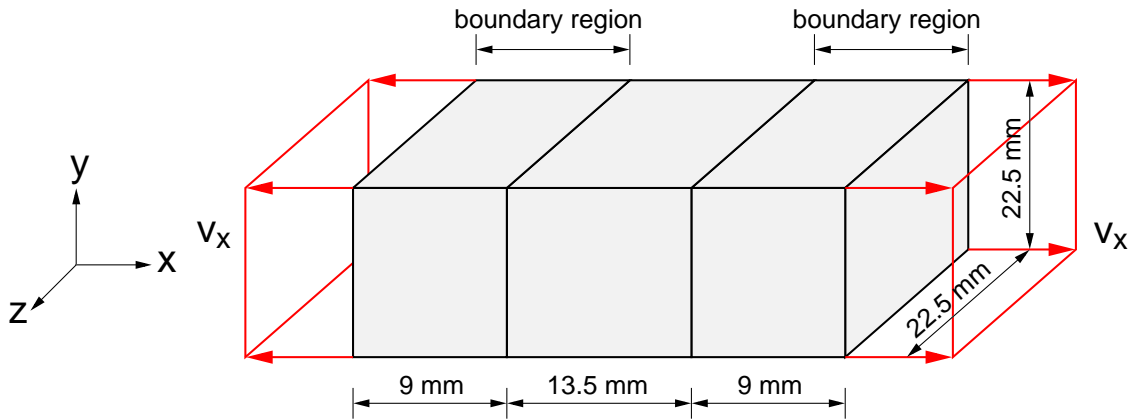


Figure 6.6: Peridynamic bar subjected to tension.

## 6.4 Numerical studies

### 6.4.1 Material behavior and modeling

Consider a peridynamic bar subjected to tension as shown in Figure 6.6. The dimensions of the bar are taken to be 31.5 mm in length, 22.5 mm in width and thickness. The boundary regions shown in Figure 6.6 are subjected to a constant velocity  $v_x$  in the longitudinal direction. Magnitudes of the velocity  $v_x$  are 10 mm/s for both boundary regions, but directions are opposite. The horizon is set to  $\delta = 3.0$  mm, and the bar is discretized with the grid spacing  $\Delta x = 1.5$  mm. The material model defined for peridynamic bonds is shown in Figure 6.7(a), which demonstrates perfect plasticity at the bond level. The density of the bar is  $8000 \text{ kg/m}^3$ . Setting Young's modulus  $E = 200 \text{ GPa}$ , we can calculate the micromodulus  $c = 1.1968 \times 10^{22} \text{ N/m}^6$ . The computational step is set to  $5 \times 10^{-8} \text{ s}$ , which is less than the critical time step for the explicit time integration.

The macroscopic material behavior of the peridynamic bar is shown in Figure 6.7(b), in which  $\sigma_x$  is the cross-sectional stress in the middle of the bar and  $\varepsilon_x$  is the strain imposed by the boundary displacements. As indicated in Figure 6.7(b), the peridynamic bar yields at the value very close to the yield stress 490 MPa, which is calculated by multiplying Young's modulus by the yield stretch. Unlike the material model at the bond level that shows perfect plasticity after yielding, the cross-sectional stress  $\sigma_x$  at the macroscopic level continues increasing till the value of around 930 MPa as shown in Figure 6.7(b). The reason is that peridynamic bonds do not yield at the same time. After reaching the value at around  $\sigma_x = 930 \text{ MPa}$ , most bonds yield and the peridynamic bar demonstrates a small amount of strain hardening as shown in Figure 6.7(c), and the cross-sectional stress starts to decrease

at the strain  $\varepsilon_x = 0.3$ .

Figure 6.7(d) shows the comparison of peridynamic material behavior at the macroscopic level to the experimental result of Weldox 460 E steel presented in [21]. The Weldox 460 E steel has Young's modulus  $E = 200$  GPa and the yield stress of 490 MPa, which are the same as the values that we use to define the material model for peridynamic bonds. The peridynamic model demonstrates close agreement with the experimental results before yielding, but the flow stress of the peridynamic model is larger than the experimental results due to the scale of the constitutive model defined at the bond level for peridynamics. Strain  $\varepsilon_x$  distributions by calculating the average bond stretches within the grid width  $\Delta x$  as nodal strains are plotted in Figure 6.8. As the displacements at boundary regions increase, bonds in the peridynamic model first yield and then break as the bond stretch reaches the critical value  $s_0 = 0.5$ . Note that if the state-based peridynamics [156, 181, 58, 59] is used with a proper constitutive model in the classical theory, better agreement with the experimental results in the macroscopic material properties might be obtained.

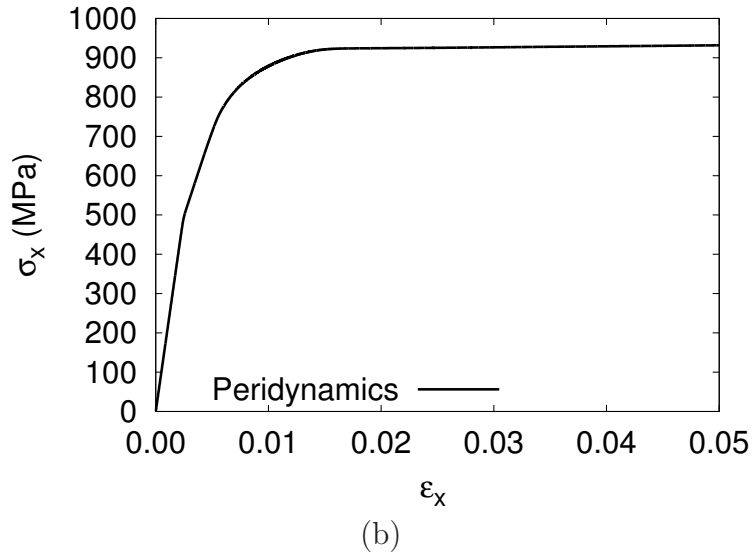
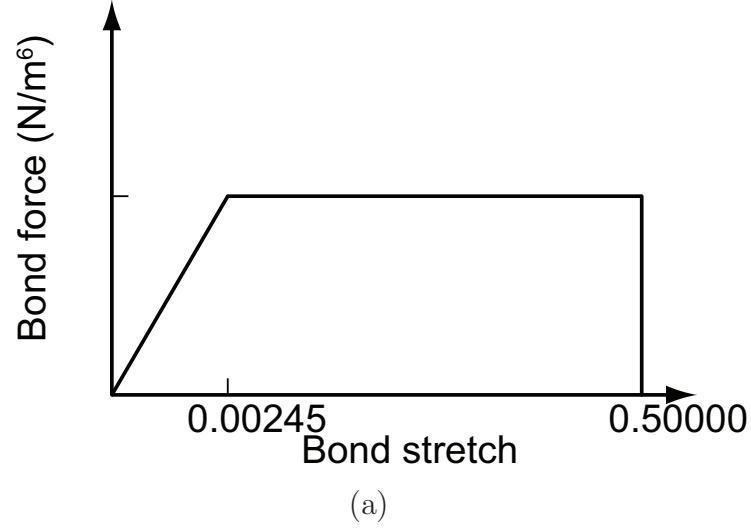
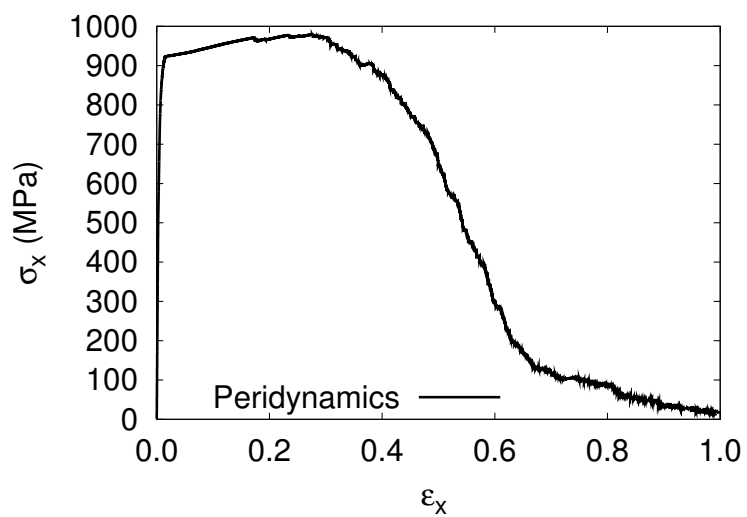
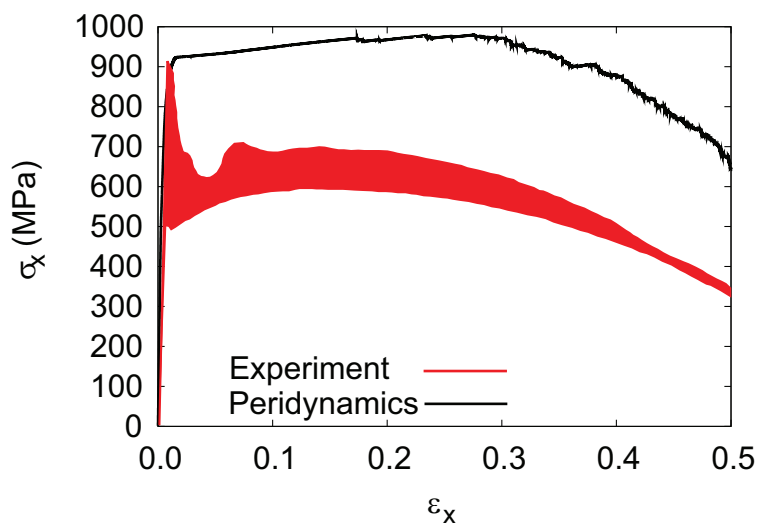


Figure 6.7: (a) Constitutive model defined for peridynamic bonds; (b) macroscopic material response of the peridynamic bar (strain  $\epsilon_x$  in the range of 0.00 to 0.05); (c) macroscopic material response of the peridynamic bar; (d) comparison of peridynamic material behavior at the macroscopic level to the experimental result of Weldox 460 E steel (strain rate in the range of  $0.00074 \text{ s}^{-1}$  to  $1522 \text{ s}^{-1}$ ) presented in [21].

Figure 6.7 (cont'd)



(c)



(d)

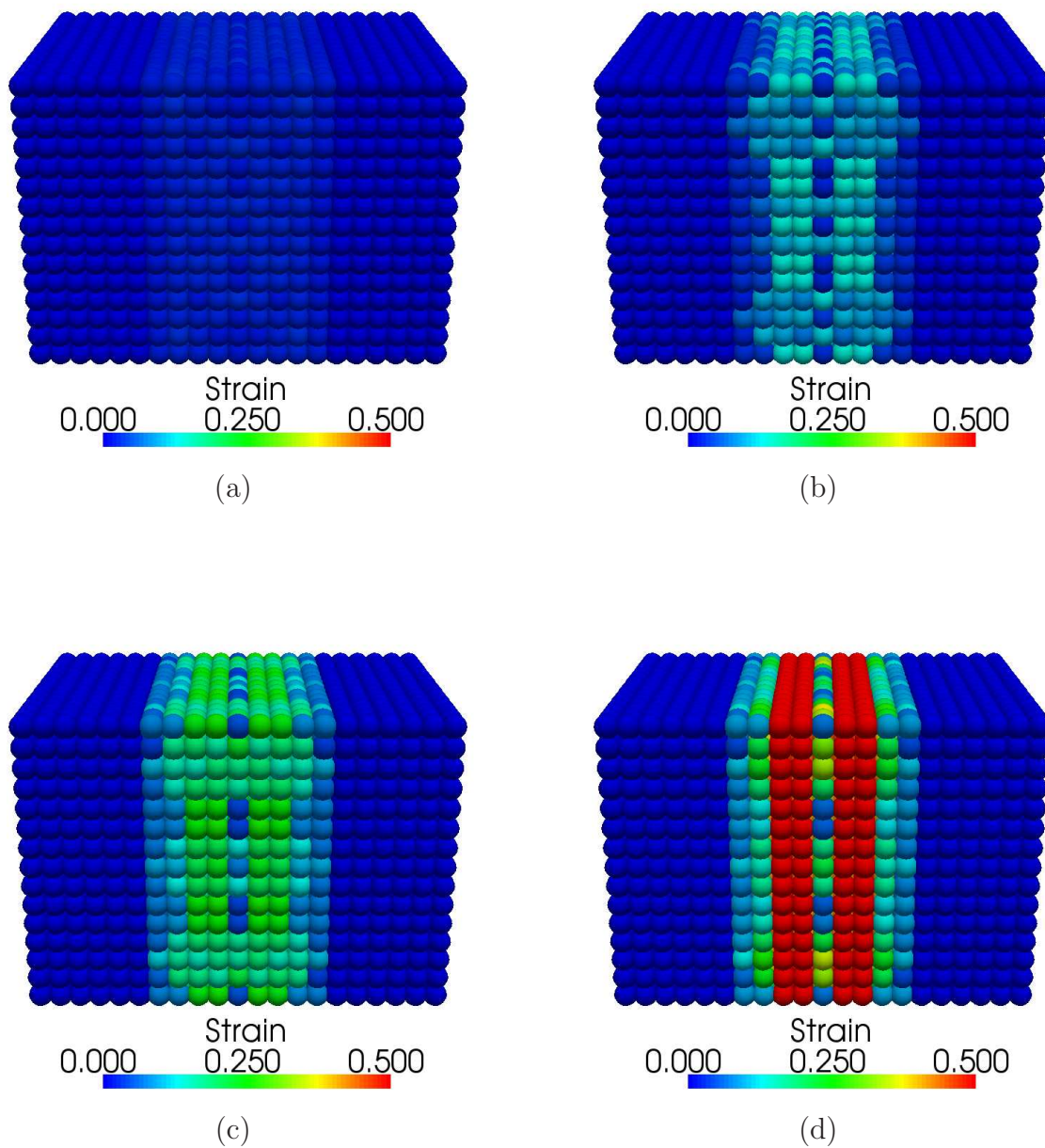


Figure 6.8: Strain  $\varepsilon_x$  contour: (a) boundary displacement  $u_x = 0.12$  mm; (b) boundary displacement  $u_x = 0.50$  mm; (c) boundary displacement  $u_x = 1.00$  mm; (d) boundary displacement  $u_x = 2.50$  mm.

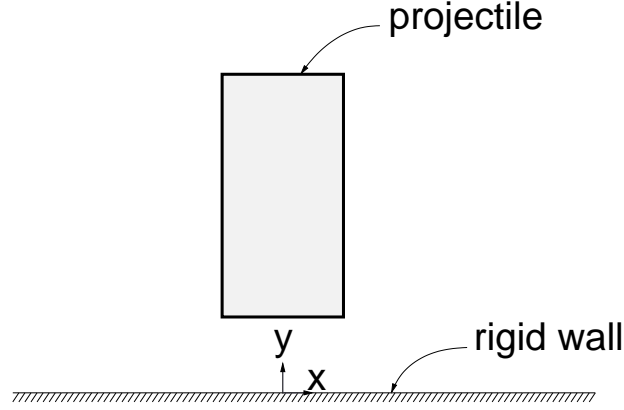


Figure 6.9: Impact between two rigid bodies.

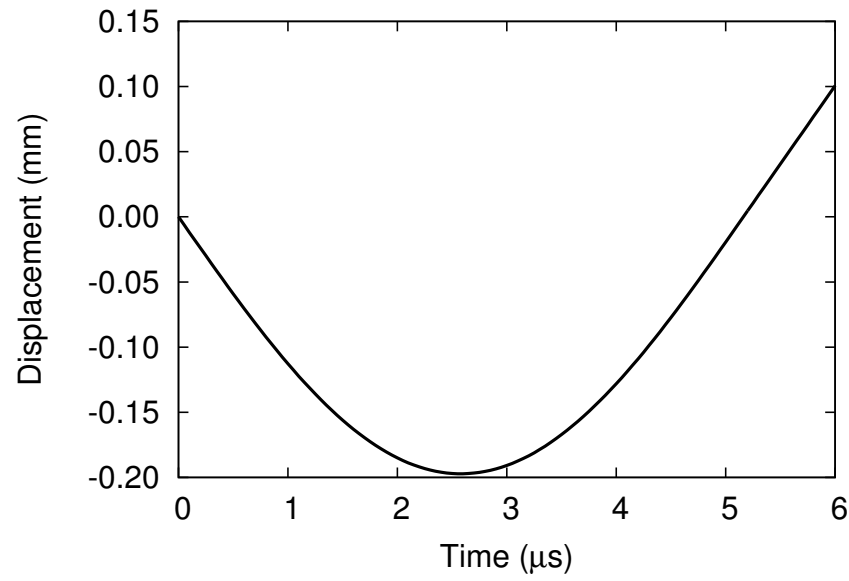
### 6.4.2 Rigid-body impact

In order to verify the contact algorithm, a rigid-body impact problem shown in Figure 6.9 is examined. The length of the cylindrical projectile is 80 mm, and the diameter is 20 mm. The mass of the rigid projectile is 0.197 kg, and the initial velocity is  $v_i = -120$  m/s. For the sake of detecting penetration and calculating the penetration length, the cylindrical projectile is modeled with eight-node solid elements, and the bottom surface of the projectile is comprised of 48 quadrilateral segments. The rigid wall is discretized into nodes with a uniform Cartesian grid of 1.5 mm in width. The nodes in the rigid wall after discretization, which serve as slave nodes, are constrained in all degrees of freedom during the calculation, and the calculation time step  $dt$  is set to  $5 \times 10^{-8}$  s.

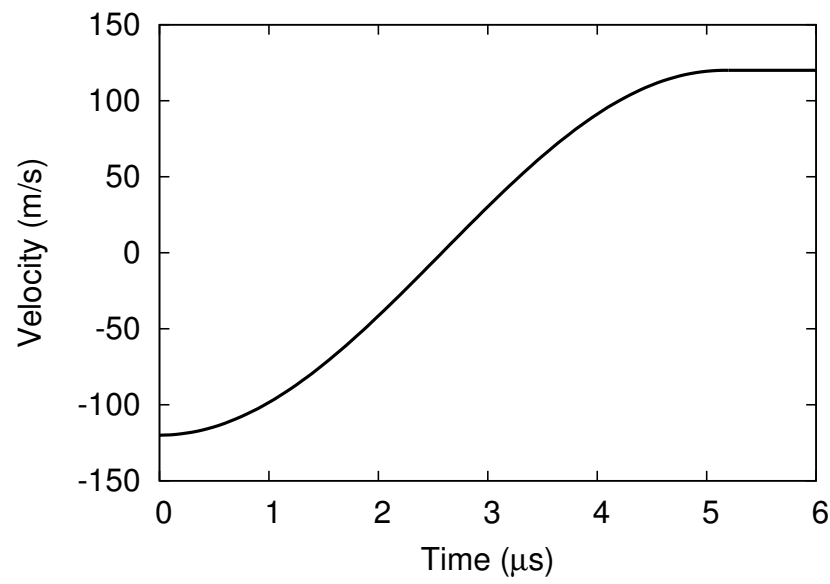
The displacement of the projectile is plotted in Figure 6.10(a). The maximum penetration depth into the rigid wall is around 0.20 mm, and then the projectile is gradually bounced up by the contact forces. As indicated in Figure 6.10(b), the final velocity of the projectile after impact is  $v = 120.01$  m/s, which is very close to the analytical value  $v = 120$  m/s by considering the conservation of kinetic energy. Hence, the proposed contact-impact procedure

is validated for this rigid-body impact problem.





(a)



(b)

Figure 6.10: (a) Displacement of the projectile and (b) velocity of the projectile.

### 6.4.3 Ballistic perforation

The ballistic penetration of a plate impacted by a blunt-nosed cylindrical projectile is examined for benchmarking. The blunt-nosed cylindrical projectile has the mass of 197 g, diameter of 20 mm, and length of 80 mm. The plate dimensions are taken to be 60 mm in length, 60 mm in width, and 12 mm in thickness. The density of the steel plate is  $8000 \text{ kg/m}^3$ , Young's modulus is 200 GPa, and the yield stress is 490 MPa, which are the same as material properties of Weldox 460 E steel. The ballistic penetration of Weldox 460 E steel is studied in [24], where a 12 mm thick plate is clamped in a rigid frame with the inner clamp diameter of 500 mm. Due to the high computational cost, we cannot afford modeling of the plate with the same in-plane dimensions as in the experiment in [24].

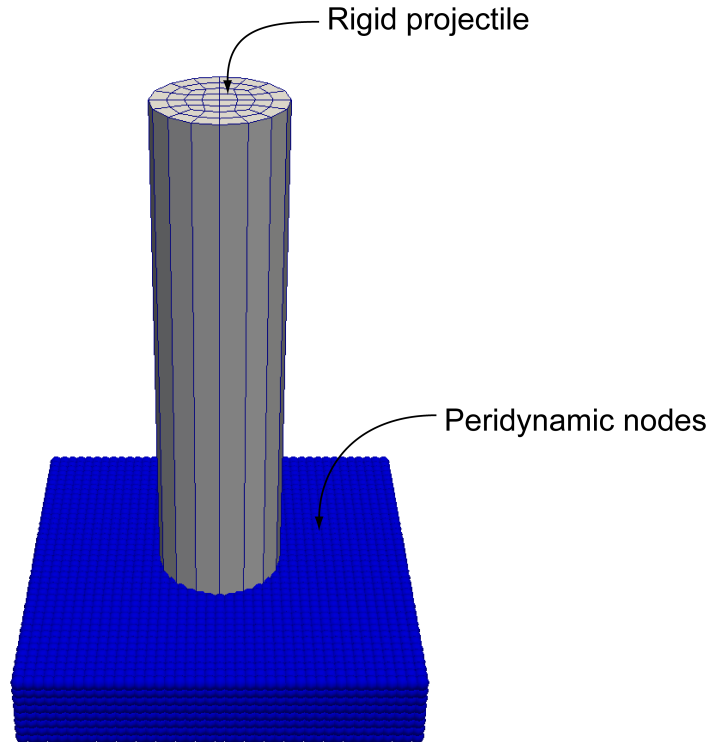


Figure 6.11: Modeling of a peridynamic plate impacted by a cylindrical projectile.

The target steel plate is modeled using peridynamics as shown in Figure 6.11. The

constitutive model at the bond level is defined as perfect plasticity such that the yield stretch  $s_y$  is 0.00245, and the critical stretch  $s_0$  is set to 0.5. The horizon is chosen to be  $\delta = 3.0$  mm, and the grid spacing is  $\Delta x = 1.5$  mm. A finer grid spacing might be utilized, but the corresponding computational cost will increase significantly. The projectile is modeled as a rigid body with 48 eight-node solid elements as shown in Figure 6.11. In the simulations, four lateral surfaces of the plate are constrained in  $x$ ,  $y$ , and  $z$  directions. The computational step is set to  $dt = 1 \times 10^{-7}$  s.

Initial velocity $v_i$	Residual velocity $v_r$
265 m/s	33.12 m/s
280 m/s	68.67 m/s
300 m/s	114.97 m/s
330 m/s	161.47 m/s
370 m/s	232.75 m/s
400 m/s	254.84 m/s

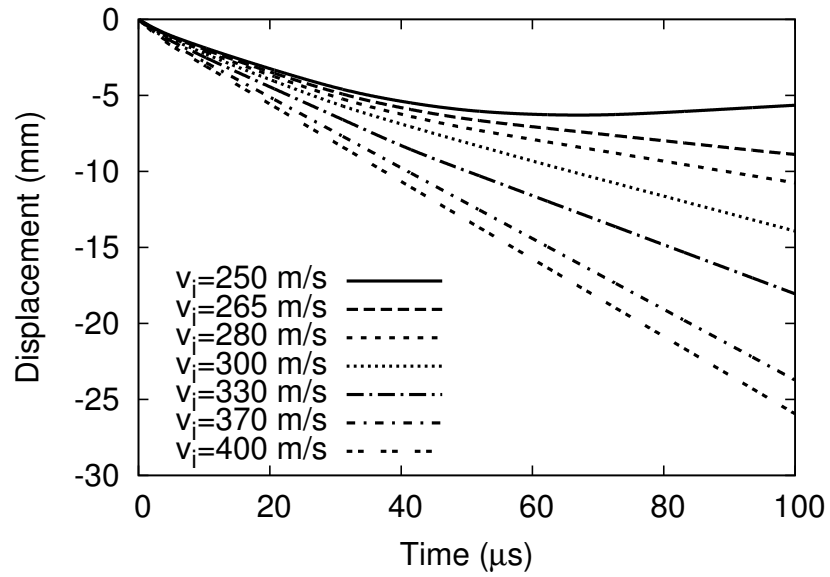
Table 6.2: Numerical results of residual velocities.

Displacements of the projectile with different initial velocities are shown in Figure 6.12(a). With the initial velocity  $v_i = 250$  m/s, the projectile indents the plate without perforation. The maximum indentation depth is 6.2946 mm at the time  $t = 67$   $\mu$ s, and then the projectile bounces back. The indentation formed by impact is shown in Figure 6.13, and a large part of the plate is deformed by the indentation.

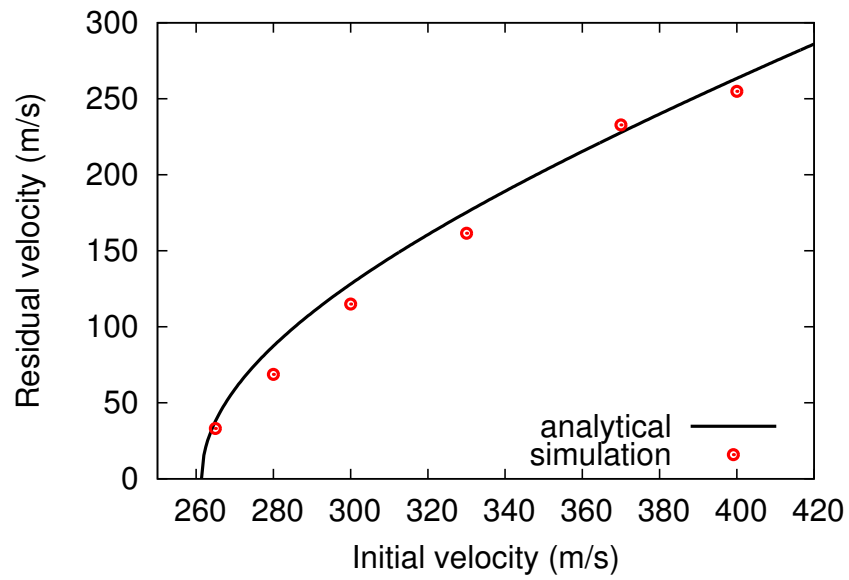
By performing a set of numerical experiments, the ballistic limit velocity is found to be 261.4 m/s, which is larger than the value of 184.5 m/s determined by the experiments presented in [24]. A few reasons can be considered herein. First, it has been found that the ballistic limit velocity is sensitive to the mesh size in the finite element analysis [21], and the numerically determined value of the ballistic limit velocity converges to the experimental value as the number of elements over the plate thickness increases [21]. Therefore, we might

anticipate that the numerically determined ballistic limit velocity would be closer to the experimental result if a smaller grid spacing  $\Delta x$  is used, which, however, would incur excessive computational cost. Second, as indicated in Figure 6.7, the bond-based peridynamic model demonstrates a larger increase in the flow stress beyond the yield point than the experimental result. To yield better agreement with the experimental result in the ballistic limit velocity, further investigation of the material model using the state-based peridynamics is required in the future. Third, the in-plane dimensions of the plate in the numerical simulations are different from those in the experiments by [24].

For the perforations by blunt projectiles, the analytical model [145] has been proven to be effective to estimate residual velocities. To compare numerical results with analytical solutions of the projectile residual velocity, the approximated mass ratio  $a$  given in Equation (6.14) is calculated to be 0.87. By substituting  $a = 0.87$  and  $v_{bl} = 261.4$  m/s into Equation (6.13), analytical values of the residual velocity can be obtained. The numerically determined residual velocities for the projectile with different initial velocities are summarized in Table 6.2, and the comparison of the numerical results to the analytical solutions of the residual velocity is plotted Figure 6.12(b). Since the analytical model is derived by considering the conservation of energy and momentum, the numerical results of residual velocities for the projectile with the initial velocities beyond the ballistic limit still demonstrate good agreement with the analytical model, regardless of the higher ballistic limit velocity in the numerical simulations.

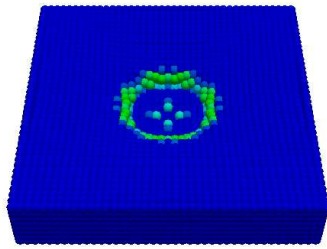


(a)



(b)

Figure 6.12: (a) Projectile displacement and (b) residual velocity.



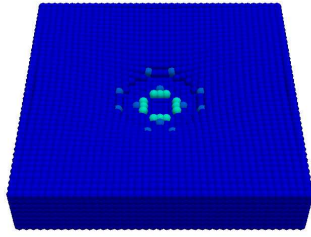
(a)



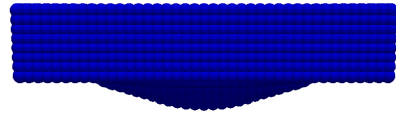
(b)

Figure 6.13: Indentation formed by the projectile with an initial velocity  $v_i = 250$  m/s: (a) bird's-eye view of the plate; (b) lateral view of the plate.

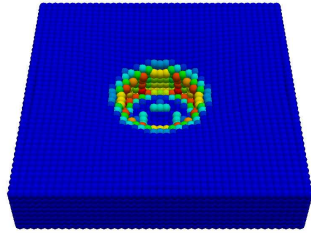
The deformed target plates during perforation are plotted in Figures 6.14 and 6.15 for the initial velocities  $v_i = 300$  m/s and  $v_i = 400$  m/s, respectively. The overall physical behavior of the perforation process is captured by the numerical simulations. In the first phase, the projectile indents the target, and the bending of the plate dominates. Then, the mass in front of the projectile is accelerated by the contact forces. Subsequently, damages occur near the shear zone surrounding the projectile after the peridynamic bond stretches reach the critical value. In the last phase, a plug is formed after severe indentation. The shape of the plug in numerical simulations is similar to the typical experimental observations. By comparing Figures 6.14 and 6.15, it is observed that as the initial velocity increases, the bulge on the rear side of the plate becomes localized, and the radius of deformation outside of the indented area is reduced. This observation agrees with the investigation presented in [24].



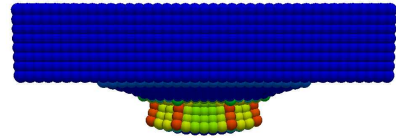
(a)



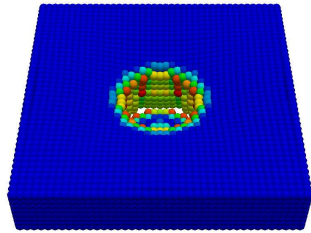
(b)



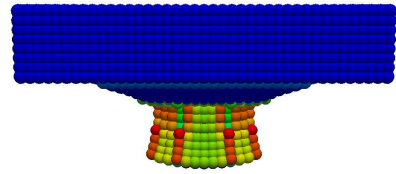
(c)



(d)



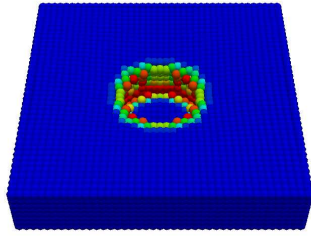
(e)



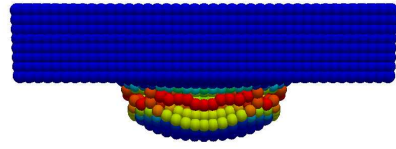
(f)

Figure 6.14: Perforation of the plate by the projectile an the initial velocity  $v_i = 300$  m/s: (a)  $t = 30 \mu s$ , bird's-eye view of the plate; (b)  $t = 30 \mu s$ , lateral view of the plate; (c)  $t = 70 \mu s$ , bird's-eye view of the plate; (d)  $t = 70 \mu s$ , lateral view of the plate; (e)  $t = 120 \mu s$ , bird's-eye view of the plate; (f)  $t = 120 \mu s$ , lateral view of the plate.

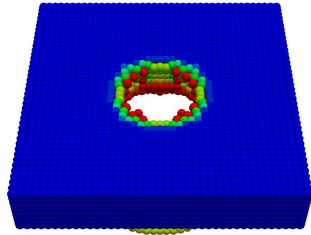




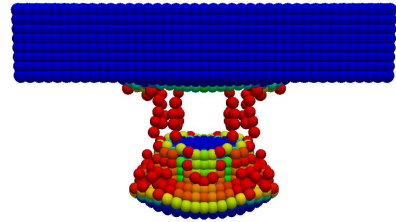
(a)



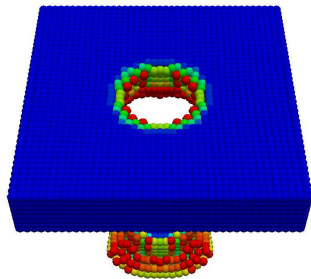
(b)



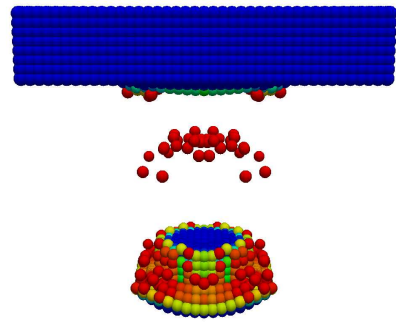
(c)



(d)



(e)



(f)

Figure 6.15: Perforation of the plate by the projectile an the initial velocity  $v_i = 400$  m/s: (a)  $t = 30 \mu\text{s}$ , bird's-eye view of the plate; (b)  $t = 30 \mu\text{s}$ , lateral view of the plate; (c)  $t = 70 \mu\text{s}$ , bird's-eye view of the plate; (d)  $t = 70 \mu\text{s}$ , lateral view of the plate; (e)  $t = 120 \mu\text{s}$ , bird's-eye view of the plate; (f)  $t = 120 \mu\text{s}$ , lateral view of the plate.

## 6.5 Summary

In this chapter, a numerical scheme is proposed for the modeling of contact of a peridynamic domain and a non-peridynamic domain (e.g. conventional finite elements and rigid bodies) under high velocities. Starting with the peridynamic theory, an approach for the three-dimensional inverse isoparametric mapping based on Taylor's series is then summarized. The inverse isoparametric mapping is effective to determine whether a slave node is within a solid element by determining the natural coordinates of the slave node. A contact algorithm for the calculation of the contact point and the penetration depth is then explained. For transient analyses by the explicit time integration, a penalty method is employed to enforce displacement constraints on the contact surfaces. The contact forces applied on the slave node and the master segment are proportional to the penetration depth.

The contact-impact problems are investigated numerically. First, the material behavior of a three-dimensional peridynamic model is examined. The results indicate that the macroscopic material behavior of a peridynamic bar is different from the material model defined at the bond level for peridynamics. Then the impact of a rigid projectile into a rigid wall is studied. By comparing the kinetic energy before and after impact, the proposed numerical scheme for the contact-impact procedure between two rigid bodies is validated. The last numerical example is the perforation of a steel plate by a blunt-nosed cylindrical rigid projectile. The plate, where severe damage develops during perforation, is modeled using peridynamics. Indentation is formed if the initial velocity of the projectile is smaller than the ballistic limit velocity, and the value of ballistic limit velocity is determined by running a set of numerical experiments. Compared with the ballistic limit velocity to perforate the plate investigated by experiments in [24], the numerically determined value of the ballistic

limit velocity is larger due to the differences in the macroscopic material properties and the geometry of the target plate. For the projectile with an initial velocity beyond the ballistic limit velocity, a comparison of numerical results to the analytical solutions of the residual velocity is conducted, and good agreement is observed. The overall physical behavior of the perforation process is captured by the numerical simulations employing the proposed contact-impact procedure.

# Chapter 7

## Modeling of Porous Brittle Solids using Peridynamics

### 7.1 Introduction

Heterogeneous materials consist of more than one materials, insoluble in one another [26]. A finite and heterogeneous solid made of  $m$  subdomains is shown in Figure 7.1. Heterogeneous materials have been widely used throughout human history from concrete, the earliest application of which was by Romans [119], to composites used by the aircraft industry. Typical heterogeneous materials include, for example, metal alloys, polycrystalline, composites, and porous media. The macroscopic material behaviors of heterogeneous materials are determined by the size, shape, properties, and spatial arrangement of constituents [96].

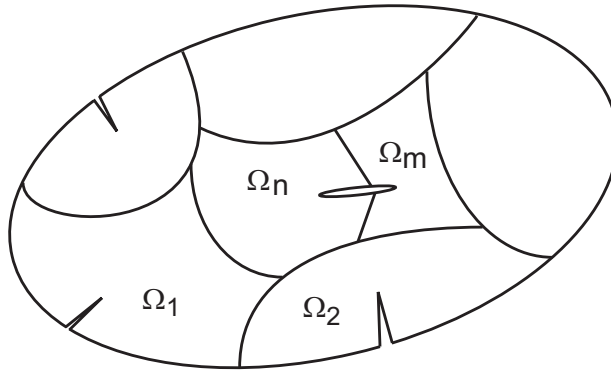


Figure 7.1: Finite and heterogeneous solid [169].

As a type of heterogeneous material, porous materials comprise a solid phase and pores

[105]. It has been found that the porosity has a significant effect on the elastic modulus of materials. Spriggs [163] proposed an empirical equation describing the effect of porosity on the elastic modulus of solids. Wang [177, 178] obtained a theoretical relationship between the porosity and Young's modulus by considering a cubic stacking pattern and Young's modulus of porous alumina with different pore structures. Phani and Niyogi [137] derived a semi-empirical equation for the porosity dependence of Young's modulus of brittle solids.

Similarly, the porosity also has significant effects on the strength of materials. In a commentary on the investigations by Ryshkewitch [152], Duckworth [43] suggested an expression for the influence of porosity on the strength. Considering the combined effect of porosity and grain size, Knudsen [95] developed an empirical equation. Hasselman [74] proposed relations between effects of porosity on the strength and Young's modulus of elasticity of polycrystalline materials. Vardar *et al.* [175] investigated the effect of spherical pores on the strength of a ceramic material, and compared the experimental results of brittle strength and the predictions using the Weibull probabilistic approach. Krstic [99, 100] proposed an analytical model describing the strength degradation of brittle solids containing spherical pores and annular flaws, and developed a unified approach to determine the effect of microstructure on fracture of brittle materials. An evaluation of strength-porosity relationships was presented by Dutta [45], and a semi-empirical relationship for the assessment of strength by Young's modulus was proposed. Wagh *et al.* [176] proposed an analytical model incorporating connected-grain model to describe the dependence of flexural strength of ceramics on the porosity. Nielsen [129] studied relations between the stiffness and the strength of porous materials considering the pore geometry. Kearsley and Wainwright [89] studied the effect of porosity on the strength of foamed concrete. Rössler and Odler [149] investigated the relationships between the porosity and the strength for a series of cement paste specimens.

Kumar and Bhattacharjee [102] experimentally studied the in situ concrete, and presented an empirical model relating in situ strength of concrete with the porosity, pore size distribution, and binder content. Weiler *et al.* [184] used the X-ray tomography to examine the magnesium alloy, and found that the tensile properties are mainly determined by the local areal fraction of porosity.

In many engineering applications, it is necessary to determine the macroscopic characteristics of heterogeneous materials. However, the complexities in the material properties and microstructural characteristics make it difficult to study heterogeneous materials. The simplest method is to homogenize properties of a heterogeneous material as an average over the properties of the constituents [96]. With the development of computational methods, research progresses for the analyses of heterogeneous materials have been made. For example, Sumi and Wang [169] used the finite element method to study the growth of non-collinear cracks in a two-dimensional heterogeneous solid. Due to the length scales involved in heterogeneous materials, it is not possible to generate meshes that can accurately represent the microstructure. Therefore, multi-scale modelings are promising alternative approaches. For example, the spatially periodic representative volume element has been applied to study the large-strain mechanical responses of voided polycarbonate [162]. Kouznetsova *et al.* [96, 97] presented a micro-macro strategy for the modeling of heterogeneous materials at large deformations.

In this chapter, peridynamics is employed to study brittle materials containing pores. First, analytical and empirical equations describing the effect of porosity on Young's modulus and strength of solid materials are summarized. A few numerical examples are then presented. Specimens containing randomly distributed cubic voids with varying amounts of porosity are studied. The degradation of Young's modulus and strength with increasing

porosity in the numerical results is compared with analytical and empirical models. Brittle solids containing spherical voids are studied for different porosities, and a comparison between numerical results and analytical solutions is conducted.

## 7.2 Theory

For porous brittle solids, the porosity  $P$  can be described using the volume fraction porosity as

$$P = \frac{\text{Void volume}}{\text{Total volume}}. \quad (7.1)$$

The empirical equation, proposed by Spriggs [163], for the prediction of Young's modulus at the porosity value of  $P$  has been widely used as

$$E = E_0 e^{-bP}, \quad (7.2)$$

where  $E_0$  is the zero-porosity Young's modulus, and  $b$  is an empirical constant. Considering the densification of spherical particles in a simple cubic array, Wang [177, 178] derived the theoretical solution of Young's modulus of porous materials. The relative density  $X$ , which equals  $1 - P$ , is described by [177]

$$X(\theta) = \begin{cases} \frac{\pi}{12} \left( \frac{9}{\cos^2 \theta} - 3 - \frac{4}{\cos^3 \theta} \right), & \text{for } \theta \leq 45^\circ \\ (\tan^2 \theta - 1)^{1/2} + \frac{1}{4\cos^3 \theta} \int_{\theta}^{\sin^{-1}(\sqrt{2}\cos\theta)} [\sin^3 \phi (\pi - 4\alpha + 2\sin 2\alpha)] d\phi, & \text{for } \theta \geq 45^\circ \end{cases}, \quad (7.3)$$

where  $\theta$  is the angle of coalescence, and  $\alpha = \cos^{-1}(\cos\theta/\sin\phi)$ .  $\theta = 0^\circ$  if the sphere is inscribed within the unit cell, and  $\theta = 54.74^\circ$  for the 100% density. For the ideal case in

which the load is applied on a perfect cubic array, the normalized Young's modulus is given as [177]

$$\frac{E}{E_0}(\theta) = \begin{cases} \frac{1}{4\cos\theta} \left[ \frac{1}{\pi} \ln \frac{\tan(\pi/4-\theta/2)}{\tan(\theta/2)} + \int_{\pi/2-\theta}^{\pi/2} \frac{d\phi}{\sin\phi(\pi-4\alpha+2\sin 2\alpha)} \right]^{-1}, & \text{for } \theta \leq 45^\circ \\ \left[ (\tan^2\theta - 1)^{1/2} + 4\cos\theta \int_{\theta}^{\sin^{-1}(\sqrt{2}\cos\theta)} \frac{d\phi}{\sin\phi(\pi-4\alpha+2\sin 2\alpha)} \right]^{-1}, & \text{for } \theta \geq 45^\circ \end{cases}. \quad (7.4)$$

Figure 7.2(a) shows the value of the relative density that is a function of the angle of coalescence, and Figure 7.2(b) shows Young's modulus of porous materials as a function of the relative density by numerically evaluating Equations (7.3) and (7.4), respectively. Based on the theoretical solution, Wang [177] proposed an approximated solution as

$$E = E_0 e^{-(bP+cP^2)}, \quad (7.5)$$

where  $b$  and  $c$  are material constants.

The dependence of strength on the porosity has been represented by a few empirical equations. Based on experimental data by Ryshkewitch [152], Duckworth [43] described the relationship as

$$\sigma_f = \sigma_0 e^{-bP}. \quad (7.6)$$

where  $\sigma_0$  is the zero-porosity strength, and  $b$  is a constant. Dutta *et al.* [45] proposed an empirical equation as

$$\sigma_f = \sigma_0 (1 - P)^m, \quad (7.7)$$

where  $m$  is a constant. Krstic [99] derived the strength of a solid containing spherical voids



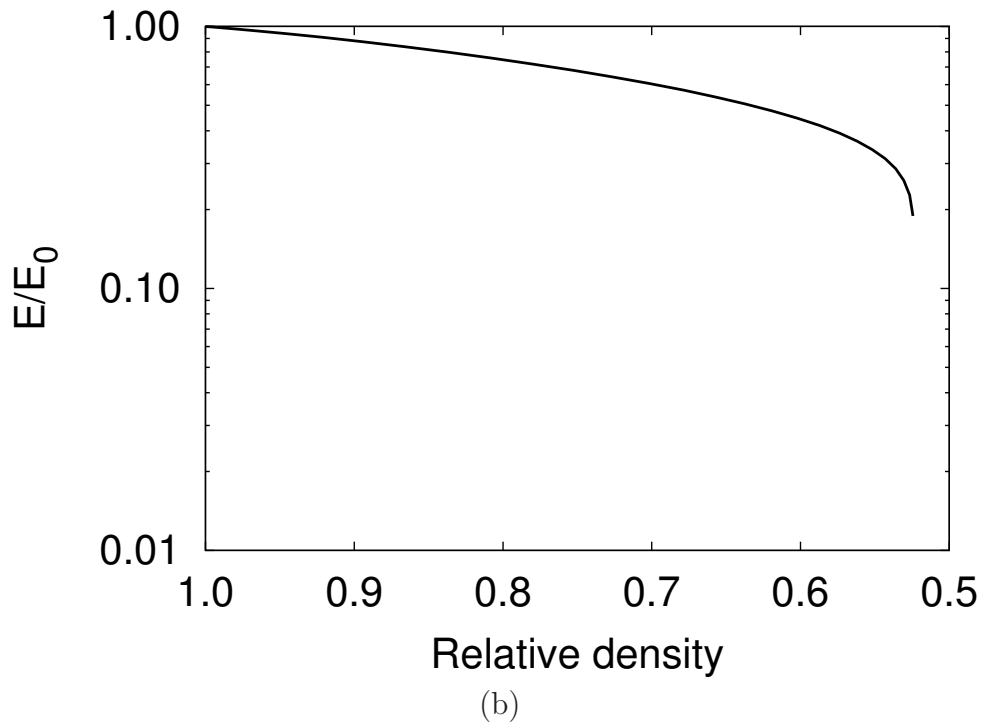
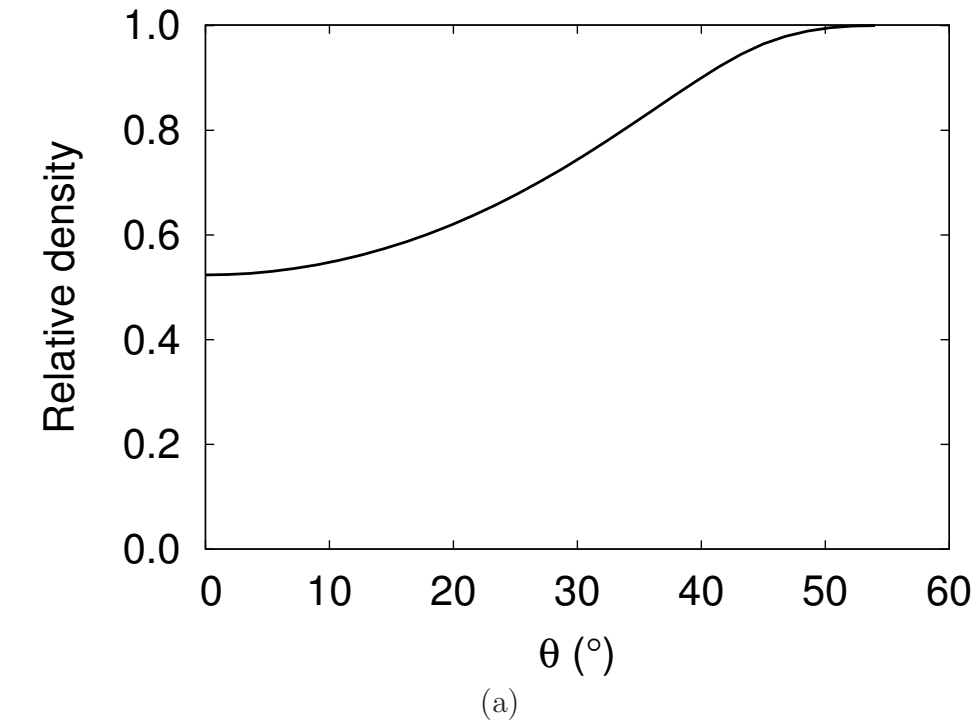


Figure 7.2: (a) Relative density versus angle of coalescence and (b) theoretical solution of Young's modulus of porous materials.

as

$$\sigma_f = \sqrt{\frac{\pi\gamma E_0}{D(1-\nu^2)(1+s/R)}} \times \left\{ 1 + \frac{4P(1-\nu^2)}{\pi} \times \left[ 2(1+s/R)^3 + \frac{3}{2(7-5\nu)(1+s/R)^2} + \frac{(4-5\nu)}{2(7-5\nu)} \right] \right\}^{-1/2}, \quad (7.8)$$

where  $\gamma$  is the fracture surface energy of a crack which equals  $G_f/2$  for ideally brittle materials [5],  $D$  and  $R$  are the diameter and radius of spherical pores respectively, and  $s$  is the annular flaw size as shown in Figure 7.3.

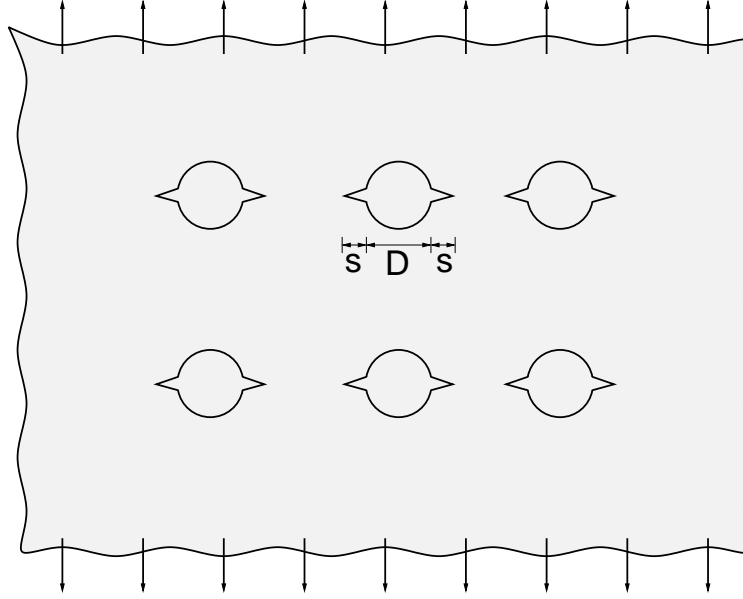


Figure 7.3: Spherical pores with annular flaws [99].

## 7.3 Numerical implementation

For numerical simulations, voids are generated on the discretization grid of a peridynamic domain. First, the Fortran intrinsic function `random_seed` is used to initialize the random seed based on the system's time. Then the Fortran intrinsic function `random_number` is

invoked to return an array consisting three numbers from the uniform distribution over the range of 0 to 1. By multiplying the number of discretization nodes in  $x$ ,  $y$ ,  $z$  directions and rounding to integers, we can obtain the position to generate a void in the discretization grid. A spherical void can be generated by deleting peridynamic nodes within the spherical radius with the center determined by random numbers. A number of iterations are performed till the volume fraction is close to the desired value of porosity within a tolerance. The algorithm to generate spherical voids is summarized in Table 7.1.

- 
1. Discretize the peridynamic domain.
  2. Call `random_seed` to initialize the random seed.
  3. Call `random_number` to generate three random numbers in the range of 0 to 1.
  4. Determine the center to generate a spherical void in the discretization grid.
  5. Determine the distance to the nearest void and specimen boundaries.
  6. Go to step 3 if the distance determined in step 5 is less than the predefined value.
  7. Delete all nodes within the radius of the spherical voids.
  8. Calculate the volume fraction.
  9. Go to step 3 to generate additional spherical pores if the volume fraction is less than the desired value of porosity.
- 

Table 7.1: Algorithm to generate randomly distributed spherical voids.

## 7.4 Case studies

### 7.4.1 Cubic voids

Peridynamics is employed to study material behaviors of a porous brittle material. The material properties of the non-porous body are taken to be Young's modulus  $E_0 = 70$  GPa and the critical bond stretch  $s_0 = 0.05$ . Consider a three-dimensional model of dimensions  $25.5 \text{ mm} \times 25.5 \text{ mm} \times 25.5 \text{ mm}$ . The size of the horizon is set to  $\delta = 1.0 \text{ mm}$ , and the

peridynamic model is discretized with the grid spacing  $\Delta x = 0.5$  mm, which ends up with  $51 \times 51 \times 51$  peridynamic nodes. The horizon to the grid spacing ratio is selected to be 2 since it is good to match the macroscopic material behavior in the elastic range. The numerical simulations are conducted on a workstation with an NVIDIA C1060 GPU. A constant velocity of 10 mm/s is applied on boundary regions at both ends of the specimen for tensile loading, and the width of each boundary region is 2.5 mm. For the numerical calculation, the time step  $dt$  is set to be  $5 \times 10^{-8}$  s.

In order to introduce cubic voids into the peridynamic model, the random number generator is utilized to select a number of peridynamic nodes so that the volume fraction of selected nodes equal to the desired porosity as described by Equation (7.1). The flowchart is similar to the algorithm described in Table 7.1. Voids can be introduced by either deleting the selected peridynamic nodes or deleting all peridynamic bonds connecting to those nodes. In the algorithm to generate randomly distributed cubic voids, it is prescribed that no adjacent peridynamic nodes are deleted simultaneously. Therefore, only cubic voids are generated in the peridynamic model. Figure 7.4 shows the specimen that contains 5% cubic voids.

Porosity	Young's modulus (GPa)	Tensile strength (MPa)
0%	71.7742	281.3537
5%	67.1853	236.0355
10%	62.1410	210.6670
15%	57.7252	188.7893
20%	52.7812	165.6249

Table 7.2: Young's modulus and tensile strength of specimens containing cubic voids.

The cross-sectional stresses are plotted in Figure 7.5 for peridynamic models with varying amounts of porosity. For the nonporous model, the resultant Young's modulus by calculating

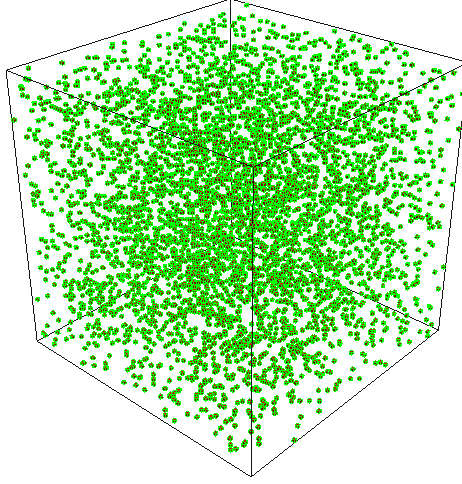


Figure 7.4: Cubic voids in a specimen of dimensions of 25 mm×25 mm×25 mm. Porosity  $P = 5\%$  .

the tangent of the stress-strain curve is  $E = 71.87$  GPa, which is close the exact Young's modulus of the material. The strength of the nonporous model is  $\sigma_f = 280.97$  MPa. As the porosity  $P$  increases, both Young's modulus and strength decrease as shown in Figure 7.5. Young's moduli and strengths for different porosities are summarized in Table 7.2. The effect of porosity on Young's modulus is plotted in Figure 7.6(a). For the comparison, the empirical equation given in Equation (7.2), the approximate solution presented in Equation (7.5), and the theoretical solution given in Equation (7.4) are utilized. As indicated in Figure 7.6(a), the numerical results are in good agreement with empirical, approximate, and theoretical solutions. Similarly, the effect of porosity on the strength is plotted in Figure 7.6(b). The numerical results are compared with the solutions by fitting empirical models given in Equations (7.6) and (7.7) to the numerical data. Close agreement between the numerical results and empirical models is observed in Figure 7.6(b).

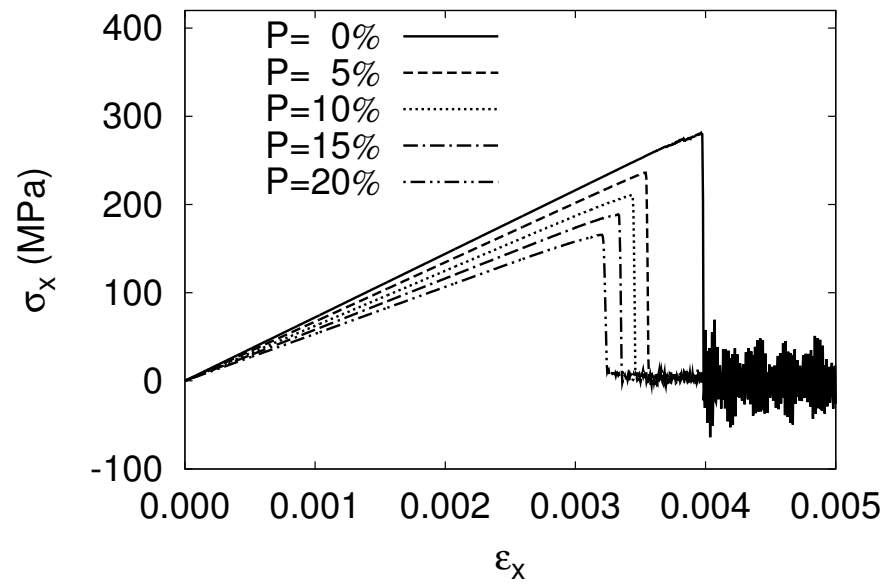
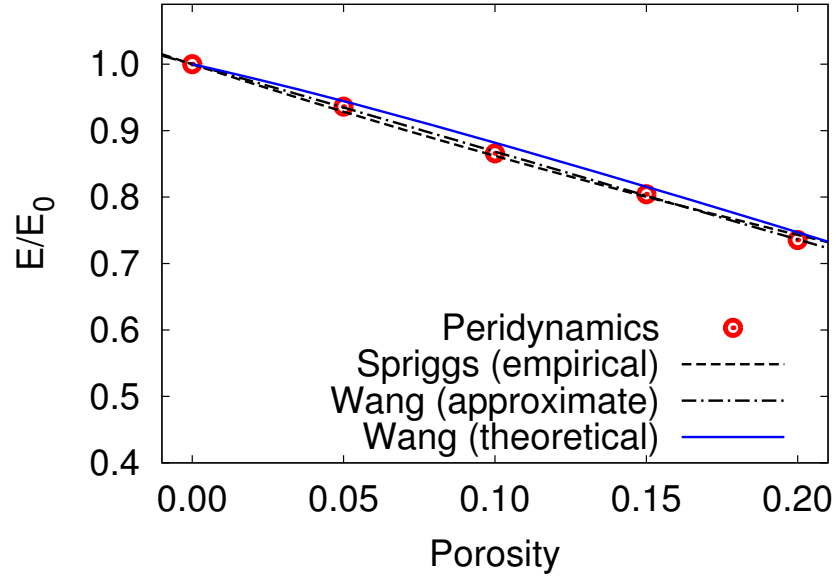
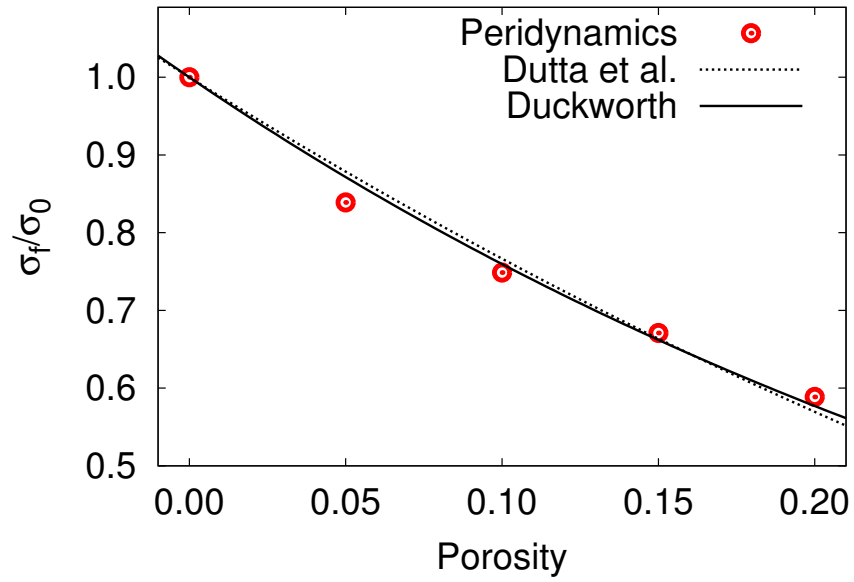


Figure 7.5: Cross-sectional stress versus strain of specimens containing cubic voids.



(a)



(b)

Figure 7.6: (a) Normalized Young's modulus and (b) normalized tensile strength of specimens containing cubic pores.

### 7.4.2 Spherical voids

In the following, peridynamic models that contain spherical pores are examined for different porosities. The dimensions of the peridynamic model are 55 mm in length, 35 mm in width, and 35 mm in thickness. The grid spacing  $\Delta x$  is 0.5 mm, and the horizon  $\delta$  is set to be  $2\Delta x$ . Spherical pores are randomly generated within the boundary of peridynamic models, and specimens containing 5%, 10%, 15%, and 20% porosities are demonstrated in Figure 7.7. The diameter of spherical pores is set to  $D = 11\Delta x$ . Young's modulus of nonporous body is  $E_0 = 70$  GPa, and Poisson ratio is 0.25. For the computation, time step  $dt$  is set to be  $5 \times 10^{-8}$  s. A constant velocity of 10 mm/s is applied on boundary regions at both ends of specimens for tensile loading, and the width of each boundary region is 2.5 mm.

Figure 7.8 shows the cross-sectional stress versus strain imposed by the boundary displacement for models of different porosities. The resultant Young's modulus of the nonporous model is 71.65 GPa, and the strength is  $\sigma_f = 266.56$  MPa. As the porosity increases, both Young's modulus and strength decrease as shown in Figure 7.8. Young's moduli and strengths of peridynamic models for different porosities are summarized in Table 7.3. In Figure 7.9(a), the normalized Young's modulus is compared with the theoretical solution given in Equation (7.4) and the fitted curves by Spriggs' empirical relation given in Equation (7.2) and Wang's approximated solution given in Equation (7.5). As indicated in Figure 7.9(a), Young's moduli of peridynamic models for different porosities show close agreement to the theoretical solutions and the fitted curves using empirical and approximate models. The tensile strength of peridynamic models containing spherical pores is compared to the theoretical solution given in Equation (7.8). Note that a flaw size of  $s$  is assumed at pore edges in Equation (7.8). Theoretical solutions considering flaw sizes of 0,  $\Delta x$  and  $2\Delta x$  are plotted



in Figure 7.9(b). Since the horizon  $\delta = 2\Delta x$  is utilized for the peridynamic model, we might anticipate that  $s = \Delta x$  might yield the best agreement to the theoretical solution, which is confirmed in Figure 7.9(b).

Porosity	Young's modulus (GPa)	Tensile strength (MPa)
0%	71.6015	272.1414
5%	66.0444	167.2611
10%	63.1007	159.1419
15%	57.8934	145.0795
20%	54.2525	138.0373

Table 7.3: Young's modulus and tensile strength of specimens containing spherical voids within the boundary.

Similar to the case that spherical voids are generated within the boundary as shown in Figure 7.7, the spherical voids intersecting with boundaries can also be generated as shown in Figure 7.10. The stress-strain curves with different porosities in the peridynamic model are plotted in Figure 7.11, which indicates that both Young's modulus and strength decrease as the porosity increases. The resultant Young's modulus and strength are summarized in Table 7.4. Figure 7.12(a) shows the comparison of the numerical results to the analytical and empirical models in the degradation of Young's modulus, and good agreement is observed. The trend of decreasing strength with increasing porosity is plotted in Figure 7.12(b). The numerical results are compared with the theoretical values by solving Equation (7.8). As demonstrated in Figure 7.12(b), the numerical results are close to the theoretical values considering the annular flaw size in the range of  $s = 1\Delta x$  to  $s = 2\Delta x$ .

By comparing Tables 7.2 and 7.3 which summarize Young's moduli and tensile strengths for solids containing cubic and spherical voids respectively, the effect of the shape of voids on material properties can be found. The difference in Young's modulus of models containing cubic and spherical pores is inconsiderable. On the other hand, tensile strengths of models

Porosity	Young's modulus (GPa)	Tensile strength (MPa)
0%	71.6015	272.1414
5%	66.8800	164.3560
10%	62.9406	138.5337
15%	59.0915	136.4608
20%	54.3961	129.4621

Table 7.4: Young's modulus and tensile strength of specimens containing spherical voids intersecting with boundaries.

containing spherical pores decrease. Similarly, by comparing Tables 7.3 and 7.4, we can notice that the difference in Young's modulus of specimens containing spherical pores intersecting with boundaries is insignificant compared to the results of spherical pores placed within the boundaries. On the other hand, the strength decreases if spherical pores having intersections with the boundaries as indicated by comparing Figures 7.9(b) and 7.12(b).

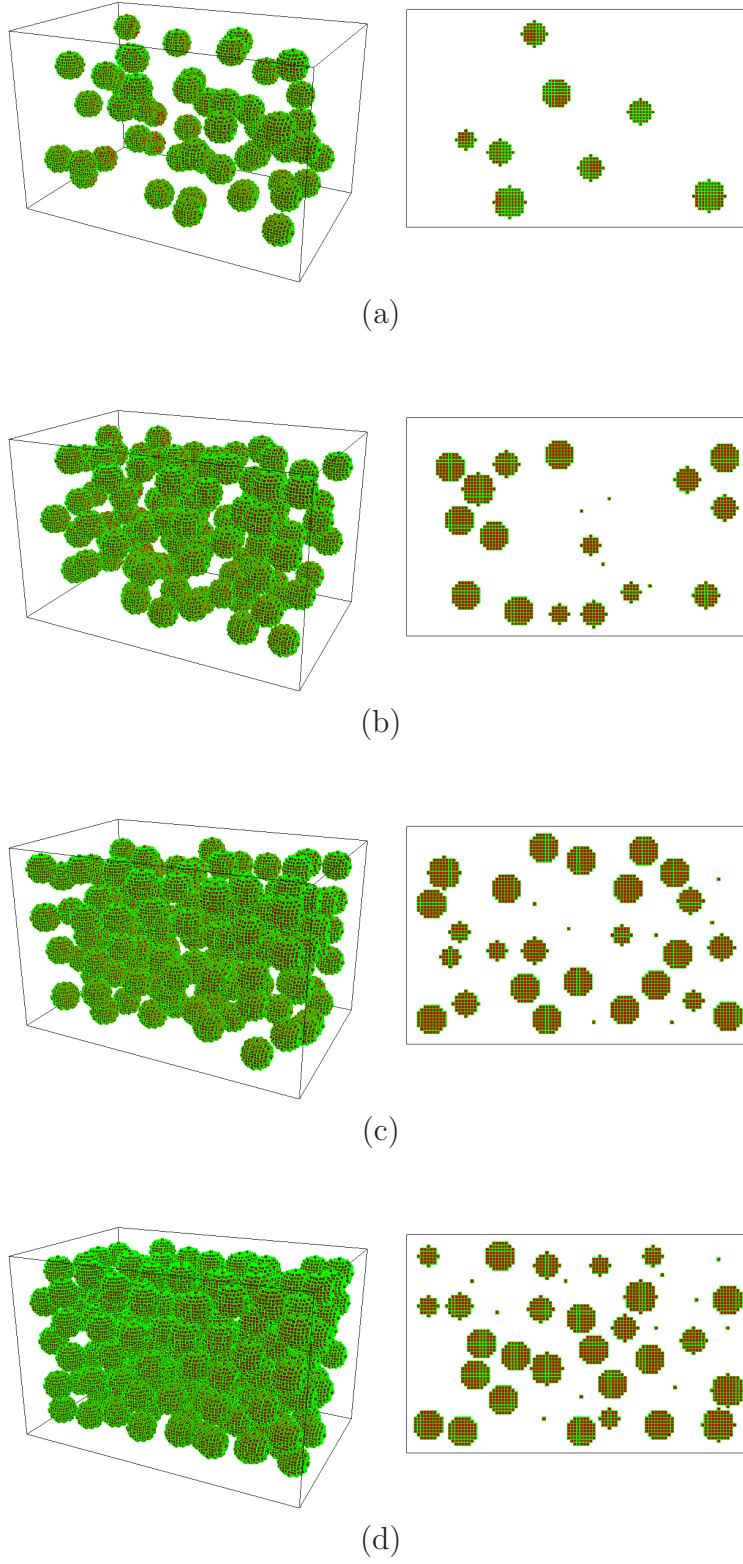


Figure 7.7: Spherical pore distributions in the specimen and distributions at the cross section along the longitudinal direction. Porosities (a)  $P = 5\%$ , (b)  $P = 10\%$ , (c)  $P = 15\%$ , and (d)  $P = 20\%$ . Pores are generated within the specimen boundaries.

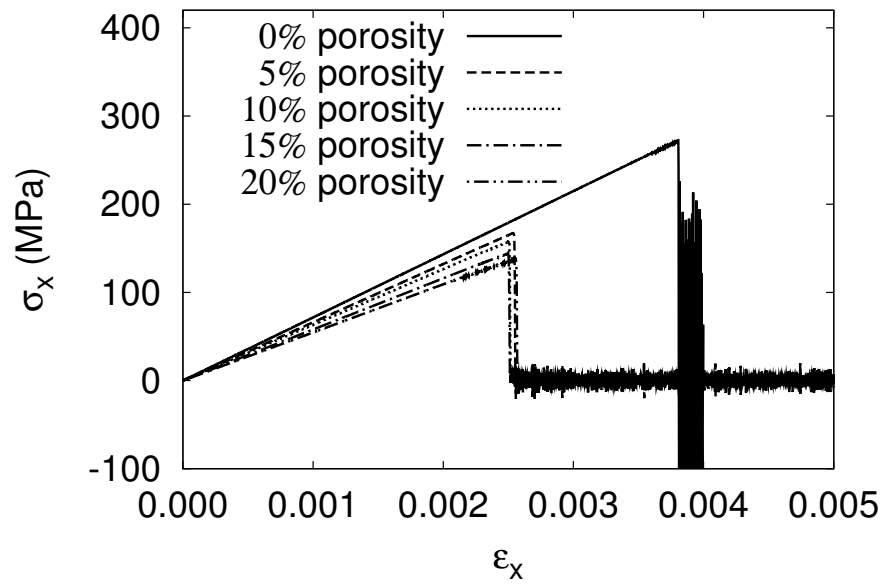
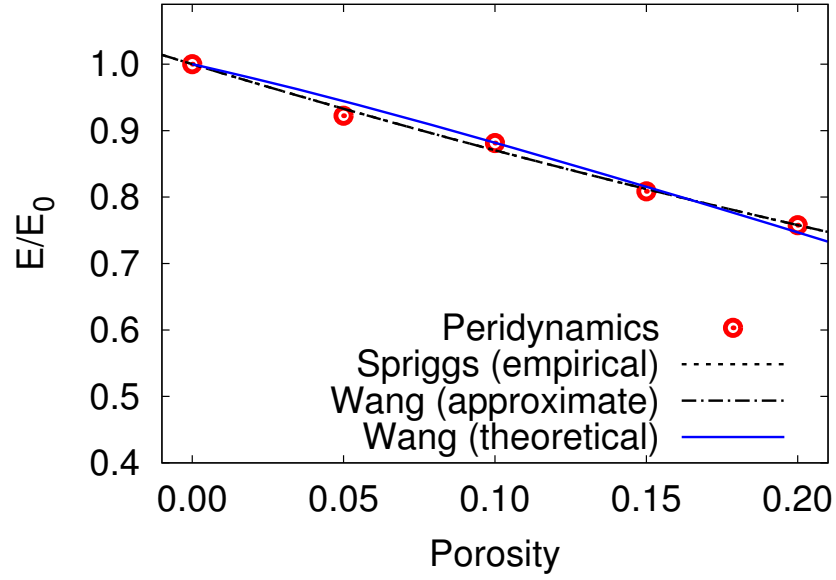
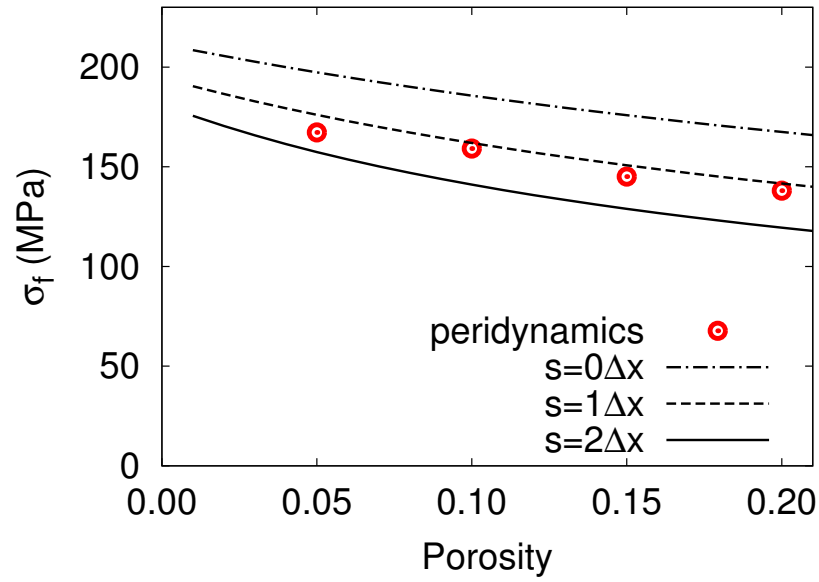


Figure 7.8: Cross-sectional stress versus strain of specimens containing spherical pores within the boundary.



(a)



(b)

Figure 7.9: (a) Normalized Young's modulus and (b) tensile strength of specimens containing spherical pores within the boundary.

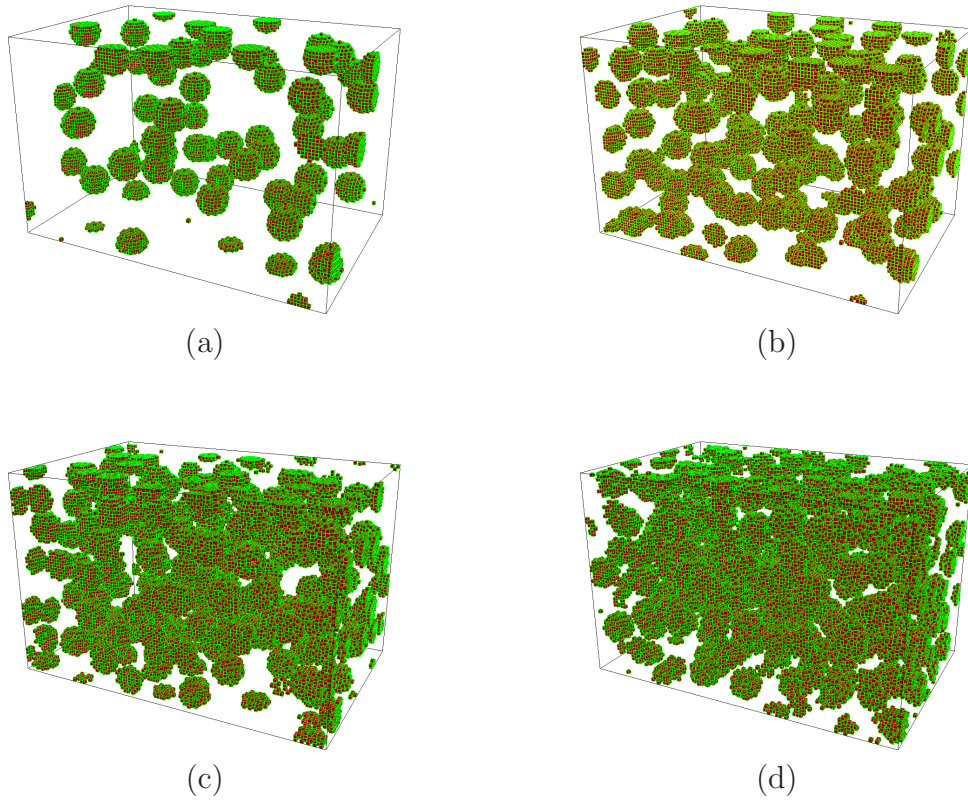


Figure 7.10: Spherical pore distributions in the specimen. Porosities (a)  $P = 5\%$ , (b)  $P = 10\%$ , (c)  $P = 15\%$ , and (d)  $P = 20\%$ . Pores intersect with specimen boundaries.

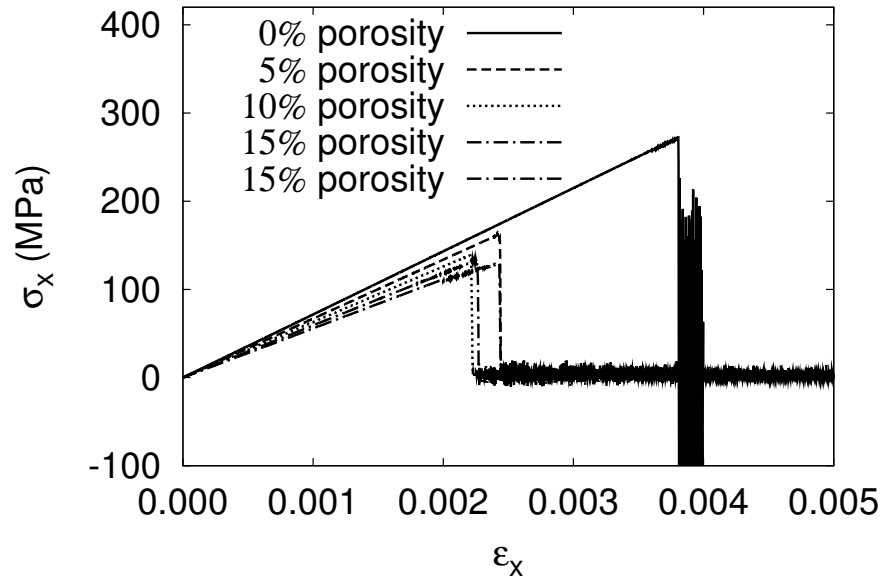
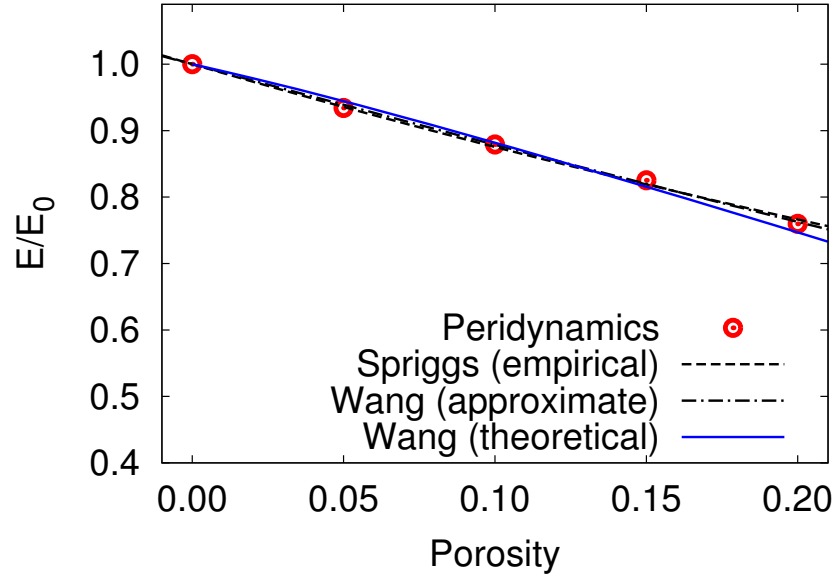
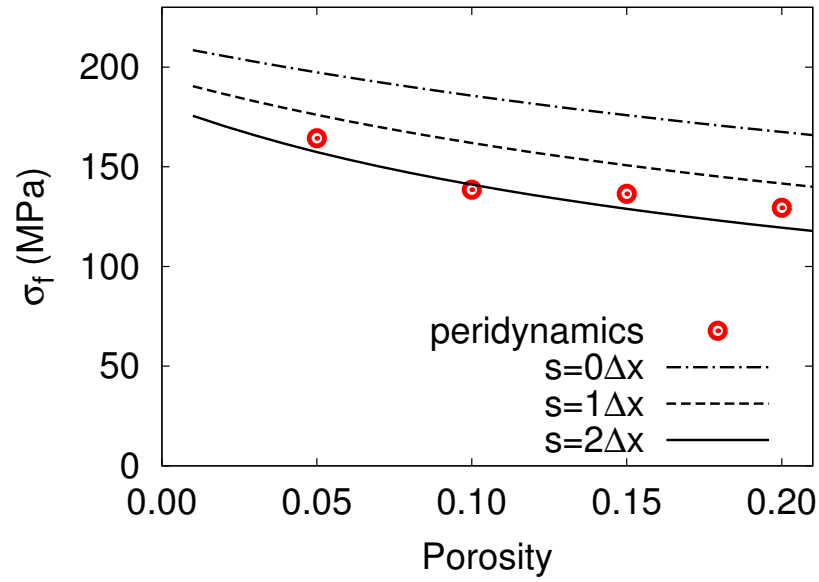


Figure 7.11: Cross-sectional stress versus strain of specimens containing spherical pores intersecting with boundaries.



(a)



(b)

Figure 7.12: (a) Normalized Young's modulus and (b) tensile strength of specimens containing spherical pores intersecting with boundaries.

## 7.5 Summary

In this chapter, peridynamics is employed to study brittle materials containing pores. Starting with analytical and empirical equations describing the effect of porosity on Young's modulus and the strength of solid materials, an algorithm is then introduced for generating cubic and spherical voids in discretized peridynamic models using the pseudorandom number generator.

Several numerical examples are given next. Specimens containing randomly distributed cubic voids with different porosities are studied. As the value of porosity increases, Young's modulus decreases, and the trend of degradation shows close agreement with the empirical models and the analytical solutions derived by considering the simple cubic stacking pattern. The degradation of strength with increasing porosity conforms to the empirical models.

Brittle solids containing spherical voids are then studied with varying amounts of porosity. Two cases, spherical pores distributed inside the specimen boundaries and pores having intersections with the boundaries, are examined. A comparison of numerical results to the empirical models and the analytical solutions in the degradation of Young's modulus is conducted, and the differences are within a few percent. The degradation of strength in the solids containing spherical pores is compared with the analytical solutions considering the effect of pore size and pore volume fraction. It is found that numerical solutions are close to analytical values if the size of the horizon is considered as the annular flaw extending from the void surface. In general, peridynamics is successfully implemented to study porous brittle solids.



# Chapter 8

## Conclusions and Recommendations

### 8.1 Conclusions

The primary focus of this research is development of the discretized peridynamics for solid mechanics. The thrust of research on peridynamics provides an alternative theory to the classical continuum mechanics that is directly applicable for numerical simulations of spontaneously formed discontinuities. The merit of peridynamics comes from the integration used for the calculation of forces on material points. This is in contrast to the classical theory in which partial derivatives are involved in the governing equation, and consequently approaches based on the framework of classical continuum mechanics fail to be directly applicable in the presence of singularities.

Chapter 3, Chapter 4, Chapter 5, Chapter 6, and Chapter 7, each has a different area within the framework of bond-based peridynamics. First, a connection between the classical elasticity and discretized peridynamics is established. By introducing the peridynamic stress corresponding to the classical (local) stress, calculating the corresponding peridynamic Young's modulus, and equilibrating the peridynamic Young's modulus with the conventional Young's modulus, micromoduli for one- and three-dimensional models are derived. The micromoduli derived in this research are referred to as *numerical micromoduli* since the value of micromodulus for a given horizon size is determined by numerical calculations on a dis-

cretization grid. The numerical micromoduli are different from the analytical micromoduli presented in [20, 49, 50] in that a finite number of peridynamic bonds are considered within the horizon of a node in the numerical micromoduli. It is found that the one-dimensional analytical micromoduli can yield the numerical micromoduli by substituting discretization parameters into the analytical micromoduli. For three-dimensional models, numerical micromoduli converge to the analytical micromoduli as the ratio of the horizon to the grid spacing increases. In the bond-based peridynamic theory, Poisson ratio  $\nu$  is a fixed value of  $1/4$ . For numerical simulations of an elastic body which has Poisson ratio not equal to  $1/4$ , a pairwise compensation scheme is introduced in this research. Compensation forces  $\hat{\mathbf{f}}$  are superposed in the directions perpendicular to the direction of the bond force  $\mathbf{f}$ , resulting in additional transverse deformations to simulate the effect of Poisson ratio other than  $1/4$ . The numerical results applying the proposed pairwise compensation scheme match the classical (local) solutions in the material responses including the stress, the strain, back-calculated Young's modulus, and Poisson ratio.

The research-purpose peridynamics code is implemented in the NVIDIA graphics processing unit (GPU) Tesla C1060 for the highly parallel computation. To the best of our knowledge, it was the first implementation of peridynamics on a GPU. An algorithm separating nested loops into independent loops is introduced to eliminate the loop dependency in the peridynamics code for the efficient parallelization. For three-dimensional problems, a significant speedup over the serial calculation on a CPU is achieved. With the high computational efficiency of GPU, numerical studies are conducted to investigate the responses of brittle and ductile material models. Stress-strain behaviors with different grid sizes and horizons are studied for a brittle material model. A comparison of stresses and strains between finite element analyses and peridynamic solutions is performed for a ductile material. To

bridge material models at different scales, a multiscale procedure is proposed. First, material properties are retrieved from the macroscopic responses of the peridynamic model. These retrieved properties are then used to modify the material model for finite element analyses. By applying the proposed procedure, the differences between finite element analyses and peridynamic solutions reduce substantially.

An approach to couple the discretized peridynamics and FEM is proposed to take advantage of the generality of peridynamics and the computational efficiency of FEM. The coupling of peridynamic and finite element subregions is achieved by means of interface elements. The proposed method in this research is different from the coupling method implementing peridynamics in a conventional finite element analysis code [115], the approach using overlapping regions [94], the submodeling approach [2, 133], and the morphing strategy [113]. Depending on how coupling forces are subdivided to FE nodes in an interface element, two types of coupling schemes, the VL-coupling scheme and the CT-coupling scheme respectively, are discussed. In the VL-coupling scheme, coupling forces are subdivided among all FE nodes comprising the interface elements. In the CT-coupling scheme, interfaces between peridynamic subregions and finite element subregions are defined in the reference configuration, and coupling forces are subdivided only among FE nodes at interfaces. For one-dimensional simulations, it is found that the CT-coupling scheme yields the solution very close to the analytical solution in all the domain including the finite element subregion, peridynamic subregion, and interfaces. For three-dimensional simulations, it is observed that the CT-coupling scheme is effective in resolving displacements normal to the interface of peridynamic and FE subregions. On the other hand, the VL-coupling scheme is capable to preserve Poisson effect at the interfaces. The proposed coupling approach is used to model the mixed mode fracture in a double-edge-notched concrete specimen, and numerical predictions of crack paths show

good agreement with the experimental result of crack patterns presented in [130].

A numerical scheme for the contact-impact procedure ensuring compatibility between a peridynamic domain and a non-peridynamic domain is developed. The contact between a discretized peridynamic domain and a non-peridynamic domain is modeled as a node-to-surface type. A penalty method is used to enforce displacement constraints, and dynamic analyses are performed by an explicit algorithm without iterations, which is different from the contact method used in [115, 107]. In the numerical examples, the impact between two rigid bodies is presented to validate the contact algorithm. The ballistic perforation of a steel plate is investigated numerically. Good agreement between the numerical simulations and the analytical model is found in the results of residual velocities. The physical process of perforation is well captured in the simulations using the proposed contact-impact scheme.

Peridynamics is applied to study porous brittle materials. An algorithm is developed to generate randomly distributed cubic voids and spherical voids for a given porosity. The material behaviors at the macroscopic level including the resultant Young's modulus and the strength are studied for varying amounts of porosity. The comparison of numerical results to the empirical models and the analytical solutions in the degradation of Young's modulus is conducted, and the differences are within a few percent. The degradation of strength in the solids containing spherical pores is compared with the analytical solution in which the effect of pore size and pore volume fraction are considered. It is found that the numerical solution is close to the analytical value if the horizon size is considered as the annular flaw extending from the void surface. In general, peridynamics is successfully implemented to study porous brittle solids.

## 8.2 Contributions

The contributions in this dissertation are summarized in the following:

- Connection between the classical elasticity and discretized peridynamics is established in terms of peridynamic stress.
- Numerical micromoduli for one- and three-dimensional discretized models are derived.
- A pairwise compensation scheme is introduced for numerical simulations of materials with Poisson ratio not equal to  $1/4$ .
- The research-purpose peridynamics code is implemented in a GPU for highly parallel computation, and a significant speedup is achieved.
- A multiscale procedure is proposed to bridge material models at different scales.
- An approach to couple the discretized peridynamics and the finite element method is proposed, and two types of coupling schemes are investigated.
- The mixed-mode crack pattern is investigated using the proposed coupling approach.
- A numerical scheme for the contact-impact procedure ensuring compatibility between a peridynamic domain and a non-peridynamic domain is developed.
- The physical process of perforation is well captured using the proposed contact-impact scheme.
- Peridynamics is employed to study porous brittle materials.

### 8.3 Recommendations for future research

Compared with the classical theory, peridynamics is a relatively new development. While this research has served to advance the development of peridynamics in establishing a connection between the discretized peridynamic models and classical continuum mechanics, the high performance computation of peridynamics, bridging material models at the peridynamic bond level and the macroscopic level for finite element analyses, coupling peridynamics with the conventional finite element method, the contact-impact procedure between a peridynamic domain and a non-peridynamic domain, and applications on porous brittle materials, there is considerable further research to be undertaken. The following are some aspects for further research of peridynamics.

First, the focus in this research is the bond-based peridynamics. Since constitutive models are defined at the bond level, the macroscopic material behavior might be different from the material behavior at the bond level especially for plastic materials. In Chapter 4, a multiscale approach is proposed to define a constitutive model for the finite element analysis based on the macroscopic material behavior of a peridynamic model. But it is difficult to recast a material model at the bond level based on the constitutive model in the classical theory, which is dependent on the stress tensor. A generalized formulation of the bond-based peridynamics is proposed by Silling *et al.* [156], which is referred to as the state-based peridynamics. A force state  $\underline{\mathbf{T}}$ , which is similar to the stress tensor, is proposed, and constitutive models in the classical theory are more likely to be implemented in the state-based peridynamic theory. The force density acting on the material point  $\mathbf{x}$  is defined by  $\underline{\mathbf{T}} - \underline{\mathbf{T}}'$ , where  $\underline{\mathbf{T}}'$  is the force state on the material point  $\mathbf{x}'$ . Note that the direction of the force state  $\underline{\mathbf{T}}$  might be different from the direction of the force state  $\underline{\mathbf{T}}'$  in the state-based peridynamic theory as shown in

Figure 8.1.

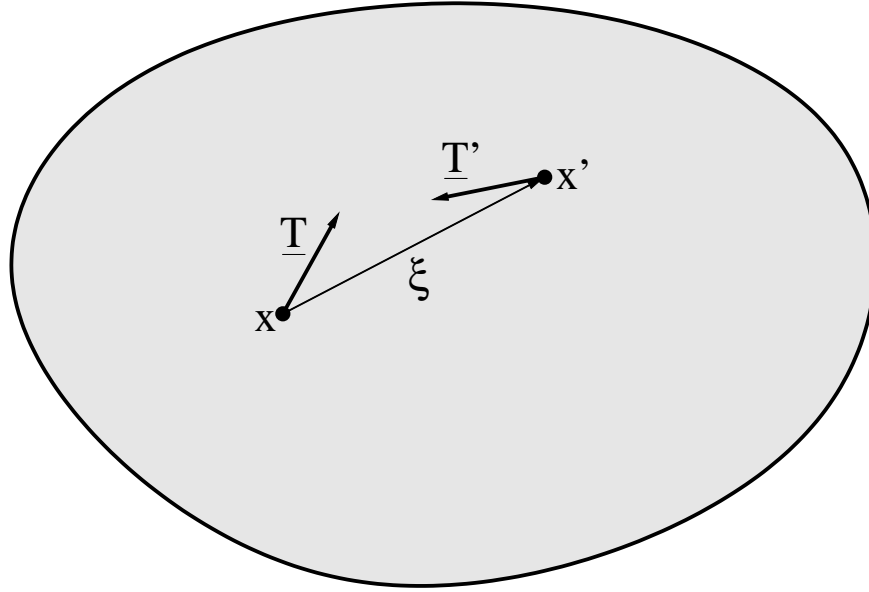


Figure 8.1: State-based peridynamics [156].

The coupling approach of peridynamics with the finite element method has been proven to be effective in Chapter 5. The numerical examples are validated under the quasi-static condition. It is interesting to study coupling models subjected to the dynamic loading. Since the stress waves have influence on the fracture behavior, particular attention is deserved on the stress waves at interfaces of coupling models. Furthermore, the coupling approach presented in Chapter 5 and the contact-impact procedure presented in Chapter 6 can be combined together to further reduce the computational burden. For example, a hybrid model discretized by peridynamic regions and finite element regions subjected to the impact of another body can further take advantage of the generality of peridynamics in the presence of continuities and the efficiency of FEM.

Most research efforts in the area of peridynamics have been concentrated on metals. In Chapter 5, the mixed mode fracture in a concrete specimen is studied, and numerical predictions of crack patterns are compared with experimental results. In the peridynamic

model, the concrete specimen is modeled using an ideally brittle material model. With the framework of porous materials presented in Chapter 7, a more realistic model of concrete using peridynamics can be developed. In the modeling of porous materials, randomly distributed voids are generated by deleting peridynamic bonds. Instead, voids can be treated as aggregates by introducing corresponding material properties, and bonds acting on voids can be considered as interactions between aggregates and cement if weak bond forces are introduced accordingly.



# APPENDICES

# Appendix A

## Derivation of Three-dimensional Micro-modulus

Applying the volume reduction scheme, we have

$$V_J = \beta_J V_J = \beta_J (\Delta x)^3. \quad (\text{A.1})$$

The peridynamic bond force is a function of the bond stretch  $s$  as

$$f = c_3 s. \quad (\text{A.2})$$

The projection of bond force  $f$  into the  $x$  axis is given as

$$f_x = f \frac{|x_J - x_I|}{\|\boldsymbol{\xi}\|} = c_3 s \frac{|x_J - x_I|}{\|\boldsymbol{\xi}\|}. \quad (\text{A.3})$$

The peridynamic stress is expressed as

$$\begin{aligned}
\sigma_x &= \frac{1}{A_I} \sum_{J=1}^{N_{\mathcal{L}}} (f_x \beta_J V_J) V_I \\
&= \frac{1}{A_I} \sum_{J=1}^{N_{\mathcal{L}}} \left( c_3 s \frac{|x_J - x_I|}{\|\boldsymbol{\xi}\|} \beta_J V_J \right) V_I \\
&= \frac{1}{(\Delta x)^2} \sum_{J=1}^{N_{\mathcal{L}}} \left( c_3 s \frac{|x_J - x_I|}{\|\boldsymbol{\xi}\|} \beta_J (\Delta x)^3 \right) (\Delta x)^3 \\
&= \sum_{J=1}^{N_{\mathcal{L}}} \left( c_3 s \frac{|x_J - x_I|}{\|\boldsymbol{\xi}\|} \beta_J \right) (\Delta x)^4.
\end{aligned} \tag{A.4}$$

Since the elastic body is subjected to the isotropic expansion, the stresses in  $y$ - and  $z$ -directions are identical to the  $x$ -directional stress  $\sigma_x$ , we have

$$\sigma_y = \sigma_z = \sigma_x. \tag{A.5}$$

By applying Hooke's law of linear elasticity, the peridynamic Young's modulus  $E_{pd}$  can be obtained as

$$\begin{aligned}
E_{pd} &= \frac{\sigma_x}{s} - \frac{\nu(\sigma_y + \sigma_z)}{s} \\
&= \frac{\sigma_x}{s} - \frac{2\sigma_x}{4s} \\
&= \frac{\sigma_x}{2s} \\
&= \frac{1}{2s} \left[ \sum_{J=1}^{N_{\mathcal{L}}} \left( c_3 s \frac{|x_J - x_I|}{\|\boldsymbol{\xi}\|} \beta_J \right) (\Delta x)^4 \right] \\
&= \frac{c_3}{2} \left[ \sum_{J=1}^{N_{\mathcal{L}}} \left( \frac{|x_J - x_I|}{\|\boldsymbol{\xi}\|} \beta_J \right) (\Delta x)^4 \right].
\end{aligned} \tag{A.6}$$

Setting peridynamic Young's modulus equal to the exact Young's modulus of the material, we have

$$E_{pd} = E. \quad (\text{A.7})$$

The three-dimensional micromodulus  $c_3$  is obtained as

$$c_3 = \frac{2E}{\left[ \sum_{J=1}^{N_{\mathcal{L}}} \left( \frac{|x_J - x_I|}{\|\boldsymbol{\xi}\|} \beta_J \right) (\Delta x)^4 \right]}. \quad (\text{A.8})$$

## Appendix B

# Derivation of Modified Peridynamic Young's Modulus

The modified peridynamic Young's modulus  $\hat{E}_{pd}$  should be determined based on  $E_{pd}$  to keep the strain identical. The longitudinal strain in  $x$ -direction in Figure 3.11 equals the strain in Figure 3.10, which is written as

$$\frac{\sigma_x}{E_{pd}} = \frac{\sigma_x}{\hat{E}_{pd}} - \frac{1}{4} \left( \frac{\hat{\sigma}_y}{\hat{E}_{pd}} + \frac{\hat{\sigma}_z}{\hat{E}_{pd}} \right). \quad (\text{B.1})$$

The strains in  $y$ - and  $z$ -directions also need to be identical to the strains in the original peridynamic model shown in Figure 3.10. Therefore, the equilibrium of the strain  $\varepsilon_y$  is expressed as

$$-\nu \frac{\sigma_x}{E_{pd}} = \frac{\hat{\sigma}_y}{\hat{E}_{pd}} - \frac{1}{4} \left( \frac{\sigma_x}{\hat{E}_{pd}} + \frac{\hat{\sigma}_z}{\hat{E}_{pd}} \right). \quad (\text{B.2})$$

Since the compensation forces are identical in all lateral directions perpendicular to the pairwise force  $\mathbf{f}$ , the lateral stresses are equal as

$$\hat{\sigma}_y = \hat{\sigma}_z. \quad (\text{B.3})$$

Substituting Equation (B.3) into Equation (B.1), we have

$$\frac{\sigma_x}{E_{pd}} = \frac{\sigma_x}{\hat{E}_{pd}} - \frac{1}{2} \frac{\hat{\sigma}_y}{\hat{E}_{pd}}. \quad (\text{B.4})$$

By multiplying  $\hat{E}_{pd}$  on both sides, Equation (B.4) is written as

$$\hat{E}_{pd} \frac{\sigma_x}{E_{pd}} = \sigma_x - \frac{1}{2} \hat{\sigma}_y. \quad (\text{B.5})$$

Substituting Equation (B.3) into Equation (B.2), we have

$$-\nu \frac{\sigma_x}{E_{pd}} = \frac{3}{4} \frac{\hat{\sigma}_y}{\hat{E}_{pd}} - \frac{1}{4} \frac{\sigma_x}{\hat{E}_{pd}}. \quad (\text{B.6})$$

By multiplying  $\hat{E}_{pd}$  on both sides, Equation (B.6) is written as

$$-\hat{E}_{pd} \nu \frac{\sigma_x}{E_{pd}} = \frac{3}{4} \hat{\sigma}_y - \frac{1}{4} \sigma_x. \quad (\text{B.7})$$

Substituting Equation (B.5) into Equation (B.7), we have

$$-\nu \left( \sigma_x - \frac{1}{2} \hat{\sigma}_y \right) = \frac{3}{4} \hat{\sigma}_y - \frac{1}{4} \sigma_x. \quad (\text{B.8})$$

The transverse lateral stress is expressed as

$$\hat{\sigma}_y = \frac{1 - 4\nu}{3 - 2\nu} \sigma_x. \quad (\text{B.9})$$

By substituting Equation (B.9) and Equation (B.3) into Equation (B.1), the modified peridynamic Young's modulus is obtained as

$$\hat{E}_{pd} = \frac{5}{6 - 4\nu} E_{pd}. \quad (\text{B.10})$$

# AppendixC

## Nonlinear Least Squares Method

Consider a data set consisting of  $n$  points  $(x_i, y_i), i = 1, 2, \dots, n$ . The model function is given as  $\mathbf{f}(\mathbf{x}, \boldsymbol{\beta})$ , where  $\boldsymbol{\beta}$  consists of  $m$  adjustable parameters. A residual [1] is defined as

$$r_i = y_i - f(x_i, \boldsymbol{\beta}), \quad (\text{C.1})$$

and the least squares method is to find the minimum of

$$S = \sum_{i=1}^n r_i^2. \quad (\text{C.2})$$

Since there is no analytical solution to a nonlinear least squares problem, the solution of the adjustable parameter  $\boldsymbol{\beta}$  needs to be determined by successive iterations as

$$\beta_j^{k+1} = \beta_j^k + \Delta\beta_j. \quad (\text{C.3})$$



At each iteration, the model function can be linearized using the first-order Taylor's series about  $\beta^k$  as

$$\begin{aligned} f(x_i, \beta) &= f^k(x_i, \beta) + \sum_{j=1}^m \frac{\partial f(x_i, \beta)}{\partial \beta_j} (\beta_j - \beta_j^k) \\ &= f^k(x_i, \beta) + \sum_{j=1}^m J_{ij} \Delta \beta_j, \end{aligned} \tag{C.4}$$

where  $J_{ij}$  is the Jacobian matrix. The residual given in Equation (C.1) can be written as

$$\begin{aligned} r_i &= y_i - f^k(x_i, \beta) - \sum_{j=1}^m J_{ij} \Delta \beta_j \\ &= \Delta y_i - \sum_{j=1}^m J_{ij} \Delta \beta_j. \end{aligned} \tag{C.5}$$

To find the minimum of the sum of squares of  $r_i$ , the gradient of Equation (C.2) is set to zero as

$$\begin{aligned} \frac{\partial S}{\partial \beta_j} &= 2 \sum_{i=1}^n r_i \frac{\partial r_i}{\partial \beta_j} \\ &= -2 \sum_{i=1}^n \frac{\partial f(x_i, \beta)}{\partial \beta_j} r_i \\ &= -2 \sum_{i=1}^n J_{ij} \left( \Delta y_i - \sum_{j=1}^m J_{ij} \Delta \beta_j \right) \\ &= 0. \end{aligned} \tag{C.6}$$

Rearranging Equation (C.6), we obtain  $m$  linear equations

$$\sum_{i=1}^n \sum_{k=1}^m J_{ij} J_{ik} \Delta \beta_k = \sum_{i=1}^n J_{ij} \Delta y_i, \tag{C.7}$$

which can be written in the matrix form as

$$\mathbf{J}\mathbf{J}^T\Delta\boldsymbol{\beta} = \mathbf{J}^T\Delta\mathbf{y}. \tag{C.8}$$

# AppendixD

## Newton-Raphson Method for Multi-dimensional Nonlinear Systems

A multi-dimensional nonlinear system with  $N$  variables is given as

$$F_i(x_1, x_2, \dots, x_N) = 0 \quad i = 1, 2, \dots, N. \quad (\text{D.1})$$

Using a vector  $\mathbf{x}$  to denote values of  $x_i$  and  $\mathbf{F}$  to denote functions  $F_i$ , each function can be expanded using Taylor's series as [144]

$$F_i(\mathbf{x} + \delta\mathbf{x}) = F_i(\mathbf{x}) + \sum_{j=1}^N \frac{\partial F_i}{\partial x_j} \delta x_j + O(\delta\mathbf{x}^2). \quad (\text{D.2})$$

The matrix of partial derivatives is the Jacobian matrix as

$$J_{ij} = \frac{\partial F_i}{\partial x_j}. \quad (\text{D.3})$$

The Equation (D.2) can be rewritten in matrix form as

$$\mathbf{F}(\mathbf{x} + \delta\mathbf{x}) = \mathbf{F}(\mathbf{x}) + \mathbf{J} \cdot \delta\mathbf{x} + O(\delta\mathbf{x}^2). \quad (\text{D.4})$$

By keeping only the first order term and setting  $\mathbf{F}(\mathbf{x} + \delta\mathbf{x}) = 0$ , a set of linear equations to calculate the increment of  $\mathbf{x}$  can be obtained

$$\mathbf{J} \cdot \delta\mathbf{x} = -\mathbf{F}. \quad (\text{D.5})$$

The solution of  $\mathbf{x}$  is updated by

$$\mathbf{x}_{\text{new}} = \mathbf{x}_{\text{old}} + \delta\mathbf{x}. \quad (\text{D.6})$$

# BIBLIOGRAPHY

# BIBLIOGRAPHY

- [1] [http://en.wikipedia.org/wiki/Least\\_squares](http://en.wikipedia.org/wiki/Least_squares).
- [2] A. Agwai, I. Guven, and E. Madenci. Damage prediction for electronic package drop test using finite element method and peridynamic theory. In *Electronic Components and Technology Conference, 2009. ECTC 2009. 59th*, pages 565–569. IEEE, 2009.
- [3] A. Agwai, I. Guven, and E. Madenci. Predicting crack initiation and propagation using XFEM, CZM and peridynamics: A comparative study. In *Electronic Components and Technology Conference (ECTC), 2010 Proceedings 60th*, pages 1178–1185. IEEE, 2010.
- [4] E. Anderheggen, D. Ekchian, K. Heiduschke, and P. Bartelt. A contact algorithm for explicit dynamic fem analysis. In *Computational Techniques, Proc. 1st Int. Conf*, pages 271–283. Southampton, UK, 1993.
- [5] T. L. Anderson. *Fracture mechanics: Fundamentals and applications*. CRC, 2005.
- [6] C. E. Anderson Jr, D. L. Littlefield, and J. D. Walker. Long-rod penetration, target resistance, and hypervelocity impact. *International Journal of Impact Engineering*, 14(1-4):1–12, 1993.
- [7] C. E. Anderson Jr, D. L. Orphal, T. Behner, and D. W. Templeton. Failure and penetration response of borosilicate glass during short-rod impact. *International Journal of Impact Engineering*, 36(6):789–798, 2009.
- [8] E. Askari, J. Xu, and S.A. Silling. Peridynamic analysis of damage and failure in composites. In *44th AIAA Aerospace Sciences Meeting and Exhibit, Reno, Nevada. Reston, VA: AIAA*, 2006.
- [9] M. E. Backman and W. Goldsmith. The mechanics of penetration of projectiles into targets. *International Journal of Engineering Science*, 16(1):1–99, 1978.
- [10] G. I. Barenblatt. The mathematical theory of equilibrium cracks in brittle fracture. *Advances in applied mechanics*, 7(55-129):104, 1962.

- [11] K. J. Bathe. *Finite element procedures*. Prentice Hall, Englewood Cliffs, NJ, 2006.
- [12] T. Behner, C. E. Anderson, D. L. Orphal, V. Hohler, M. Moll, and D. W. Templeton. Penetration and failure of lead and borosilicate glass against rod impact. *International Journal of Impact Engineering*, 35(6):447–456, 2008.
- [13] T. Belytschko and T. Black. Elastic crack growth in finite elements with minimal remeshing. *International Journal for Numerical Methods in Engineering*, 45(5):601–620, 1999.
- [14] T. Belytschko and J. I. Lin. A three-dimensional impact-penetration algorithm with erosion. *International Journal of Impact Engineering*, 5(1-4):111–127, 1987.
- [15] T. Belytschko and M. O. Neal. Contact-impact by the pinball algorithm with penalty and lagrangian methods. *International Journal for Numerical Methods in Engineering*, 31(3):547–572, 1991.
- [16] G. Ben-Dor, A. Dubinsky, and T. Elperin. Ballistic impact: recent advances in analytical modeling of plate penetration dynamics—a review. *Applied Mechanics Reviews*, 58:355, 2005.
- [17] R. F. Bishop, R. Hill, and N. F. Mott. The theory of indentation and hardness tests. *Proceedings of the Physical Society*, 57:147, 1945.
- [18] S. J. Bless and C. E. Anderson Jr. Penetration of hard layers by hypervelocity rod projectiles. *International Journal of Impact Engineering*, 14(1-4):85–93, 1993.
- [19] S. J. Bless, Z. Rosenberg, and B. Yoon. Hypervelocity penetration of ceramics. *International Journal of Impact Engineering*, 5(1-4):165–171, 1987.
- [20] F. Bobaru, M. Yang, L. F. Alves, S. A. Silling, E. Askari, and J. Xu. Convergence, adaptive refinement, and scaling in 1D peridynamics. *International Journal for Numerical Methods in Engineering*, 77(6):852–877, 2009.
- [21] T. Børvik, O. S. Hopperstad, T. Berstad, and M. Langseth. A computational model of viscoplasticity and ductile damage for impact and penetration. *European Journal of Mechanics-A/Solids*, 20(5):685–712, 2001.
- [22] T. Børvik, O. S. Hopperstad, S. Dey, E. V. Pizzinato, M. Langseth, and C. Albertini. Strength and ductility of weldox 460 E steel at high strain rates, elevated temperatures and various stress triaxialities. *Engineering fracture mechanics*, 72(7):1071–1087, 2005.

- [23] T. Børvik, O. S. Hopperstad, M. Langseth, and K. A. Malo. Effect of target thickness in blunt projectile penetration of weldox 460 E steel plates. *International journal of impact engineering*, 28(4):413–464, 2003.
- [24] T. Børvik, M. Langseth, O. S. Hopperstad, and K. A. Malo. Ballistic penetration of steel plates. *International journal of impact engineering*, 22(9-10):855–886, 1999.
- [25] M. J. Buehler and H. Gao. Dynamical fracture instabilities due to local hyperelasticity at crack tips. *Nature*, 439(7074):307–310, 2006.
- [26] V. A. Buryachenko. *Micromechanics of heterogeneous materials*. Springer Verlag, 2007.
- [27] C. A. Calder and W. Goldsmith. Plastic deformation and perforation of thin plates resulting from projectile impact. *International Journal of Solids and Structures*, 7(7):863–868, 1971.
- [28] N. J. Carpenter, R. L. Taylor, and M. G. Katona. Lagrange constraints for transient finite element surface contact. *International Journal for Numerical Methods in Engineering*, 32(1):103–128, 1991.
- [29] A. B. Chaudhary and K. J. Bathe. A solution method for static and dynamic analysis of three-dimensional contact problems with friction. *Computers & Structures*, 24(6):855–873, 1986.
- [30] J. S. Chen, C. Pan, C. T. Wu, and W. K. Liu. Reproducing kernel particle methods for large deformation analysis of non-linear structures. *Computer Methods in Applied Mechanics and Engineering*, 139(1-4):195–227, 1996.
- [31] C. Chinnaswamy, B. Amadei, and T. H. Illangasekare. A new method for finite element transitional mesh generation. *International journal for numerical methods in engineering*, 31(7):1253–1270, 1991.
- [32] J. D. Cinnamon, S. E. Jones, J. W. House, and L. L. Wilson. A one-dimensional analysis of rod penetration. *International journal of impact engineering*, 12(2):145–166, 1992.
- [33] R. Citarella and F. G. Buchholz. Comparison of crack growth simulation by DBEM and FEM for SEN-specimens undergoing torsion or bending loading. *Engineering Fracture Mechanics*, 75(3-4):489–509, 2008.
- [34] R. D. Cook, D. S. Malkus, M. E. Plesha, and R. J. Witt. *Concepts and applications of finite element analysis*. A1bazaar, 2007.



- [35] J. V. Cox. An extended finite element method with analytical enrichment for cohesive crack modeling. *International Journal for Numerical Methods in Engineering*, 78(1):48–83, 2009.
- [36] K. Dayal and K. Bhattacharya. Kinetics of phase transformations in the peridynamic formulation of continuum mechanics. *Journal of the Mechanics and Physics of Solids*, 54(9):1811–1842, 2006.
- [37] S. De, J. W. Hong, and K. J. Bathe. On the method of finite spheres in applications: towards the use with ADINA and in a surgical simulator. *Computational Mechanics*, 31(1):27–37, 2003.
- [38] R. De Borst. Some recent developments in computational modelling of concrete fracture. *International journal of fracture*, 86(1):5–36, 1997.
- [39] R. De Borst. Numerical aspects of cohesive-zone models. *Engineering fracture mechanics*, 70(14):1743–1757, 2003.
- [40] P. N. Demmieand and S. A Silling. An Approach to Modeling Extreme Loading of Structures using Peridynamics. *Bulletin of the American Physical Society*, 2006.
- [41] M. Di Prisco, L. Ferrara, F. Meftah, J. Pamin, R. De Borst, J. Mazars, and J. M. Reynouard. Mixed mode fracture in plain and reinforced concrete: some results on benchmark tests. *International journal of fracture*, 103(2):127–148, 2000.
- [42] J. F. Doyle. Determining the contact force during the transverse impact of plates. *Experimental Mechanics*, 27(1):68–72, 1987.
- [43] W. Duckworth. Discussion of paper by e. ryshkewitch, 'compressive strength of porous sintered alumina and zirconia'. *Journal of the American Ceramic Society*, 36:68, 1953.
- [44] D. S. Dugdale. Yielding of steel sheets containing slits. *Journal of the Mechanics and Physics of Solids*, 8(2):100–104, 1960.
- [45] S. K. Dutta, A. K. Mukhopadhyay, and D. Chakraborty. Assessment of strength by young's modulus and porosity: a critical evaluation. *Journal of the American Ceramic Society*, 71(11):942–947, 1988.
- [46] D. G. B. Edelen, A. E. Green, and N. Laws. Nonlocal continuum mechanics. *Archive for Rational Mechanics and Analysis*, 43(1):36–44, 1971.

- [47] N. Elabbasi, J. W. Hong, and K. J. Bathe. On the reliable solution of contact problems in engineering design. *International Journal of Mechanics and Materials in design*, 1(1):3–16, 2004.
- [48] M. Elices, G. V. Guinea, J. Gomez, and J. Planas. The cohesive zone model: advantages, limitations and challenges. *Engineering fracture mechanics*, 69(2):137–163, 2002.
- [49] E. Emmrich and O. Weckner. The peridynamic equation of motion in non-local elasticity theory. In *III European Conference on Computational Mechanics. Solids, Structures and Coupled Problems in Engineering, Lisbon,, Springer*, volume 19, 2006.
- [50] E. Emmrich and O. Weckner. On the well-posedness of the linear peridynamic model and its convergence towards the navier equation of linear elasticity. *Communications in Mathematical Sciences*, 5(4):851–864, 2007.
- [51] F. Ercolessi. A molecular dynamics primer. *Spring College in Computational Physics, ICTP, Trieste*, pages 24–25, 1997.
- [52] M. J. Forrestal, B. S. Altman, J. D. Cargile, and S. J. Hanchak. An empirical equation for penetration depth of ogive-nose projectiles into concrete targets. *International Journal of Impact Engineering*, 15(4):395–405, 1994.
- [53] M. J. Forrestal, D. J. Frew, J. P. Hickerson, and T. A. Rohwer. Penetration of concrete targets with deceleration-time measurements. *International Journal of Impact Engineering*, 28(5):479–497, 2003.
- [54] M. J. Forrestal, V. K. Luk, Z. Rosenberg, and N. S. Brar. Penetration of 7075-T651 aluminum targets with ogival-nose rods. *International journal of solids and structures*, 29(14-15):1729–1736, 1992.
- [55] M. J. Forrestal, K. Okajima, and V. K. Luk. Penetration of 6061-T651 aluminum targets with rigid long rods. *Journal of applied mechanics*, 55:755, 1988.
- [56] M. J. Forrestal and A. J. Piekutowski. Penetration experiments with 6061-T6511 aluminum targets and spherical-nose steel projectiles at striking velocities between 0.5 and 3.0 km/s. *International journal of impact engineering*, 24(1):57–67, 2000.
- [57] M. J. Forrestal, D. Y. Tzou, E. Askari, and D. B. Longcope. Penetration into ductile metal targets with rigid spherical-nose rods. *International journal of impact engineering*, 16(5-6):699–710, 1995.

- [58] J. T. Foster, S. A. Silling, and W. W. Chen. Viscoplasticity using peridynamics. *International Journal for Numerical Methods in Engineering*, 81(10):1242–1258, 2009.
- [59] J. T. Foster, S. A. Silling, and W. W. Chen. An energy based failure criterion for use with peridynamic states. *International Journal for Multiscale Computational Engineering*, 9:112, 2011.
- [60] J. W. Foulk, D. H. Allen, and K. L. E. Helms. Formulation of a three-dimensional cohesive zone model for application to a finite element algorithm. *Computer Methods in Applied Mechanics and Engineering*, 183(1-2):51–66, 2000.
- [61] D. J. Frew, M. J. Forrestal, and S. J. Hanchak. Penetration experiments with limestone targets and ogive-nose steel projectiles. *Journal of applied mechanics*, 67:841–845, 2000.
- [62] D. J. Frew, S. J. Hanchak, M. L. Green, and M. J. Forrestal. Penetration of concrete targets with ogive-nose steel rods. *International Journal of Impact Engineering*, 21(6):489–497, 1998.
- [63] H. Gao, Y. Huang, and F. F. Abraham. Continuum and atomistic studies of intersonic crack propagation. *Journal of the Mechanics and Physics of Solids*, 49(9):2113–2132, 2001.
- [64] T. C. Gasser and G. A. Holzapfel. 3D crack propagation in unreinforced concrete: A two-step algorithm for tracking 3D crack paths. *Computer Methods in Applied Mechanics and Engineering*, 195(37-40):5198–5219, 2006.
- [65] W. Gerstle, N. Sau, and S. A. Silling. Peridynamic modeling of concrete structures. *Nuclear Engineering and Design*, 237(12-13):1250–1258, 2007.
- [66] W. Goldsmith. *Impact: the theory and physical behaviour of colliding solids*. Dover Pubns, 1960.
- [67] J. T. Gomez and A. Shukla. Multiple impact penetration of semi-infinite concrete. *International journal of impact engineering*, 25(10):965–979, 2001.
- [68] F. I. Grace. Long-rod penetration into targets of finite thickness at normal impact. *International journal of impact engineering*, 16(3):419–433, 1995.
- [69] Y. D. Ha and F. Bobaru. Studies of dynamic crack propagation and crack branching with peridynamics. *International Journal of Fracture*, 162(1-2):229–244, 2010.

- [70] Y. D. Ha and F. Bobaru. Characteristics of dynamic brittle fracture captured with peridynamics. *Engineering Fracture Mechanics*, 78(6):1156 – 1168, 2011.
- [71] C. Hahn and P. Wriggers. An explicit multi-body contact algorithm. *PAMM*, 3(1):280–281, 2003.
- [72] J. O. Hallquist. *LS-DYNA theory manual*. Livermore Software Technology Corporation, 2006.
- [73] M. J. Harris. Fast fluid dynamics simulation on the GPU. *GPU gems*, 1:637–665, 2004.
- [74] D. P. H. Hasselman. Relation between effects of porosity on strength and on young’s modulus of elasticity of polycrystalline materials. *Journal of the American Ceramic Society*, 46(11):564–565, 1963.
- [75] M. W. Heinstein, F. J. Mello, S. W. Attaway, and T. A. Laursen. Contact–impact modeling in explicit transient dynamics. *Computer methods in applied mechanics and Engineering*, 187(3-4):621–640, 2000.
- [76] S. A. Hill. Determination of an empirical model for the prediction of penetration hole diameter in thin plates from hypervelocity impact. *International journal of impact engineering*, 30(3):303–321, 2004.
- [77] V. Hohler, A. J. Stilp, and K. Weber. Hypervelocity penetration of tungsten sinter-alloy rods into aluminum. *International journal of impact engineering*, 17(1-3):409–418, 1995.
- [78] B. L. Holian and R. Ravelo. Fracture simulations using large-scale molecular dynamics. *Physical Review B*, 51(17):11275–11288, May 1995.
- [79] J. W. Hong and K. J. Bathe. On analytical transformations for efficiency improvements in the method of finite spheres. *Computational fluid and solid mechanics*, pages 1990–1994, 2003.
- [80] J. W. Hong and K. J. Bathe. Coupling and enrichment schemes for finite element and finite sphere discretizations. *Computers & Structures*, 83(17-18):1386–1395, 2005.
- [81] W. Hu, Y. D. Ha, and F. Bobaru. Modeling dynamic fracture and damage in a fiber-reinforced composite lamina with peridynamics. *International Journal for Multiscale Computational Engineering*, 9(6), 2011.

- [82] W. Hu, Y. D. Ha, and F. Bobaru. Peridynamic model for dynamic fracture in uni-directional fiber-reinforced composites. *Computer Methods in Applied Mechanics and Engineering*, 217:247–261, 2012.
- [83] R. Huang, N. Sukumar, and J. H. Prévost. Modeling quasi-static crack growth with the extended finite element method Part II: Numerical applications. *International journal of solids and structures*, 40(26):7539–7552, 2003.
- [84] T. J. R. Hughes, R. L. Taylor, J. L. Sackman, A. Curnier, and W. Kanoknukulchai. A finite element method for a class of contact-impact problems. *Computer Methods in Applied Mechanics and Engineering*, 8(3):249–276, 1976.
- [85] A. Ibrahimbegovic and A. Delaplace. Microscale and mesoscale discrete models for dynamic fracture of structures built of brittle material. *Computers & structures*, 81(12):1255–1265, 2003.
- [86] G. R. Irwin. Linear fracture mechanics, fracture transition, and fracture control. *Engineering Fracture Mechanics*, 1(2):241–257, 1968.
- [87] G. R. Irwin and D. E. Wit. A summary of fracture mechanics concepts. *Journal of Testing and Evaluation*, 11:56–65, 1983.
- [88] S. E. Jones, P. P. Gillis, and J. C. Foster. On the penetration of semi-infinite targets by long rods. *Journal of the mechanics and physics of solids*, 35(1):121–131, 1987.
- [89] E. P. Kearsley and P. J. Wainwright. The effect of porosity on the strength of foamed concrete. *Cement and concrete research*, 32(2):233–239, 2002.
- [90] B. Kilic. *Peridynamic theory for progressive failure prediction in homogeneous and heterogeneous materials*. PhD thesis, The University of Arizona, 2009.
- [91] B. Kilic, A. Agwai, and E. Madenci. Peridynamic theory for progressive damage prediction in center-cracked composite laminates. *Composite Structures*, 90(2):141–151, 2009.
- [92] B. Kilic and E. Madenci. Prediction of crack paths in a quenched glass plate by using peridynamic theory. *International Journal of Fracture*, 156(2):165–177, 2009.
- [93] B. Kilic and E. Madenci. Structural stability and failure analysis using peridynamic theory. *International Journal of Non-Linear Mechanics*, 44(8):845–854, 2009.

- [94] B. Kilic and E. Madenci. Coupling of peridynamic theory and the finite element method. *Journal of mechanics of materials and structures*, 5,No.5:707–733, 2010.
- [95] F. P. Knudsen. Dependence of mechanical strength of brittle polycrystalline specimens on porosity and grain size. *Journal of the American Ceramic Society*, 42(8):376–387, 1959.
- [96] V. Kouznetsova, W. A. M. Brekelmans, and F. P. T. Baaijens. An approach to micro-macro modeling of heterogeneous materials. *Computational Mechanics*, 27(1):37–48, 2001.
- [97] V. Kouznetsova, M. G. D. Geers, and W. A. M. Brekelmans. Multi-scale constitutive modelling of heterogeneous materials with a gradient-enhanced computational homogenization scheme. *International Journal for Numerical Methods in Engineering*, 54(8):1235–1260, 2002.
- [98] J. Kozicki and J. Teichman. Modelling of fracture process in concrete using a novel lattice model. *Granular Matter*, 10(5):377–388, 2008.
- [99] V. D. Krstic. Porosity dependence of strength in brittle solids. *Theoretical and applied fracture mechanics*, 10(3):241–247, 1988.
- [100] V. D. Krstic. Effect of microstructure on fracture of brittle materials: Unified approach. *Theoretical and applied fracture mechanics*, 45(3):212–226, 2006.
- [101] J. Kruger and R. Westermann. Linear algebra operators for GPU implementation of numerical algorithms. In *ACM SIGGRAPH 2005 Courses*, page 234. ACM, 2005.
- [102] R. Kumar and B. Bhattacharjee. Porosity, pore size distribution and in situ strength of concrete. *Cement and concrete research*, 33(1):155–164, 2003.
- [103] P. Lall, S. Shantaram, and D. Panchagade. Peridynamic-models using finite elements for shock and vibration reliability of leadfree electronics. In *Thermal and Thermo-mechanical Phenomena in Electronic Systems (ITherm), 2010 12th IEEE Intersociety Conference on*, pages 1–12. IEEE, 2010.
- [104] R. B. Lehoucq and S. A. Silling. Force flux and the peridynamic stress tensor. *Journal of the Mechanics and Physics of Solids*, 56(4):1566–1577, 2008.
- [105] R. W. Lewis, B. A. Shrefler, and R. W. Lewis. *The finite element method in the static and dynamic deformation and consolidation of porous media*. John Wiley, 1998.

- [106] S. Li and W. K. Liu. Meshfree and particle methods and their applications. *Applied Mechanics Reviews*, 55:1, 2002.
- [107] D. J. Littlewood. Simulation of dynamic fracture using peridynamics, finite element modeling, and contact. In *Proceedings of the ASME 2010 International Mechanical Engineering Congress and Exposition (IMECE)*, 2010.
- [108] G. R. Liu and Y. T. Gu. Coupling of element free galerkin and hybrid boundary element methods using modified variational formulation. *Computational Mechanics*, 26(2):166–173, 2000.
- [109] G. R. Liu and M. B. Liu. *Smoothed particle hydrodynamics: a meshfree particle method*. World Scientific Pub Co Inc, 2003.
- [110] W. Liu and J. W. Hong. Three-dimensional lamb wave propagation excited by a phased piezoelectric array. *Smart Materials and Structures*, 19:085002, 2010.
- [111] W. K. Liu, Y. Chen, S. Jun, J. S. Chen, T. Belytschko, C. Pan, R. A. Uras, and C. T. Chang. Overview and applications of the reproducing kernel particle methods. *Archives of Computational Methods in Engineering*, 3(1):3–80, 1996.
- [112] Livermore Software Technology Corporation. *LS-DYNA keyword user’s manual*, 2007.
- [113] G. Lubineau, Y. Azdoud, F. Han, C. Rey, and A. Askari. A morphing strategy to couple non-local to local continuum mechanics. *Journal of the Mechanics and Physics of Solids*, 2012.
- [114] P. Lundberg, R. Renström, and B. Lundberg. Impact of metallic projectiles on ceramic targets: transition between interface defeat and penetration. *International Journal of Impact Engineering*, 24(3):259–275, 2000.
- [115] R. W. Macek and S. A. Silling. Peridynamics via finite element analysis. *Finite Elements in Analysis and Design*, 43(15):1169–1178, 2007.
- [116] S. Manavski and G. Valle. CUDA compatible GPU cards as efficient hardware accelerators for Smith-Waterman sequence alignment. *BMC bioinformatics*, 9(Suppl 2):S10, 2008.
- [117] S. Mariani and U. Perego. Extended finite element method for quasi-brittle fracture. *International Journal for Numerical Methods in Engineering*, 58(1):103–126, 2003.



- [118] G. T. Mase, R. E. Smelser, and G. E. Mase. *Continuum mechanics for engineers*. CRC, 1999.
- [119] P. K. Mehta and P. J. M. Monteiro. *Concrete: structure, properties, and materials*. Prentice-Hall, 1986.
- [120] J. M. Melenk and I. Babuska. The partition of unity finite element method: basic theory and applications. *Computer methods in applied mechanics and engineering*, 139(1-4):289–314, 1996.
- [121] G. Meschke and P. Dumstorff. Energy-based modeling of cohesive and cohesionless cracks via X-FEM. *Computer methods in applied mechanics and engineering*, 196(21-24):2338–2357, 2007.
- [122] N. Moës and T. Belytschko. Extended finite element method for cohesive crack growth. *Engineering Fracture Mechanics*, 69(7):813–833, 2002.
- [123] N. Moës, J. Dolbow, and T. Belytschko. A finite element method for crack growth without remeshing. *International Journal for Numerical Methods in Engineering*, 46(1):131–150, 1999.
- [124] J. J. Monaghan. Smoothed particle hydrodynamics. *Reports on Progress in Physics*, 68:1703, 2005.
- [125] H. Moslemi and A. R. Khoei. 3D adaptive finite element modeling of non-planar curved crack growth using the weighted superconvergent patch recovery method. *Engineering Fracture Mechanics*, 76(11):1703–1728, 2009.
- [126] L. E. Murr, S. A. Quinones, E. Ferreyra T, A. Ayala, O. L. Valerio, F. Hörz, and R. P. Bernhard. The low-velocity-to-hypervelocity penetration transition for impact craters in metal targets. *Materials Science and Engineering: A*, 256(1):166–182, 1998.
- [127] V. Murti and S. Valliappan. Numerical inverse isoparametric mapping in remeshing and nodal quantity contouring. *Computers & structures*, 22(6):1011–1021, 1986.
- [128] V. Murti, Y. Wang, and S. Valliappan. Numerical inverse isoparametric mapping in 3d fem. *Computers & structures*, 29(4):611–622, 1988.
- [129] L. F. Nielsen. Strength and stiffness of porous materials. *Journal of the American Ceramic Society*, 73(9):2684–2689, 1990.



- [130] M. B. Nooru-Mohamed, E. Schlangen, and J. G. M. van Mier. Experimental and numerical study on the behavior of concrete subjected to biaxial tension and shear. *Advanced Cement Based Materials*, 1(1):22–37, 1993.
- [131] NVIDIA. *NVIDIA CUDA Programming Guide*, version 2.3.1 edition, 2009.
- [132] E. T. Ooi and Z. J. Yang. Modelling dynamic crack propagation using the scaled boundary finite element method. *International Journal for Numerical Methods in Engineering*, 2011.
- [133] E. Oterkus. Peridynamic theory for modeling three-dimensional damage growth in metallic and composite structures. 2010.
- [134] M. L. Parks, R. B. Lehoucq, S. J. Plimpton, and S. A. Silling. Implementing peridynamics within a molecular dynamics code. *Computer Physics Communications*, 179(11):777–783, 2008.
- [135] M. L. Parks, S. J. Plimpton, R. B. Lehoucq, and S. A. Silling. Peridynamics with LAMMPS: A user guide. Technical report, Technical Report SAND 2008-1035, Sandia National Laboratories, 2008.
- [136] B. Patzák and M. Jirásek. Adaptive resolution of localized damage in quasi-brittle materials. *Journal of engineering mechanics*, 130:720, 2004.
- [137] K. K. Phani and S. K. Niyogi. Young’s modulus of porous brittle solids. *Journal of materials science*, 22(1):257–263, 1987.
- [138] E. H. Phillips, R. L. Davis, and J. D. Owens. Unsteady Turbulent Simulations on a Cluster of Graphics Processors. In *Proceedings of the 40th AIAA Fluid Dynamics Conference*, number AIAA-2010-5036. 40th AIAA Fluid Dynamics Conference, 2010.
- [139] A. J. Piekutowski, M. J. Forrestal, K. L. Poormon, and T. L. Warren. Penetration of 6061-T6511 aluminum targets by ogive-nose steel projectiles with striking velocities between 0.5 and 3.0 km/s. *International journal of impact engineering*, 23(1):723–734, 1999.
- [140] P. Pivonka, J. Ožbolt, R. Lackner, and H. A. Mang. Comparative studies of 3D-constitutive models for concrete: application to mixed-mode fracture. *International journal for numerical methods in engineering*, 60(2):549–570, 2004.

- [141] J. Planas, M. Elices, G. V. Guinea, F. J. Gómez, D. A. Cendón, and I. Arbilla. Generalizations and specializations of cohesive crack models. *Engineering fracture mechanics*, 70(14):1759–1776, 2003.
- [142] The Portland Group. *PGI Fortran & C Accelerator Programming Model v1.2*, 1.2 edition, 3 2010.
- [143] The Portland Group. *PGI User’s Guide*, release 2010 edition, 2010.
- [144] W. H. Press. *Numerical recipes in FORTRAN: the art of scientific computing*, volume 1. Cambridge Univ Pr, 1992.
- [145] R. F. Recht and T. W. Ipson. Ballistic perforation dynamics. *Journal of Applied Mechanics*, 30:384, 1963.
- [146] J. Réthoré, S. Roux, and F. Hild. Mixed-mode crack propagation using a hybrid analytical and extended finite element method. *Comptes Rendus Mécanique*, 338(3):121–126, 2010.
- [147] Z. Rosenberg and E. Dekel. On the deep penetration and plate perforation by rigid projectiles. *International Journal of Solids and Structures*, 46(24):4169–4180, 2009.
- [148] Z. Rosenberg, E. Dekel, V. Hohler, A. J. Stilp, and K. Weber. Hypervelocity penetration of tungsten alloy rods into ceramic tiles: experiments and 2-D simulations. *International journal of impact engineering*, 20(6-10):675–683, 1997.
- [149] M. Rössler and I. Odler. Investigations on the relationship between porosity, structure and strength of hydrated portland cement pastes: I. effects of porosity. *Cement and Concrete Research*, 15:320–330, 1985.
- [150] C. L. Rountree, R. K. Kalia, E. Lidorikis, A. Nakano, L. Van Brutzel, and P. Vashishta. Atomistic aspects of crack propagation in brittle materials: Multimillion atom molecular dynamics simulations. *Annual Review of Materials Research*, 32(1):377–400, 2002.
- [151] G. Ruiz, A. Pandolfi, and M. Ortiz. Three-dimensional cohesive modeling of dynamic mixed-mode fracture. *International Journal for Numerical Methods in Engineering*, 52(1-2):97–120, 2001.
- [152] E. Ryshkewitch. Compression strength of porous sintered alumina and zirconia. *Journal of the American Ceramic Society*, 36(2):65–68, 1953.

- [153] S. A. Silling. Reformulation of elasticity theory for discontinuities and long-range forces. *Journal of the Mechanics and Physics of Solids*, 48(1):175–209, 2000.
- [154] S. A. Silling. Linearized theory of peridynamic states. *Journal of Elasticity*, 99(1):85–111, 2010.
- [155] S. A. Silling and E. Askari. A meshfree method based on the peridynamic model of solid mechanics. *Computers & Structures*, 83(17-18):1526–1535, 2005.
- [156] S. A. Silling, M. Epton, O. Weckner, J. Xu, and E. Askari. Peridynamic states and constitutive modeling. *Journal of Elasticity*, 88(2):151–184, 2007.
- [157] S. A. Silling and R. B. Lehoucq. Convergence of peridynamics to classical elasticity theory. *Journal of Elasticity*, 93(1):13–37, 2008.
- [158] S. A. Silling and R. B. Lehoucq. Peridynamic theory of solid mechanics. *Advances in Applied Mechanics*, 44:73 – 168, 2010.
- [159] S. A. Silling and R. B. Lehoucq. Peridynamic theory of solid mechanics. *Advances in Applied Mechanics*, 44:73–168, 2010.
- [160] S. A. Silling, O. Weckner, E. Askari, and F. Bobaru. Crack nucleation in a peridynamic solid. *International Journal of Fracture*, 162(1):219–227, 2010.
- [161] S. A. Silling, M. Zimmermann, and R. Abeyaratne. Deformation of a peridynamic bar. *Journal of Elasticity*, 73(1):173–190, 2003.
- [162] R. J. M. Smit, W. A. M. Brekelmans, and H. E. H. Meijer. Prediction of the large-strain mechanical response of heterogeneous polymer systems: local and global deformation behaviour of a representative volume element of voided polycarbonate. *Journal of the Mechanics and Physics of Solids*, 47(2):201–221, 1999.
- [163] R. M. Spriggs. Expression for effect of porosity on elastic modulus of polycrystalline refractory materials, particularly aluminum oxide. *Journal of the American Ceramic Society*, 44(12):628–629, 1961.
- [164] T. A. C. Stock and K. R. L. Thompson. Penetration of aluminum alloys by projectiles. *Metallurgical and Materials Transactions B*, 1(1):219–224, 1970.
- [165] W. J. Stronge. *Impact mechanics*. Cambridge University Press, 2004.

- [166] R. Subramanian, S. J. Bless, J. Cazamias, and D. Berry. Reverse impact experiments against tungsten rods and results for aluminum penetration between 1.5 and 4.2 km/s. *International journal of impact engineering*, 17(4-6):817–824, 1995.
- [167] N. Sukumar, N. Moës, B. Moran, and T. Belytschko. Extended finite element method for three-dimensional crack modelling. *International Journal for Numerical Methods in Engineering*, 48(11):1549–1570, 2000.
- [168] N. Sukumar and J. H. Prévost. Modeling quasi-static crack growth with the extended finite element method Part I: Computer implementation. *International Journal of Solids and Structures*, 40(26):7513–7537, 2003.
- [169] Y. Sumi and Z. N. Wang. A finite-element simulation method for a system of growing cracks in a heterogeneous material. *Mechanics of Materials*, 28(1-4):197 – 206, 1998.
- [170] A. Tate. A theory for the deceleration of long rods after impact. *Journal of the Mechanics and Physics of Solids*, 15(6):387–399, 1967.
- [171] A. Tate. Further results in the theory of long rod penetration. *Journal of the Mechanics and Physics of Solids*, 17(3):141–150, 1969.
- [172] E. A. Taylor, K. Tsembeles, C. J. Hayhurst, L. Kay, and M. J. Burchell. Hydrocode modelling of hypervelocity impact on brittle materials: depth of penetration and conchoidal diameter. *International journal of impact engineering*, 23(1):895–904, 1999.
- [173] T. G. Trucano and D. E. Grady. Impact shock and penetration fragmentation in porous media. *International journal of impact engineering*, 17(4-6):861–872, 1995.
- [174] J. F. Unger, S. Eckardt, and C. Konke. Modelling of cohesive crack growth in concrete structures with the extended finite element method. *Computer methods in applied mechanics and engineering*, 196(41-44):4087–4100, 2007.
- [175] Ö. Vardar, I. Finnie, D.R. Biswas, and RM Fulrath. Effect of spherical pores on the strength of a polycrystalline ceramic. *International Journal of Fracture*, 13(2):215–223, 1977.
- [176] A. S. Wagh, J. P. Singh, and R. B. Poeppel. Dependence of ceramic fracture properties on porosity. *Journal of materials science*, 28(13):3589–3593, 1993.
- [177] J. C. Wang. Young’s modulus of porous materials: Theoretical derivation of modulus-porosity correlation. *Journal of materials science*, 19(3):801–808, 1984.

- [178] J. C. Wang. Young’s modulus of porous materials: Young’s modulus of porous alumina with changing pore structure. *Journal of Materials Science*, 19:809–814, 1984. 10.1007/BF00540452.
- [179] T. L. Warren and M. J. Forrestal. Effects of strain hardening and strain-rate sensitivity on the penetration of aluminum targets with spherical-nosed rods. *International journal of solids and structures*, 35(28):3737–3753, 1998.
- [180] T. L. Warren and K. L. Poormon. Penetration of 6061-T6511 aluminum targets by ogive-nosed VAR 4340 steel projectiles at oblique angles: experiments and simulations. *International journal of impact engineering*, 25(10):993–1022, 2001.
- [181] T. L. Warren, S. A. Silling, A. Askari, O. Weckner, M. A. Epton, and J. Xu. A non-ordinary state-based peridynamic method to model solid material deformation and fracture. *International Journal of Solids and Structures*, 46(5):1186–1195, 2009.
- [182] T. L. Warren and M. R. Tabbara. Simulations of the penetration of 6061-T6511 aluminum targets by spherical-nosed VAR 4340 steel projectiles. *International journal of solids and structures*, 37(32):4419–4435, 2000.
- [183] O. Weckner and R. Abeyaratne. The effect of long-range forces on the dynamics of a bar. *Journal of the Mechanics and Physics of Solids*, 53(3):705–728, 2005.
- [184] J. P. Weiler, J. T. Wood, R. J. Klassen, E. Maire, R. Berkmortel, and G. Wang. Relationship between internal porosity and fracture strength of die-cast magnesium am60b alloy. *Materials Science and Engineering: A*, 395(1):315–322, 2005.
- [185] M. L. Wilkins. Mechanics of penetration and perforation. *International Journal of Engineering Science*, 16(11):793–807, 1978.
- [186] M. Wolfe. The pgi accelerator programming model on NVIDIA GPUs. Technical report, The Portland Group, 2009.
- [187] P. Wriggers. *Computational contact mechanics*. Springer Verlag, 2006.
- [188] J. Xu, A. Askari, O. Weckner, and S. A. Silling. Peridynamic analysis of impact damage in composite laminates. *Journal of Aerospace Engineering*, 21:187, 2008.
- [189] M. Zimmermann. *A continuum theory with long-range forces for solids*. PhD thesis, Massachusetts Institute of Technology, 2005.